December 2002 • NREL/SR-520-33173

Subcontractor Report

Photocharge Transport and Recombination Measurements in Amorphous Silicon Films and Solar Cells by Photoconductive Frequency Mixing

Final Subcontract Report
20 April 1998–30 June 2002

R. Braunstein, M. Boshta, S. Sheng,
A. Kattwinkel, J. Liebe, and G. Sun
University of California
Los Angeles, California

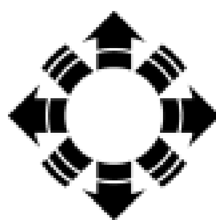

National Renewable Energy Laboratory

1617 Cole Boulevard
Golden, Colorado 80401-3393

NREL is a U.S. Department of Energy Laboratory
Operated by Midwest Research Institute • Battelle • Bechtel

Contract No. DE-AC36-99-GO10337

December 2002 • NREL/SR-520-33173

Photocharge Transport and Recombination Measurements in Amorphous Silicon Films and Solar Cells by Photoconductive Frequency Mixing

Final Subcontract Report
20 April 1998–30 June 2002

R. Braunstein, M. Boshta, S. Sheng,
A. Kattwinkel, J. Liebe, and G. Sun
University of California
Los Angeles, California

NREL Technical Monitor: B. von Roedern

Prepared under Subcontract No. XAK-8-17619-24

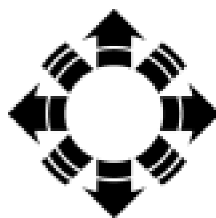

National Renewable Energy Laboratory

1617 Cole Boulevard
Golden, Colorado 80401-3393

NREL is a U.S. Department of Energy Laboratory
Operated by Midwest Research Institute • Battelle • Bechtel

Contract No. DE-AC36-99-GO10337

NOTICE

This report was prepared as an account of work sponsored by an agency of the United States government. Neither the United States government nor any agency thereof, nor any of their employees, makes any warranty, express or implied, or assumes any legal liability or responsibility for the accuracy, completeness, or usefulness of any information, apparatus, product, or process disclosed, or represents that its use would not infringe privately owned rights. Reference herein to any specific commercial product, process, or service by trade name, trademark, manufacturer, or otherwise does not necessarily constitute or imply its endorsement, recommendation, or favoring by the United States government or any agency thereof. The views and opinions of authors expressed herein do not necessarily state or reflect those of the United States government or any agency thereof.

Available electronically at http://www.osti.gov/bridge

Available for a processing fee to U.S. Department of Energy
and its contractors, in paper, from:
U.S. Department of Energy
Office of Scientific and Technical Information
P.O. Box 62
Oak Ridge, TN 37831-0062
phone: 865.576.8401
fax: 865.576.5728
email: reports@adonis.osti.gov

Available for sale to the public, in paper, from:
U.S. Department of Commerce
National Technical Information Service
5285 Port Royal Road
Springfield, VA 22161
phone: 800.553.6847
fax: 703.605.6900
email: orders@ntis.fedworld.gov
online ordering: http://www.ntis.gov/ordering.htm

Printed on paper containing at least 50% wastepaper, including 20% postconsumer waste

Preface

The prime candidate material for thin-film photovoltaic high efficient solar cells for large-scale power generation is hydrogenated amorphous silicon and alloys. The objectives of the technology in this field are to achieve stable and efficient units for cost effective bulk-power generation. The strategy in this field is to optimize amorphous thin film growth for greater efficiency, to suppress the light-induced instability, and to achieve high deposition rates so as to improve the throughput for a given machine, and also to reduce the costs and the capital investment. Material preparation efforts of amorphous semiconductors have concentrated on the reduction of "Urbach" edges, sub-bandgap absorption, and the density of deep defects to the end to maximize the photoconductive gain of the material. Most material efforts have been to optimize mobility-lifetime product ($\mu\tau$) as measured by steady state photoconductivity which does not determine μ and τ separately. To evaluate various photocharge transport models, it is essential that a simultaneous determination of the mobility and lifetime be performed so as to predict the performance of solar cells. We have developed a photomixing technique to separately determine the mobility and lifetime to characterize materials to predict solar cell performance and to allow the testing of new materials and devices in actual solar cell configurations. The present program formed part of the NREL High-Bandgap Alloy Team, the Metastability and the Mid- and Low-Bandgap Alloy Teams. Various groups were concerned with material synthesis and device fabrication. The UCLA Group performed photoconductive frequency mixing measurements on these material and solar cell devices to determine the optimum growth conditions for photocharge transport. The continuous feedback of the results of the UCLA Group to the synthesis groups relating material properties to device performance gave insight into the light-induced degradation mechanisms.

Table of Contents

Preface i

Table of Contents ii

List of Figures iv

List of Tables x

Executive Summary 1

Introduction 3

Results and Analysis 4

1. Improvement of Photomixing Instrumentation 4
2. Initial experiments on single film samples with coplanar and perpendicular contact geometry 6
3. Hydrostatic pressure dependence of the charge transport in amorphous silicon 9
4. Hydrostatic Pressure Dependence of Charged Transport and Small Angle X-ray Scattering Measurements 14
5. The "uninterrupted growth/annealing" method 15
6. Charge transport properties near and above the transition from amorphous to microcrystalline silicon 22
   - 6.1 Material produced at NREL 22
   - 6.2 Charge transport properties near and above the transition from amorphous to microcrystalline silicon produced at MVSystems 32
   - 6.3 Charge transport properties of microcrystalline silicon prepared by Pulsed PECVD technique (MVSystems Inc.) 47
7. High Deposition Rate Preparation of a-Si:H by HWCVD 54
   - 7.1 First series of samples 54
   - 7.2 The second series of samples 63
   - 7.3 Characterization of high deposition rate HWCVD a-Si:H films deposited on stainless steel substrates by Driven Level Capacitance Spectroscopy and transient photocapacitance at the University of Oregon. 75
   - 7.4 The effect of deposition rate on the transport properties of HWCVD a-Si:H films with respect to the substrate temperature, deposition pressure and silane flow rate 77
8. Measurements of amorphous (Si,Ge) alloys 85
   - 8.1 Measurements of homogenous a-SiGe alloy samples produced at NREL 85
   - 8.2 Charge transport properties of PECVD a-SiGe:H films produced by BP Solar 93

8.3 Electrical and optical properties of high quality low bandgap amorphous (Ge, Si) alloys prepared by ECR plasma deposition 96

9. Attempt at finding evidence of the existence of long range potential fluctuations in single crystal GeSi alloys 103

10. Photoconductive Frequency Mixing Measurements on TCO 104

11. Comparison of intrinsic film properties and device performance 105

12. Photomixing Measurements on SiGe P-I-N Devices (Supplied by Xunming Deng, Univerity of Toledo) 110

13. Photo-emission in Air 119

I. Statement of the problem 119
II. Implementation of photo-emission in Air 119
III. Results 120

14. Subcontract Supported Publications 134

15. References 135

List of Figures

Figure 1. Current through the μc-Si sample MVS723 (supplied by MVSystems, see previous section) during one 50ms BIAS pulse under illumination (a) and in dark condition (b). 4

Figure 2. Photomixing and dc – signal averaging and fitting (solid curves) 5

Figure 3. Sample schematics for measurements in two field directions. 6

Figure 4. DC and AC currents with perpendicular contact geometry(Film thickness 5244Å) .. 7

Figure 5. Field dependent mixing power for both configurations. For the TCO–a-Si:H–Al sample, the zero-field point was shifted according to the mixing power minimum at V = -0.5V (Fig. 4) 8

Figure 6. The Photoconductivity vs. Illumination time for three different pressures. 10

Figure 7. The drift mobility and lifetime as functions of illumination time under different pressures. 10

Figure 8. Infrared transmission of T516 under annealed ("ann"), pressured ("press"), and reannealed ("reann") conditions. 12

Figure 9. T516 – film thickness after pressure application. 12

Figure 10. Pressure-dependent transport parameters. After initial annealing, the sample was pressurized and released again. We performed four cycles in the same way, with the transport parameters monitored in situ. The x-axis position is associated with the over-all illumination period during the measurement. 12

Figure 11. DC photocurrent and photomixing signal under different pressures in single crystalline silicon. Both decrease with increasing pressure. The curves show only an elastic effect. 13

Figure 12. Samples G202 and G179, dilution ratio is kept constant at 1:5 17

Figure 13. Samples G203 and G204, dilution ratio is kept constant at 1:5 18

Figure 14. Samples I70426 and I80929. 19

Figure 15. Samples P60715I with flat and rough surface. These are prepared by employing the "uninterrupted growing/annealing" technique. 20

Figure 16. Photoconductivity of amorphous and microcrystalline silicon vs hydrogen content 24

Figure 17. The photomixing lifetime of amorphous and microcrystalline Si:H vs hydrogen content 25

Figure 18. The mobility of amorphous and microcrystalline Si:H vs. hydrogen content. 25

Figure 19. Drift mobility in the case of entirely amorphous samples 26

Figures 20 and 21. Range and depth of long-range potential fluctuations in amorphous and microcrystalline silicon-hydrogen 26

Figure 22. Normalized photoconductivity vs. illumination duration for T516, T531and T534 (amorphous state). The light intensities are given in the Figure. 27
Figure 23. Photoconductivity, mobility and lifetime vs. illumination duration, T529. 28
Figure 24. Photoconductivity, mobility and lifetime vs. illumination duration, T530. 28
Figure 25. Photoconductivity, mobility and lifetime vs. illumination duration, T532. 29
Figure 26. IR – spectra, sample T516 (a-Si:H) on polycrystalline substrate. 30
Figure 27. Stretching modes in a-Si:H. According to this double peak, a significant part of H atoms is bonded as monohydide in a dense Si network. 31
Figure 28. Stretching modes in microcrystalline silicon – high dilution (note the low 2000 - absorption). 31
Figure 29. Bending mode related absorption peak at around 900cm^{-1} in the mixed state sample T532. 31
Figure 30. Microcrystalline Silicon with low dilution ratio 31
Figure 31. Deconvolution of 2000/2100-peak (T516) 32
Figure 32. Stretching modes for several amorphous and microcrystalline samples. 32
Figure 33. MVS722 (a-Si:H) Results for the mobility, lifetime, and photoconductivity during light-soaking. 33
Figure 34. MVS823 (a-Si:H) Results for the mobility, lifetime, and photoconductivity during light-soaking. 33
Figure 35. MVS723 (μc-Si) Results for the mobility, lifetime, and photoconductivity during light-soaking 34
Figure 36. Light-induced changes of photoconductivity, mobility, and lifetime for sample MVS 968 36
Figure 37. XRD patterns of the HWCVD intrinsic Si films samples. The H-dilution degree and film thickness are also given 40
Figure 38. The photoconductivity of the samples as a function of H-dilution 41
Figure 39. The lifetime (a) and mobility (b) as a function of H-dilution 41
Figure 40. The depth (a) and range (b) of potential fluctuations as a function of H-dilution 42
Figure 41. The relative change in the density of charged defects as a function of H-dilution ... 42
Figure 42. The photoconductivity of the samples as a function of H-dilution 44
Figure 43. The mobility (a) and lifetime (b) as a function of H-dilution 45
Figure 44. The depth (a) and range (b) of potential fluctuations as a function of H-dilution 45
Figure 45. The relative change in the density of charged defects as a function of H-dilution ... 46
Figure 46. The effect of H-dilution on the photoconductivity of the samples........................... 49
Figure 47. The effect of H-dilution on the mobility (a) and lifetime (b) 50

Figure 48. The effect of H-dilution on the depth (a) and range (b) of potential fluctuations 50

Figure 49. The effect of H-dilution on the relative change in the density of charged defects.... 51

Figure 50. The effect of substrate temperature on the photoconductivity of the samples 52

Figure 51. The effect of substrate temperature on the mobility (a) and lifetime (b) 52

Figure 52. The effect of substrate temperature on the depth (a) and range (b) of potential fluctuations 53

Figure 53. The effect of substrate temperature on the relative change in the density of charged defects 53

Figure 54. The photoconductivity as a function of deposition rate 56

Figure 55. The drift mobility as a function of deposition rate 56

Figure 56. The lifetime as a function of deposition rate 56

Figure 57. Field dependence of the drift mobility (a) and lifetime (b) for sample L183 57

Figure 58. The depth (a) and range (b) of the long range potential fluctuations as a function of deposition rate 57

Figure 59. The relative change in the charged defects as a function of deposition rate 58

Figure 60. The hydrogen content as a function of deposition rate 58

Figure 61. Normalized photoconductivity, drift mobility and lifetime for high deposition rate HWCVD a-Si:H samples as a function of illumination 59

Figure 62. The light-induced changes in the photoconductivity, drift mobility and lifetime as a function of deposition rate 60

Figure 63. The light-induced changes in the depth and range of potential fluctuations as a function of deposition rate 61

Figure 64. The light-induced relative change in the charged defect density as a function of deposition rate. 62

Figure 65. The photoconductivity as a function of deposition rate ....

Figure 66. The lifetime as a function of deposition rate 65

Figure 67. The drift mobility as a function of deposition rate 65

Figure 68. Field dependence of the drift mobility (a) and the lifetime (b) as a function of deposition rate 66

Figure 69. The depth (a) and range (b) of the long range potential fluctuations as a function of deposition rate 67

Figure 70. The relative change in the density of charged defects as a function of deposition rate 67

Figure 71. The light-induced changes in the photoconductivity as function of deposition rate. 70

Figure 72. The light-induced changes in the drift mobility as a function of deposition rate...... 70

Figure 73. The light-induced changes in the lifetime as a function of deposition rate.. 70

Figure 74. Effect of light-soaking on the electric field dependence of the drift mobility as a function of deposition rate 71
Figure 75. Effect of light-soaking on the electric field dependence of the lifetime as a function of deposition rate 72
Figure 76. The light-induced changes in the depth (a) and range (b) of potential fluctuations as a function of deposition rate 73
Figure 77. The light-induced relative change in the charged defect density as a function of deposition rate 74
Figure 78. Deposition pressure dependence of the conductivity of the samples as a function of deposition rate 78
Figure 79. Deposition pressure dependence of the mobility (a) and lifetime (b) as a function of deposition rate 79
Figure 80. Deposition pressure dependence of the depth (a) and range (b) of the potential fluctuations as a function of deposition rate 79
Figure 81. Deposition pressure dependence of the relative change in the density of charged defects as a function of deposition rate 80
Figure 82. Deposition pressure dependence of the hydrogen content as a function of deposition rate 80
Figure 83. Silane flow rate dependence of the conductivity of the samples as a function of deposition rate 80
Figure 84. Silane flow rate dependence of the mobility (a) and lifetime (b) as a function of deposition rate 81
Figure 85. Silane flow rate dependence of the depth (a) and range (b) of the potential fluctuations as a function of deposition rate 81
Figure 86. Silane flow rate dependence of the relative change in the density of charged defects as a function of deposition rate 82
Figure 87. Silane flow rate dependence of the hydrogen content as a function of deposition rate 82
Figure 88. Substrate temperature dependence of the conductivity of the samples as a function of deposition rate 83
Figure 89. Substrate temperature dependence of the mobility (a) and lifetime (b) as a function of deposition rate 83
Figure 90. Substrate temperature dependence of the depth (a) and range (b) of the potential fluctuations as a function of deposition rate 84
Figure 91. Substrate temperature dependence of the relative change in the density of charged defects as a function of deposition rate 84
Figure 92. Substrate temperature dependence of the hydrogen content as a function of deposition rate 84

Figure 93. The normalized photoconductivity, mobility, and lifetime in a-Si:H as a function of illumination time. 86

Figure 94. The normalized photoconductivity, mobility, and lifetime as a function of illumination time. The GeH_4 gas flow ratio is 3%. 86

Figure 95. The normalized photoconductivity, mobility, and lifetime as a function of illumination time. The GeH_4 gas flow ratio is 3%. 87

Figure 96. The normalized photoconductivity, mobility, and lifetime as a function of illumination time. The GeH_4 gas flow ratio is 8%. 87

Figure 97. The normalized photoconductivity, mobility, and lifetime as a function of illumination time. The GeH_4 gas flow ratio is 17%. 88

Figure 98. RMS roughness vs. GeH_4 gas ratio. 89

Figure 99. Photoconductivity, mobility, lifetime, LRPF range and depth vs. germanium hydrogen gas flow ratio (annealed state). 90

Figures 100-102. The AFM scanning images and surface height distribution of the samples HGe 121, 113, and 100 91

Figures 103-104. The AFM scanning images and surface height distribution of the samples HGe 114 and HGe 118 92

Figure 105. The photoconductivity of the samples as a function of Ge content 94

Figure 106. The mobility (a) and lifetime (b) of the samples as a function of Ge content 94

Figure 107. The depth (a) and range (b) of potential fluctuations as a function of Ge content 95

Figure 108. The relative change in the density of charged defects as a function of Ge content 95

Figure 109. The optical absorption spectra of the samples. The Si content and Tauc gapE_g 99

Figure 110. The sub-gap absorption spectra of some of the samples. The Si content and the Urbach energy (E_o) of the valence band-tail are also given 100

Figure 111. The photoconductivity of the samples as a function of the Tauc gap 100

Figure 112. The mobility (a) and lifetime (b) of the samples as a function of the Tauc gap 101

Figure 113. The electric field dependence of the drift mobility as a function of the Tauc gap. The solid curves are fit of the data to equation (1) 101

Figure 114. The depth (a) and range (b) of potential fluctuations as a function of the Tauc gap 102

Figure 115. The relative change in the density of charged defects as a function of the Tauc gap. 102

Figure 116. Light-induced changes in photoconductivity, mobility, and lifetime of film R8796 (H_2 diluted, using 106

Figure 117. Light-induced changes in photoconductivity, mobility, and lifetime of film R8794 (H_2 diluted, using 106

Figure 118. dc-photoconductivity for nip-devices in the annealed state 108

Figure 119. Square root of mixing signal for nip-devices in the annealed state........................ 108
Figure 120. Normalized decay of the dc photocurrent in short circuit condition and the back-bias mixing signal in nip device R8791... 109
Figure 121. Normalized decay of the dc photocurrent in short circuit condition and the back-bias mixing signal in nip device R8792... 109
Figure 122. Normalized decay of the dc photocurrent in short circuit condition and the back-bias mixing signal in nip device R8793... 110
Figure 123. DC photocurrent and the square root of the photomixing power (inset: derivative of sqrt(P_{mix})). 112
Figure 124. Light intensity dependent photomixing current. Right hand-side:......................... 113
Figure 125. dc and mixing currents after different illumination times (Sample Toledo-GD112)... 114
Figure 126. dc and mixing currents after different illumination times (Sample Toledo-GD111)... 115
Figure 127. Sample Toledo-GD110... 116
Figure 128. dc and mixing currents after different illumination times (Sample Toledo-GD109)... 117
Figure 129. BIAS-dependent ac – photocurrent for two different spots 118
Figure 130. Schematic diagram of Photo-emission in air... 121
Figure 131. Electron energies between the anode and cathode in a diode under bias conditions. (a) Anode reversed bias (retarding field); (b) emission of space charge limited barrier results from space- charge just outside cathode surface; (c) saturation emission ... 122
Figure 132. Photo-emission current vs voltage bias 123
Figure 133. The photo-emission intensity of ITO and a-Si:H on stainless steel substrate......... 124
Figure 134. The photo-emission intensity of ITO on a-Si:H on stainless steel substrate.......... 125
Figure 135. The photo-emission intensity of ITO/pin/SS layers... 126
Figure 136. The photo-emission intensity of Pd/ni/SS layers. 127
Figure 137. The photo-emission intensity of a-Si:H on c-Si substrate..................................... 128
Figure 138. The photo-emission intensity the 16 pads which are a-Si:H to μc-Si:H and a-SiGe:H to μc-SiGe:H on stainless steel substrate. 129
Figure 139(a). The photo-emission intensity of a-SiC:H on stainless steel substrate. 130
Figure 139(b). The photo-emission intensity of a-SiC:H on stainless steel substrate. 131
Figure 139(c). The photo-emission intensity of a-SiC:H on stainless steel substrate. 132
Figure 139(d). The photo-emission intensity of a-SiC:H on stainless steel substrate. 133

List of Tables

Table 1. Deposition conditions 16

Table 2. Long range potential fluctuations 21

Table 3. Summary of the sample characterization results (Qi Wang). 23

Table 4. LRPF Range and Depth for the MVS – samples (the thickness of the intrinsic layers were about 5000Å). 34

Table 5. Sample data as provided by MVSystems 35

Table 6. Preparation conditions and thickness of HWCVD μc-Si:H samples provided by MVSystems Inc. 37

Table 7. The effect of hydrogen dilution on the transport properties of μc-Si:H samples provided by MVSystems Inc. 38

Table 8. The effect of substrate temperature on the transport properties of μc-Si:H samples provided by MVSystems Inc. 38

Table 9. The effect of flament-substrate distance on the transport properties of μc-Si:H samples provided by MVSystems Inc. 39

Table 10. Preparation conditions and thickness of HWCVD μc-Si:H samples provided by MVSystems Inc. 43

Table 11. Deposition conditions and properties of Pulsed PECVD μc-Si:H samples provided by MVSystems 48

Table 12. XRD characterizations of Pulsed PECVD μc-Si:H samples provided by MVSystems. 48

Table 13. Growth conditions and properties of high deposition rate HWCVD samples. 55

Table 14. Growth conditions and properties of high deposition rate HWCVD samples. 64

Table 15. Characterization of high deposition rate HWCVD a-Si:H samples deposited on stainless steel substrates. (supplied by the University of Oregon) 75

Table 16. Preparation Conditions of High Deposition Rate HWCVD a-Si:H Samples. 78

Table 17. The characteristics of a-SiGe:H and a-Si:H. 85

Table 18. The photoconductivity, drift mobility, lifetime, and range and depth of long range potential fluctuations in annealed state for a-SiGe:H alloys prepared with different GeH_4 gas flow ratio. 88

Table 19. The photoconductivity, drift mobility, lifetime, and range and depth of long range potential fluctuations in light-soaked state for a-SiGe:H alloys prepared with different GeH_4 gas flow ratio. 89

Table 20. The Ge content and film thickness for the samples produced by BP Solar. 93

Table 21. Growth conditions and properties of ECR a-GeSi:H/a-Ge:H samples. 97

Table 22. Growth conditions of the films and the respective i-layers in the n-i-p structures. 105
Table 23. Long-range potential fluctuations. 107
Table 24. I-V data for a-SiGe solar cells with different i-layers (~2000Å). 117

Executive Summary

The instrumentation of the photomixing measurements has been improved by applying BIAS pulses of arbitrary width and frequency. This pulsed photomixing method enables the determination of transport properties of samples with high conductivity, and can considerably improve the accuracy of the measurements at low electrical fields applied.

Measurements of the transport parameters under hydrostatic pressure were initiated to investigate whether the application of hydrostatic pressure could alter light induced degradation behavior and as a possible test of the various theories that have been recently been developed to explain the cause of light-degradation involving the mobility of hydrogen. Furthermore, we investigated the hydrostatic pressure dependence of small angle X-ray scattering measurements to try to find out the origin of the inelastic effect observed.

The charge transport and structural properties and their light-induced changes near and above the transition from amorphous to microcrystalline silicon prepared by HWCVD and Pulsed PECVD techniques have been investigated in detail by the photomixing, FTIR and XRD techniques. A study of the effects of the H-dilution, substrate temperature and filament-substrate distance (F-S) on transport properties of the HWCVD samples showed that higher H-dilution, higher substrate temperature and shorter F-S can help improve the transport properties. XRD results of the Pulsed PECVD samples showed that the ratio of the (220) XRD peak area to the (111) peak area is seen to be in the range of 700% for the films near the transition regime, indicating that the transition films are strongly (220) oriented. Moreover, higher substrate temperature is required for the Pulsed PECVD technique to produce high quality films and related devices near the transition regime. We found both improved stability against light-soaking and dramatically different values for the lifetime and mobility close to the onset of microcrystallinity as compared to the amorphous state. In particular, the lifetime of charge carriers in some of the μc-Si:H samples turns out to lie about two orders of magnitude higher than that of a-Si:H films. The mobility, on the other hand, is shown rather to decrease in and above the transition regime. Additional measurements of the range and the depth of long range potential fluctuations yield a possible explanation for our results in that grain boundaries may serve as scattering centers and barriers against recombination.

The electronic transport properties in both annealed and light-soaked states of high deposition rate a-Si:H films prepared by HWCVD has been investigated in detail by the photomixing technique and Driven Level Capacitance Spectroscopy and transient photocapacitance. The high deposition rate (up to 1 μm/min.) was achieved by increasing deposition pressure, silane flow rate, and decreasing filament-to-substrate distance. The effects of the deposition rate on the resultant film properties with respect to the substrate temperature, deposition pressure and silane flow rate were studied. It was found that the film transport properties do not change monotonically with increasing deposition rate. The photoconductivity peaks at ~70-90 Å/s, where both the drift mobility and lifetime peak, consistent with the deposition rate dependence of the range and depth of the potential fluctuations. High quality, such as a photoconductivity-to-dark-conductivity ratio of $\sim 10^5$ and nearly constant low charged defect density, can be maintained at deposition rates up to ~130 Å/s, beyond which the film properties deteriorate

rapidly as a result of an enhanced effect of long-range potential fluctuations due to a considerable increase in the concentration of the charged defects. Our results indicate that medium silane flow rate, low pressure, and higher substrate temperature are generally required to maintain high quality films at high deposition rates.

The charge transport and optical properties of amorphous (Si,Ge) alloys prepared by HWCVD, PECVD and ECR plasma deposition techniques as a function of alloy composition have been investigated in detail by the photomixing technique and optical absorption spectroscopy. Evidence for the presence of long-range potential fluctuations in a-SiGe:H was revealed from the measurements of electric field dependence of the drift mobility, and the effect of the long-range potential fluctuations is enhanced by the addition of Ge to the alloy system that results in the deterioration of the opto-electronic properties of a-SiGe:H. It was found that at a composition of ~10% Ge in Si for HWCVD, and ~20% for PECVD, the photoresponse begins to decrease monotonically with increasing Ge content due to the decreases in both the drift mobility and the lifetime as a result of an increase in the concentration of charged defects, which lead to the long-range potential fluctuations whose depth increases, while the range decreases. On the other hand, High quality low bandgap a-(Ge, Si):H alloys at the Ge end were successfully prepared using ECR plasma deposition with high H dilution and ppm B-doping. Incorporating these high quality materials into devices leads to much lower gap a-(Ge, Si) solar cells (down to ~1 eV in a-Ge:H) with acceptable performance. It was found that at $SiH_4/(SiH_4+GeH_4)$ ~30%, the photoresponse begins to decrease rapidly with increasing Si content due to the decreases in the mobility and lifetime, and meanwhile, both the charged defect density and the Urbach energy increase significantly. The latter indicates an increase in the compositional disorder. It is the potential fluctuations whose effect can be also enhanced by incorporating Si to the alloy system that result in the deterioration of the opto-electronic properties of a-(Ge, Si):H alloys, similar to the case of the incorporation of Ge at the Si end. The increased charged scattering centers and compositional disorder upon adding Si or Ge to the alloys observed play an important role in the potential fluctuations.

We also attempted to employ the photomixing technique to find evidence of the existence of long-range potential fluctuations in single crystal GeSi alloys, and to measure the drift mobility of TCO.

Photomixing experiments were initiated on study of the impact of the changed contact geometry on the results of our photomixing measurements. Photomixing experiments were also initiated on p-i-n devices, and on comparison of intrinsic film properties and related device performance.

Time resolved photo- and thermoelectric effects (TTE) were used to simultaneously determine the thermal diffusivity, carrier lifetime, carrier mobility, and trap level density in crystalline and amorphous Si (a-Si:H) and Si/Ge (a-Si/Ge:H) samples.

Introduction

The research pursued during the past three years under NREL subcontract #XAK-8-17619-24 were part of a collaboration with members of the NREL Wide-bandgap Alloy Team, the Metastability and the Mid- and Low-Bandgap Alloy Teams. The tasks were focused on the characterization of the charge transport, opto-electronic and structural properties of a number of amorphous and microcrystalline semiconductors prepared by a number of techniques. The dominant approach to accomplish the tasks of the present phase of the program is the photoconductive frequency mixing technique. This technique enabled us to separately determine the drift mobility and the photomixing lifetime of the photogenerated carriers [1-6]. The technique is based on the idea of heterodyne detection for photoconductors. When two similarly polarized monochromatic optical beams of slightly different frequencies are incident upon a photoconductor, the photocurrent produced, when a dc bias applied, will contain components resulting from the square of the sum of the incident electric fields. Consequently, a photocurrent composed of a dc and a microwave current due to the beat frequency of the incident fields will be produced; these two currents allow a separate determination of the drift mobility and the photomixing lifetime. In the present work, we improved the instrumentation of the photomixing measurements by applying BIAS pulses of arbitrary width and frequency. The longitudinal modes of a He-Ne laser were employed to generate a beat frequency of 252 MHz; all the measurements were performed at this frequency for the data indicated in the accompanying figures and tables. Employing this technique, as well as other techniques, including FTIR, XRD, SAXS, Optical Spectroscopy, etc., the following topics were explored whose results will be presented in the following sections:

1. Improvement of Photomixing Instrumentation.
2. Initial experiments on single film samples with coplanar and perpendicular contact geometry.
3. Hydrostatic pressure dependence of the charge transport in amorphous silicon.
4. Hydrostatic pressure dependence of charged transport and Small Angle X-ray Scattering measurements.
5. Photomixing measurements on samples prepared by the “uninterrupted growth/annealing” method.
6. Charge transport and structural properties near and above the transition from amorphous to microcrystalline silicon prepared by HWCVD and Pulsed PECVD.
7. Charge transport properties of high deposition rate HWCVD a-Si:H.
8. The charge transport and optical properties of amorphous (Si,Ge) alloys prepared by HWCVD, PECVD and ECR plasma deposition.
9. Attempt at finding evidence of the existence of long range potential fluctuations in single crystal GeSi alloys.
10. Photoconductive frequency mixing measurements on TCO.
11. Comparison of intrinsic film properties and device performance.
12. Photomixing measurements on SiGe P-I-N Devices.

Results and Analysis

1. Improvement of Photomixing Instrumentation

Lately, several groups have taken steps into development and investigation of silicon films in the microcrystalline or μc-/a-Si:H mixed state. These films typically show relatively high dark currents at room temperature, which in turn limited the maximum electric BIAS we could apply to rather low values. Accordingly, the accuracy of the photomixing lifetime and mobility determinations suffered from both low electrical fields, i.e. low photomixing signals, and, more seriously, a heating of the sample during measurements that led to an increase of the current of one order of magnitude over the actual photocurrent.

In order to meet the requirements of high accuracy and stable sample temperature, we modified our Photoconductive Frequency Mixing setup and are now able to apply BIAS pulses of arbitrary width and frequency. The dc-current is now monitored sampling the voltage over a 1kΩ resistor by a PC-DAQ board. The whole setup is controlled using LabVIEW programs.

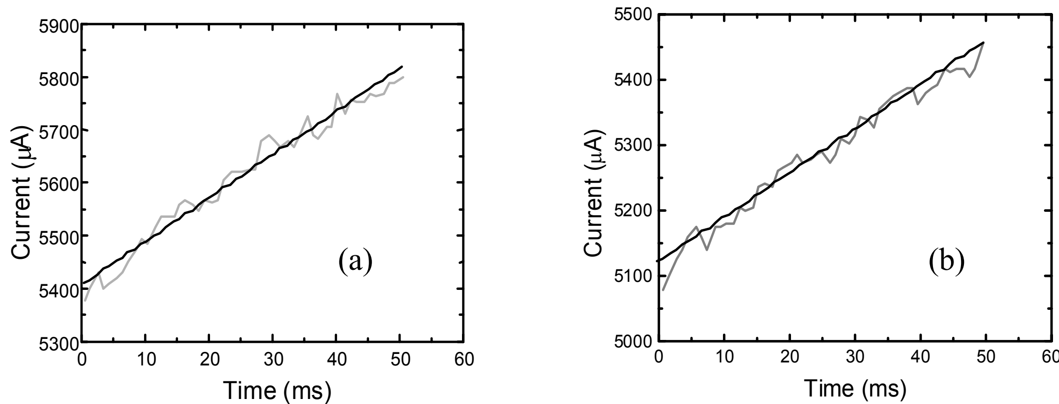

Figure 1. Current through the μc-Si sample MVS723 (supplied by MVSystems, see previous section) during one 50ms BIAS pulse under illumination (a) and in dark condition (b).

Figure 1 shows the time dependent dc-current under BIAS application in the dark and illumination case. The sampling rate here is 1000 samples per second (applies for both dc-current and ac-signal), one 50ms - pulse is applied per second whereby one measurement cycle consists of one dark and one light signal acquisition. When the light current is to be measured during a field dependent measurement, the shutter is opened 100ms in advance, which means a total illumination duration of 0.25 seconds per two-second-cycle. In the case of decay measurements, the sample is illuminated 1.75 seconds per cycle. These results are then averaged over at least 100 points for each BIAS point in the field-dependent dc- and ac-curves (see Fig. 2).

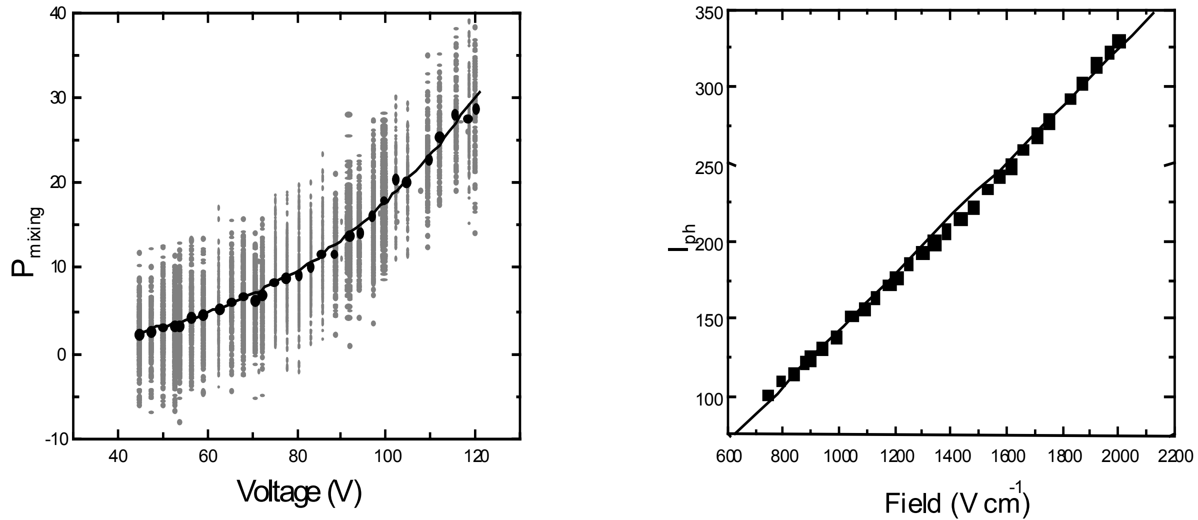

Figure 2. Photomixing and dc – signal averaging and fitting (solid curves) (sample: MVS723, light-soaked state).

As to be seen in the above figure, given enough data points to average, we obtain curves with satisfying accuracy whereas the effective power dissipated within the sample is reduced by a factor of 20 (50ms BIAS vs. 1s per half-cycle). Therefore, electrical fields of much higher magnitude are possible. Also, as shown in Fig. 1, the slope in the current due to sample heating during one pulse is well defined so that a linear fit yields the currents at room temperature; in addition, they yield a good measure for the temperature stability, i.e. a preferred BIAS-width / frequency ratio.

However, the total illumination duration of about 15 minutes during one field-dependent measurement makes degradation corrections necessary, i.e. data points have to be corrected according to the progress of the transport decay at the time they were taken. For this purpose, decay data that was taken separately is used.

2. Initial experiments on single film samples with coplanar and perpendicular contact geometry

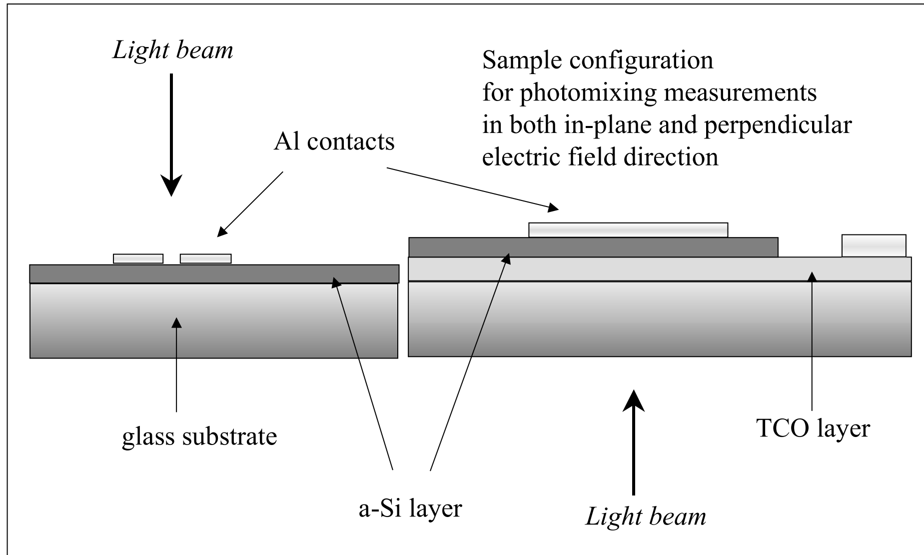

Figure 3. Sample schematics for measurements in two field directions.

It is clear that the electronic transport properties of plain films do not *directly* scale with the actual performance of solar cells built with those films as i-layers. Many complications such as non-uniform electric field, interface effects, etc. result in a dc-photocurrent which is highly convoluted and therefore no measure for the i-layer properties alone. The i-layer transport dependency of the photomixing signal, in particular, is obscured by the non-uniform electric field profile and the contact geometry related capacitance, which acts as a parallel complex resistance muting the mixing signal. In an effort to separate these contributions we have initiated first measurements on single a-Si:H films with both coplanar and sandwich contact configuration.

As described in Fig. 3, Brent Nelson (NREL) has prepared a sample for measurements in both cross-layer and in-plane electric field direction so that we have the chance to study the impact of the changed contact geometry on the results of our photomixing measurements. Two substrates, one plain glass and one TCO-coated, were evaporated with an intrinsic a-Si:H layer in the same run. The layer thickness is 0.524 microns (L148). Coplanar Al contacts were evaporated in coplanar configuration (glass substrate) and sandwich configuration (TCO-coated glass substrate).

Figure 4 shows our preliminary results for both the ac and dc signals. The sample shows pronounced non-ohmic behavior, which can be due to the TCO—a-Si interface, the aluminum contacts or both.

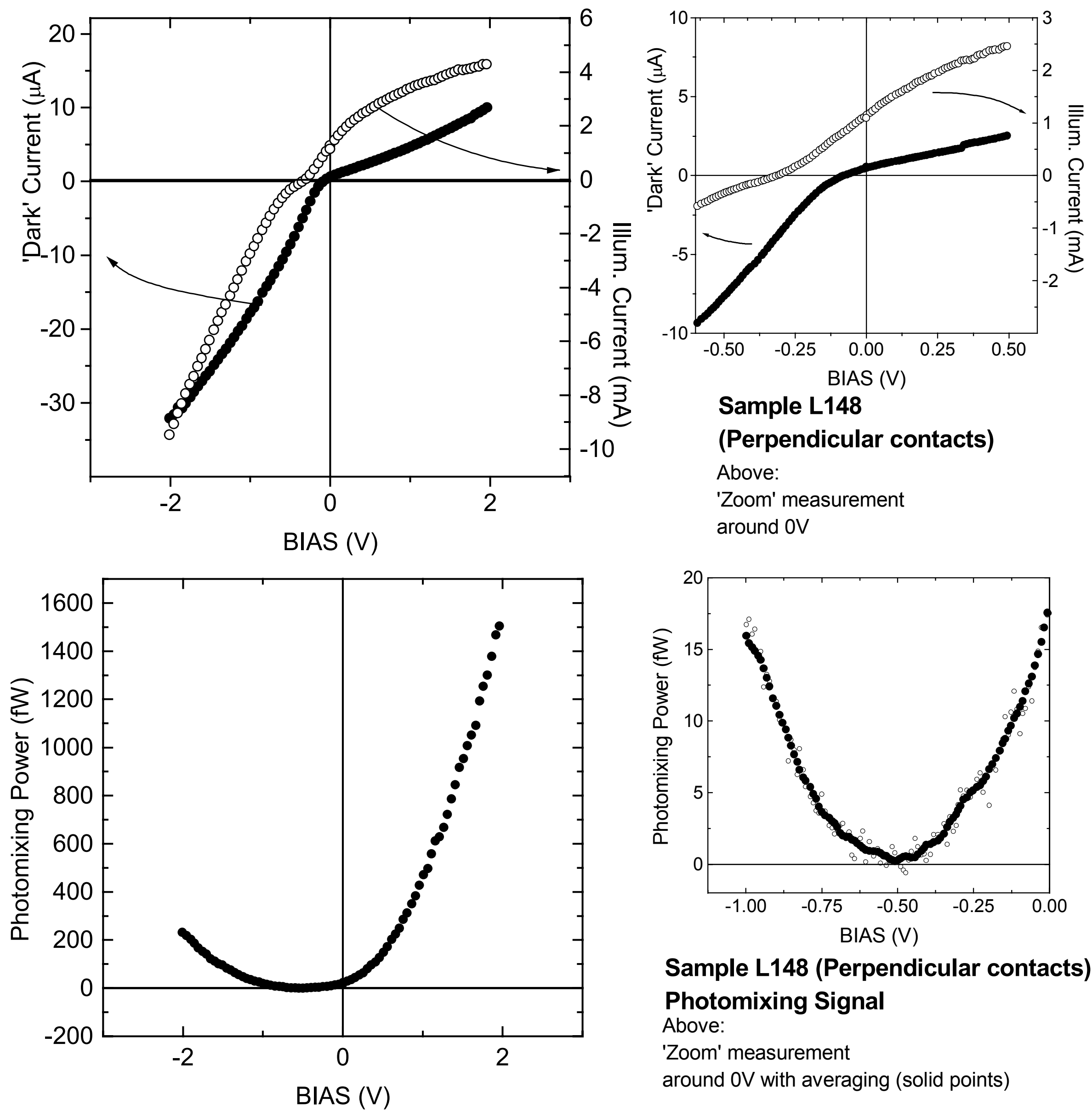

Figure 4. DC and AC currents with perpendicular contact geometry(Film thickness 5244Å)

While, according to B. Nelson and Qi Wang (NREL), it is very difficult to obtain ohmic contacts between TCO and intrinsic silicon layers, it seems possible to reduce the accompanying effects (field profile distortion etc.) by increasing the layer thickness (which of course is limited by the light absorption profile to around 2μm) and choosing contact materials according to their work function.

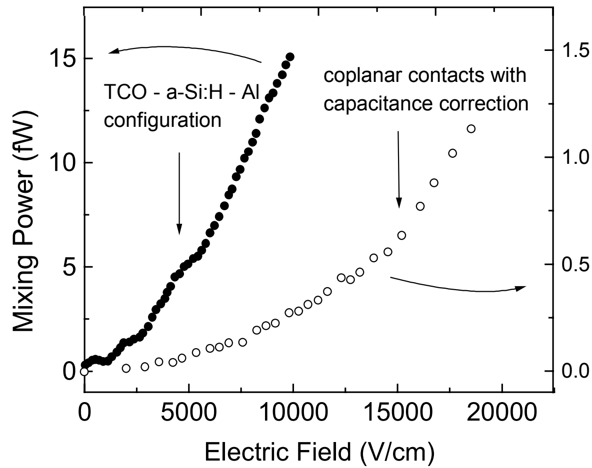

Figure 5. Field dependent mixing power for both configurations. For the TCO–a-Si:H–Al sample, the zero-field point was shifted according to the mixing power minimum at V = -0.5V (Fig. 4)

However, while the dc-curves suggest at least two non-ohmic contributions, we only find one distinct minimum of the mixing curve, which indicates a zero-field condition within the intrinsic layer at an external BIAS of –0.5V.

Figure 5 shows a comparison between the mixing power obtained from the perpendicular contact configuration (solid points) and the sample with coplanar contacts.

For the sake of comparability, we estimated the power losses due to the inherent capacitance of the sample as 1.2nF (contact diameter = 2.5mm, film thickness = 0.54µm, dielectric constant for a-Si (GHz region) = 13.7). Using these assumptions the sample capacitance is 1.2 nF and accordingly, at a frequency of 252MHz, the complex resistance parallel to the photocurrent source is about 100 times lower than the setup impedance. With according corrections applied, it turns out that the mixing signal of the sample with coplanar contacts is much lower than in the transverse electric field case. Moreover, in the case of transverse field direction, we find a rather parabolic field dependence of the mixing power (Best seen in Fig. 4, small graph). Both indicate that with the electric field in transverse direction most charge carriers contributing to the current are swept out. Measurements on different samples with the above mentioned improvements will be carried out in order to show whether there is any significant impact of the i-layer preparation on the photomixing results.

3. Hydrostatic pressure dependence of the charge transport in amorphous silicon

Models to explain the Staebler-Wronski effect in hydrogenated amorphous silicon have been proposed which involve the motion of H atoms. Hydrogen motion in turn may be affected by atomic distances; so it was of interest to study the hydrostatic pressure dependence of the charge transport parameters in amorphous silicon. By employing the photomixing technique, a measurement of the hydrostatic pressure dependence of the mobility and lifetime in the annealed and the light–soaked states could give insight into the dynamics of the Staebler-Wronski effect. Hydrostatic pressure as well as uniaxial stress and substrate misfit stress measurements has been performed over the years; however, at first sight many results seem inconsistent or even contradictory. Many of the measurements employed diamond anvil techniques, which result in uniaxial stress that varies bond angles rather than bond distances; one would expect that the mobility of the hydrogen atoms would be affected by the change in the lattice distance.

For our photomixing measurements we employed a clamped pressure cell with a quartz window. The pressure transmitting fluid was 3M Fluorinert, an electronic fluid with flat optical transmission throughout the visible region and high dielectric strength. The latter is of importance since it is necessary to apply high electric field to the samples in order to measure the electric field dependence of the mobility and so determine the range and the depth of the long-range potential fluctuations. For these initial measurements, an a-Si:H sample produced by the hot-wire technique with 7-9% H was employed.

Figure 6 shows the results of a first pressure dependent photoconductivity measurement of a-Si:H during light soaking. The starting points show that the photocurrent drops with increasing pressure. But also the decay is reduced under higher pressure. The 3 kBar and the 1 kBar curves cross at about 100 minutes which means that after that time the photoconductivity, though starting at a lower value, is still higher after long time irradiation. Figure 7a shows the pressure dependence of the drift mobility as a function of illumination time indicating that at 3 kBar it becomes independent of illumination time. Figure 7b shows the pressure dependence of the lifetime as function of illumination. The lifetime curves though also starting at lower values under pressure show pressure independent slopes.

From this we can conclude that the *generation rate* of recombination centers during light exposition is pressure independent, as well. However, the number of dangling bonds seems to rise under pressure (starting points), which supports the collapsing-void-presumption. The different decay rates of mobility and lifetime under pressure indicate that the rate of generation of charged and neutral scattering defects vary with pressure.

Summarizing our first pressure results one can think of two different ways to describe the pressure dependency of the SW-effect:

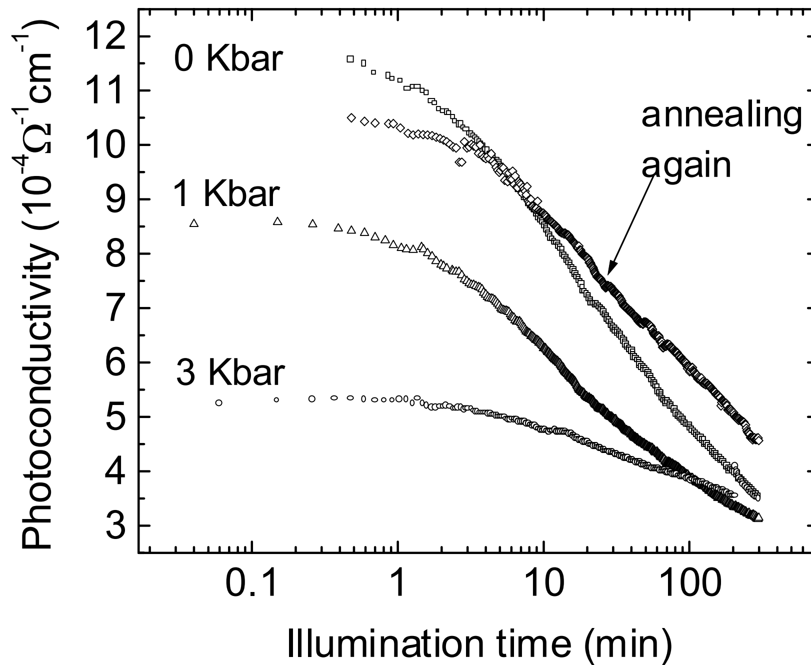

Figure 6. The Photoconductivity vs. Illumination time for three different pressures.

The temporal order of the measurements: 0 kBar ⇒ 1 kBar ⇒ 3 kBar ⇒ 0 kBar ("annealing again"). After each turn the sample was reannealed under atmosphere pressure for 1 h at 150 ^{0}C and then put into the pressure cell again.

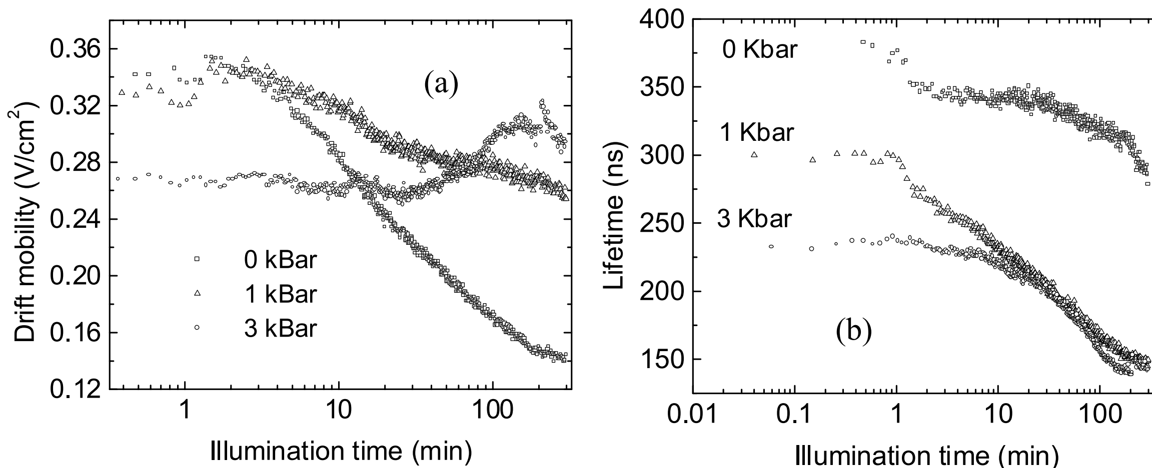

Figure 7. The drift mobility and lifetime as functions of illumination time under different pressures.

Under pressure voids can collapse and weak bonds can break resulting in additional dangling bonds reducing both the dark current and photoresponse. This would mean that pressure does more or less the same as light illumination does: it creates local defects. The pressure dependence of the light soaking experiments may then be regarded as time–shifted. That means, even before illumination there are as many pressure induced defects as though the sample would have been exposed to light as long as it takes to turn down the photoresponse to the value under

pressure at the start. These additional dangling bonds result in a decrease in mobility and consequently a decrease in the photoresponse.

It seems possible that pressure application first introduces local defects that can be observed promptly in a change of lifetime and mobility; additionally, pressure related lattice variations change the time dependence of the mobility during illumination, which may indicate different generation rates of charged defects. We plan to perform further pressure experiments on samples prepared by different preparation techniques to resolve these questions.

Change of the film thickness after pressure application

Further measurements on the pressure dependence of the transport parameters of amorphous silicon films were performed, with emphasis on possible defects introduced by pressure application. We show both FTIR- and photomixing measurements on amorphous silicon samples.

We measured the change of the IR - spectra of the sample T516 (Qi Wang) first in the annealed state, then after the application of hydrostatic pressure of 3 kBar. After this, we annealed the sample for one hour and repeated the FTIR measurement. From the interference fringes occurring in the spectra it is basically possible to determine the film thickness. The fringes occur as a result of a small refraction index mismatch at the film–substrate-interface ($n=3.0 \leftrightarrow n=3.4$). From the periodicity one can easily determine the respective film thicknesses. Figures 8 and 9 show both the fringes from which the thickness was determined and the results for the respective cases. The initial value of 4.408 µm is in good agreement with the value of 44,100Å given by Qi Wang. After pressurizing the sample the film seems to remain around one hundred nanometers thinner than in the initial state, which would mean a decline of 2.3%. This number seems quite high, though; on the other hand, the apparent thickness change may also be due to a change of the index of refraction. Though reannealing for one hour recovers the sample in part, the thickness remains 40 nm under the initial thickness. However, the results show permanent structural changes introduced by pressure application.

From the actual hydrogen related absorption peaks we could not detect any change in the hydrogen configuration, at least as far as the 2000/2100 – double peak is concerned.

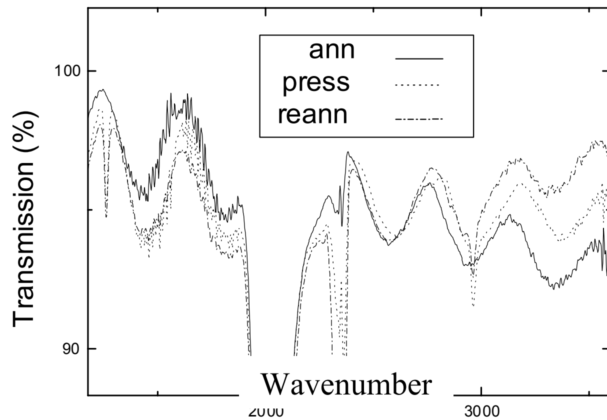

Waveno

Figure 8. Infrared transmission of T516 under annealed ("ann"), pressured ("press"), and reannealed ("reann") conditions.

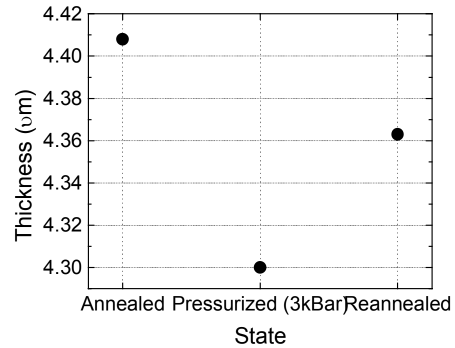

Figure 9. T516 – film thickness after pressure application.

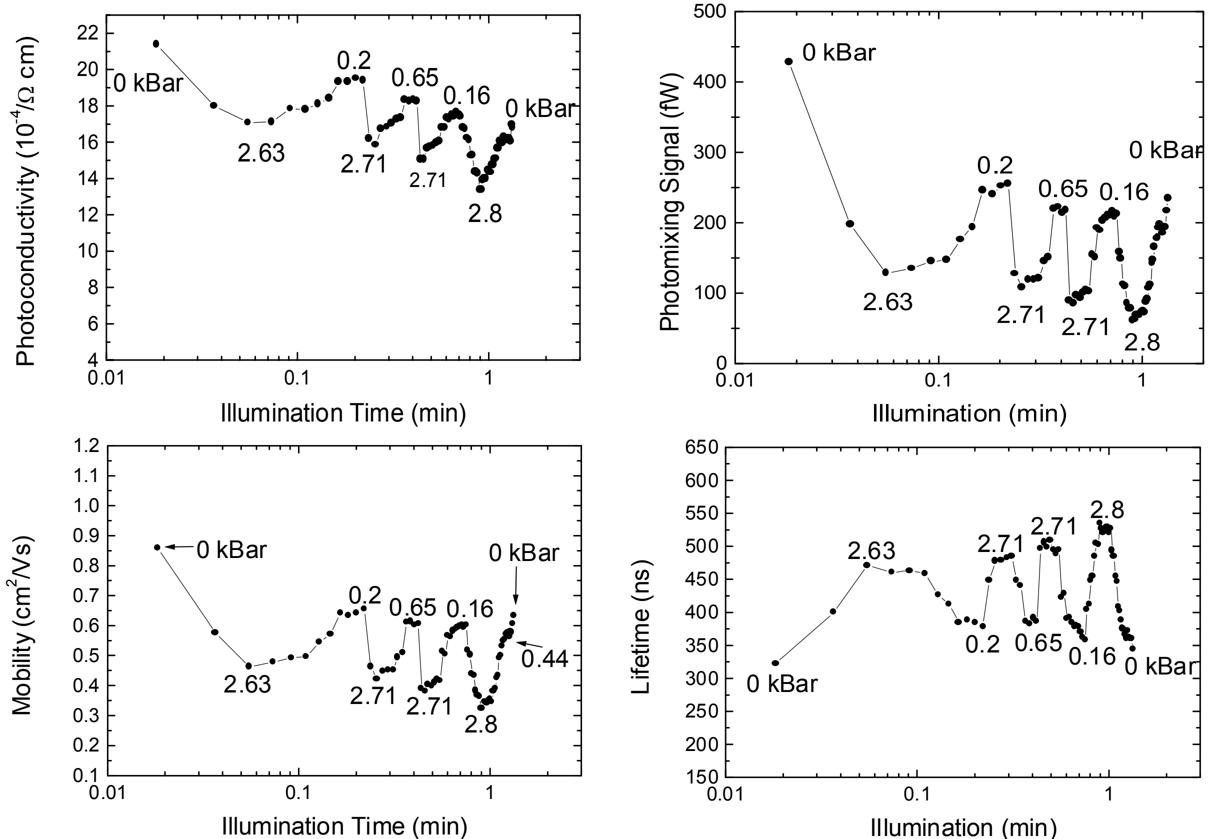

Figure 10. Pressure-dependent transport parameters. After initial annealing, the sample was pressurized and released again. We performed four cycles in the same way, with the transport parameters monitored in situ. The x-axis position is associated with the over-all illumination period during the measurement.

Transport vs. Pressure Hysteresis Measurements

Four cycles with a pressure from 0 to 2.8 kBar being applied and released were run during the measurement. The photoconductivity, mobility, and lifetime were measured at each stage. The results are shown in the Figure 10. It was found that under a given pressure the photoconductivity and mobility decreased while the lifetime increased. However, when the pressure was released a partial recovery of the photoconductivity and mobility was observed but not to the values obtained at the initial zero pressure. These results indicate that there are two effects of hydrostatic pressure; one an *elastic* effect where the mobility decreases under pressure but is restorable when the pressure is released and an inelastic effect where the mobility is decreased due to the introduction of charge scattering centers.

In order to illucidate the participating effects in amorphous silicon under pressure we also performed a similar measurement on single crystalline silicon with the results shown in Figure 11. They show that for single crystals there is only an elastic effect.

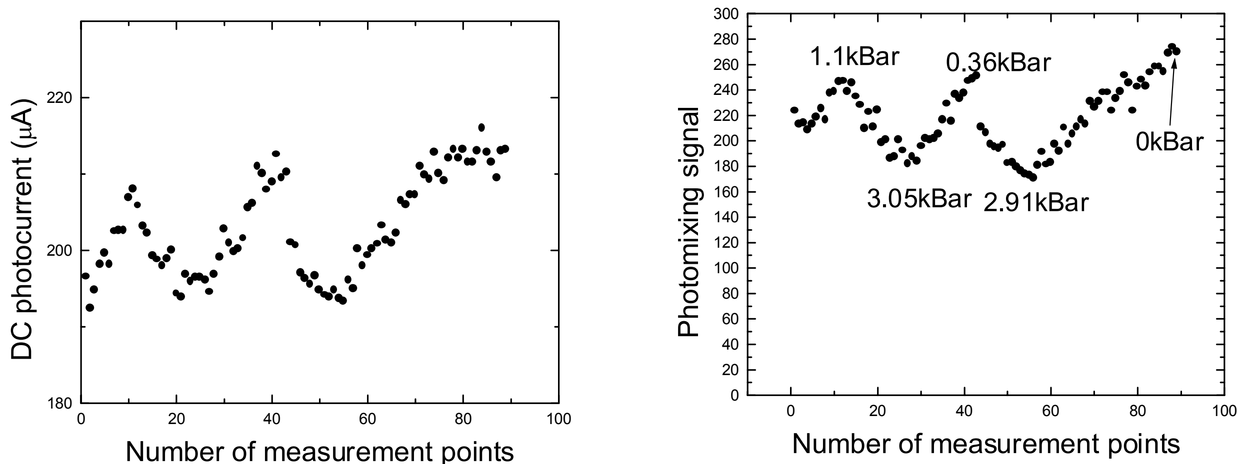

Figure 11. DC photocurrent and photomixing signal under different pressures in single crystalline silicon. Both decrease with increasing pressure. The curves show only an elastic effect.

4. Hydrostatic Pressure Dependence of Charged Transport and Small Angle X-ray Scattering Measurements

We had previously reported on a series of measurements on the charge transport properties of amorphous silicon determined by photomixing as a function of hydrostatic pressure. It was found that under a given pressure the photoconductivity and mobility decreased while the lifetime increased. However, when the pressure was released a partial recovery of the photoconductivity and mobility was observed but not to the values obtained at the initial zero pressure. These results indicate there are two effects of hydrostatic pressure; one an *elastic* effect where the mobility decreases under pressure but is restorable when the pressure is released and an *inelastic* effect where the mobility stays decreased due to the introduction of charge scattering centers. It was conjectured that a permanent collapse of the voids in a-Si:H may be responsible for the inelastic component.

To this end samples were supplied by Don Williams, which we subjected to hydrostatic pressure. Subsequently, the SAXS measurements were performed by Don Williams at the Colorado School of Mines. The samples consisted of one low temperature preparation with a relatively high void fraction (about 2 vol%) and one a high substrate temperature with a very low void fraction (≤ 0.02 vol%). The SAXS data showed no evidence for residual microvoid collapse. Therefore, the origin of the inelastic component is still unknown. Other changes to be considered are bond angles and bond lengths.

5. The “uninterrupted growth/annealing” method

During the last period a series of a-Si single film samples supplied by Guanglin Kong[1] was measured by means of the Photoconductive Frequency Mixing method. The series consists of four samples with varied deposition temperature (G179 – G204), two samples which were prepared for the investigation of light-induced structural changes, and two more samples prepared by means of the “uninterrupted growth/annealing” PECVD method, which was developed by the Kong-group.

In contrast to the “Chemical Annealing” or layer-by-layer deposition where growth and H^+ annealing alternate, the hydrogen treatment happens during the deposition process. This approach which essentially amounts to hydrogen dilution as has been studied for years by, e.g., Tsu [7]. As also suggested by Tsu, the hydrogen plasma is kept at a level near the threshold to the formation of microcrystalline silicon. At this level, the etching effect of hydrogen during the growth process results in a more dense and stable Si network without the formation of larger microcrystalline regions. This leads to amorphous films with improved stability yet without the typical drawbacks of mixed or μc-Si films, i.e. lower optical response due to partly indirect transition, and lower mobility due to grain boundaries.

A slight boron compensation is believed to shift the Fermi level down towards the midgap which results in a higher photosensitivity as well as a higher electron mobility. CPM measurements on appropriately compensated a-Si samples also suggest a lowered subgap absorption which might be due to a passivation of native donor-like impurities through the formation donor-acceptor pairs, compensation of dangling bonds and release of local strain in the Si network.

According to [8] and [9],appropriate hydrogen dilution results in amorphous silicon films with light-induced decay of the photocurrent of about one half order of magnitude with saturation tendency after 10^4 seconds of illumination. With additional boron compensation, the samples show essentially stable transport properties. In comparison, an a-Si:H standard sample showed a photocurrent decay of about one order of magnitude. With samples where both hydrogen dilution and boron compensation were applied, even an *increase* of the photocurrent was found in some samples [8] which is explained in terms of an additional light-induced effect which involves a bond-switching from fourfold to threefold B configurations forming neutral acceptor dangling bond pairs. These, in turn, lower the B doping efficiency and therefore, in the case of slight B compensation, result in a shift of E_f towards E_c and accordingly an increase of the electron mobility.

[1] Institute of Semiconductors, Chinese Academy of Sciences, Beijing, China

Photomixing Measurements on samples supplied by Guanglin Kong

The sample properties are given in Table 1.

Table 1. Deposition conditions

Sample ID	SiH_4:H_2	Ingredient	$T_{substr.}$ (^oC)	T_{dep} (hrs)	Thickness (µm)	Deposition Rate (Å/s)
I 70426	1:1		360	4.5	1.5	0.93
I 80929	1:3		300	3.5	3	2.40
P 60715 I	1:12	0.2% $B_2H_6(10^{-4})$	225	3.0	0.89	0.82
P 60717 II	1:12	2% $B_2H_6(10^{-4})$	225	2.6	0.79	0.84
G 179	1:5		350	1.5	1.25	2.31
G 202	1:5		400	4.0	1.7	1.18
G 203	1:5		300	5.0	3.2	1.78
G204	1:5		200	3.0	2.2	2.04

As shown in Table 1, a series of four samples, G179 - G204, is prepared with the substrate temperature being varied at constant dilution ratio. The respective light-induced decay curves are shown in figures 12 and 13 beginning with the highest substrate temperature. For all samples, the mobility after three hours of illumination lies somewhere between 50% and 60% of the initial value. The lifetime decay, however, seems to scale with the deposition temperature, i.e. the lower the deposition temperature the lower the final lifetime with respect to the initial value. Also the initial photomixing mobility is clearly higher for films deposited with higher T_s. For the photoconductivity this means that for lower deposition temperatures ($T_s < 350^oC$) both the initial value (due to the lower initial mobility) and the decay rate (due to the higher decay of the lifetime) turn out to be rather poor as compared to samples with $T_s \geq 350^oC$. It seems that given a moderate dilution ratio the network reconstruction during growth requires more activation through the substrate temperature than, e.g. in the case of Hot-Wire CVD. From this series it is clear that the best sample is also the most expensive one in terms of substrate temperature and deposition rate.

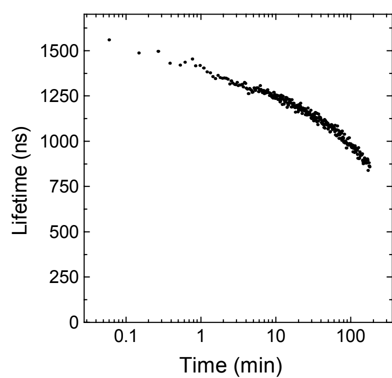

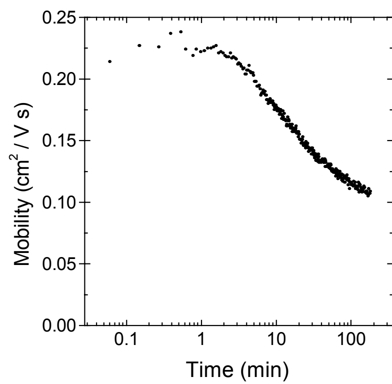

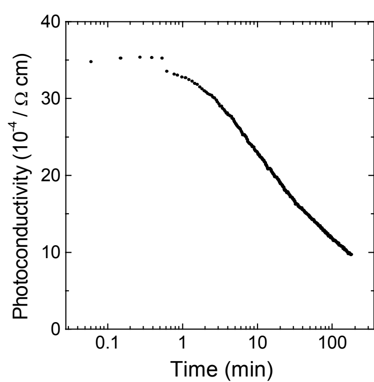

Sample G202

$T_{depos.}$ = 400 °C

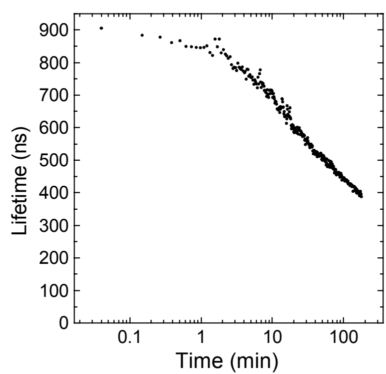

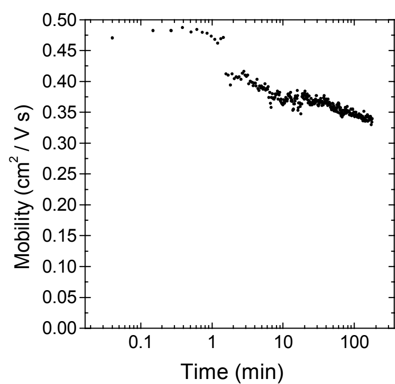

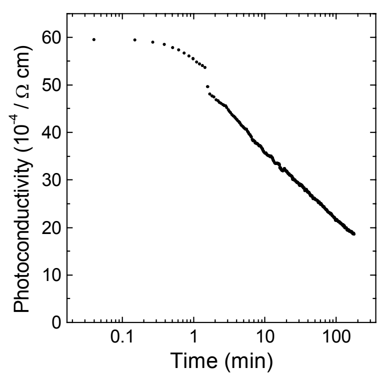

Sample G179

$T_{depos.}$ = 350 °C

Figure 12. Samples G202 and G179, dilution ratio is kept constant at 1:5

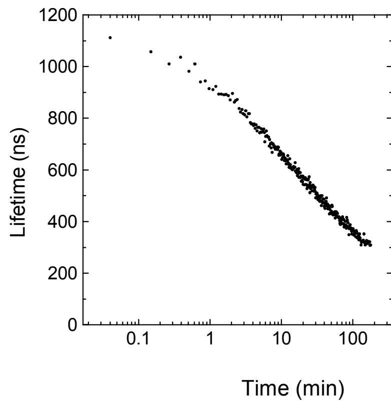

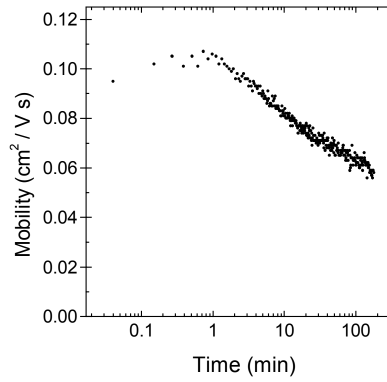

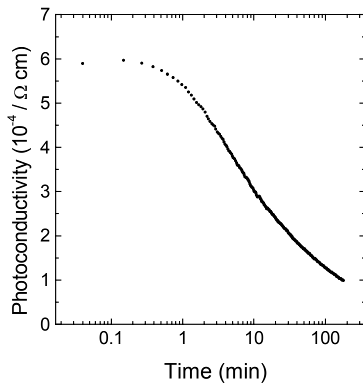

Sample G203

$T_{depos.} = 300\ ^{o}C$

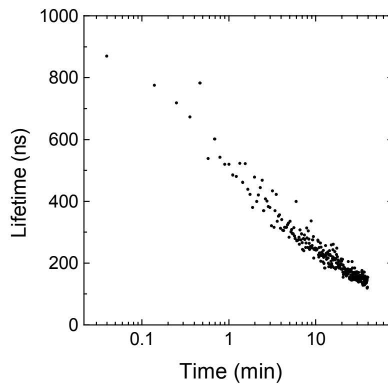

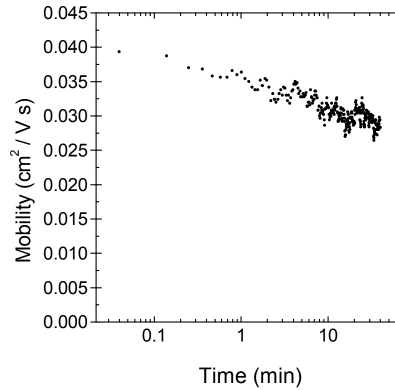

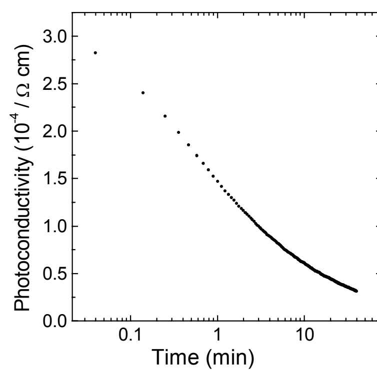

Sample G204

$T_{depos.} = 200\ ^{o}C$

Figure 13. Samples G203 and G204, dilution ratio is kept constant at 1:5

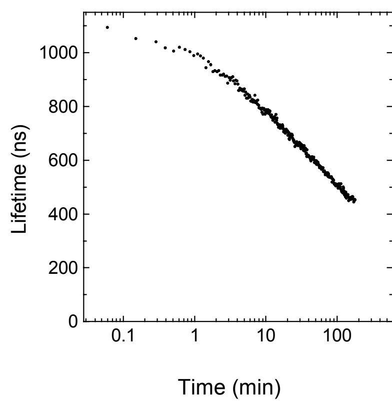

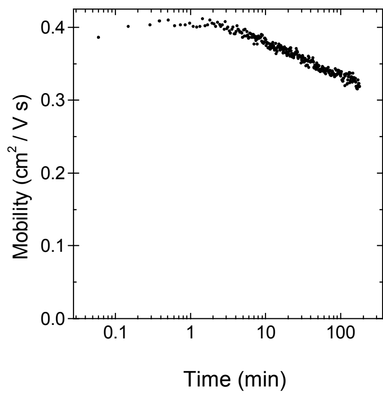

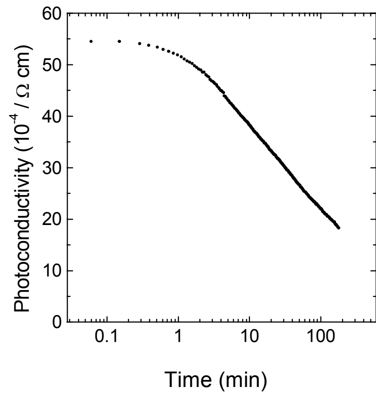

Sample I70426

$T_{depos.}$ = 360 °C
$SiH_4 : H_2 = 1:1$

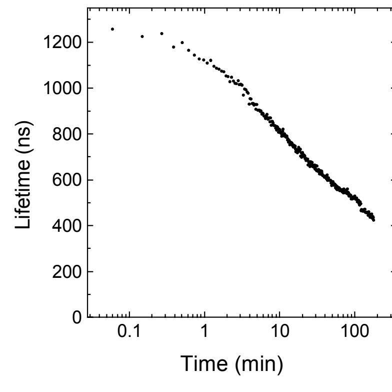

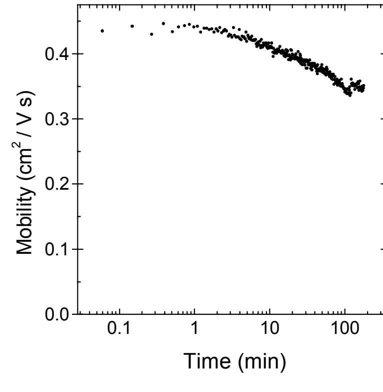

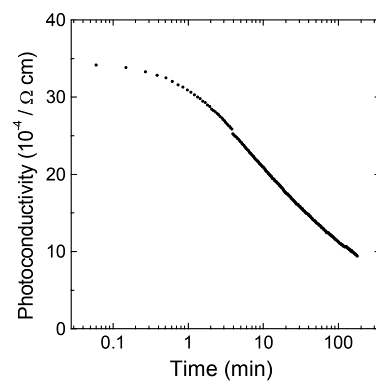

Sample I80929

$T_{depos.}$ = 300 °C
$SiH_4 : H_2 = 1:3$

Figure 14. Samples I70426 and I80929.

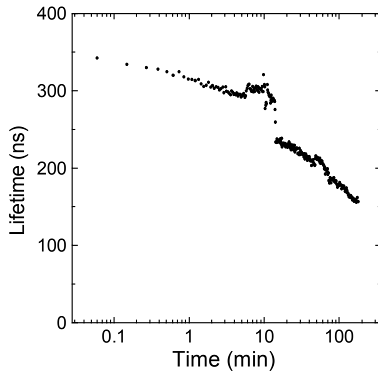

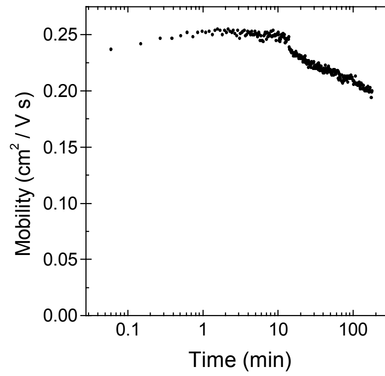

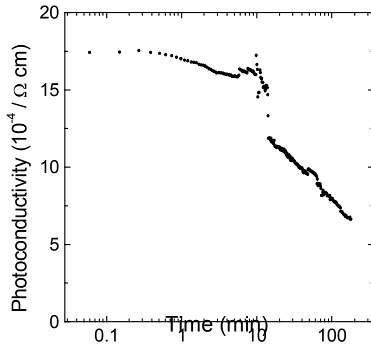

Sample P60715I

$T_{depos.}$ = 225 °C
$SiH_4 : H_2$ = 1:12
+0.2% $B_2H_6(10^{-4})$

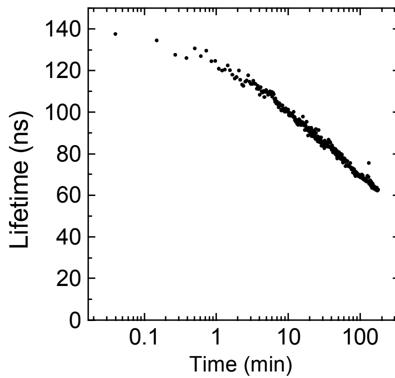

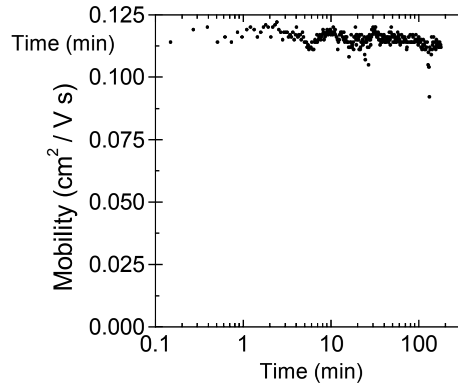

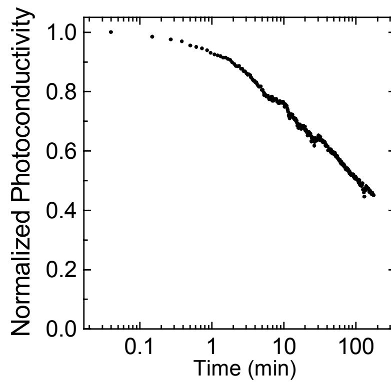

Sample P60715I
(rough surface)

$T_{depos.}$ = 225 °C
$SiH_4 : H_2$ = 1:12
+0.2% $B_2H_6(10^{-4})$

Figure 15. Samples P60715I with flat and rough surface.
These are prepared by employing the "uninterrupted growing/annealing" technique.

From Figure 14, we can see that samples I70426 and I80929 again suggest that the substrate temperature has a large impact on the film stability. The sample with lower hydrogen dilution ratio but higher substrate temperature shows better stability at a higher performance level. The deposition rate of I80929, on the other hand, is about three times that of I70426. This means that other parameters not specified by the Kong group may have been changed, too. However, the thicknesses of I70426 and I80929 were just estimated from the deposition period.

Finally, Figure 15 shows our results for the two samples prepared by "uninterrupted growth/annealing" PECVD, P60715I and P60717II. Actually, we had two 'P60715I' samples available, one with a flat and one textured surface. Both P60715I samples show a decay of all transport quantities in the range of 20% (mobility) through about 50% - 60% (lifetime, photoconductivity). However, a first slight increase in mobility is observable (P60715I – flat surface) but after about 15 min the mobility begins to decrease, too. In comparison to the samples with mere dilution and from our results of the light-induced decay, we cannot detect any noticeable impact of boron doping on transport for the present samples other than what is mentioned above, but samples are more stable.

Unfortunately, we were unable to detect any reasonable mixing signal on the P60717II. This is particularly disappointing since this would have been the only sample that we have access to independent data for [8].

Table 2 below summarizes the Long-range potential fluctuation data we acquired for the whole series. The values for LRPF range and depth reflect the good stability of the mobility in most samples, particularly I70426 and I80929.

Table 2. Long range potential fluctuations

Sample ID	H-Dilution	Substrate Temperature	Range (nm)	Range (nm)	Depth (eV)
I 70426	1:1	360	Annealed	83.3	0.10
			Light-soaked	83.3	0.11
I80929	1:3	300	Annealed	89.0	0.10
			Light-soaked	88.7	0.11
P60715I	1:12 $+B_2H_6$	225	Annealed	30.1	0.11
			Light-soaked	30.1	0.12
P60715I (rough s.)	1:12 $+B_2H_6$	225	Annealed	39.0	0.13
			Light-soaked	38.0	0.13
G179	1:5	350	Annealed	19.1	0.13
			Light-soaked	16.3	0.14
G202	1:5	400	Annealed	40.8	0.09
			Light-soaked	46.4	0.13
G203	1:5	300	Annealed	24.2	0.12
			Light-soaked	25.8	0.15
G204	1:5	200	Annealed	*Weak mixing signal / Low mobility*	
			Light-soaked		

6. Charge transport properties near and above the transition from amorphous to microcrystalline silicon

6.1 Material produced at NREL

Microcrystalline silicon (μc–Si:H) has been the object of studies for many years to understand its electronic, optical and structural properties. However, recently there has been a renewed interest in incorporating μc – Si:H in different solar cell structures since such devices have shown no degradation after prolonged light soaking [7,10]. It has been shown that a-Si:H films grown under hydrogen dilution close to the onset of microcrystallinity exhibit a higher degree of stability against light soaking compared to a-Si:H. In hot-wire assisted chemical vapor deposition (HW-CVD) [11-15], the decomposition of silane and hydrogen gas mixture allows one to prepare material with a transition from to amorphous to microcrystalline growth by variation of the silane to hydrogen dilution. By varying the grain size, an enhanced absorption of microcrystalline compared to crystalline silicon has been observed [16]. The (HW-CVD) method allows a continuous preparation of material with a smooth transition from amorphous hydrogenated silicon to microcrystalline silicon. The photoconductivity in microcrystalline silicon has been studied as a function of Fermi-level to determine the mobility-lifetime product ($\mu\tau$) [17] with the observation that ($\mu\tau$) increased significantly by shifting the Fermi level from the mid-gap towards the conduction or valence band; this was attributed to the increase in the majority carrier lifetime due to a change in the thermal occupation of defect centers by the shift of the Fermi level. It is of interest to separately determine the mobility and lifetime in the transition from the amorphous to the microcrystalline state; dc photoconductivity measurements determine the $\mu\tau$ product. The independent determination of μ and τ was accomplished by employing the photoconductive frequency mixing technique [1-6]. By observing the increase in the drift mobility as a function of electric field, the range and the depth of the long-range potential fluctuations [4] as a function of hydrogen content and hence the change in these quantities in the transition from amorphous to microcrystalline states were determined.

In this report we present results from electronic transport measurements of a series of samples prepared employing the hot-wire chemical vapor deposition technique supplied by Qi Wang. Within this series a transition from the amorphous to the microcrystalline state is realized. Since there is evidence that one finds improved stability against light-induced degradation in the mixed state it is interesting to study the (photo-) transport properties and stability with respect to this transition. Table 3 shows a summary of the sample characterization:

Table 3. Summary of the sample characterization results (Qi Wang).

Sample ID	H/SiH_4	XRD Structure	(μc) av. Grain size (nm)	Sample Thickness (Å)	H-content (%)	Deposition rate (Å/s)
T516	1	a-Si		41,400	13.3	17.25
T517	5	μc Si	12	21,350	5.2	5.93
T518	10	μc Si	13	14,300	4.7	3.97
T519	20	μc Si	14	11,200	3.9	2.33
T528	5	μc Si	18	25,400	3.1	7.05
T529	4	μc Si	12	24,000	4.2	8.00
T530	3	a-Si+μc Si	9	16,400	4.4	7.80
T531	2	a-Si		25,000	8.9	10.41
T532	3	a-Si+μc Si	11	17,000	4.0	7.08
T534	2	a-Si		30,000	10.9	12.50

Results of photomixing measurements

We employed the photoconductive frequency mixing technique to determine the transport properties in terms of the charge carrier (photomixing) lifetime and mobility as well as the over-all photoresponse.

In a-Si:H, the electronic transport depends tightly on the hydrogen content, so the photoconductivity is usually plotted against the amount of H-atoms introduced into the samples. A look at Table 3 indicates that within this series of samples microcrystalline structure results in a low hydrogen content. Therefore, we decided to plot the transport properties against the hydrogen content, including all given samples, as shown in Fig. 16.

With the decrease of the H-content the photoconductivity is more or less constant as long as the hydrogen concentration is over about 5% to 6%. However, it shows a sudden increase when the H-concentration drops below 5%, i.e. the microcrystalline regime is entered.

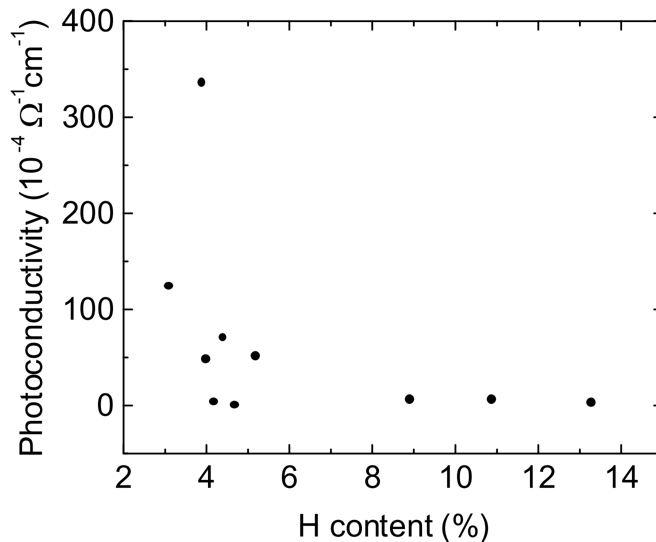

Figure 16. Photoconductivity of amorphous and microcrystalline silicon vs. hydrogen content.

To investigate what quantity this increase is due to, we determined the photomixing lifetime τ and mobility μ for each sample in the annealed state. The results are shown in Figures 17 and 18. Both τ and μ are affected by the transition. Similarly to the behavior of the photoconductivity, the lifetime exhibits a sudden increase up to two orders of magnitude when the hydrogen content drops to values less than 5% (Figure 17). The mobility, however, shows somewhat opposite behavior. In the amorphous region, the mobility *increases* with decreasing H-concentration. This is surprising since one usually finds the mobility to increase when the hydrogen content grows. As a comparison, Figure 19 shows the results for a set of samples also produced by hot-wire CVD, but entirely within the amorphous region. For H-contents under 5%, the mobility *drops* to values not detectable anymore. However, except for the samples T518 and T528, μ only drops to about 20% of its maximum value, so the photoconductivity, being straight proportional to τ and μ, still increases dramatically.

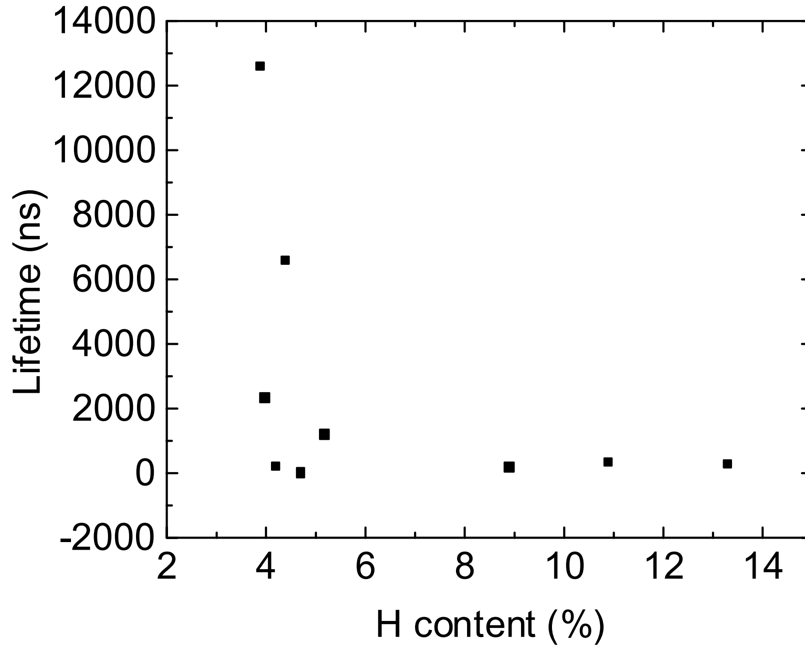

Figure 17. The photomixing lifetime of amorphous and microcrystalline Si:H vs. hydrogen content.

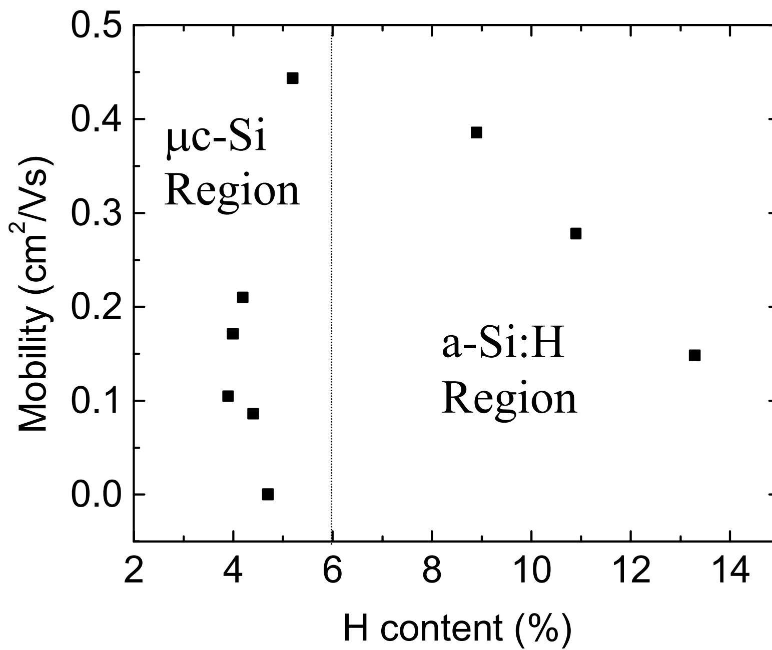

Figure 18. The mobility of amorphous and microcrystalline Si:H vs. hydrogen content.

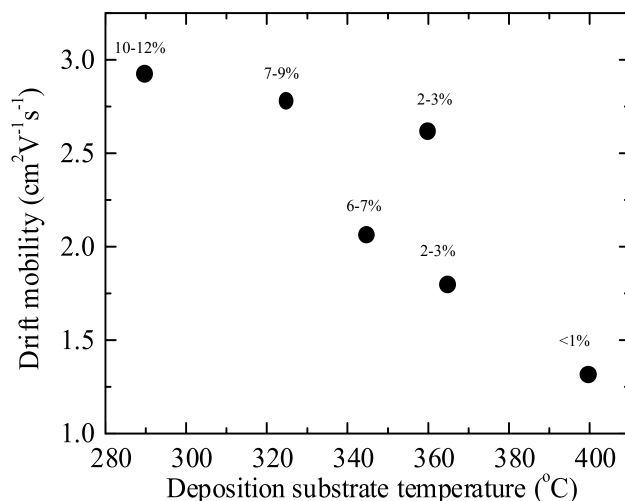

Figure 19. Drift mobility in the case of entirely amorphous samples (Hot-wire assisted PECVD a-Si:H from NREL).

Long-Range Potential Fluctuation

Long-range Potential Fluctuations (LRPF) are thought to reflect the density and arrangement of *charged* defects in amorphous silicon. To determine the LRPF within the samples, we performed field-dependent measurements of the mobility and lifetime. The results are shown in Figures 20 and 21. Note that the range increases to values of around 50nm in the μc – regime, which might reflect the occurrence of grain boundaries. Also the depth of the potential fluctuations increases, whereas both quantities decrease with decreasing hydrogen content for H-concentrations over 6% (i.e. the amorphous regime).

These results lead to a possible explanation for both the drop of the mobility and the dramatic increase of the lifetime in the case of microcrystalline silicon. Grain boundaries might serve as scattering centers as well as barriers against recombination.

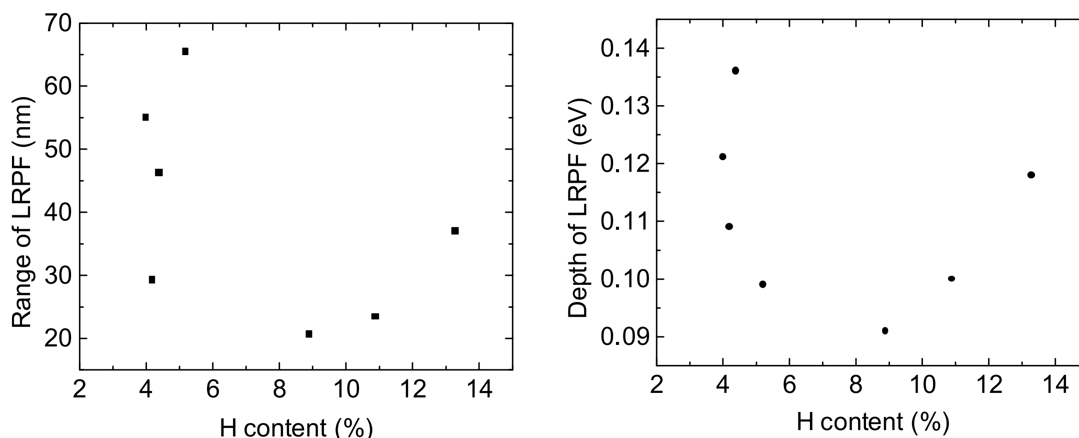

Figures 20 and 21. Range and depth of long-range potential fluctuations in amorphous and microcrystalline silicon-hydrogen.

Light-induced Decay Measurements

This section covers measurements of the light-induced degradation (Staebler-Wronski-effect) for samples in the amorphous state, mixed state (a-Si + μc-Si) and the microcrystalline state (μc-Si). Figure 22 shows the normalized photoconductivity for the three amorphous samples, which exhibit behavior as expected from former results. In each case the samples were first annealed for 1 hour at a temperature of 150 ^{0}C.

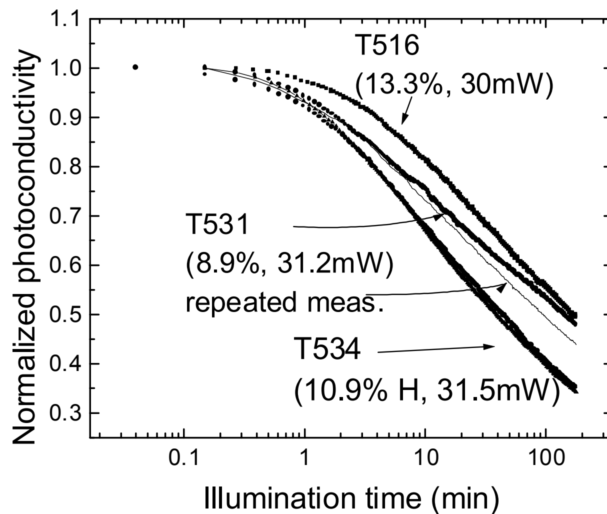

Figure 22. Normalized photoconductivity vs. illumination duration for T516, T531 and T534 (amorphous state). The light intensities are given in the Figure.

Since in the case of microcrystalline silicon we found both high dark and photocurrent, we had to restrict the number of points in order to prevent those samples from heating. Also, we could not measure lifetime and mobility at high fields. This results in an increased error and so a certain scattering of both lifetime and mobility. Nonetheless the Figures 23-25 show increased stability against light-induced defects for samples in both the mixed and microcrystalline phase. The increase of the photocurrent in the case of the samples T529 and T532 is probably due to a slight heating.

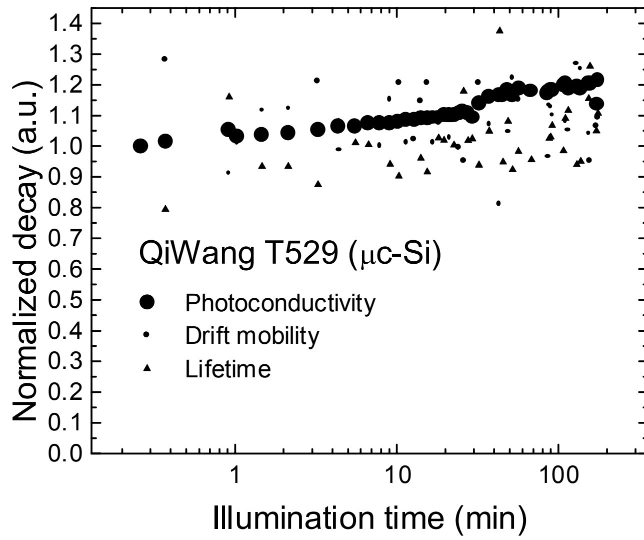

Figure 23. Photoconductivity, mobility and lifetime vs. illumination duration, T529.

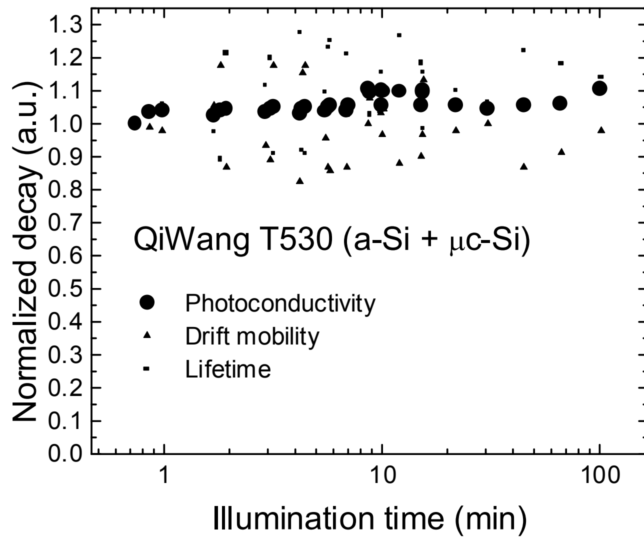

Figure 24. Photoconductivity, mobility and lifetime vs. illumination duration, T530.

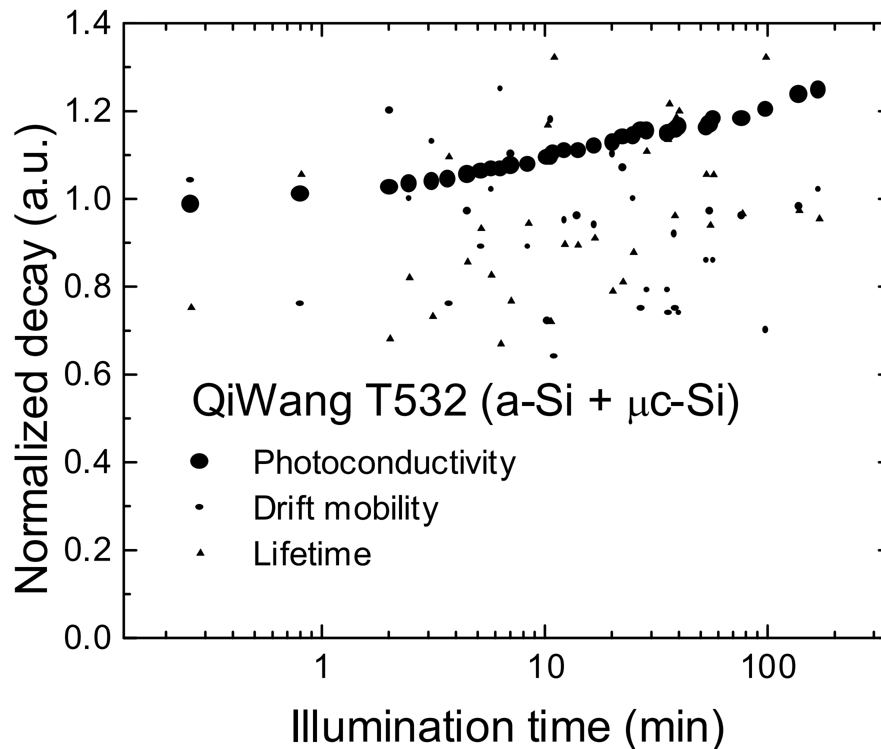

Figure 25. Photoconductivity, mobility and lifetime vs. illumination duration, T532.

Summarizing the above results, we found both increased stability and a huge increase of the photomixing lifetime resulting in an increase of the photoresponse for samples entering the microcrystalline regime. The increase in lifetime and decrease in mobility as the microcrystalline regime is entered indicates that grain boundaries can serve as scattering centers as well as barriers against recombination. In order to further illucidate the mechanisms responsible for the dramatic change in lifetime and mobility as one makes the transition from the amorphous to the microcrystalline state, it would be useful to perform similar measurements on samples prepared by different methods which result in different microstructures.

FTIR measurements

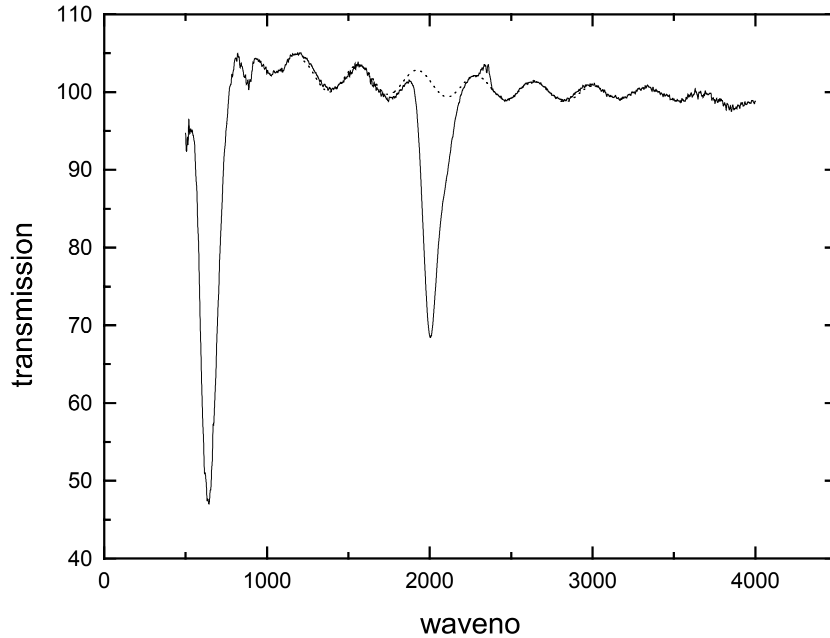

Figure 26. IR – spectra, sample T516 (a-Si:H) on polycrystalline substrate.

Figure 26 shows a typical a-Si:H spectrum we acquired in the wavelength region from 400 to 4000 cm^{-1}. The total hydrogen content was obtained from the rocking modes of hydrogen in all possible bonding configurations which give rise to an absorption peak at 640cm^{-1}. To calculate the hydrogen content from the integrated absorption of this peak we used values for the oscillation strength parameters given in [18]:

$N_H = AI$,

where N_H is the hydrogen concentration and

$$I = \int \frac{\alpha}{\omega} d\omega$$

is the integrated absorbance.

and

$$A_{640} = (2.1 \pm 0.2) * 10^{19} cm^{-2}$$
$$A_{2000} = (9.0 \pm 1.0) * 10^{19} cm^{-2}$$
$$A_{2100} = (2.2 \pm 0.2) * 10^{20} cm^{-2}$$

We found good agreement with the values for the hydrogen content given by NREL. The stretching modes at 2000 and 2100cm^{-1} are related to isolated SiH in a Si network or SiH_x, hydrogen clusters, and also SiH bondings at surfaces (e.g. voids) whereas only the latter group gives rise to a 2100 – peak. Figure 27 shows an example of the stretching mode related double-peak in the case of a-Si:H and Figure 31 contains the respective deconvolution.

In microcrystalline silicon most hydrogen is bonded at grain boundaries facing intergrain voids and so gives rise to usually at least two peaks around 2100 with respect to the crystalline grain orientation (figure 28). The intensity ratio of the 2000 and 2100 peaks depends on the dilution as can be seen in figures 28 and 30.

In the mixed state samples, also bending mode related absorption at around 900cm^{-1} occurs as shown in figure 29.

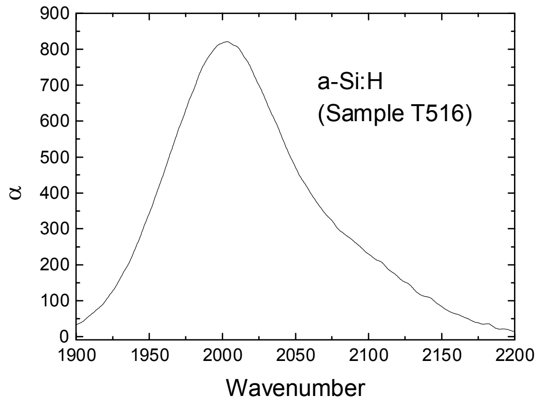

Figure 27. Stretching modes in a-Si:H. According to this double peak, a significant part of H atoms is bonded as monohydide in a dense Si network.

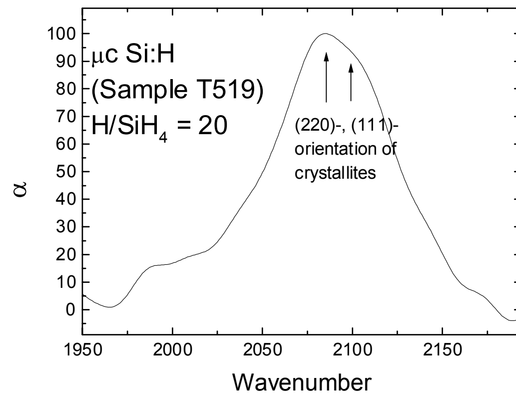

Figure 28. Stretching modes in microcrystalline silicon – high dilution (note the low 2000 - absorption).

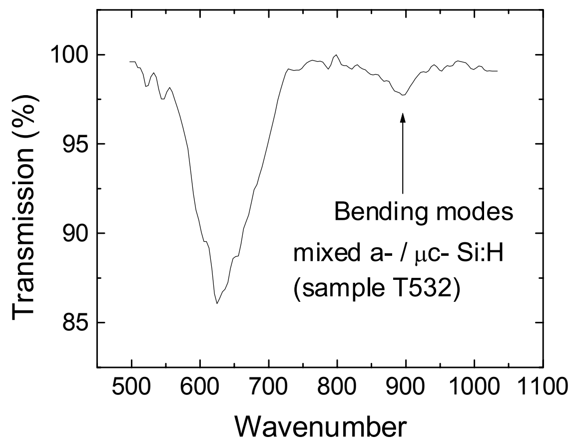

Figure 29. Bending mode related absorption peak at around 900cm-1 in the mixed state sample T532.

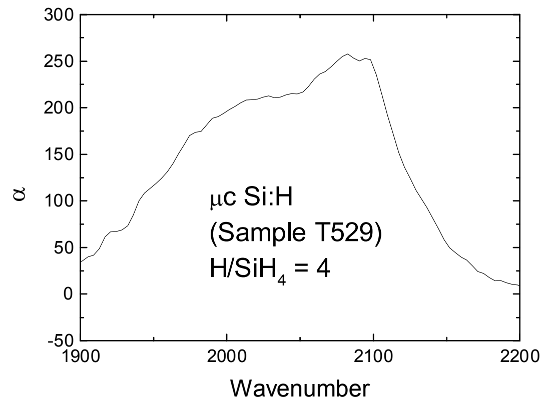

Figure 30. Microcrystalline Silicon with low dilution ratio.

Figure 32 summarizes the stretching modes of samples in the amorphous and mixed state. Note the scaling of the 2000 peak with the dilution ratio.

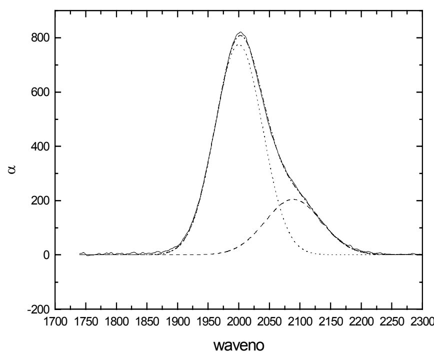

Figure 31. Deconvolution of 2000/2100-peak (T516).

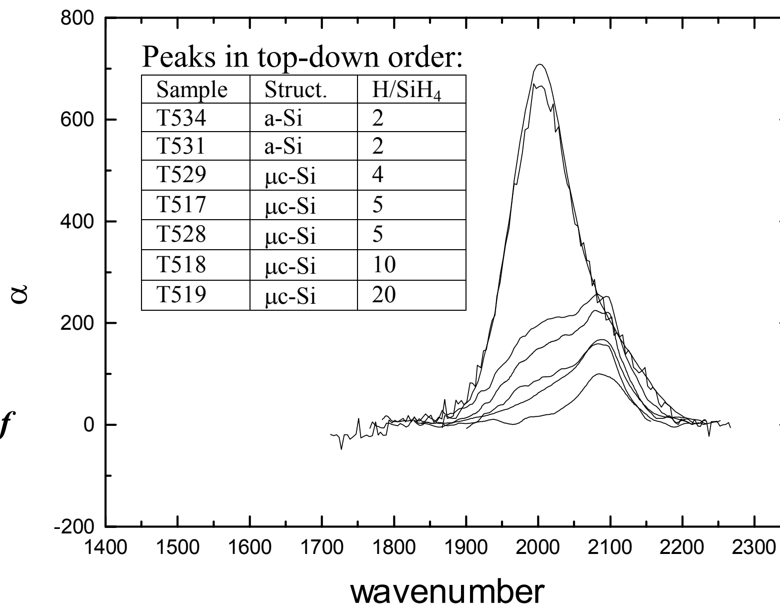

Sample	Struct.	H/SiH_4
T534	a-Si	2
T531	a-Si	2
T529	μc-Si	4
T517	μc-Si	5
T528	μc-Si	5
T518	μc-Si	10
T519	μc-Si	20

Figure 32. Stretching modes for several amorphous and microcrystalline samples.

6.2 Charge transport properties near and above the transition from amorphous to microcrystalline silicon produced at MVSystems

The first set of samples

We studied the transport properties of three samples supplied by MV-Systems, Inc, Golden, CO, one microcrystalline silicon film (MVS723) and two amorphous silicon films, MVS722 and MVS823. The respective preparation parameters have not been disclosed by MVSystems at this time. Figures 33-35 show the respective decay curves for all three samples, whereby the a-Si:H – films are investigated the "classical" way as described earlier.

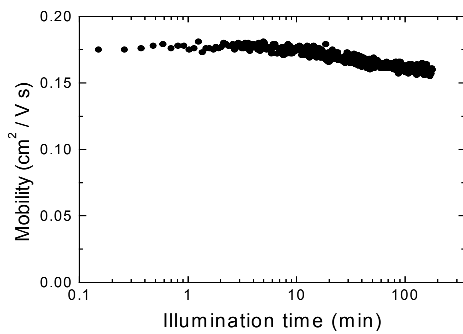

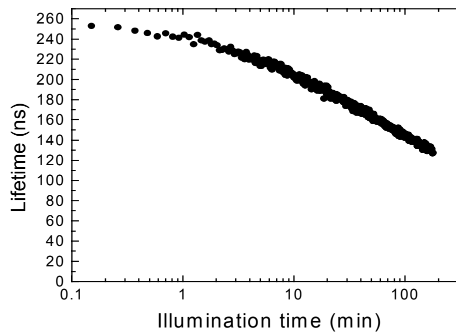

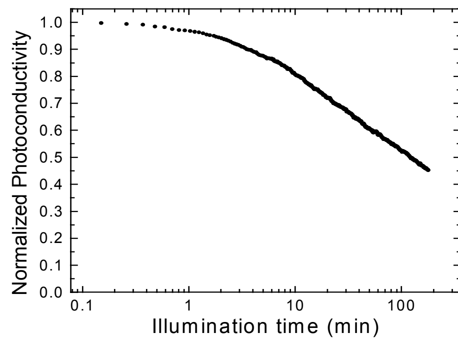

Figure 33.
MVS722 (a-Si:H)
Results for the mobility, lifetime, and photoconductivity during light-soaking.

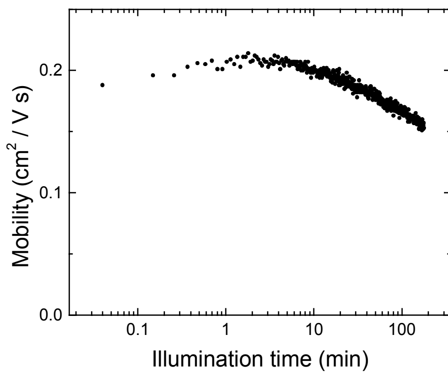

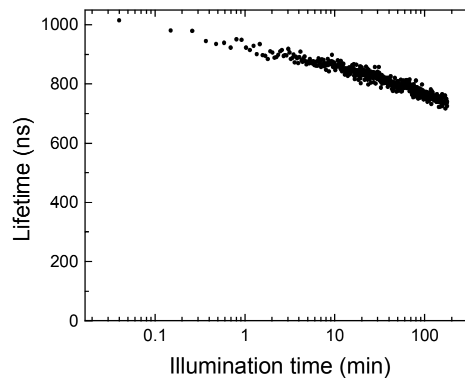

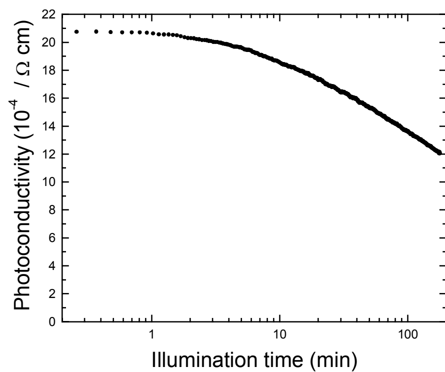

Figure 34.
MVS823 (a-Si:H)
Results for the mobility, lifetime, and photoconductivity during light-soaking.

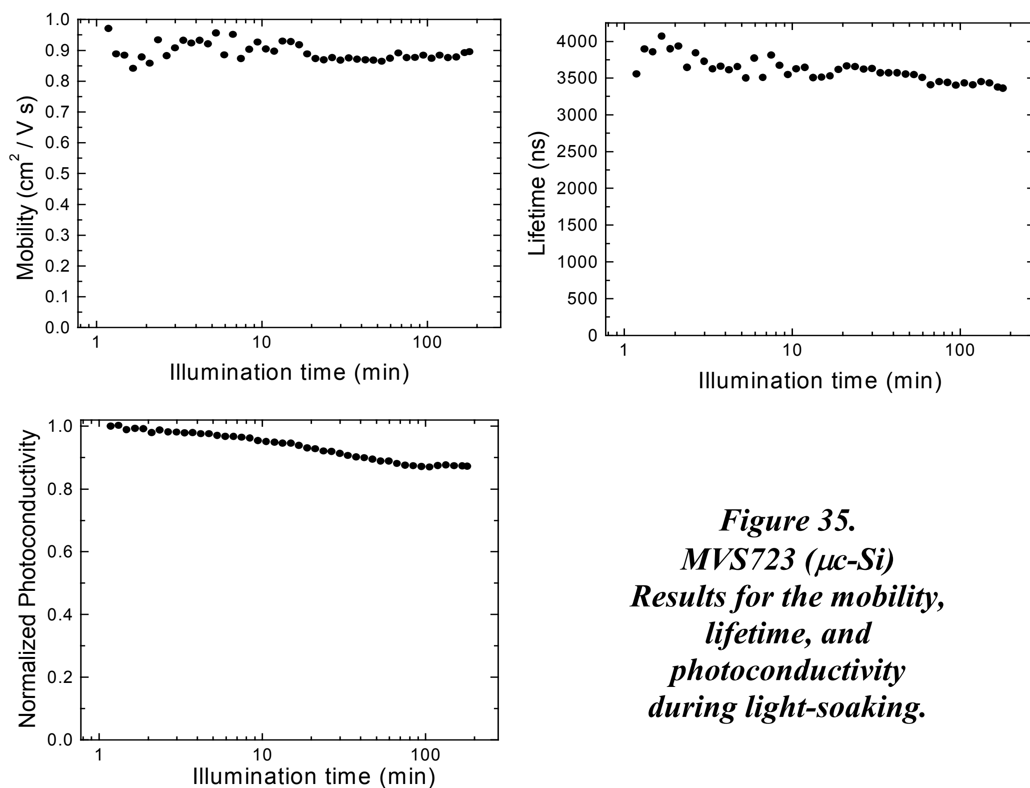

Figure 35.
MVS723 (μc-Si)
Results for the mobility, lifetime, and photoconductivity during light-soaking.

The range and depth of the long range potential fluctuations (LRPF) of these samples were determined by the electric field dependence of the mobility and are shown in Table 4.

Table 4. LRPF Range and Depth for the MVS – samples (the thickness of the intrinsic layers were about 5000Å).

Sample ID	***Annealed State***		***Light-soaked Sate***	
	Range (nm)	**Depth (eV)**	**Range (nm)**	**Depth (eV)**
MVS722 (a-Si)	52.9	0.125	51.6	0.13
MVS823 (a-Si)	51.8	0.11	53.54	0.13
MVS723 (μc Si)	400	0.08	400	0.082

The Second set of samples

The series discussed here was provided by MVSystems. It consists of eight samples starting in the completely amorphous regime (MVS 968) in numerical order through to microcrystallinity (MVS 975 and MVS 1003). In Table 5 the corresponding sample data is listed.

Table 5. Sample data as provided by MVSystems

Sample ID	**Filament Temperature**	**H_2 dilution**	**Dark cond. $(\Omega cm)^{-1}$**	**Light cond. $(\Omega cm)^{-1}$**	**Thickness (Å)**
968	Low	0	1.0×10^{-10}	3.1×10^{-5}	6,000
969	High	0	1.5×10^{-7}	1.8×10^{-7}	70,000
970	High	20	8.5×10^{-7}	2.5×10^{-6}	9,200
971	High	50	9.5×10^{-10}	1.3×10^{-8}	19,000
972	High	80	3.0×10^{-8}	6.8×10^{-8}	16,000
973	High	90	4.3×10^{-7}	4.7×10^{-7}	9,000
975	High	95	2.2×10^{-6}	2.4×10^{-6}	7,300
1003	High	93	3.1×10^{-5}	3.2×10^{-5}	22,500

Figure 36 shows the decay data of the amorphous sample 968. The electric field dependent mobility for this sample yields the range (R) and depth (D) of the Long-Range Potential Fluctuations:

Annealed State:R = 40.4nm, D = 0.14eV
Light-soaked state:R = 38.7nm, D = 0.16eV

Unfortunately, we were unable to obtain data on most of the other samples as the photoresponse of these is generally low and therefore not suitable for our mixing method. Only on MVS 970 we could detect a mixing signal at an electric field of 22kVcm^{-1} for which we obtained a photomixing mobility μ_D = 0.035cm^2/Vs and a photomixing lifetime of around 60ns.

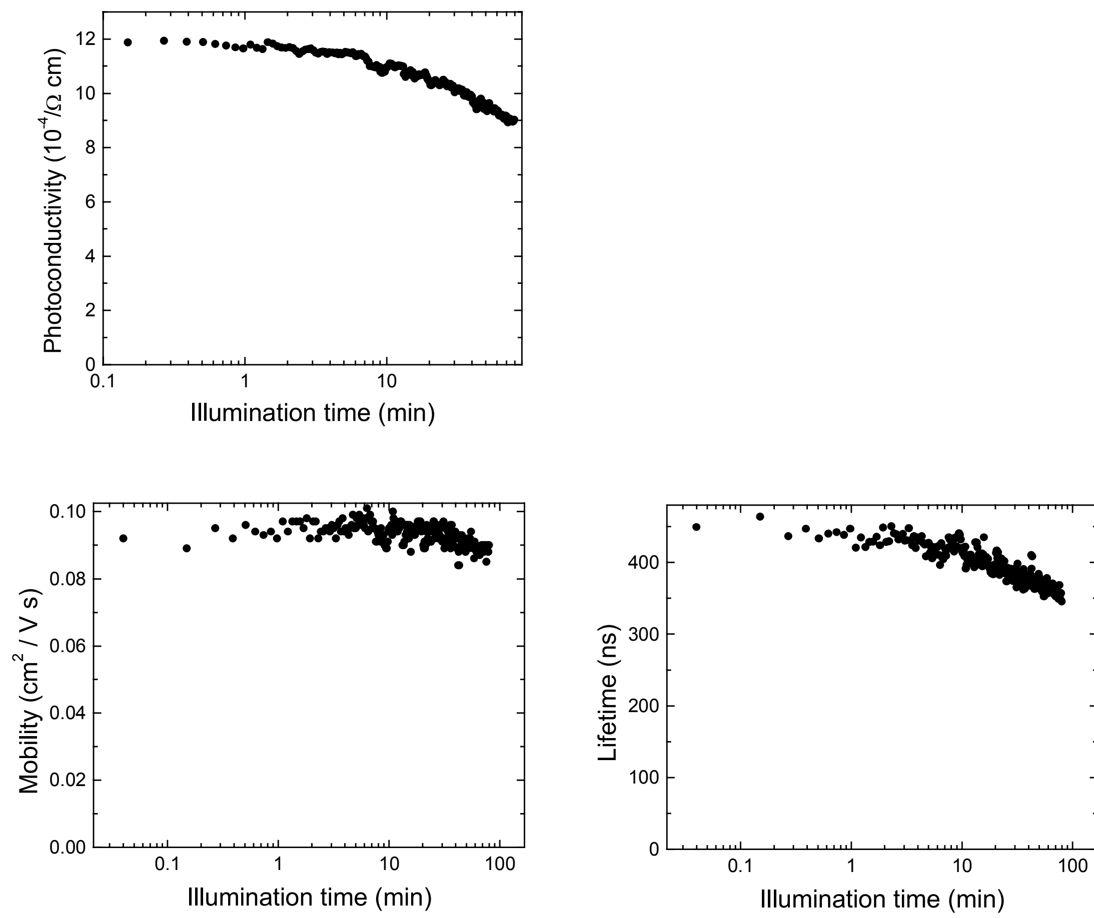

Figure 36. Light-induced changes of photoconductivity, mobility, and lifetime for sample MVS 968

Other three sets of new samples

In Phase II of this program, we reported our photomixing transport measurements of a series of a-Si:H/μc-Si:H samples provided by MVSystems starting in the completely amorphous regime through to microcrystallinity. Unfortunately, we were unable to obtain data on most of the samples as the photoresponse of these is generally very low and therefore not suitable for our mixing method.

We have received three series of new HWCVD H-diluted intrinsic amorphous and microcrystalline silicon films from MVSystems for photomixing transport measurements. These samples were deposited on glass substrates with different filament-substrate distance, substrate temperature and H-dilution. We have performed detailed photomixing measurements on these samples in the annealed state, and obtained interesting results, which were found to be somewhat similar to those we reported previously on NREL HWCVD samples in the transition from amorphous to microcrystalline silicon. While, more samples near the transition regime are required from MVSystems in order to investigate more in detail the charge transport properties in the transition materials.

1 Effects of the filament-substrate distance (F-S), substrate temperature and H-dilution on transport properties of HWCVD microcrystalline Si films.

This set of HWCVD intrinsic microcrystalline Si films were made with different filament-substrate distance (F-S), substrate temperature and H-dilution. All samples are crystallized and of high fraction of crystalline phase. Table 6 summarizes the growth conditions of the μc-Si:H samples.

Table 6. Preparation conditions and thickness of HWCVD μc-Si:H samples provided by MVSystems Inc.

Sample	Substrate Temperature	Filament-Substrate Distance	SiH_4 (%)	Thickness (Å)
MVS1412	High	Long	5.06	15600
MVS1406	High	Long	6.25	9700
MVS1407	High	Long	7.41	7500
MVS1411	Low	Short	6.25	11200
MVS1466	High	Short	5.06	8400
MVS1467	High	Short	6.25	7500

Let's first see the effect of hydrogen dilution on the transport properties of μc-Si:H samples deposited at high substrate temperature and long F-S. The results are shown in Table 7. We can see that with increasing H-dilution up to 5.06% SiH_4 in H_2, the photoconductivity increases monotonically, which is somewhat surprisingly attributed to the increase in the mobility, rather than in the lifetime that shows little change. This interesting result is consistent with the decrease observed in the density of charged scattering centers, which results mainly from the H-dilution-induced decrease in the depth of the long-range potential fluctuations.

Table 7. The effect of hydrogen dilution on the transport properties of μc-Si:H samples provided by MVSystems Inc.

Sample	**Lifetime (ns)**	**Drift Mobility (cm^2/Vs)**	**Photoconductivity (S/cm)**	**Depth of LRPF V_P (eV)**	**Range of LRPF L (nm)**	**V_P^2 / L ($\times 10^{-4}$)**
MVS1412 SiH_4: 5.06%	136.22	0.80	1.14×10^{-3}	0.066	33.97	1.29
MVS1406 SiH_4: 6.25%	173.13	0.29	8.77×10^{-4}	0.092	39.89	2.12
MVS1407 SiH_4: 7.41%	154.05	0.17	5.71×10^{-4}	0.106	31.47	3.59

Table 8 shows the substrate temperature effect on the transport properties of μc-Si:H samples grown at 6.25% SiH_4 in H_2 and short F-S. From these results, we see clearly that higher temperature can significantly improve the film transport properties.

Table 8. The effect of substrate temperature on the transport properties of μc-Si:H samples provided by MVSystems Inc.

Sample	**Lifetime (ns)**	**Drift Mobility (cm^2/Vs)**	**Photoconductivity (S/cm)**	**Depth of LRPF V_P (eV)**	**Range of LRPF L (nm)**	**V_P^2 / L ($\times 10^{-4}$)**
MVS1411 T_{sub}: Low	163.00	0.23	5.41×10^{-4}	0.099	29.26	3.34
MVS1467 T_{sub}: High	546.87	0.31	3.61×10^{-3}	0.091	50.26	1.64

Table 9 shows the influence of filament-substrate distance (F-S) on the transport properties of μc-Si:H samples grown at high substrate temperature and two different H-dilution (5.06% and

6.25% SiH_4 in H_2, respectively). We can see that although the short F-S increases the photoconductivity despite different degrees of H-dilution, it increases both the lifetime and mobility for lower H-dilution due to a reduction in the charged defect density, while increases only the lifetime for higher H-dilution.

Table 9. The effect of flament-substrate distance on the transport properties of μc-Si:H samples provided by MVSystems Inc.

Sample	Lifetime (ns)	Drift Mobility (cm^2/Vs)	Photoconductivity (S/cm)	Depth of LRPF V_P (eV)	Range of LRPF L (nm)	V_P^2 / L ($\times 10^{-4}$)
MVS1412 F-S: Long	136.22	0.80	1.14×10^{-3}	0.066	33.97	1.29
MVS1466 F-S: Short	178.14	0.71	2.41×10^{-3}	0.069	29.23	1.62
MVS1406 F-S: Long	173.13	0.29	8.77×10^{-4}	0.092	39.89	2.12
MVS1467 F-S: Short	546.87	0.31	3.61×10^{-3}	0.091	50.26	1.64

From the above results, we see that higher H-dilution, higher substrate temperature and short F-S can help improve the transport properties of μc-Si:H films. While, due to fewer samples provided, we do not observe the considerable decrease in the mobility and huge increase in the lifetime, as we previously observed for NREL HWCVD samples in the transition from amorphous to microcrystalline silicon when the completely microcrystalline regime is entered.

2 Effect of H-dilution on transport properties of HWCVD amorphous/microcrystalline Si films.

The series discussed here consists of six HWCVD intrinsic Si films. These samples were prepared under the same conditions (middle substrate temperature and long flament-substrate distance), except for the H-dilution, and they cover from microcrystalline Si films made with high H-dilution to amorphous Si films made with low H-dilution. Figure 37 shows the XRD patterns of the samples (these measurements made by Don Willimason of the Colorado School of Mines), where the H-dilution degree and film thickness are also given. We can see that when the

H-dilution degree is over (<) ~6% SiH_4 in H_2, the film becomes partially microcrystalline material, which is demonstrated by considerably enhanced μc-Si:H XRD (111) and (220) peaks.

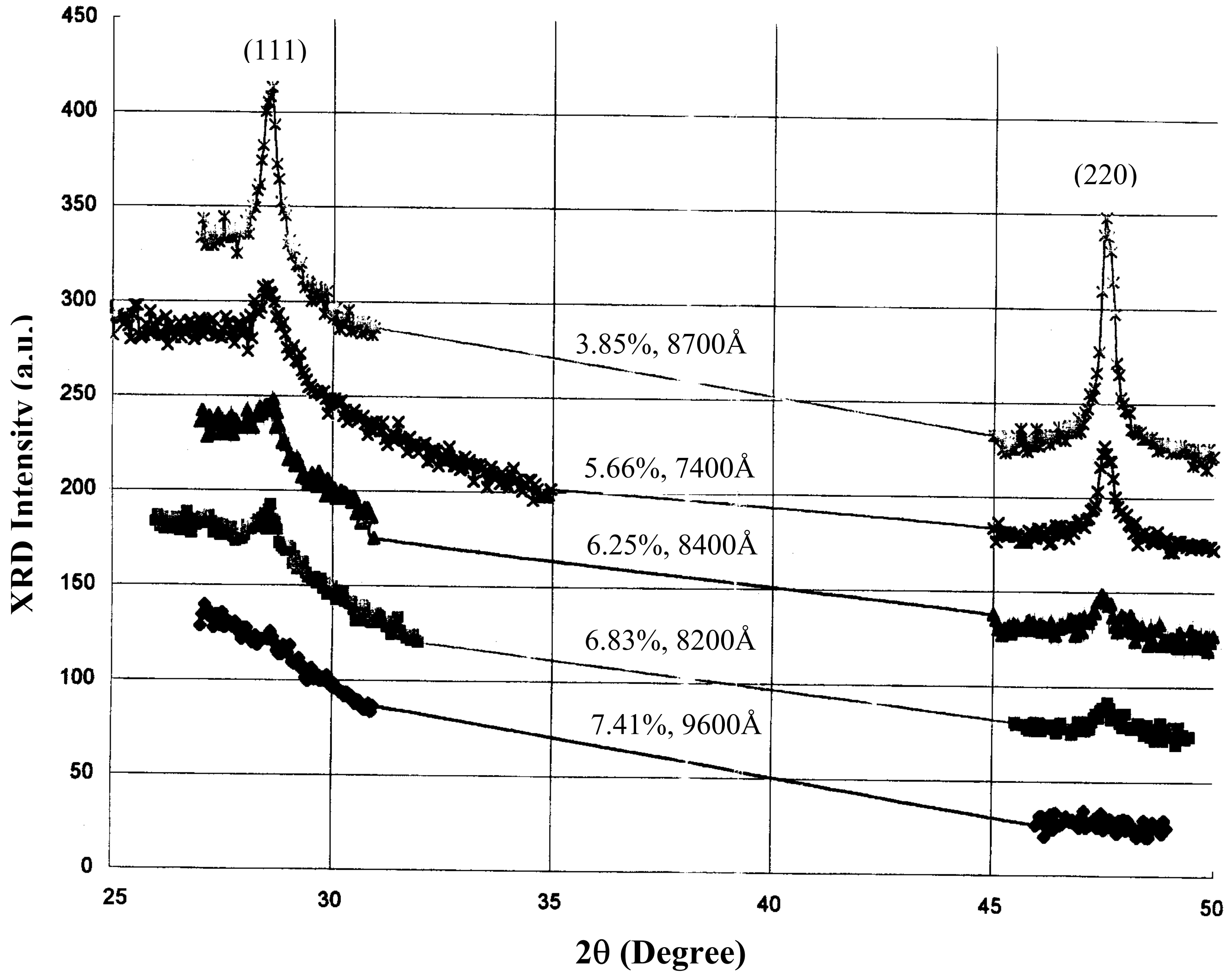

Figure 37. XRD patterns of the HWCVD intrinsic Si films samples. The H-dilution degree and film thickness are also given.

Figure 38 shows the photoconductivity of the samples as a function of H-dilution. It is seen that with increasing H-dilution up to 5.06% SiH_4 in H_2 where the microcrystalline regime has begun to be entered, the photoconductivity increase dramatically, which is found to be due to a considerable increase in the lifetime, as shown in Fig. 39 (a). While, the mobility does not show the expected significant decrease (Fig. 39 (b)). When further increasing H-dilution to 3.85%, the photoconductivity abruptly decreases by one order of magnitude mainly due to a rapid decrease in the lifetime; the mobility seems to be lowered a little.

From the electric field dependence of the mobility, we have calculated the range and depth of the potential fluctuations, and consequently estimated the relative changes in the charged defect

density in the films as a function of H-dilution. The results are shown in Figures 40 and 41, respectively. Unfortunately, we do not observe any apparent trend of changes in the depth and range, as well as the charged defects with H-dilution ranging from 7.41% to 3.85%.

The above results indicate that as for this series of samples, perhaps neutral defects, as effective recombination centers affecting the lifetime of carriers, play a dominant role in the charge transport.

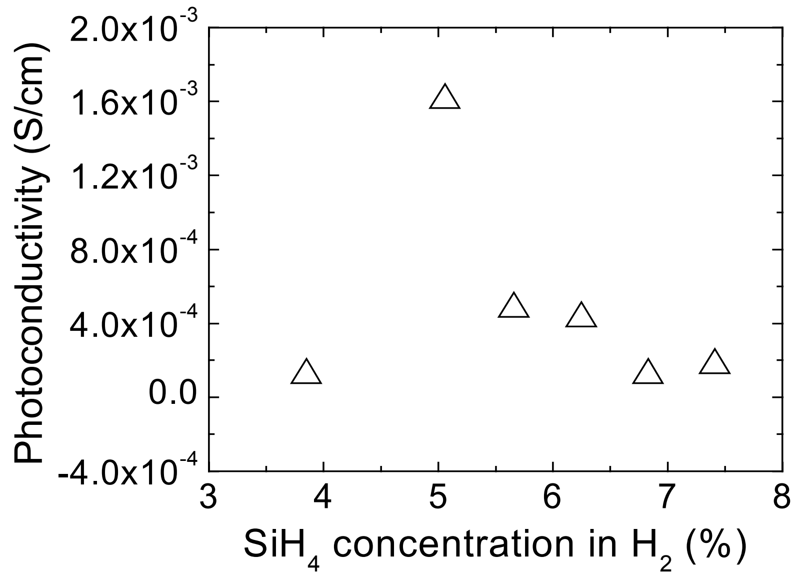

Figure 38. The photoconductivity of the samples as a function of H-dilution.

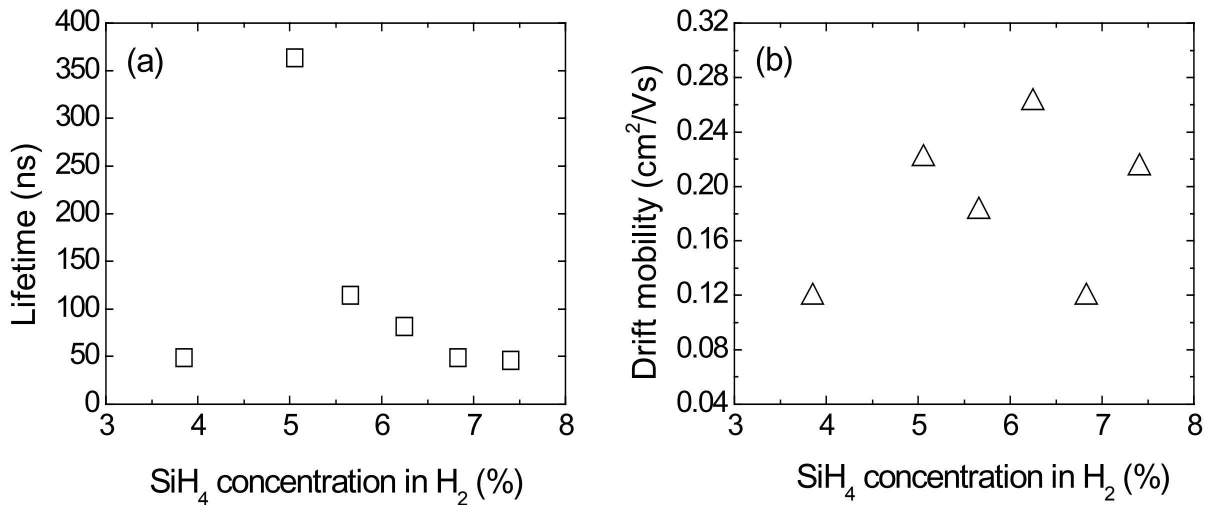

Figure 39. The lifetime (a) and mobility (b) as a function of H-dilution.

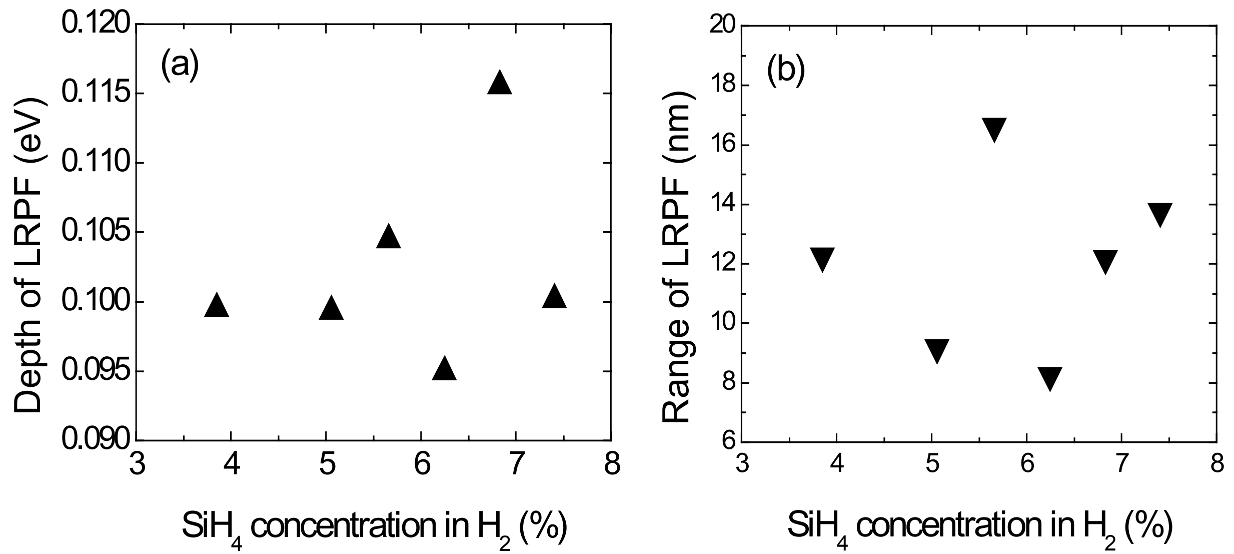

Figure 40. The depth (a) and range (b) of potential fluctuations as a function of H-dilution.

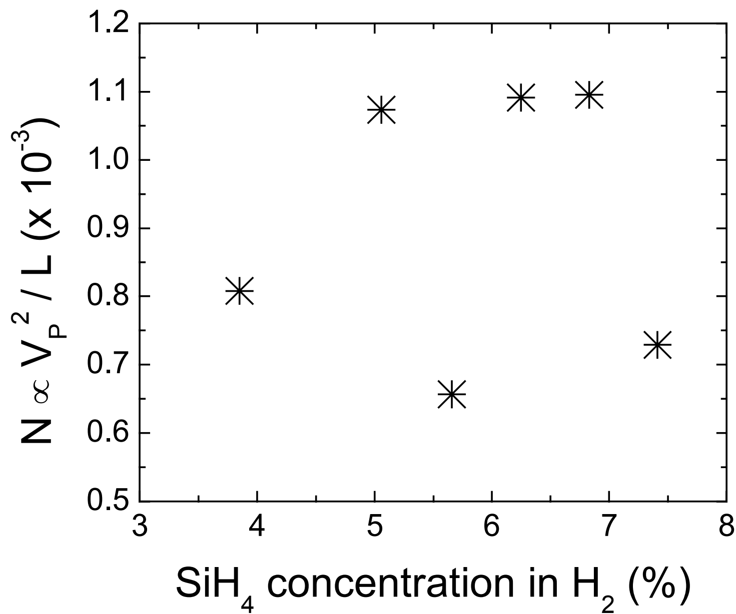

Figure 41. The relative change in the density of charged defects as a function of H-dilution.

3. *Effect of H-dilution on transport properties of HWCVD amorphous/microcrystalline Si films prepared under optimized conditions.*

We have studied above the transport properties of HWCVD amorphous/microcrystalline Si films with respect to deposition parameters, such as filament-substrate distance (F-S), substrate temperature and H-dilution. We have found that higher H-dilution, higher substrate temperature and short F-S can improve the transport properties of films. While, we do not see yet well-behaved properties near the amorphous to microcrystalline transition regime. Fortunately, we have received the third set of HWCVD samples from MVSystems Inc. These samples were grown under optimized conditions (short filament-substrate distance and high substrate temperature) with a little wider range of H-dilution. This set of samples may allow us to investigate more in detail the charge transport properties in the transition materials. Table 10 summarizes the H-dilution used (silane concentration in H_2) and the film thickness.

Table 10. Preparation conditions and thickness of HWCVD μc-Si:H samples provided by MVSystems Inc.

Sample	SiH_4 (%)	Thickness (Å)	
MVS1480	8.75	8200	**Short** filament-substrate (F-S) distance **High** substrate temperature
MVS1481	8.75	11000	
MVS1482	5.00	8200	
MVS1483	7.50	11300	
MVS1484	6.25	9800	
MVS1485	10.00	11300	
MVS1486	3.75	9300	
MVS1487	7.00	8800	
MVS1488	8.00	9900	
MVS1489	9.50	7800	
MVS1490	7.50	13000	

Figure 42 shows the photoconductivity of the samples as a function of H-dilution. It is seen that the photoconductivity does not change monotonically with H-dilution. With increasing H-dilution up to about 7-8% SiH_4 in H_2, the photoconductivity surprisingly decrease at first, but with further increasing H-dilution, it begins to increase considerably; when H-dilution is increased over 4%, the photoconductivity is increased by about two orders of magnitude. This non-monotonic change is attributed to the similar changes in both the mobility and lifetime with H-dilution (see Fig. 43), in contrast to the case of the samples prepared at middle substrate temperature and long F-S distance.

The non-monotonic change observed particularly in the mobility has been confirmed by the determination of the depth and range of the potential fluctuations, and subsequently the relative changes in the charged defect density in the films as a function of H-dilution. From Fig. 44, we see that the depth peaks at medium H-dilution (7-8%), while decreases rapidly when H-dilution is over 4%, which leads to similar changes in the charged defect density shown in Fig. 45.

The above results suggest that both charged defects and neutral defects may be involved in the charge transport of the third set of films.

From the photomixing transport results of these three series of HWCVD amorphous/microcrystalline Si samples, we have seen some different behaviors with H-dilution. This might be due to different microstructure in the films. Therefore, to further understand the transport properties, it is necessary to perform detailed studies of structural properties of the samples prepared at different conditions, particularly across the entire range of H-dilution (0-100%). We anticipate more samples near the transition regime are available from MVSystems in order to investigate more in detail the charge transport properties in the transition materials.

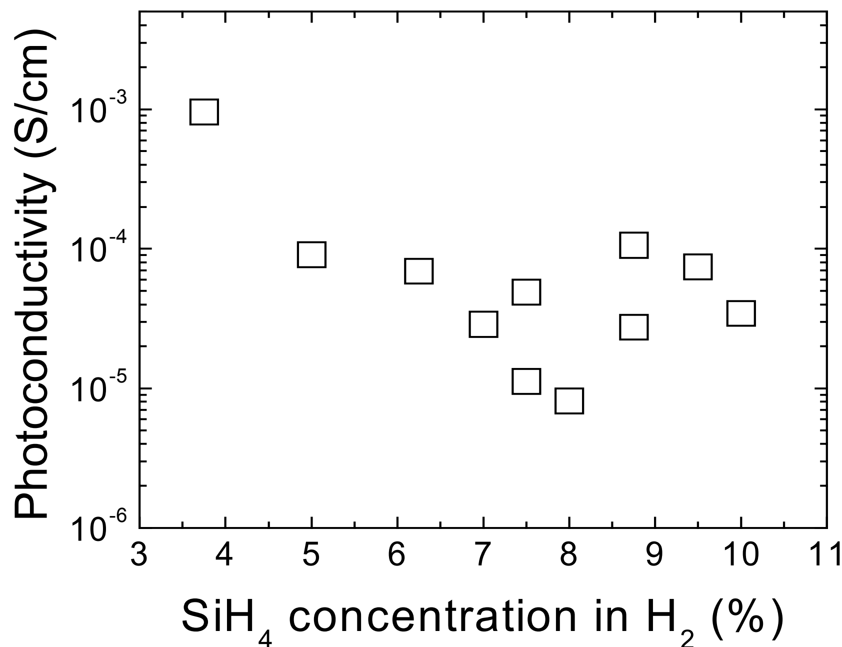

Figure 42. The photoconductivity of the samples as a function of H-dilution.

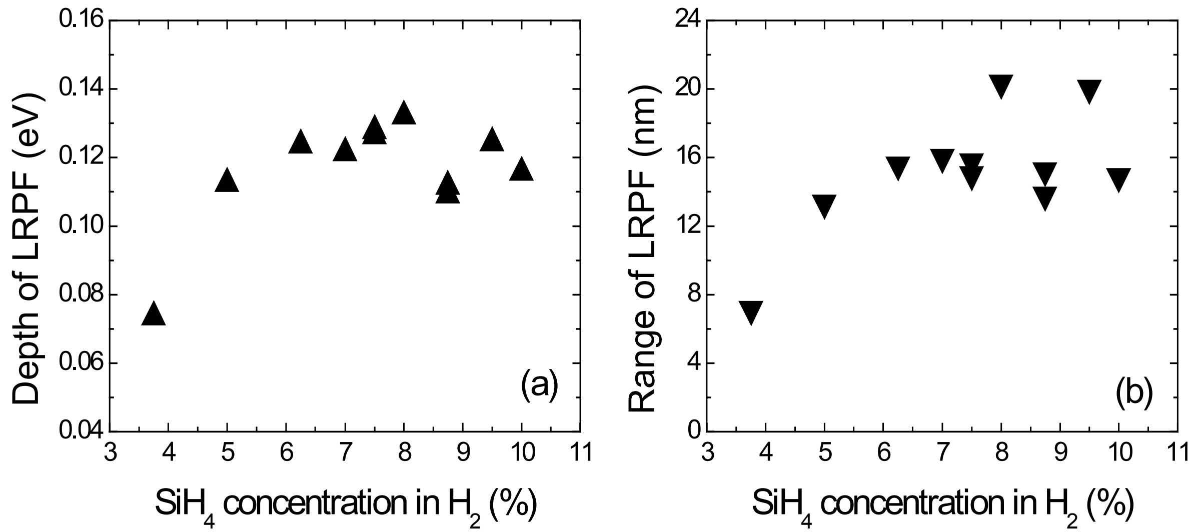

Figure 43. The mobility(a) and lifetime (b) as a function of H-dilution.

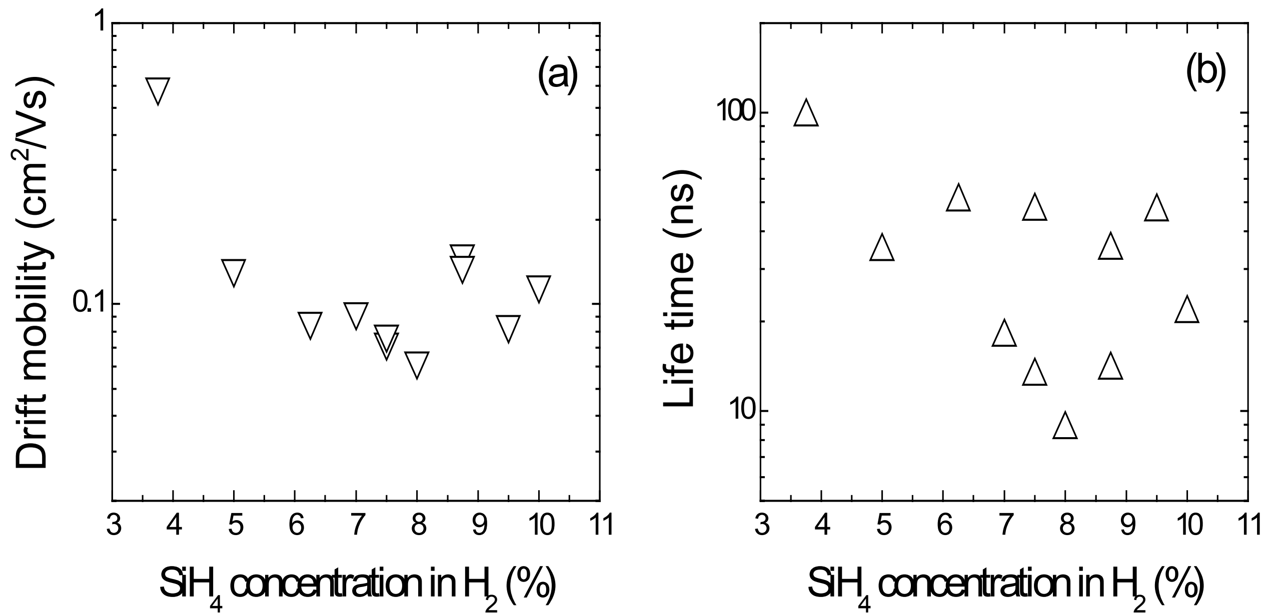

Figure 44. The depth (a) and range (b) of potential fluctuations as a function of H-dilution.

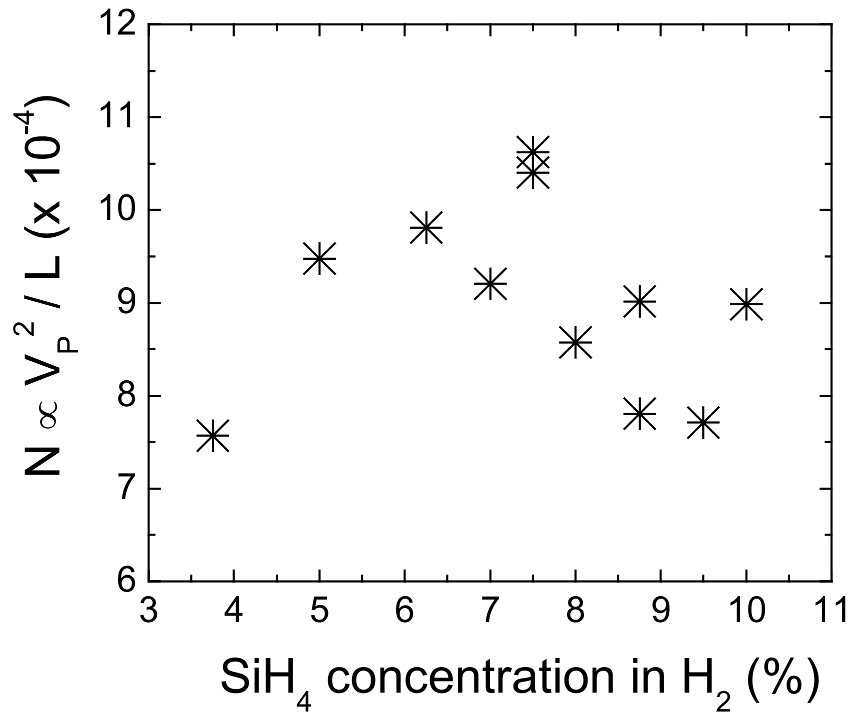

Figure 45. The relative change in the density of charge defects as a function of H-dilution.

6.3 Charge transport properties of microcrystalline silicon prepared by Pulsed PECVD technique (MVSystems Inc.)

During the third quarter of Phase III, We have conducted detailed photomixing transport measurements on three series of new HWCVD H-diluted intrinsic amorphous and microcrystalline silicon films supplied by MVSystems. These samples were deposited on glass substrates with different filament-substrate distance, substrate temperature and H-dilution. It was found that higher H-dilution, higher substrate temperature and short F-S help improve the film transport properties. The results were found to be somewhat similar to those we reported previously on NREL HWCVD samples in the transition from amorphous to microcrystalline silicon. While, more samples near the transition regime are required from MVSystems in order to perform well-defined studies of the charge transport properties in the transition materials.

We have received a series of microcrystalline silicon films prepared by the Pulsed PECVD technique from MVSystems for photomixing transport measurements. These samples were deposited on glass substrates with varying H-dilution and substrate temperature. They made n/i/p solar cells using the same recipe for some of the respective films. This may allow us to correlate intrinsic film properties with the related device performance.

Table 11 shows the deposition conditions and some measured properties of the microcrystalline Si samples, as disclosed by MVSystems. The samples nrct#149-154 are a series of μc-Si:H films deposited with varying H-dilution, and the samples nrct#175, 176, and 181 are μc-Si:H films deposited with differing substrate temperature.

Table 12 shows the XRD results (Don Williamson, Colorado School of Mines) of the μc-Si:H samples. The quantity R(220) is the ratio of the (220) XRD peak area to the (111) peak area. In powder Si, this ratio should be 55%; for the films near the amorphous-to-microcrystalline transition, it is seen to be in the range of 700%, indicating that the transition films are strongly (220) oriented. We can see from Table 12 that H-dilution has different effects on the (111) and (220) crystallites. Increasing H-dilution reduces the (111) grain size, but increases the (220) grain size. Furthermore, the ratio of the (220) peak area to the (111) peak area does not change monotonically with increasing H-dilution; it increases up to a maximum (740%) at H-dilution degree of 93.6%, but with further increasing H-dilution, it begins to decrease again. These results indicate that at lower H-dilution, particularly 93.6%, the films are strongly (220) oriented, and near the transition regime. When H-dilution increases beyond about 96%, the films change to dominantly (111) oriented although the (220) grain size increases.

From the XRD results of samples deposited at H-dilution degree of 93.6% with differing substrate temperature, we see that higher substrate temperature favors the microcrystalline formation. Increasing substrate temperature increases both the (111) and (220) grain size, as well as the R(220) ratio. When the substrate temperature is higher than 400ºC, the films are strongly (220) oriented, indicating near the transition regime; but for film nrct#176 deposited at 330ºC, there is no microcrystallites detectable by XRD, and also it has almost no photoresponse, suggesting very poor transport properties.

Table 11. Deposition conditions and properties of Pulsed PECVD μc-Si:H samples provided by MVSystems.

SN	Temperature (ºC)	Pressure (mTorr)	H Dilution (%)	Thickness (Å)	Light Cond. (S/cm)	Dark Cond. (S/cm)	Activation Energy (eV)
nrct#149	410	400	97.3	6000	5.40×10^{-5}	9.10×10^{-6}	—
nrct#150	410	400	96.1	4900	2.30×10^{-4}	2.20×10^{-5}	—
nrct#152	410	400	94.8	6000	1.60×10^{-4}	1.10×10^{-5}	—
nrct#153	410	400	93.6	7300	8.00×10^{-5}	5.50×10^{-6}	—
nrct#154	410	400	92.4	7300	6.00×10^{-5}	6.00×10^{-6}	—
nrct#175	410	200	93.6	6700	2.90×10^{-5}	2.80×10^{-6}	0.48
nrct#176	330	200	93.6	4850	3.40×10^{-7}	3.20×10^{-7}	0.27
nrct#181	490	200	93.6	3600	2.90×10^{-5}	7.00×10^{-7}	0.53

Table 12. XRD characterizations of Pulsed PECVD μc-Si:H samples provided by MVSystems.

SN	(111) grain size (Å)	(220) grain size (Å)	R (220) (%)
nrct#149	180	280	62
nrct#150	270	250	124
nrct#152	270	350	185
nrct#153	250	220	740
nrct#154	270	220	370
nrct#175	210	340	600
nrct#176	None visible	None visible	—
nrct#181	230	350	650

Figures 46-49 show the effects of H-dilution on photomixing transport properties of Pulsed PECVD μc-Si:H samples. From Fig.46, we see that with increasing H-dilution near the transition regime (about 93.6%), the photoconductivity decreases, which is found to be due to a decrease in the drift mobility (Fig.47(a)), while there is little change in the lifetime (Fig.47(b)). With

increasing H-dilution beyond the transition regime, the photoconductivity begins to increase quickly, but then remains almost constant with further increasing H-dilution. This increase observed in the photoconductivity beyond the transition regime results from a considerable increase in the lifetime although the mobility is reduced, as verified by a decrease in the depth of the potential fluctuations with increasing H-dilution (Fig.48(a)). Furthermore, it is interesting to observe when H-dilution is increased beyond the transition regime so that the microcrystalline regime is entered, the range of the potential fluctuations is increased considerably (Fig.48(b)), indicating more ordering in the Si network structure. A longer range is correlated with a lower concentration of charged defects as scattering centers. As shown in Fig.49, The charged defect density decreases a little when H-dilution is increased near the transition regime, and beyond the transition regime, it decreases considerably.

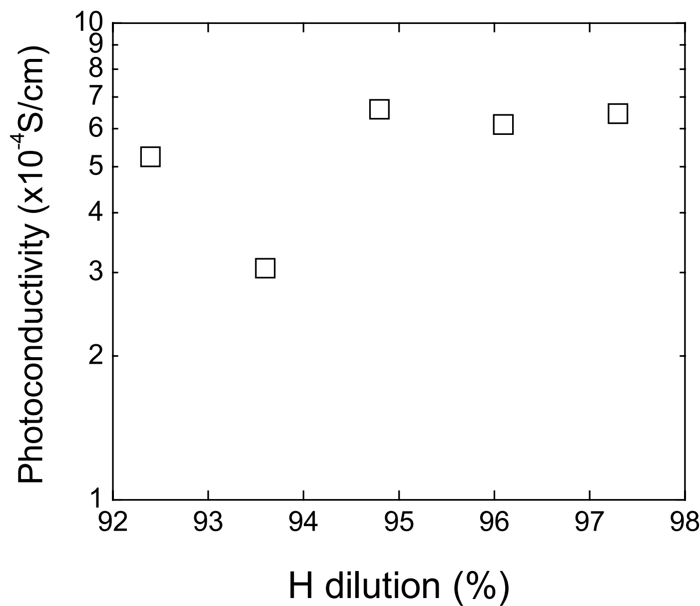

Figure 46. The effect of H-dilution on the photoconductivity of the samples.

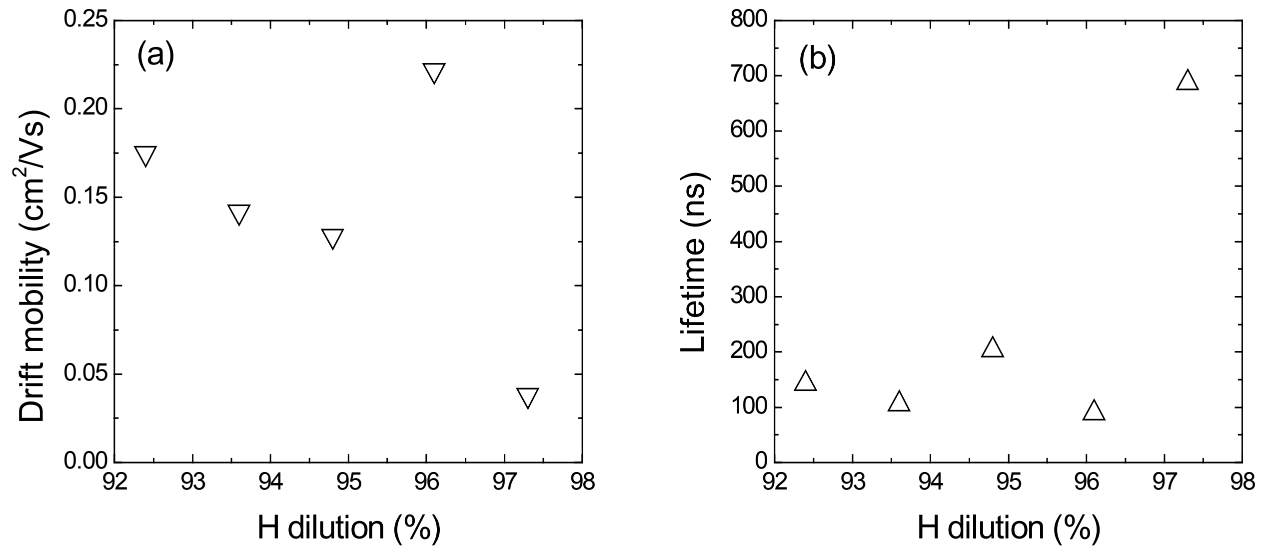

Figure 47. The effect of H-dilution on the mobility (a) and lifetime (b).

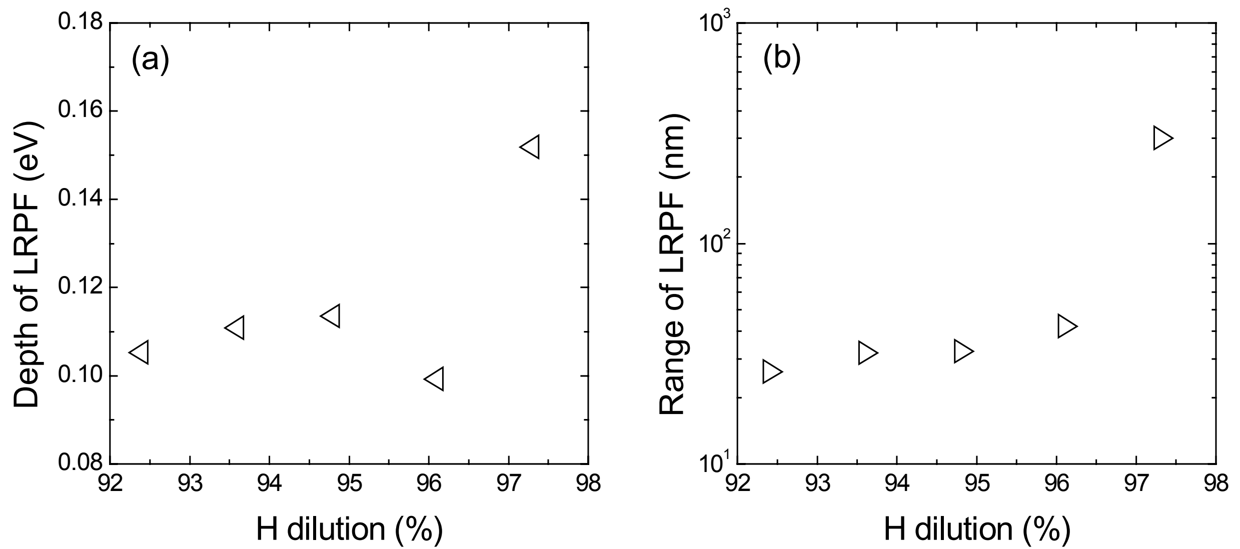

Figure 48. The effect of H-dilution on the depth (a) and range (b) of potential fluctuations.

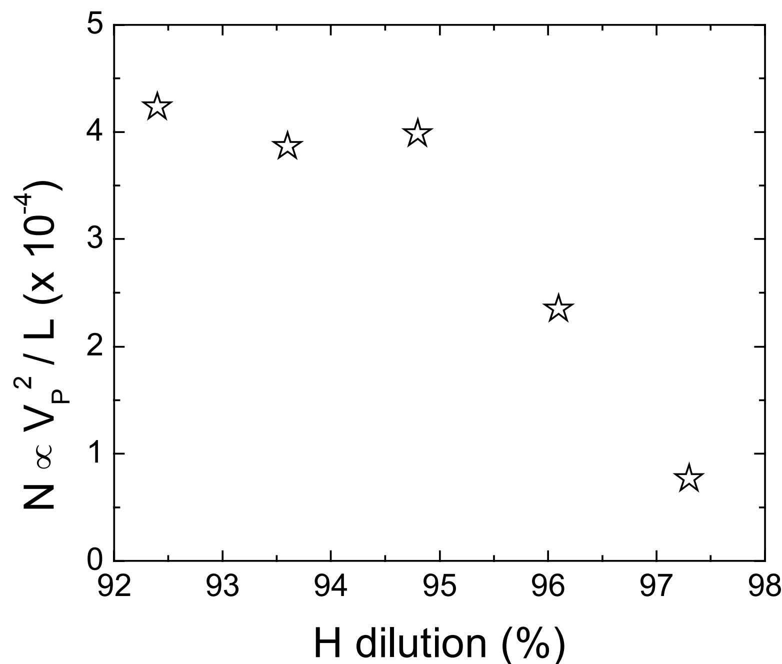

Figure 49. The effect of H-dilution on the relative change in the density of charged defects.

Figures 50-53 show the effects of substrate temperature on photomixing transport properties of Pulsed PECVD μc-Si:H samples deposited near the transition regime (93.6% H-dilution). It is seen that when the substrate temperature is lower than 400ºC, the transport properties are very poor, as the photoconductivity is more than one order of magnitude smaller (Fig.50) due to very low mobility (Fig.51(a)). This results in failure to determine the range and depth of the potential fluctuations. With increasing the substrate temperature up to 410ºC, the lifetime is increased a little, but the mobility is increased significantly, by about one order of magnitude, leading to much enhanced photoresponse. Further increasing the substrate temperature continues to increase the lifetime considerably, but reduces the mobility too, indicating a non-monotonic change in the mobility with substrate temperature. This results in almost constant photoconductivity at higher substrate temperature than 400ºC. It is note-worthy that although higher substrate temperature reduces the mobility due to an increase in the depth of the potential fluctuations (Fig.52(a)), it dramatically increases the range (Fig.52(b)), leading to much lower density of charged defects in the films (Fig.53).

n/i/p solar cells have been made by MVSystems using the same recipe for films #175 and #181. The latter film deposited at higher substrate temperature appears to result in an improved solar cell, compared to the former. This indicates that there is a scaling between the intrinsic film properties and the related device performance, and higher substrate temperature is required for the Pulsed PECVD technique to produce high quality films and related devices near the transition regime.

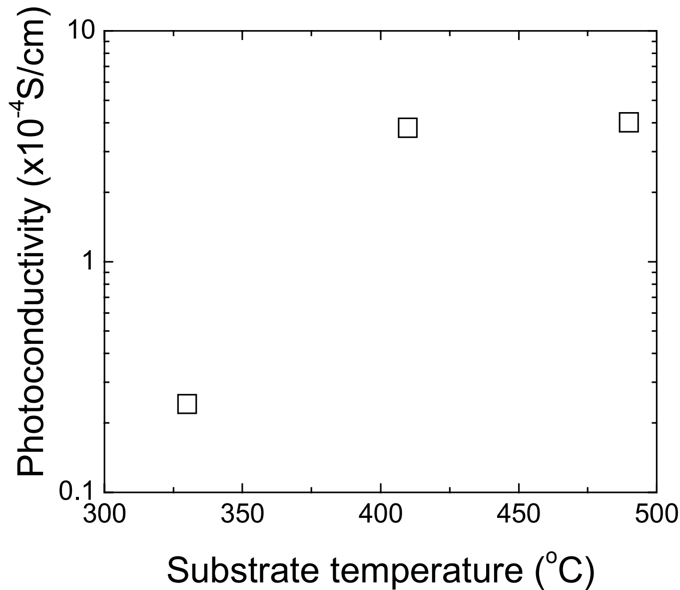

Figure 50. The effect of substrate temperature on the photoconductivity of the samples.

Figure 51. The effect of substrate temperature on the mobility (a) and lifetime (b).

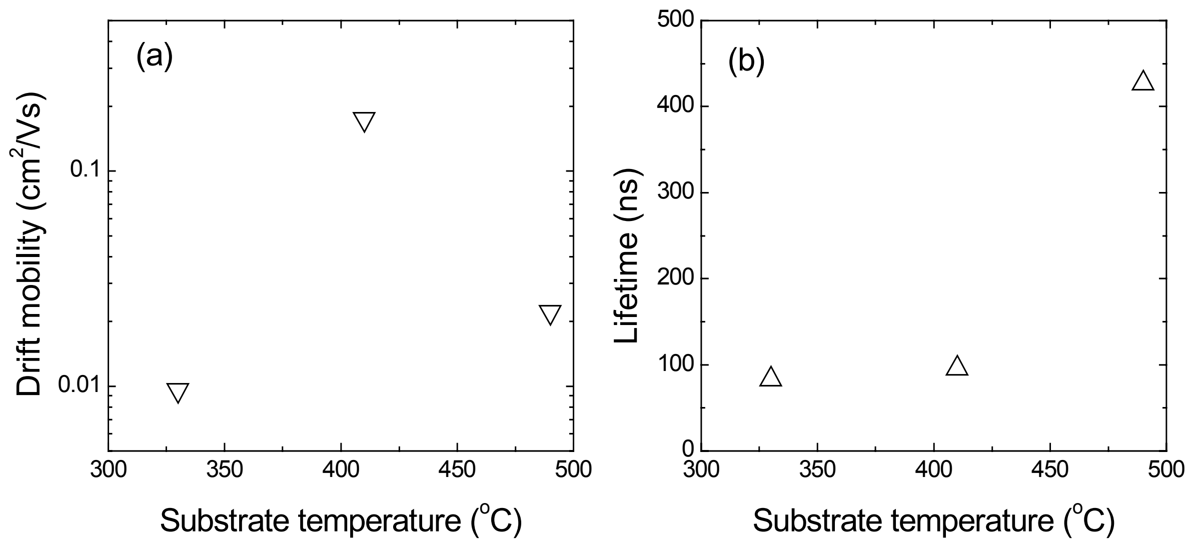

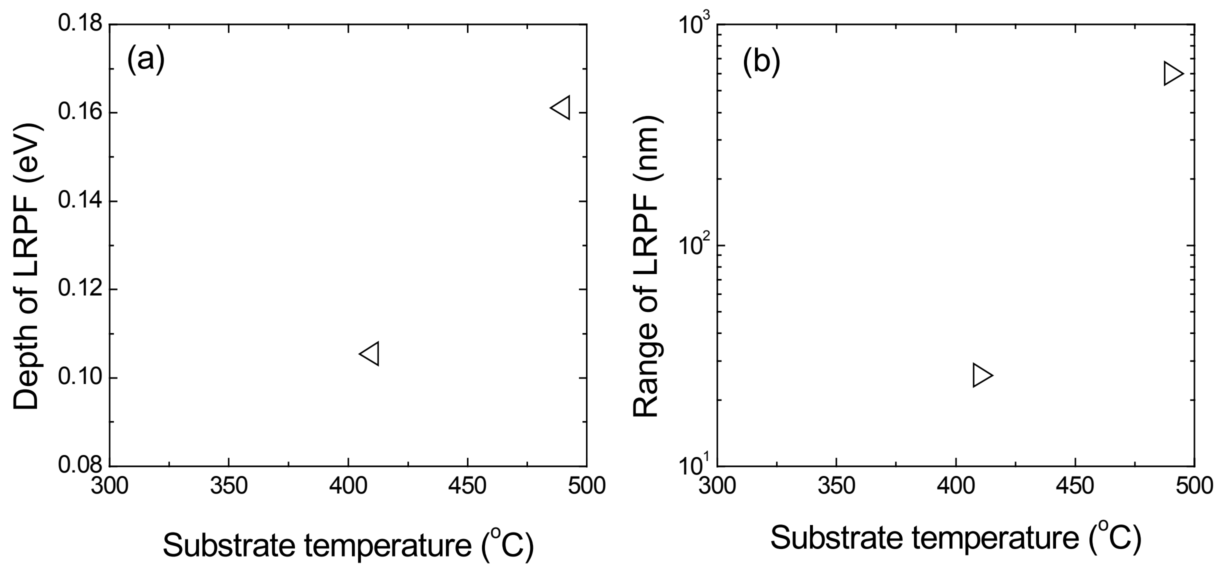

Figure 52. The effect of substrate temperature on the depth (a) and range (b) of potential fluctuations.

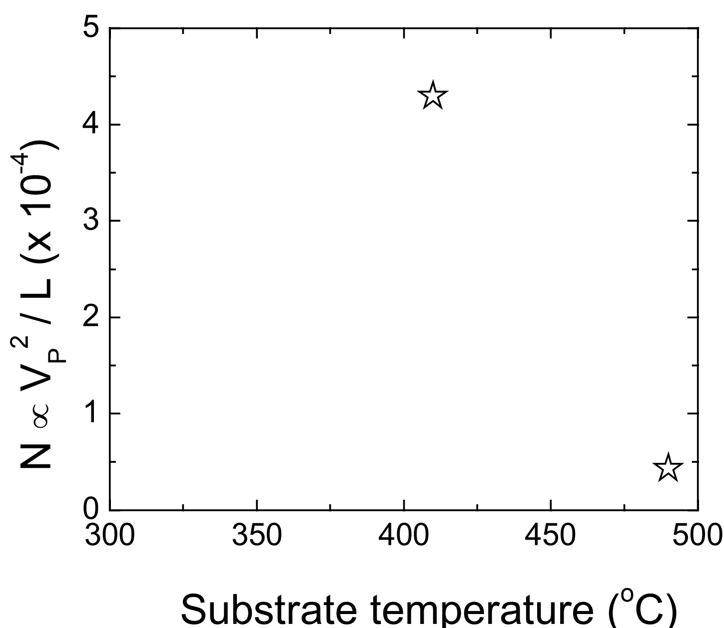

Figure 53. The effect of substrate temperature on the relative change in the density of charged defects.

7. High Deposition Rate Preparation of a-Si:H by HWCVD

7.1 First series of samples

The deployment of solar cells for large scale power generation is contingent not only upon the production of photovoltaic devices of stable high efficiency but for industrial production, high deposition rate is desirable to improve the throughput for a given machine, and also to reduce the costs and the capital investment. It has been suggested that with increasing deposition rates, higher silane related radicals, short-lifetime radicals, increased ion-bombardment energies, and hence more resultant microvoids and defects, are potential causes for deterioration of the performance and stability of hydrogenated amorphous silicon (a-Si:H) films. Various techniques to improve the deposition rate have been attempted: with plasma enhanced chemical vapor deposition (PECVD) which usually yields material with poor initial performance and poor stability when deposition rates are increased, which has been correlates with the increased density of microvoids [19]. A correlation between the gas phase species in the silane plasma and the properties of a-Si:H films deposited by PECVD has indicated that the higher-order silane species contribute to the cause of light-induced degradation in the film quality at high deposition rates [20]. The growth rate of these a-Si:H films ranged from 2 Å/s to 20 Å/s.

At present, it is generally believed that the performance of a-Si:H will deteriorate monotonically with increasing deposition rates, but the high deposition rates achieved by PECVD are relatively low, less than 20 Å/s. We have performed photoconductive frequency mixing measurements on much higher deposition rate HWCVD a-Si:H samples provided by Brent Nelson of NREL, and

found some interesting results. The charge transport properties of the samples do not change monotonically with increasing deposition rates.

Brent Nelson has employed the HWCVD technique to prepare a-Si:H films grown with deposition rates ranging from 32 to 191 Å/s. He achieved the high deposition rates by making the following changes to one of his HWCVD reactors.

Deposition Parameter	**Standard Config.**	**High Dep. Rate Config.**
Number of filaments	1	2
Filament to substrate spacing	5 cm	3.2 cm
Silane flow rate	20-50 sccm	50-100 sccm
Deposition Pressure	10-20 mTorr	20-120 m Torr

Brent Nelson has informed us: "The deposition rate is a complicated function of the pressure, silane flow, and filament current. These are the three main parameters we change to alter the deposition rate. The increase in silane flow is necessary to accommodate the increased silane depletion due to multiple filaments. The increased pressure is necessary." We were supplied with the following samples whose preparation parameters are indicated in the Table 13.

Table 13. Growth conditions and properties of high deposition rate HWCVD samples.

Sample ID	Temp. (ºC)	Press. (mTorr)	F(SiH_4) (sccm)	I(fil.) (A)	Thk. (Å)	Rate (Å/s)	Cond. Rate	H(IR) (at.%)
L079	295	20	20	30	6644	31.64	1.29×10^4	4.51
L077	295	70	20	30	8530	47.39	1.17×10^4	4.81
L110	285	19	75	30	10514	58.41	8.60×10^4	9.50
L139	315	50	50	29	8144	67.87	1.15×10^5	7.10
L169	318	50	50	30	9235	76.96	1.02×10^5	6.50
L104	350	50	50	30	10179	84.83	1.11×10^5	7.50
L183	348	70	75	30	11000	109.78	5.72×10^4	5.60
L178	317	70	75	30	11381	113.58	2.63×10^4	6.50
L182	348	70	75	30	11502	114.79	8.63×10^4	4.90
L190	326	50	75	30	9318	132.74	5.64×10^4	6.70
L196	325	75	75	30	8538	142.30	2.30×10^4	5.80
L094	385	90	75	30	13701	152.23	2.37×10^4	6.79
L194	325	70	100	30	10662	177.70	2.64×10^2	5.00
L087	295	120	75	30	22900	190.83	5.73	—

We have characterized these samples in both the annealed and light-soaked states utilizing the photoconductive frequency mixing technique enabling us to determine the drift mobility, lifetime and from the electric field dependence of these quantities, we have been able to determine the range and the depth of the long range potential fluctuations and from the latter two quantities we were able to determine the relative differences in the charge centers which exist in the samples.

Measurements of transport properties of high deposition rate HWCVD a-Si:H films in the annealed state

The photoconductivity as a function of deposition rate is shown in Figure 54. It is seen that in the deposition range from 30 Å/s to ~150 Å/s, the photoconductivity hovers at levels of 10^{-4} (S/cm) except that in the neighborhood of the deposition rate of 70 Å/s, the photoconductivity peaks in the neighborhood of 10^{-2} (S/cm), two orders of magnitude increase above the average! Above the deposition rate of ~150 Å/s, the photoconductivity starts to plummet to 10^{-8} (S/cm)!

By measuring the photomixing signal at 250 Mhz in conjunction with the dc photoconductivity, we determined the drift mobility and the lifetime. Figure 55 shows the drift mobility as a function of deposition rate. Where it is seen that the drift mobility peaks in the neighborhood of 70 Å/s where the photoconductivity peaks. However, it should be noted that the drift mobility varies by integer values, while the photoconductivity varies by orders of magnitude. These differences can be accounted for by the fact that the lifetime as a function of deposition rate varies by orders of magnitude as can be seen in Figure 56.

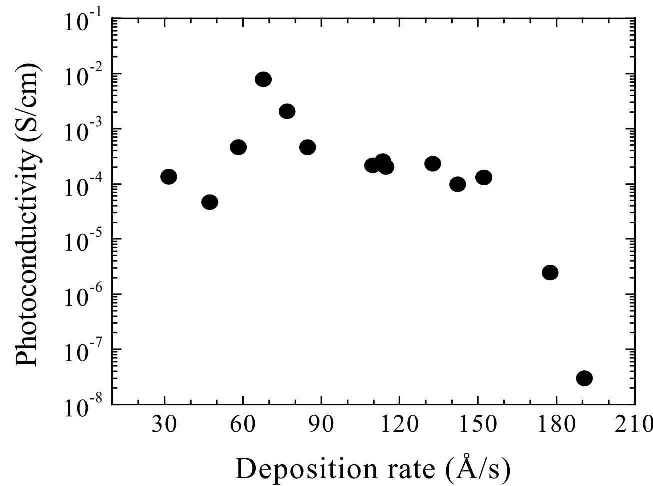

Figure 54. The photoconductivity as a function of deposition rate.

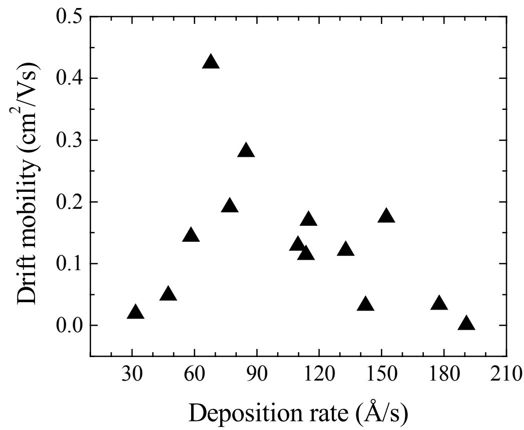

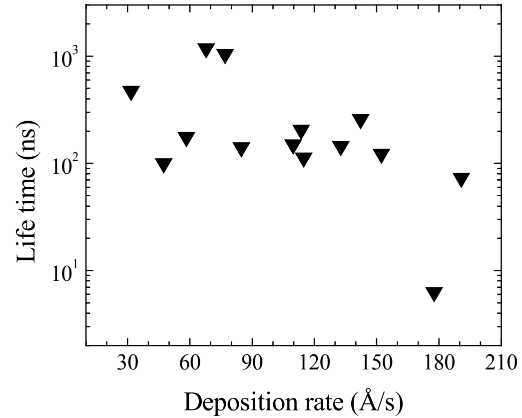

Figure 55. The drift mobility as a function of deposition rate.

Figure 56. The lifetime as a function of deposition rate.

Figure 57 shows a typical electric field dependence of the drift mobility (a) and lifetime (b). From this type of data, we have calculated the range and depth of the long range potential fluctuations which are shown in Figure 58. It should be observed that minimal depth of potential occurs in the region where the drift mobility and photoconductivity peaks as is to be expected.

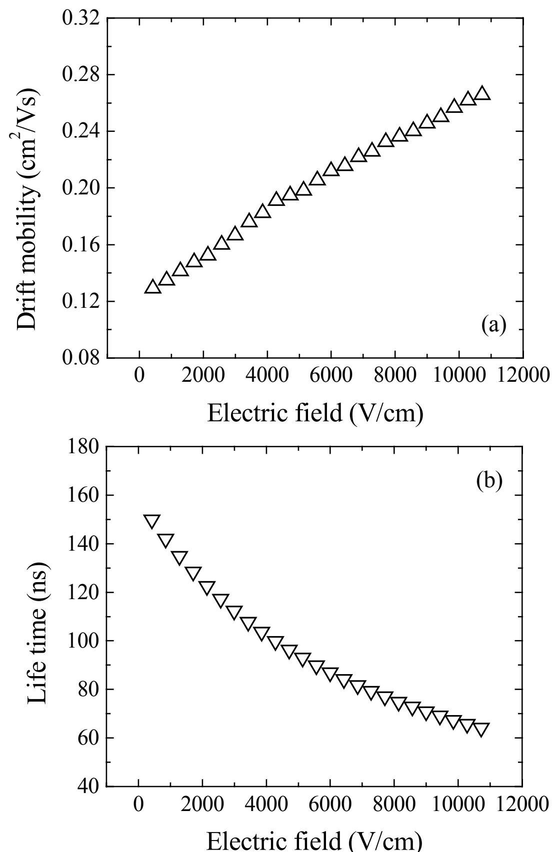

Figure 57. Field dependence of the drift mobility (a) and lifetime (b) for sample L183.

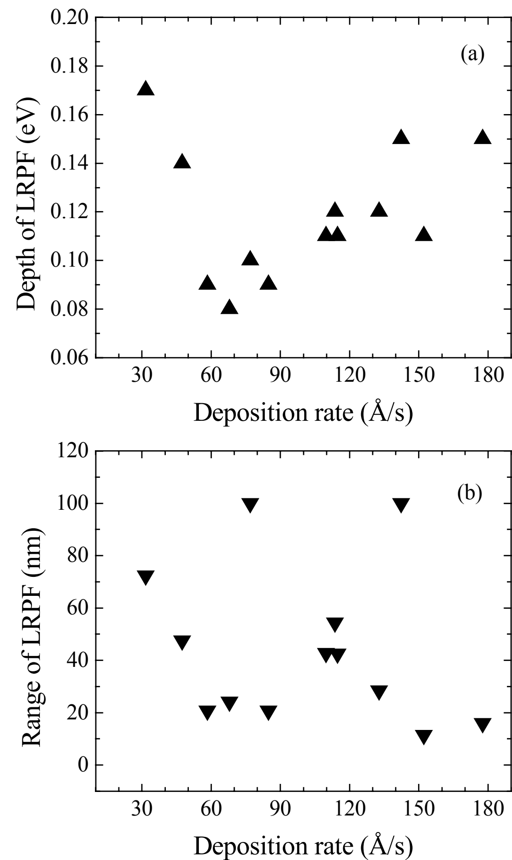

Figure 58. The depth (a) and range (b) of the long range potential fluctuations as a function of deposition rate.

It can be shown that the density of charge defects (n) is given by:

$$n \propto V_P{}^2 / L \quad (1)$$

Where V_P and L represent the depth and range of the long range potential fluctuations, respectively.

Figure 59 shows the relative change in the charged defects as a function of deposition rate. It can be seen that the charged defect density remains constant up to the deposition rate of ~150 Å/s, but above, it increases considerably.

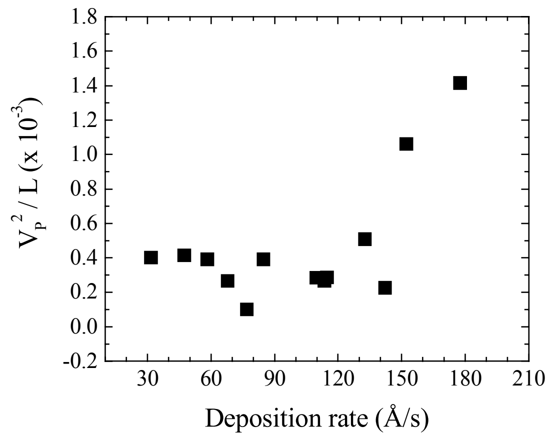

Figure 59. The relative change in the charged defects as a function of deposition rate.

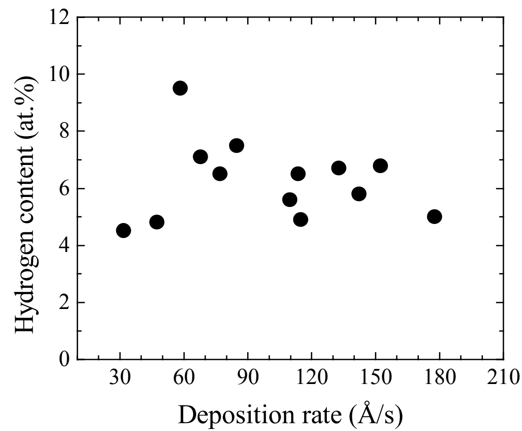

Figure 60. The hydrogen content as a function of deposition rate.

It is of great interest to ascertain what are the chemical or structural properties of the films that vary as a function the deposition rate. The hydrogen content of the samples as a function of deposition rate is shown in Figure 60. It is interesting to note that maximal hydrogen content appears to occur in the region where the drift mobility and photoconductivity peaks, while elsewhere, the hydrogen content is comparable, about 6 at.%. It is clear that it is necessary to look for other film properties that are responsible for variation of charge transport properties as a function of deposition rate. It would be of interest to determine the microvoid and higher order silane content by performing SAXS and IR measurements in the Si-H stretching mode region.

Brent Nelson has provided us some preliminary IR results. There is no increase in dihydride bonding with increasing deposition rate. Table II shows qualitative results of SiH_2 shoulder at 2009 cm^{-1} from the IR spectra. We found that both dark-conductivity and photoconductivity of the samples with detectable SiH_2 shoulder are smaller than those of other samples without detectable SiH_2 shoulder, indicating poorer performance. In addition, we anticipate David Cohen's DLCS measurements of defect density are available.

Light-induced decay measurements of transport properties of high deposition rate HWCVD a-Si:H films

Figure 61 shows the normalized photoconductivity (a), drift mobility (b) and lifetime (c), respectively, for three typical high deposition rate HWCVD a-Si:H samples as a function of illumination time.

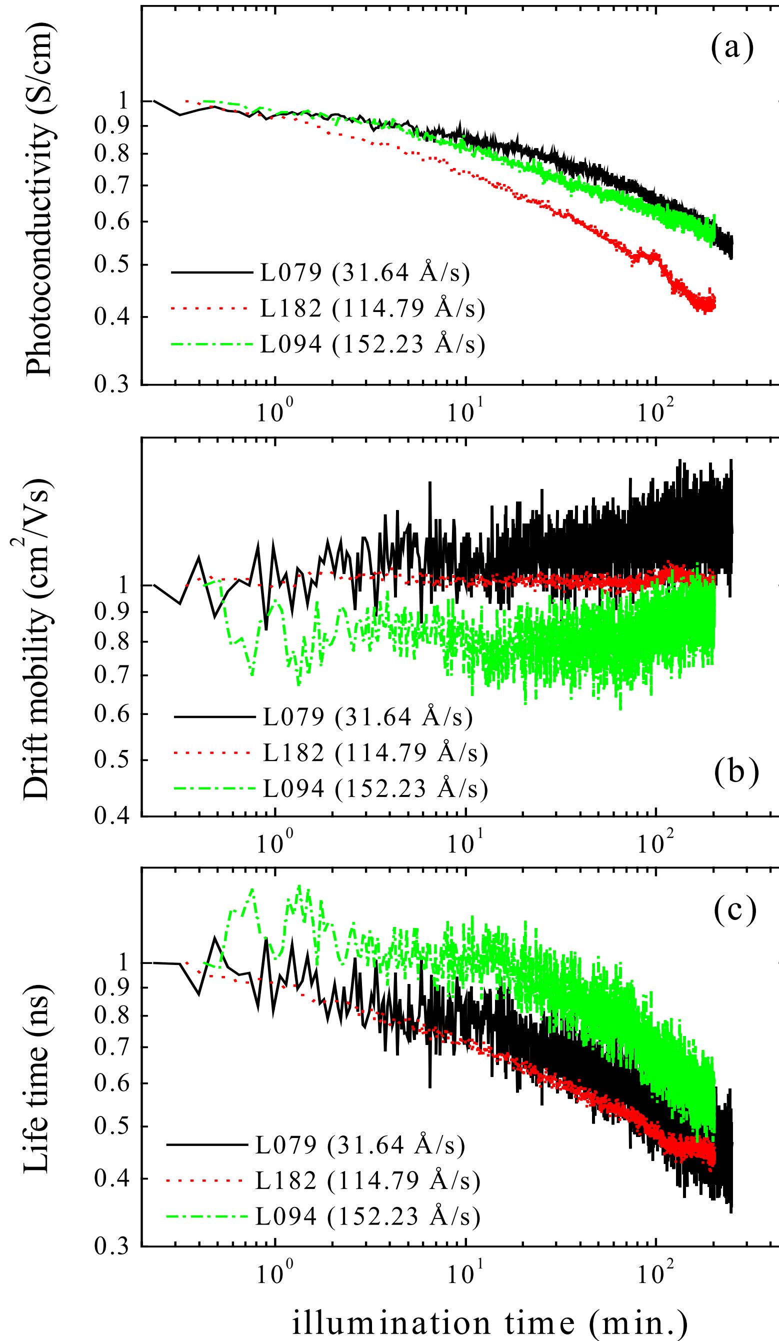

Figure 61. Normalized photoconductivity, drift mobility and lifetime for high deposition rate HWCVD a-Si:H samples as a function of illumination.

It is seen that with light-soaking, the photoconductivity for all the samples decreases, which is demonstrated to be attributed to considerable decreases in the lifetime. It is interesting to note that the drift mobility changes very small, even a little increase upon light-soaking!

In order to investigate more in detail the influence of illumination on the transport properties of the samples as a function of deposition rate, we performed systematical measurements on all samples whose deposition rates range from 32 to 191 Å/s. The photoconductivity, drift mobility and lifetime as a function of deposition rate in both the annealed and the light-induced states are shown in Figure 62 (a), (b) and (c), respectively. It can be seen that light-soaking reduces the photoconductivity and the lifetime, as observed before, while surprisingly increases the mobility for all the samples. Furthermore, the deposition rate dependence of these transport parameters in the light-soaked state is similar to that in the annealed state. Since the mobility varies only by integer values, while the lifetime varies by orders of magnitude, the light-induced decrease in the photoconductivity is mainly due to the decrease in the lifetime.

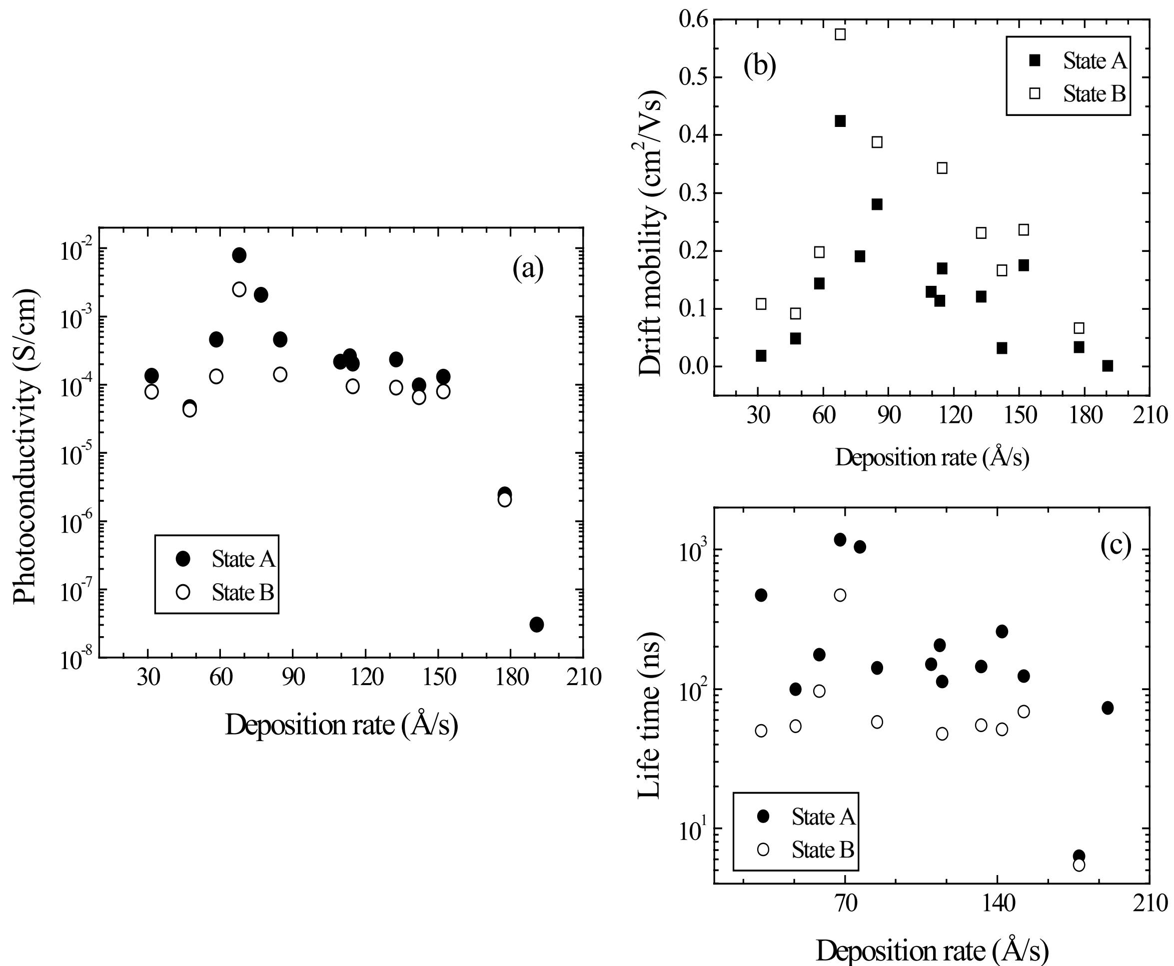

Figure 62. The light-induced changes in the photoconductivity, drift mobility and lifetime as a function of deposition rate.

From the electric field dependence of the drift mobility and lifetime, we have calculated the depth and range of the long-range potential fluctuations. Figure 63 shows the effect of light-soaking on the depth (a) and range (b) of potential fluctuations as a function of deposition rate. We see that illumination reduce considerably the range, as should be expected, but meanwhile also reduce the depth a little which verify the light-induced increase in the mobility observed above.

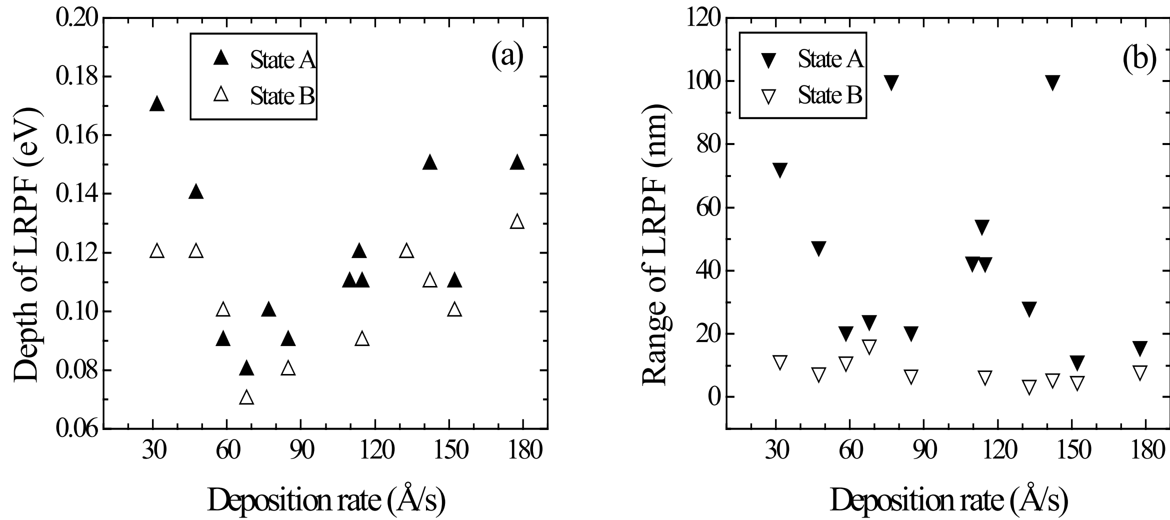

Figure 63. The light-induced changes in the depth and range of potential fluctuations as a function of deposition rate.

Figure 64 shows the light-induced relative change in the density of charged defects as a function of deposition rate. We see that the charged defect density increases upon light-soaking for all deposition rates. It is interesting to note that there appears to be the minimum light-induced increase at the intermediate deposition rates where the photoconductivity, drift mobility and lifetime peak. In addition, it is generally expected that due to the increase in the density of charged defects during the light-soaking process, the depth of the potential fluctuations has a tendency to increase, whereas the range of the potential fluctuations has a tendency to decrease. While, this is not the case here. The light-induced increase in the density of charged defects results from the much more decrease in the range than in the depth.

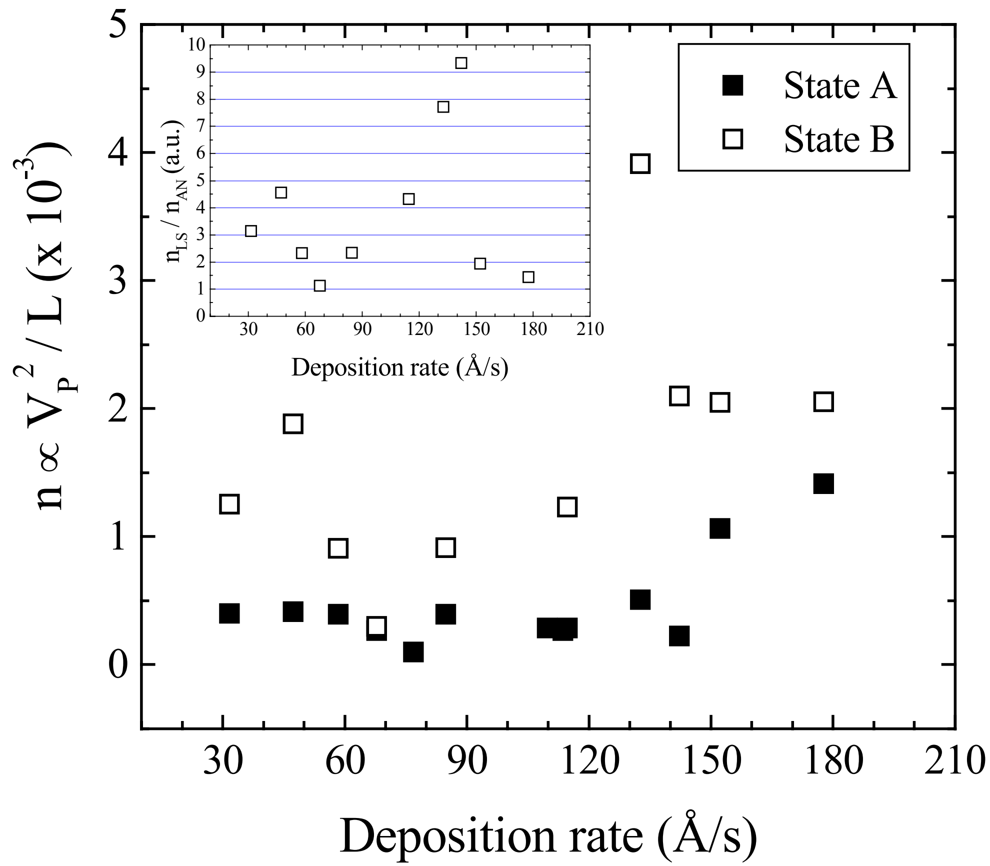

Figure 64. The light-induced relative change in the charged defect density as a function of deposition rate.

7.2 The second series of samples

Electronic Transport Properties of High Deposition Rate HWCVD a-Si:H in the annealed state.

Recently, Brent Nelson et al. at NREL have employed the HWCVD technique to prepare a-Si:H films grown with deposition rates up to 1 μm/min [21]. They found that the deposition rate increases with increasing deposition pressure, silane flow rate, and filament current and decreasing filament-to-substrate distance. There are significant interactions among these parameters that require optimization to grow films of optimal quality for a desired deposition rate. An AM1.5 photoconductivity-to-dark-conductivity ratio of 10^5 could be maintained at deposition rates up to 130 Å/s under the best conditions, beyond which the conductivity ratio decreases. Other electronic properties, e.g. the ambipolar diffusion length, Urbach energy, and as-grown defect density, decrease more rapidly with increasing deposition rate,. The density of microvoids determined by small-angle X-ray scattering (SAXS) was found to increase by well over an order of magnitude when going from one to two filaments. However, both Raman and X-ray diffraction (XRD) measurements show no change in film structure with increasing deposition rates up to 144 Å/s, and atomic force microscopy (AFM) reveals little change in topology.

In phase II of this program, we have reported the photomixing measurements of the first set of high deposition rate HWCVD a-Si:H films supplied by Brent Nelson. The deposition rates range from 32 to 191 Å/s. Shortly thereafter, we received the second set of high deposition rate a-Si:H samples. These new samples were deposited on two kinds of substrates; a 1737 glass substrate for us and a stainless steel substrate for David Cohen at the University of Oregon to determine the defect density by the drive level capacitance spectroscopy (DLCS). This new series has a couple of advantages over the first series of samples. First, it allows us to compare different characterization techniques used on samples grown simultaneously as a part of the same series. Second, some of the growth conditions have been optimized a little further than the first series. He achieved the high deposition rates by making the following changes to one of his HWCVD tube-reactors.

Deposition Parameter	**Standard Configuration**	**High Dep. Rate Config.**
Number of filaments	1	2
Filament to substrate spacing	5 cm	3.2 cm
Silane flow rate	20-50 sccm	40-75 sccm
Deposition pressure	10-20 mTorr	30-70 m Torr
Typical deposition rates	5-20 Å/s	40-150 Å/s

Brent Nelson has informed us: “The increase in silane flow is necessary to accommodate the increased silane depletion due to multiple filaments. The pressure is increased to achieve an optimal number of gas phase collisions at closer filament spacing, and the filament currents used are similar to those for the normal one filament HWCVD process in order to maintain the correct reactions with the silane and the W filament” We were supplied with the following samples whose preparation parameters are indicated in the Table.14.

Table 14. Growth conditions and properties of high deposition rate HWCVD samples.

Sample ID	Temp. (ºC)	Press. (mTorr)	$F(SiH_4)$ (sccm)	Thk. (Å)	Rate (Å/s)	Photo Cond. (S/cm)	E_{04} (eV)
L256	316	30	40	19715	50	2.36×10^{-4}	1.83
L253	316	35	50	19266	70	2.64×10^{-4}	1.83
L252	316	50	50	19084	90	3.71×10^{-4}	1.84
L254	325	50	75	19346	110	2.57×10^{-4}	1.84
L255	325	70	75	20375	130	1.61×10^{-4}	1.82

We have characterized these new samples in the annealed state utilizing the photoconductive frequency mixing technique enabling us to determine the drift mobility, lifetime and from the electric field dependence of these quantities, we have been able to determine the range and the depth of the long range potential fluctuations and from the latter two quantities we were able to determine the relative differences in the charge centers which exist in the samples.

The photoconductivity as a function of deposition rate is shown in Figure 65. It is seen that in the deposition range from 50 to 130 Å/s, the photoconductivity hovers at levels of 10^{-4} (S/cm), similar to the case of the first set of samples. While, in the neighborhood of the deposition rate of 90 Å/s, the photoconductivity also peaks around 10^{-4} (S/cm), not as large as for the first series samples.

We determined the drift mobility and the lifetime by measuring the photomixing signal at 250 MHz in conjunction with the dc photoconductivity. Figures 66 and 67 show the lifetime and the drift mobility as a function of deposition rate, respectively. It is seen from the figure 2 that the lifetime peaks in the neighborhood of 90 Å/s where the photoconductivity peaks. However, it should be noted that there is a minimal value of the drift mobility in the neighborhood of 90 Å/s, just opposite to the case of the first series samples!

Figure 68 shows the electric field dependence of the drift mobility (a) and the lifetime (b) as a function of deposition rate. From this type of data, we have calculated the range and depth of the long range potential fluctuations which are shown in Figure 69. Surprisingly, it is observed that both the depth and the range of potential fluctuations peak in the region where the drift mobility shows a minimal value. This leads us to believe that the changes in photoconductivity as a function of deposition rate are dominantly attributed to the changes in the lifetime, rather than in the drift mobility as observed for the first series samples. Actually, from the figures 66 and 67, we see clearly that the lifetime varies by about one order of magnitude, while the drift mobility varies only by integer values.

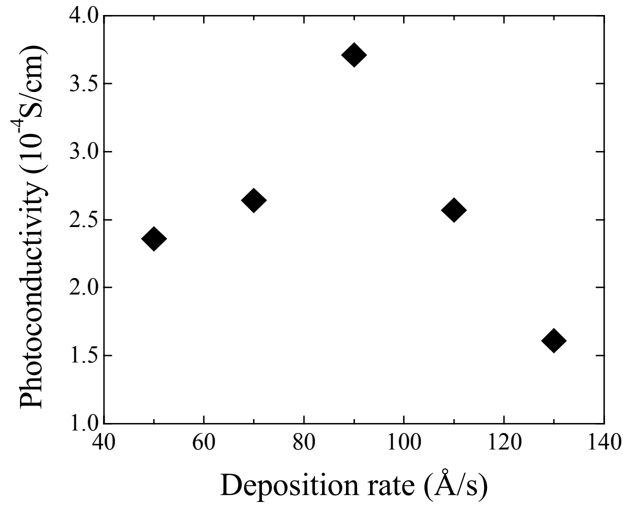

Figure 65. The photoconductivity as a function of deposition rate.

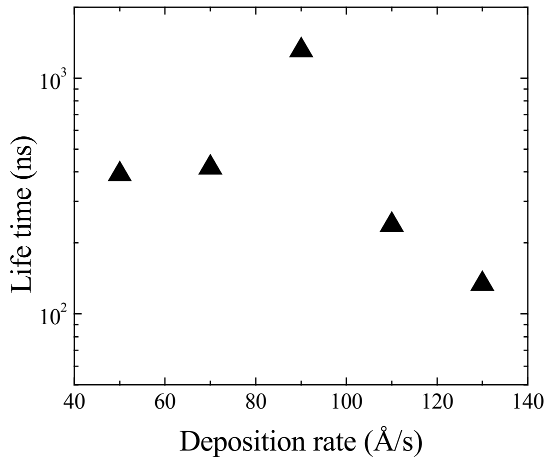

Figure 66. The lifetime as a function of deposition rate.

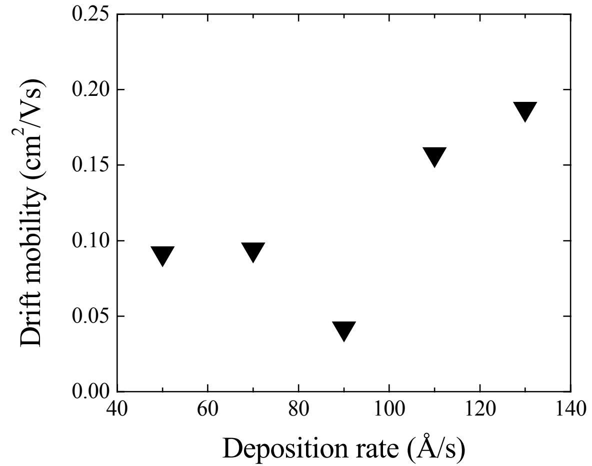

Figure 67. The drift mobility as a function of deposition rate.

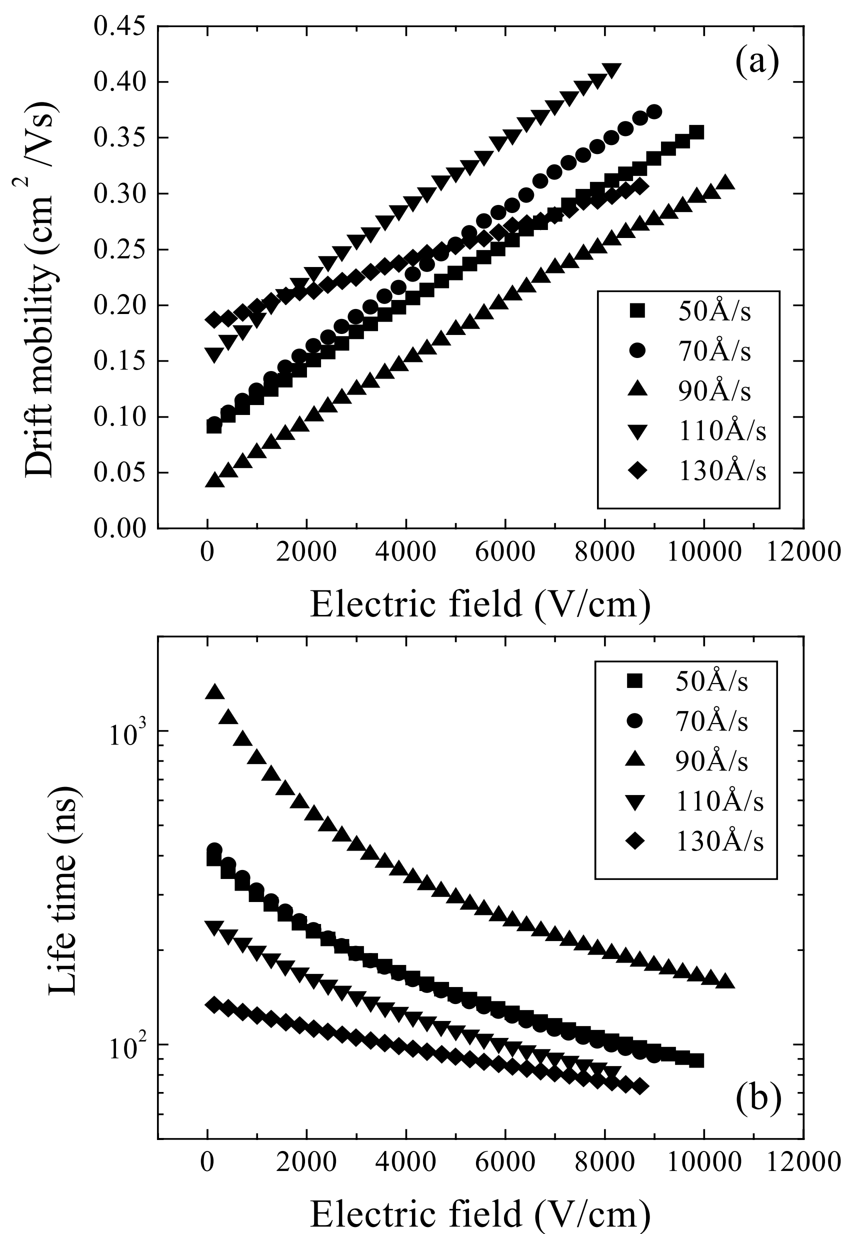

Figure 68. Field dependence of the drift mobility (a) and the lifetime (b) as a function of deposition rate.

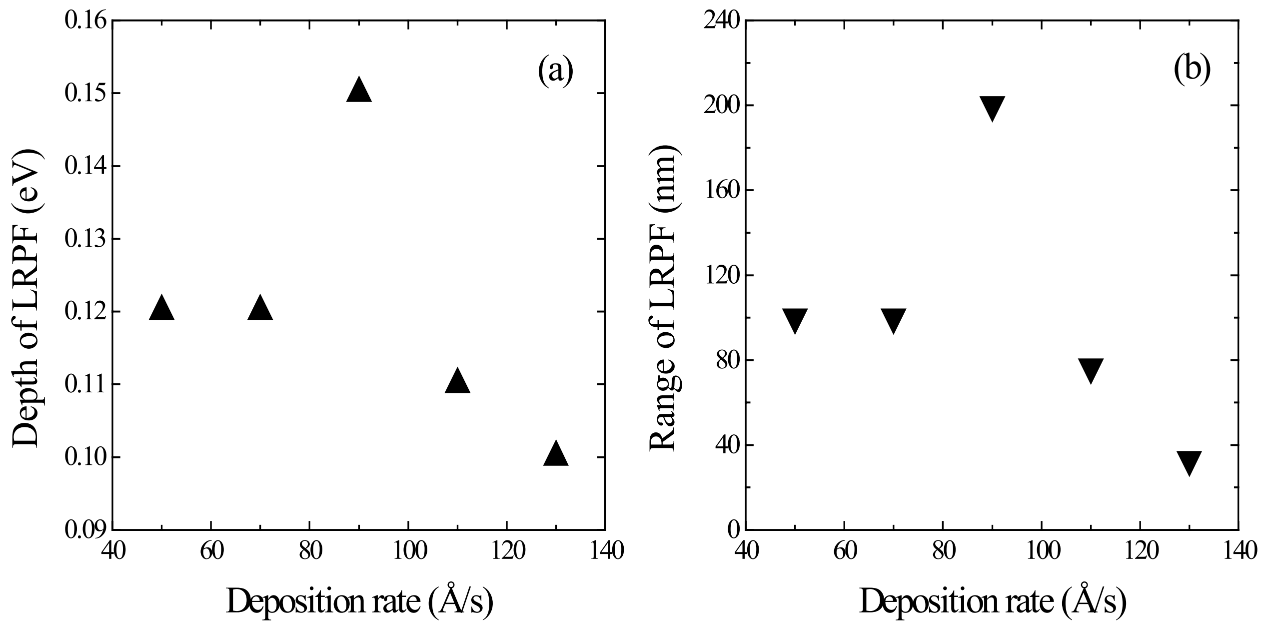

Figure 69. The depth (a) and range (b) of the long range potential fluctuations as a function of deposition rate.

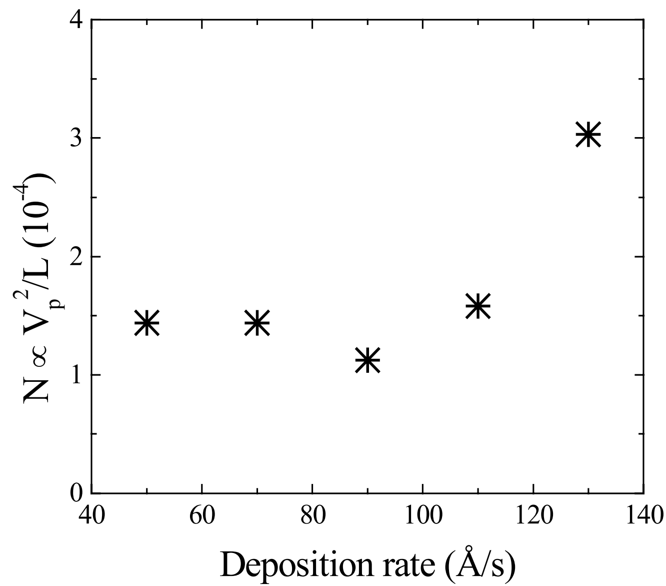

Figure 70. The relative change in the density of charged defects as a function of deposition rate.

Figure 70 shows the relative change in the charged defects as a function of deposition rate. It can be seen that the charged defect density remains constant up to the deposition rate of ~110 Å/s, but above, it begins to increase, similar to the case of the first series samples.

It is of great interest to ascertain what are the chemical or structural properties of the a-Si:H films that vary as a function of the deposition rate. Brent Nelson has performed preliminary n&k measurements on these new series samples. He found that on the stainless steel substrates, a good fit on the analysis would occasionally be obtained, but an E04 value that was significantly lower than that on the 1737 glass or other stainless steel substrates. When this would happen, the thickness used in the fit consistently turned out to be thicker (lower E04, thicker sample by fit). He and Qi Wang tried to sort out the n&k confusion, but do not have any good answers yet. Perhaps, it is because the stainless steel substrates are not perfectly flat or a number of other things. They have sent the samples to n&k Technologies to work with them in sorting this out, but as of yet do not have any answers.

Light-induced decay measurements of transport properties of high deposition rate HWCVD a-Si:H films

In phase II of this program, we reported the photomixing measurements of the first series of high deposition rate HWCVD a-Si:H films in both the annealed the light-soaked states. The deposition rates range from 32 to 191 Å/s. In the last quarterly report, we have investigated the charge transport properties of the new series of HWCVD a-Si:H films in the annealed state. We found that the results were similar to those for the first series prepared under non-optimized growth conditions; the transport properties of the samples do not change monotonically with increasing deposition rate, and peak in the neighborhood of ~70-90 Å/s, despite a monotonic deterioration in the film performance was expected before. However, we observed there indeed exist differences between two series of samples. Although the changes in the photoconductivity with deposition rate are similar for two series, the drift mobility behaves in a different way because the photoconductivity is proportional to the mobility-lifetime product.

In this report, we have characterized these new HWCVD a-Si:H samples in the light-soaked states by using the photomixing technique, which enables us to determine the drift mobility, lifetime and from the electric field dependence of these quantities, we have been able to determine the range and the depth of the long-range potential fluctuations and from the latter two quantities we can determine the relative changes of the charged defect density in the samples. The light-soaking was performed at room temperature for about 3 hours by using a He-Ne laser at the intensity of about 4 suns.

In order to investigate the influence of illumination on the transport properties of the samples as a function of deposition rate, we performed systematical measurements on all five samples in both the annealed and the light-induced states, whose deposition rates range from 50 to 130 Å/s.

The changes in the photoconductivity, drift mobility and lifetime for new series of samples with light-soaking are similar to those for the first series; with light-soaking, the photoconductivity for all the samples decreases, which is attributed to considerable decreases in the lifetime, while it is interesting to observe that the drift mobility changes very small, even a little increase upon light-soaking!

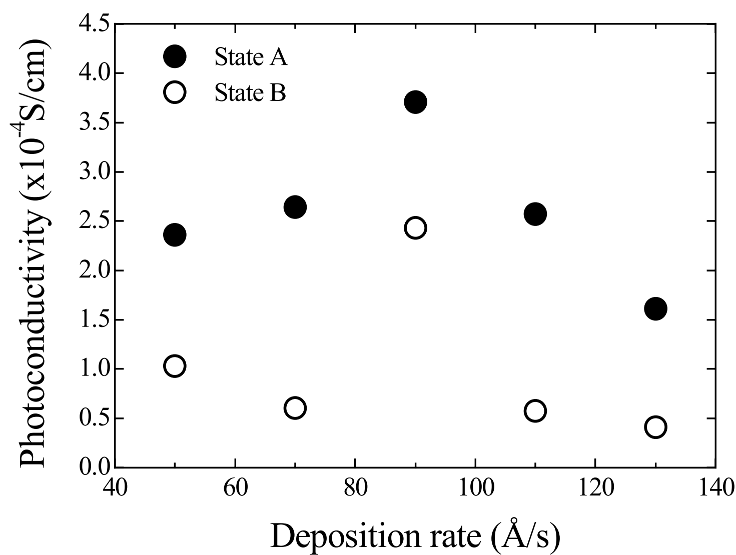

Figure 71. The light-induced changes in the photoconductivity as a function of deposition rate.

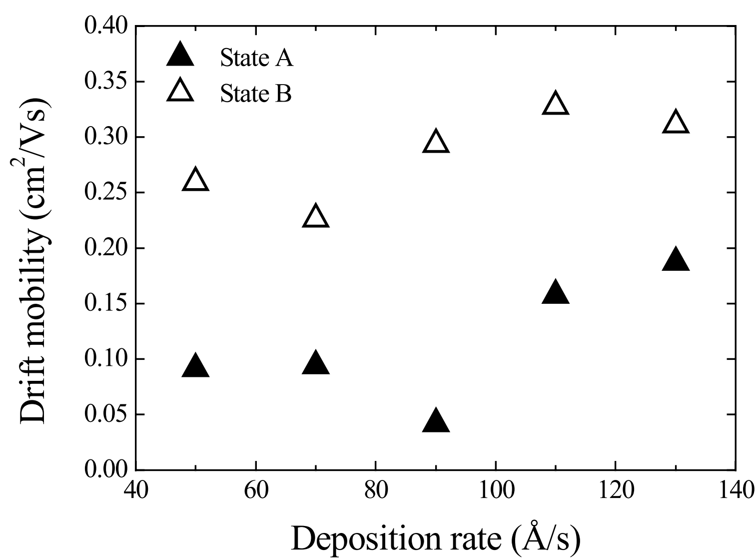

Figure 72. The light-induced changes in the drift mobility as a function of deposition rate.

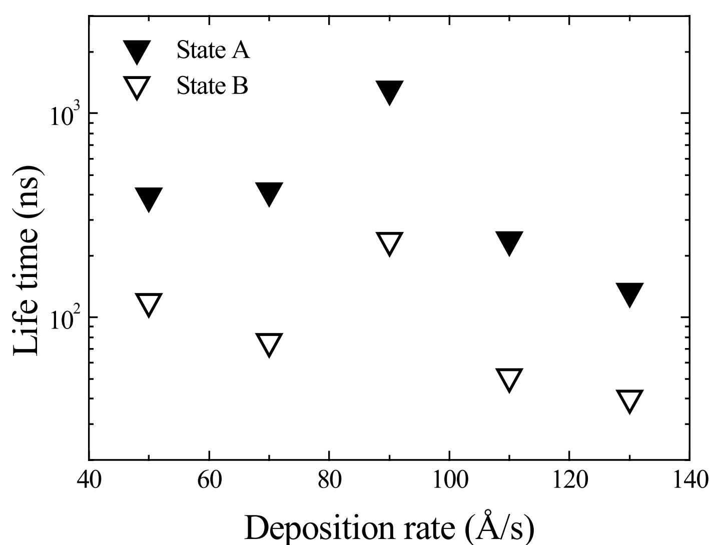

Figure 73. The light-induced changes in the lifetime as a function of deposition rate.

Figures 71-73 show the photoconductivity, drift mobility and lifetime, respectively, as a function of deposition rate in both the annealed and the light-induced states. We can see that illumination reduces the photoconductivity and the lifetime, while surprisingly increases the mobility for all the samples, similar to the case of the first series of samples. However, it should be noted that the changes in the mobility for the present samples as a function of deposition rate are opposite to those for the first series (minimal μ_d vs maximal μ_d in the neighborhood of ~70-90 Å/s)! Furthermore, the deposition rate dependence of these transport parameters in the light-soaked state is similar to that in the annealed state. The light-induced decrease in the photoconductivity is mainly due to the decrease in the lifetime since the mobility varies only by integer values, while the lifetime varies by orders of magnitude.

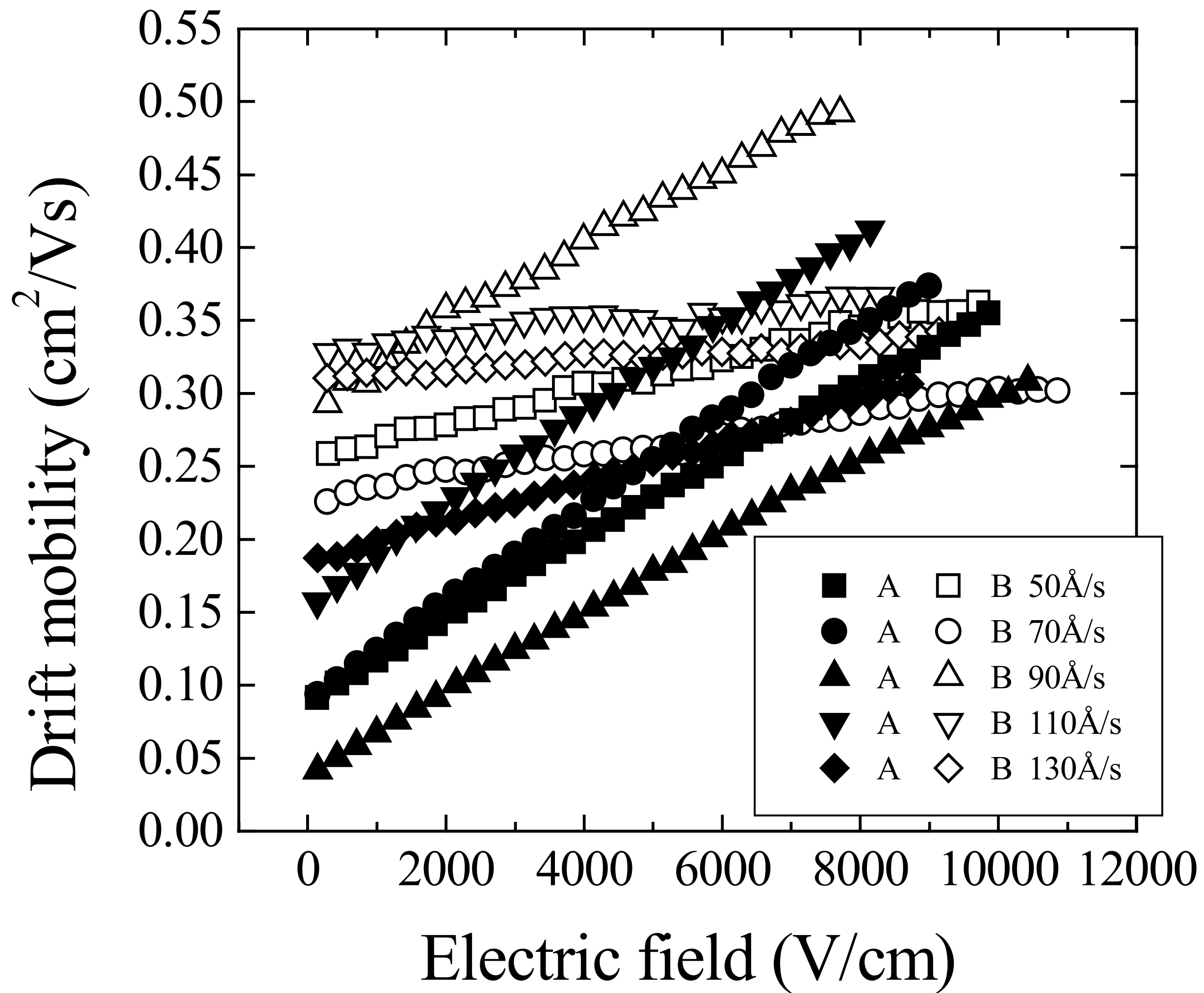

Figure 74. Effect of light-soaking on the electric field dependence of the drift mobility as a function of deposition rate.

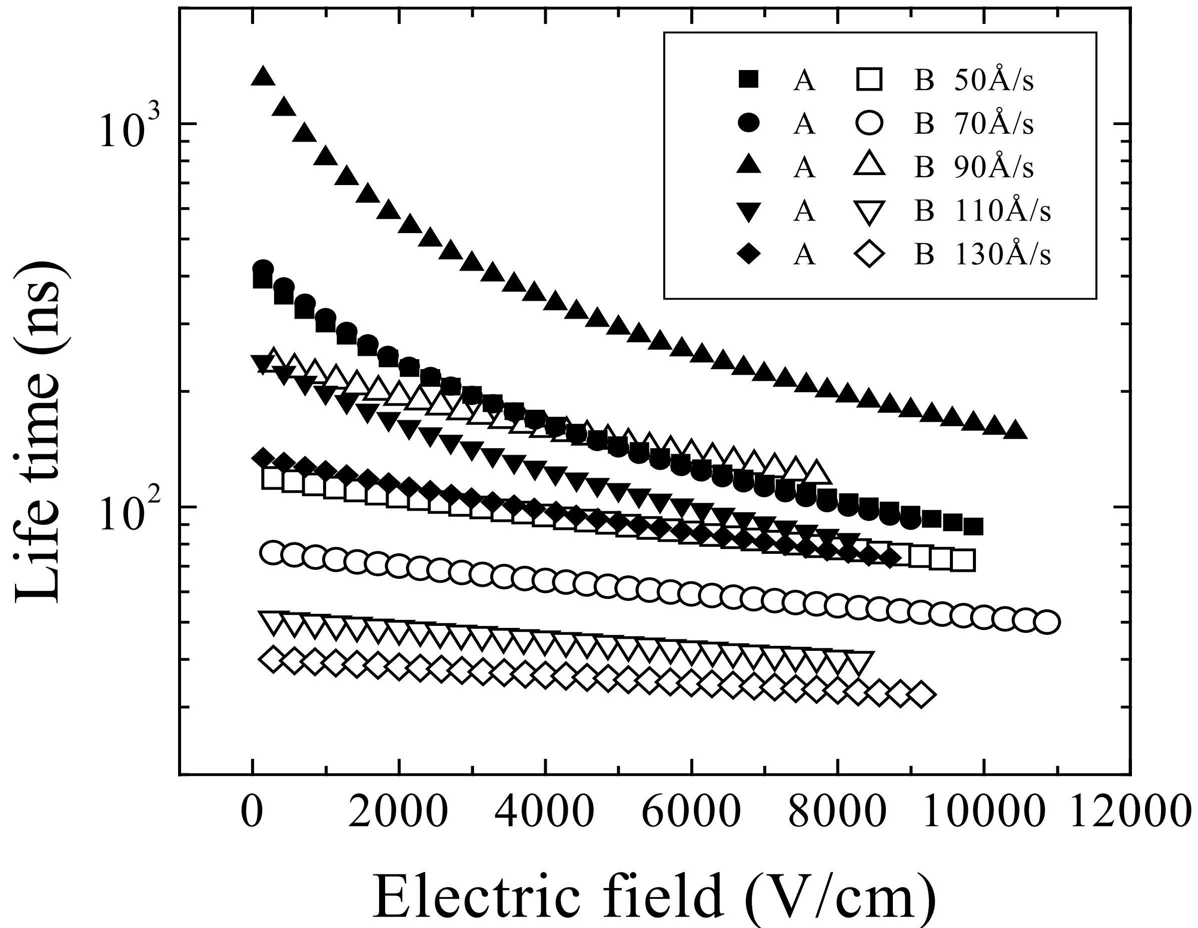

Figure 75. Effect of light-soaking on the electric field dependence of the lifetime as a function of deposition rate.

Figures 74 and 75 show the electric field dependence of the drift mobility and lifetime, respectively, of the samples as a function of deposition rate in both the annealed and the light-induced states. It is seen that for lower fields, the light-induced changes in the drift mobility and lifetime as a function of deposition rate are similar to the results shown in Figures 72 and 73. Furthermore, it is clearly seen that the degree of the field dependence of the mobility and lifetime become less after light-soaking, suggesting an enhanced effect of long-range potential fluctuations.

From the field dependence of the drift mobility shown in Figure 74, we have determined the depth and range of the long-range potential fluctuations. Figure 76 shows the influence of illumination on the depth (a) and range (b) of potential fluctuations as a function of deposition rate. We see that illumination reduces remarkably the range, as should be expected, but meanwhile also reduce the depth a little which verify the light-induced increase in the mobility observed above, in consistence with the results of the first series of samples.

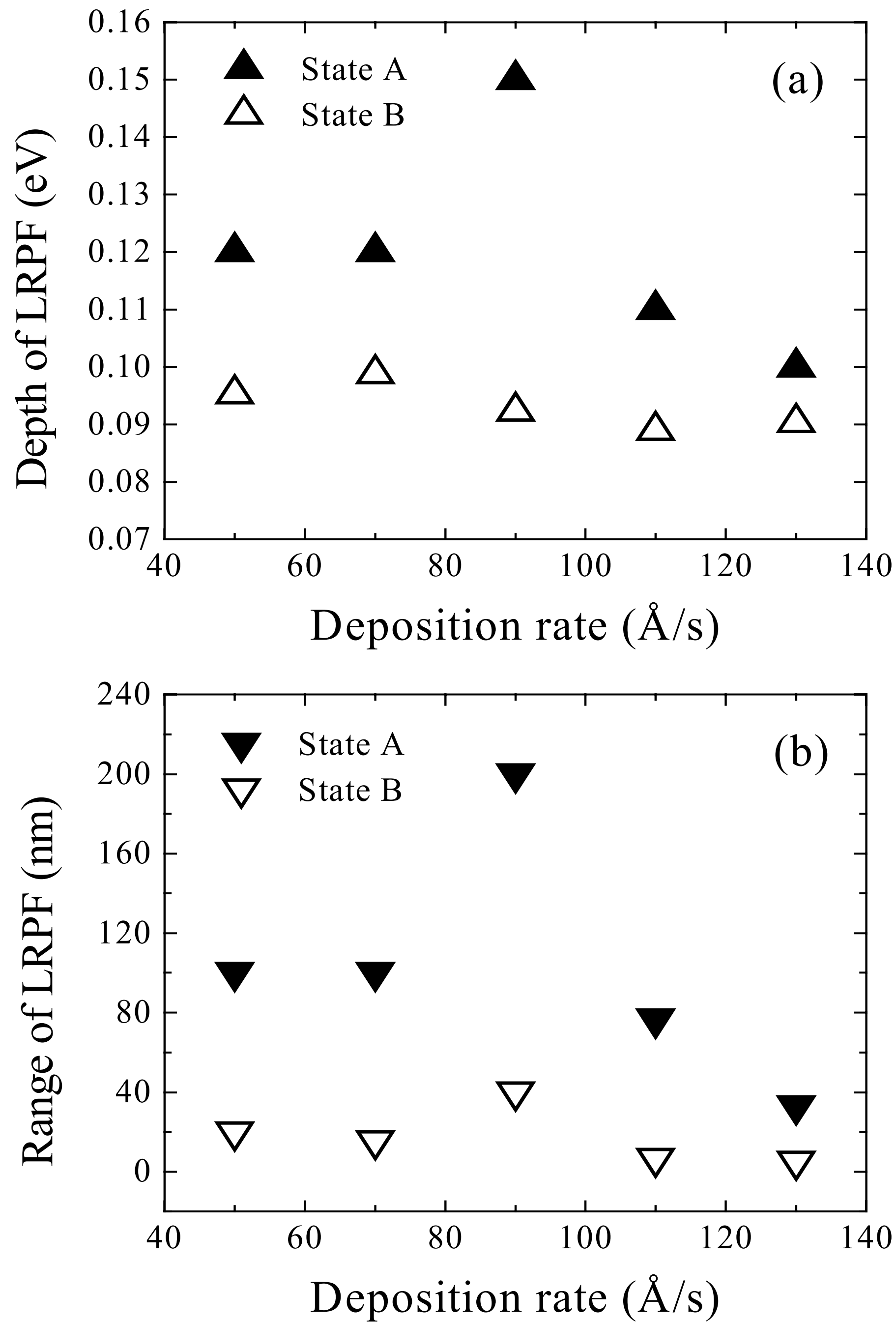

Figure 76. The light-induced changes in the depth (a) and range (b) of potential fluctuations as a function of deposition rate.

Since the density of charged defects is proportional to V_P^2 / L, where V_P and L represent the depth and range of the long-range potential fluctuations, respectively, we can estimate the relative change in the charged defect density by using the calculated values of V_P and L. Figure 77 shows the light-induced relative change in the density of charged defects as a function of deposition rate. Similarly, the charged defect density increases upon light-soaking for all deposition rates, while there appears to be the least light-induced increase at the intermediate deposition rates where the photoconductivity peaks (Fig.71). It should be noted that although the density of charged defects increases upon light-soaking, the depth of the potential fluctuations does not increase, but decreases. It appears that the light-induced increase in the charged defect density results from the much more decrease in the range.

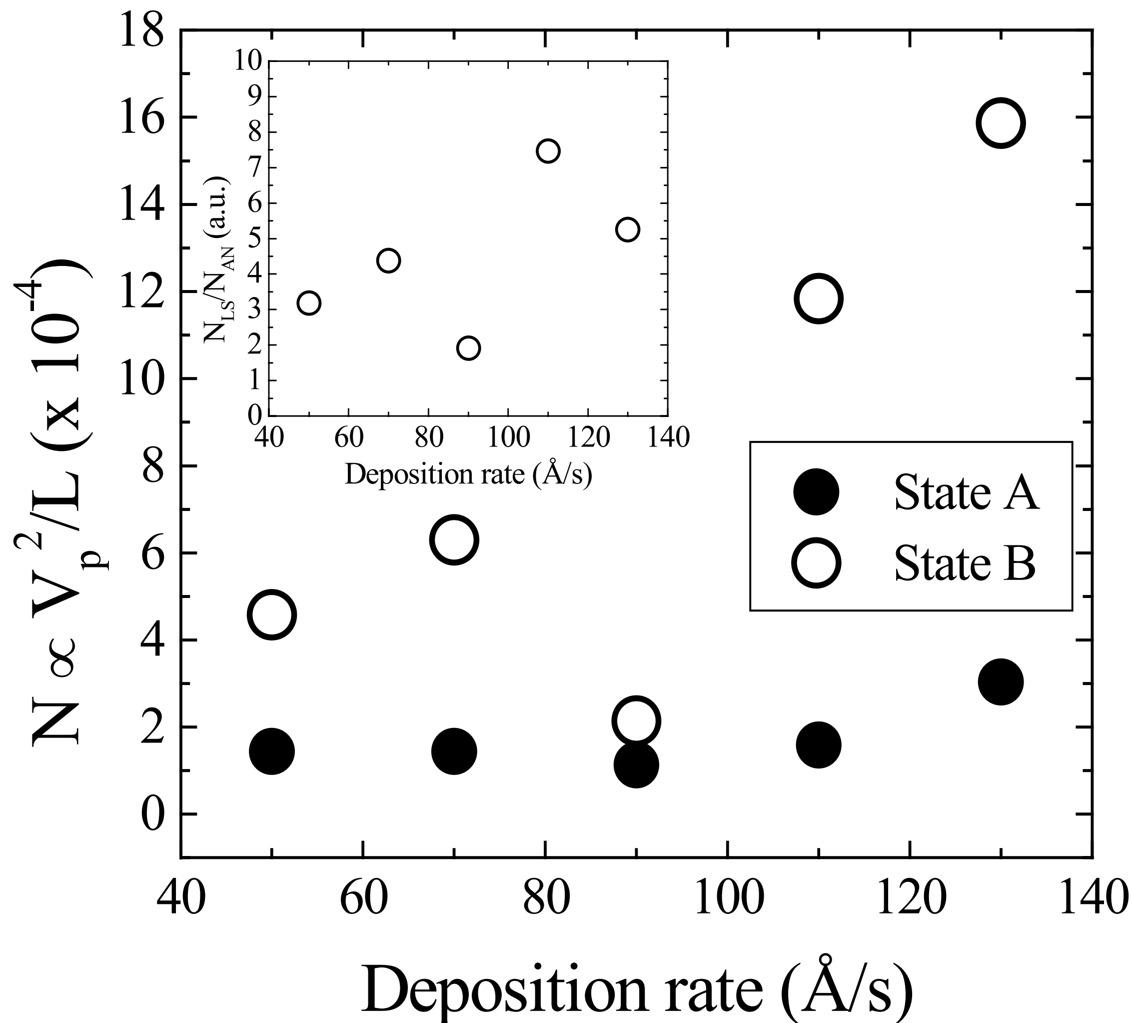

Figure 77. The light-induced relative change in the charged defect density as a function of deposition rate.

7.3 Characterization of high deposition rate HWCVD a-Si:H films deposited on stainless steel substrates by Driven Level Capacitance Spectroscopy and transient photocapacitance at the University of Oregon.

We were informed preliminary data from the University of Oregon as measured on the new series of high deposition rate HWCVD a-Si:H samples by Driven Level Capacitance Spectroscopy and transient photocapacitance. The results are shown below in Table 15.

Table 15. Characterization of high deposition rate HWCVD a-Si:H samples deposited on stainless steel substrates. (supplied by the University of Oregon).

Sample	State	Dep. Rate (Å/s)	Thk. (μm)	E_F (eV)	E_g (eV)	E_u (meV)	N_{DLCS} (10^{16} cm^{-3})	N_{PHCAP} (10^{16} cm^{-3})
L252	A	90	1.45	0.69	1.72	53	< 3	3.2
	B			**0.71**			**< 3**	**3.2**
L254	A	110	1.50	0.69	1.70	51	~ 1.7	2.4
	B			**0.72**			**~2.2**	**3.6**
L255	A	130	0.77	0.69	1.70	49	1.25	6.2
	B			**0.72**			**1.8**	**3.6**

It is strange to observe that the defect density of L255 sample decreases after light-soaking as determined by the Photocapacitance method. This is the sample giving the nicest DLCS profiles and we can see that the DLCS defect density increases from State A (as-grown) to State B (120h light-soaking at ~2W/cm^2) as it should be. They suggested that the weird result in the Photocapacitance is most likely due to the mobility-lifetime product of the holes. The bandtail of the photocapacitance is "suppressed" and only the photocurrent measurement could give us an idea by how much. It is more strongly suppressed for State A, thus making the defect density look actually larger than it really is. The photocurrent measurements cannot be applied to an a-Si:H film grown on a stainless steel substrate. Here is a reference which might clarify this issue [22].

In addition, it is interesting to note that the Urbach energy E_u decreases monotonically with increasing deposition rate, indicating more ordering network structure at higher deposition rates. This is inconsistent with the trend with deposition rate, i.e., non-monotonic change, as measured by the Constant Photocurrent Method (CPM) [21].

The present study indicates that the performance of a-Si:H films does not deteriorate monotonically with increasing deposition rate as expected before. The transport properties (for instance, the photoconductivity) of high deposition rate HWCVD a-Si:H films peak in the neighborhood of ~70-90 Å/s, and good quality can be maintained at deposition rates up to 130 Å/s. The reason why the photoconductivity peaks in the neighborhood of ~70-90 Å/s may be due to that this is where the pressure was increased at higher silane flows to increase the deposition rate. So, there may have been significant depletion of the silane that changed things. The higher

pressure allows for more collisions before a dissociated molecule makes it from the filament to the substrate. There is probably an optimal number of collisions to make good films.

From the results of two series of high deposition rate HWCVD a-Si:H samples, we have seen some different behaviors in the transport properties. This might be attributed to different microstructure in the films. Therefore, to further understand the transport properties of high deposition rate a-Si:H samples, it is of great interest to perform detailed study of structural or chemical properties as a function of deposition rate.

7.4 The effect of deposition rate on the transport properties of HWCVD a-Si:H films with respect to the substrate temperature, deposition pressure and silane flow rate

In phase II of this program, we reported the photomixing transport measurements of the first set of high deposition rate (32~191 Å/s) HWCVD a-Si:H films in both the annealed the light-soaked states; we concentrated our attention on the effect of the deposition rate itself on the resultant film properties. Since the high deposition rate (up to 1 μm/min.) was achieved by increasing deposition pressure, silane flow rate, and decreasing filament-to-substrate distance, there exist significant interactions among these parameters that require optimization to prepare films with optimal quality for a desired deposition rate. Therefore, it is of great interest to investigate the effect of the deposition rate on the resultant film properties with respect to the deposition parameters, for instance, the deposition pressure, silane flow rate, substrate temperature, etc.. This would help us find out how to maintain high quality films at high deposition rates by means of varying deposition parameters.

The preparation conditions of the first set of high deposition rate a-Si:H samples are shown in Table 16. We had characterized these samples in the annealed state utilizing the photomixing technique (see the 3rd Quarterly Report of Phase II). This technique enables us to determine the drift mobility and lifetime separately; from the electric field dependence of these quantities, the range and the depth of the long range potential fluctuations, and subsequently the relative changes in the charged defect density in the films can be determined.

Figures 78-81, and Figure 82 show the deposition pressure dependence of the photomixing transport parameters and hydrogen content, respectively, of the samples as a function of deposition rate. It can be seen that the deposition rate is monotonically increased with increasing deposition pressure; increasing pressure can increase deposition rate up to about 150 Å/s without obviously deteriorating film quality although the film quality has a trend to decrease with increasing pressure. Only too high pressure, beyond about 100 mTorr, will lead to significant deterioration of film properties in the photoconductivity, drift mobility and lifetime as a result of an increase in the concentration of charged defects, which lead to the long-range potential fluctuations whose depth increases, while the range decreases. In addition, the hydrogen content is reduced with increasing pressure (or deposition rate).

Table 16. Preparation Conditions of High Deposition Rate HWCVD a-Si:H Samples.

Sample ID	Temperature (ºC)	Pressure (mTorr)	F (SiH_4) (sccm)	I (fil.) (A)	Thickness (Å)	Rate (Å/s)
L079	295	20	20	30	6644	31.64
L077	295	70	20	30	8530	47.39
L110	285	19	75	30	10514	58.41
L139	315	50	50	29	8144	67.87
L169	318	50	50	30	9235	76.96
L104	350	50	50	30	10179	84.83
L183	348	70	75	30	11000	109.78
L178	317	70	75	30	11381	113.58
L182	348	70	75	30	11502	114.79
L190	326	50	75	30	9318	132.74
L196	325	75	75	30	8538	142.30
L094	385	90	75	30	13701	152.23
L194	325	70	100	30	10662	177.70
L087	295	120	75	30	22900	190.83

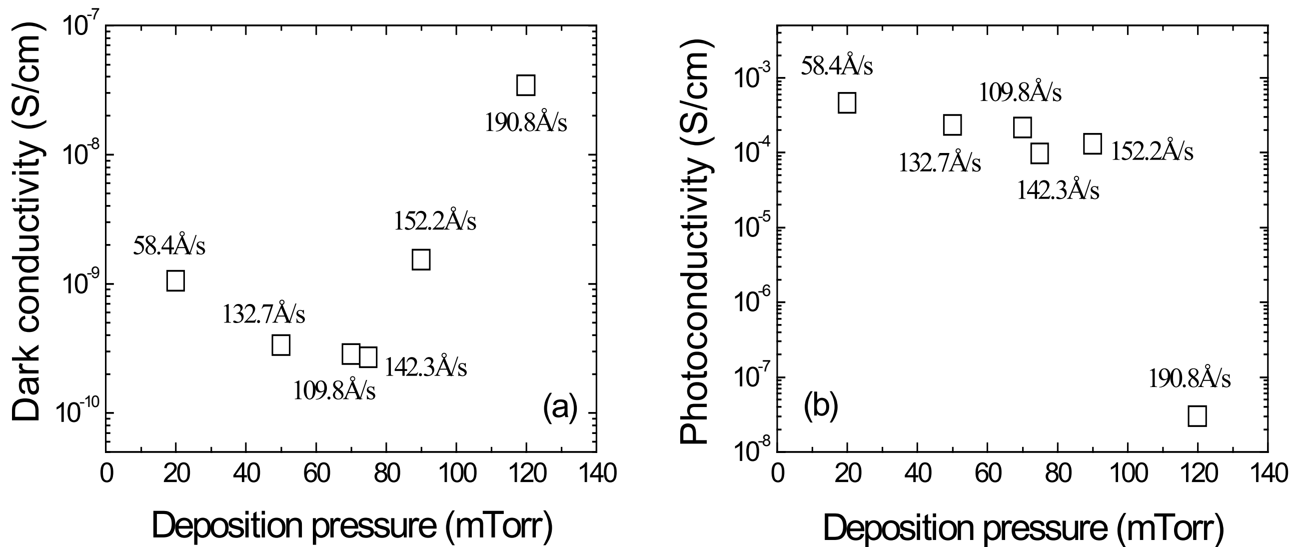

Figure 78. Deposition pressure dependence of the conductivity of the samples as a function of deposition rate.

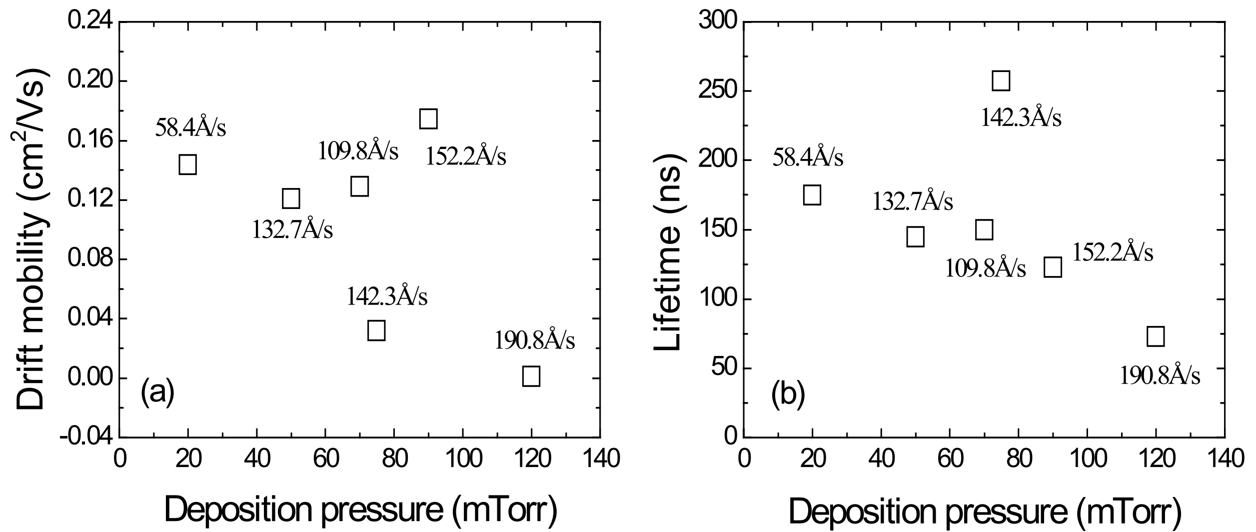

Figure 79. Deposition pressure dependence of the mobility (a) and lifetime (b) as a function of deposition rate.

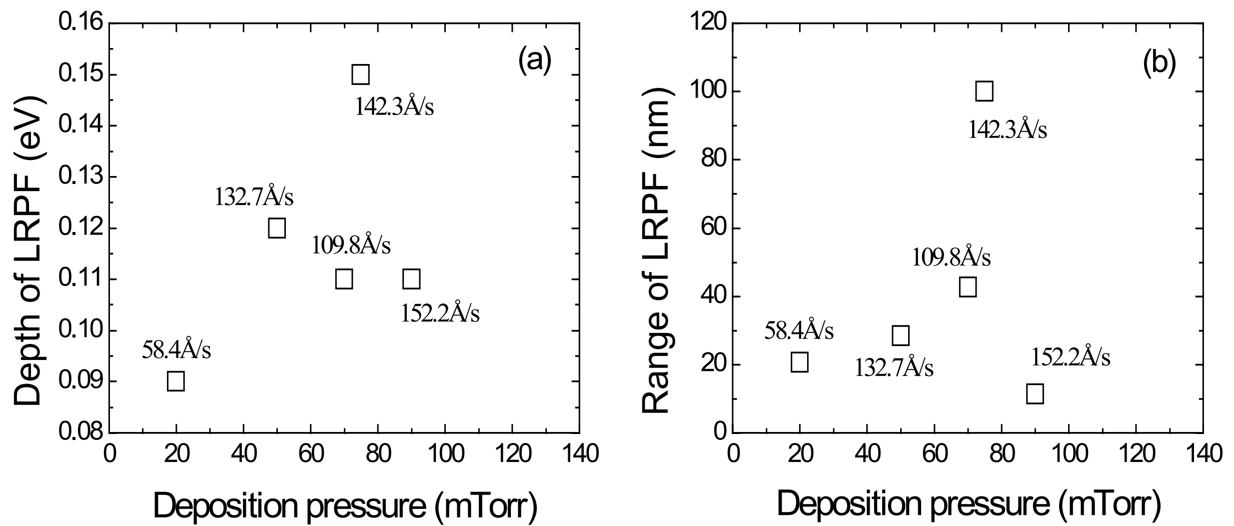

Figure 80. Deposition pressure dependence of the depth (a) and range (b) of the potential fluctuations as a function of deposition rate.

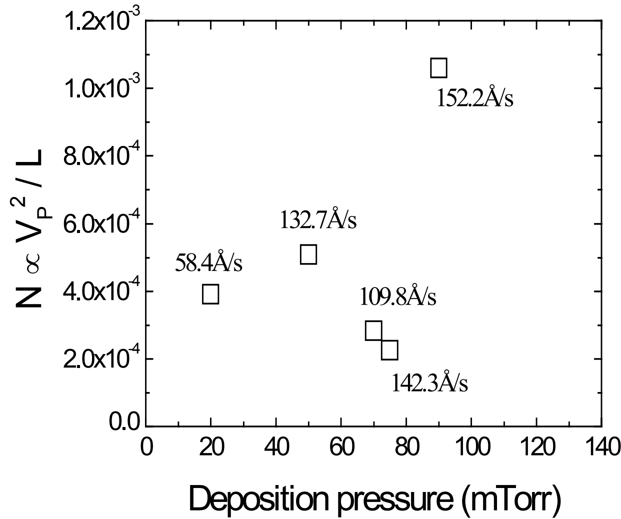

Figure 81. Deposition pressure dependence of the relative change in the density of charged defects as a function of deposition rate.

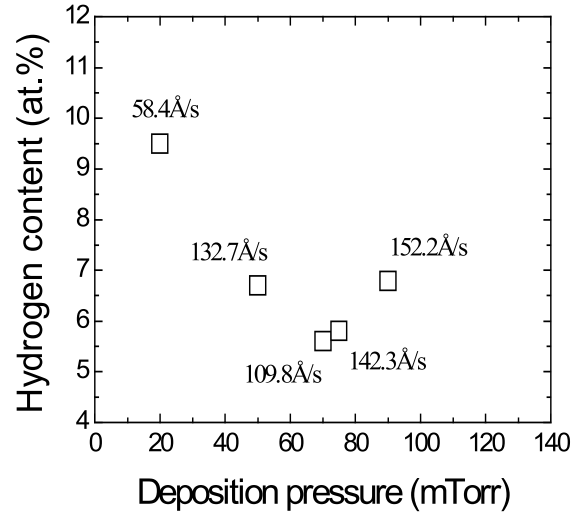

Figure 82. Deposition pressure dependence of the hydrogen content as a function of deposition rate.

Figures 83-86 and Fig. 87 show the silane flow rate dependence of the photomixing transport parameters and hydrogen content, respectively, of the samples as a function of deposition rate. Similar to the case of increasing pressure, increasing silane flow rate also monotonically increase the deposition rate. However, the film quality does not change monotonically with varying silane flow rate; there exists an optimal flow rate of around 50 sccm, where the highest photoresponse, mobility and lifetime occur as a result of the lowest charged defect density, which is confirmed by the shallowest depth and the longest range of the potential fluctuations. This optimal flow rate corresponds to intermediate deposition rates between 70-90 Å/s. From Fig.87, it is seen that the hydrogen content does not seem to change with varying flow rate.

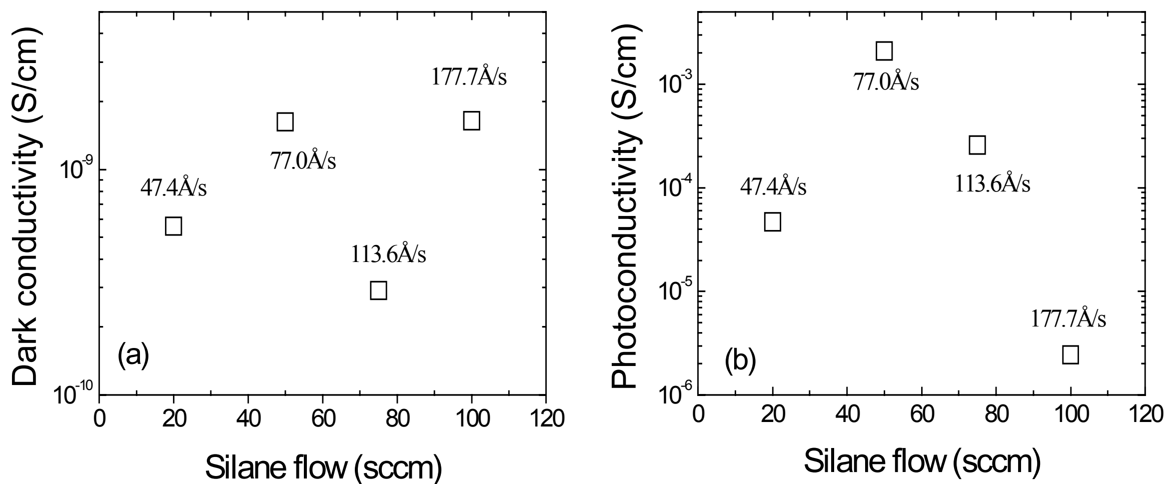

Figure 83. Silane flow rate dependence of the conductivity of the samples as a function of deposition rate.

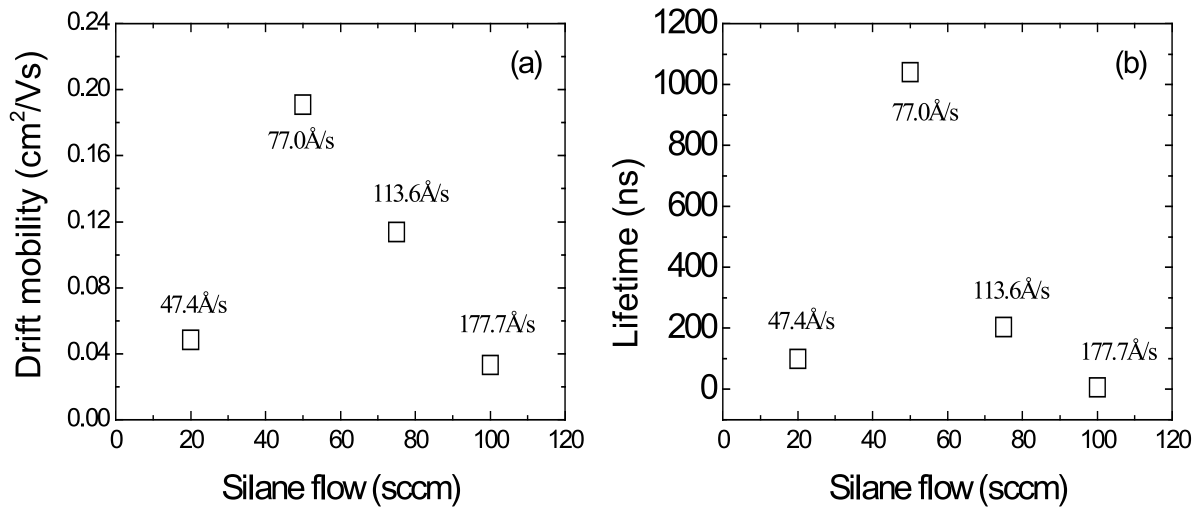

Figure 84. Silane flow rate dependence of the mobility (a) and lifetime (b) as a function of deposition rate.

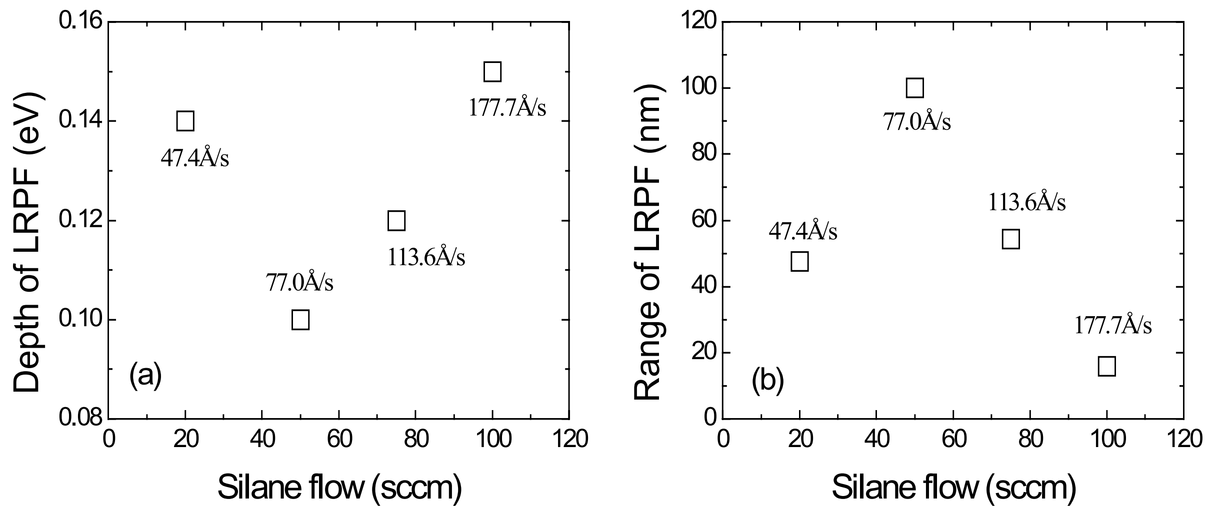

Figure 85. Silane flow rate dependence of the depth (a) and range (b) of the potential fluctuations as a function of deposition rate.

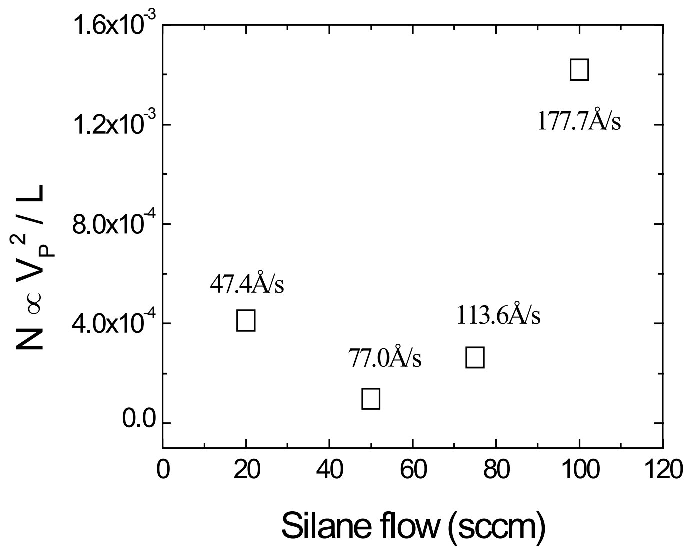

Figure 86. Silane flow rate dependence of the relative change in the density of charged defects as a function of deposition rate.

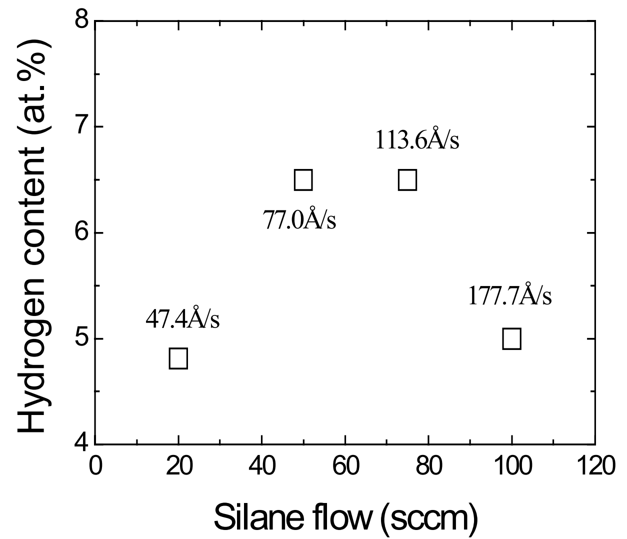

Figure 87. Silane flow rate dependence of the hydrogen content as a function of deposition rate.

Figures 88-91 and Figure 92 show the substrate temperature dependence of the photomixing transport parameters and hydrogen content, respectively, of the samples as a function of deposition rate. It is seen that as anticipated, the hydrogen content is reduced with increasing substrate temperature, but the substrate temperature does not have a significant influence on the deposition rate. However, it is worthy of note that at higher deposition rates, high quality films are grown at higher substrate temperature, suggesting that in order to produce high quality films at high rates, higher substrate temperatures are required.

From the above results, we see that low pressure, medium silane flow rate, and higher substrate temperature are generally required to maintain high quality a-Si:H films at high deposition rates. While, we should realize that due to significant interactions among these parameters, optimization is required to prepare films with optimal quality for a desired deposition rate. Therefore, further work is needed to perform well-defined studies of the deposition rate dependence of film properties, both electronic and structural, under otherwise similar circumstances, i.e., without significant change in film grown precursors and discharge conditions.

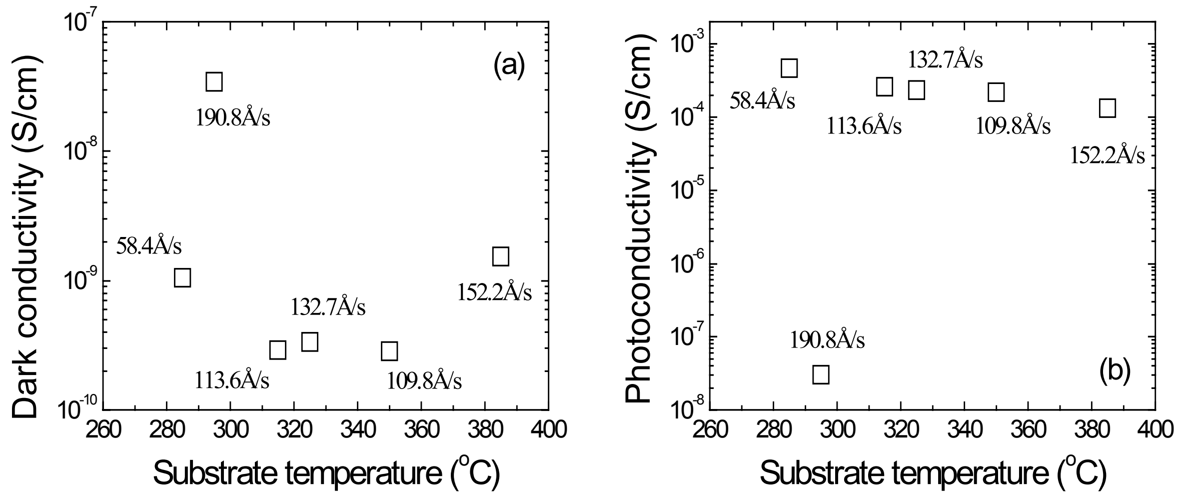

Figure 88. Substrate temperature dependence of the conductivity of the samples as a function of deposition rate.

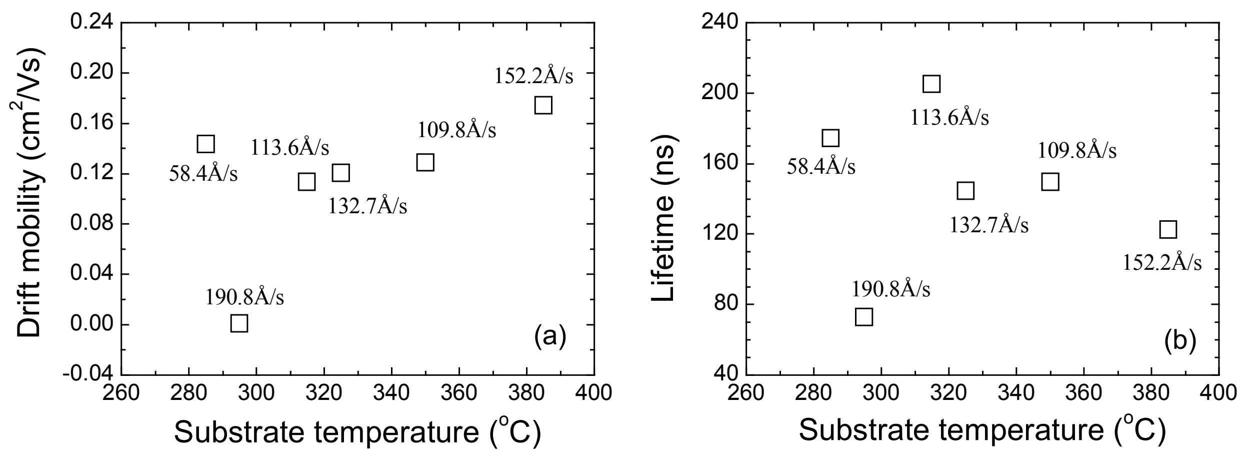

Figure 89. Substrate temperature dependence of the mobility (a) and lifetime (b) as a function of deposition rate.

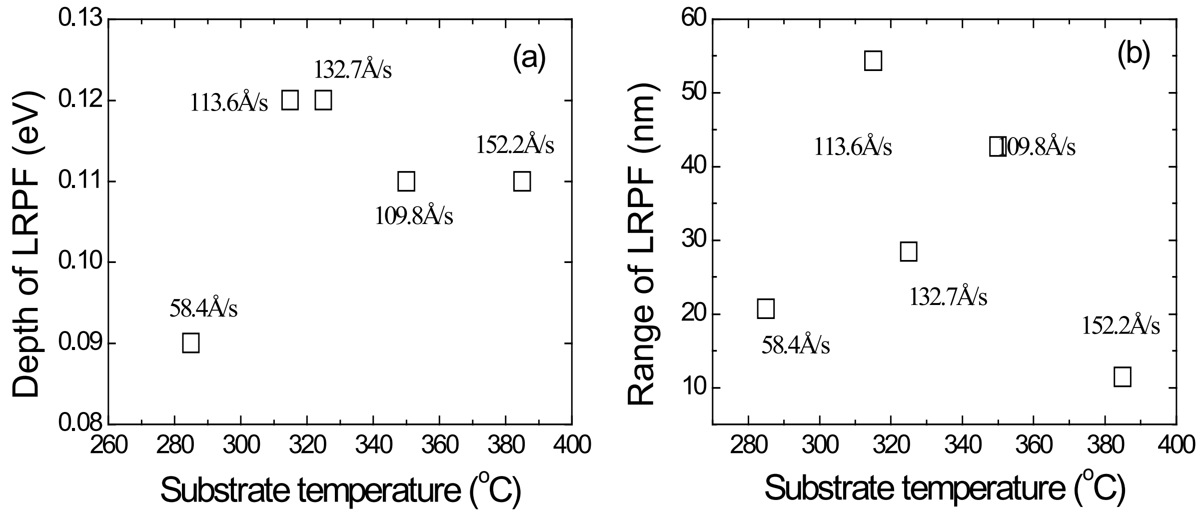

Figure 90. Substrate temperature dependence of the depth (a) and range (b) of the potential fluctuations as a function of deposition rate.

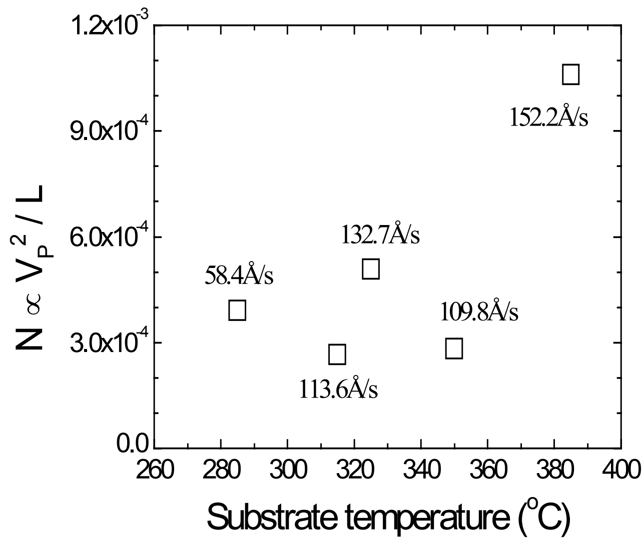

Figure 91. Substrate temperature dependence of the relative change in the density of charged defects as a function of deposition rate.

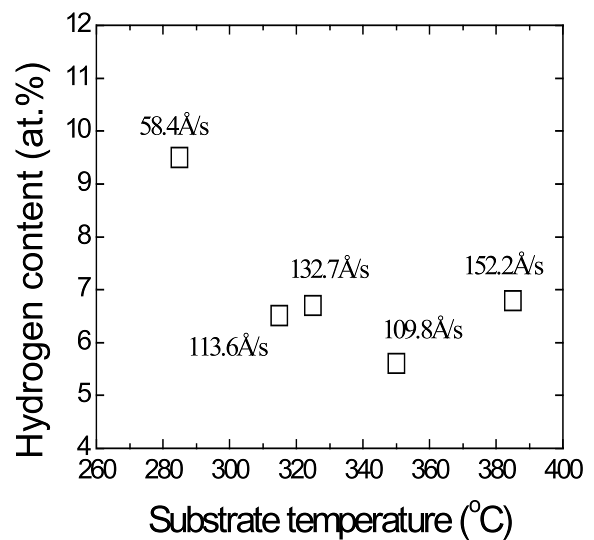

Figure 92. Substrate temperature dependence of the hydrogen content as a function of deposition rate.

8. Measurements of amorphous (Si,Ge) alloys

8.1 Measurements of homogenous a-SiGe alloy samples produced at NREL

The a-SiGe:H sub-team at NREL is presently employing the hot-wire technique to produce a-SiGe:H alloys which are to be optimized with respect to the transport parameters within two bandgap regimes: 1.40-1.45 eV to 1.60-1.65 eV. We have previously determined the transport parameters of a series a-SiGe:H alloys supplied by Brent Nelson where he explored the parameter space involving the number of collisions a reactive species makes before impinging on the substrate surface. These measurements involved a range of preparation parameters which resulted in inhomogeneity of composition. We now report on a series of samples that are homogeneous in alloy composition supplied by Nelson. The photoconductivity, drift mobility, and lifetime were studied systematically in the annealed and light-soaked states employing the photomixing technique using the longitudinal modes of a HeNe laser. All the samples were initially annealed at 150^0C for 2 hours to restore the samples to the annealed state. The characteristics of the samples are listed in Table 17.

Table 17. The characteristics of a-SiGe:H and a-Si:H.

Sample ID	Substrate Temp. ^{0}C	GeH_4 (%)	Thickness (μm)
HGe118	400	0	1.093
HGe114	475	3	1.447
HGe121	365	3	1.858
HGe113	475	8	1.482
HGe100	500	17	2.055

Figure 93 shows the normalized photoconductivity, mobility, and lifetime for a-Si:H prepared by the same hot-wire technique as a function of illumination time. During illumination, both the drift mobility and lifetime decrease. This is consistent with previous results we have obtained indicating that both neutral and charged defects are created by light-soaking.

Figures 94-97 show the normalized photoconductivity, mobility, and lifetime in a-SiGe:H alloys prepared with different GeH_4 gas flow ratios as a function of illumination time. It can be seen from these results that both the mobility and lifetime are lowered by light-soaking which is similar to a-Si:H; however it should be noted that the rate of decrease of these quantities varies as a function of the sample composition. We have also measured the electric field dependence of the mobility and thus determined the range and the depth of the long-range potential fluctuations. The results for the annealed state are shown in Table 18 while the results for the light-soaked state are shown in Table 19.

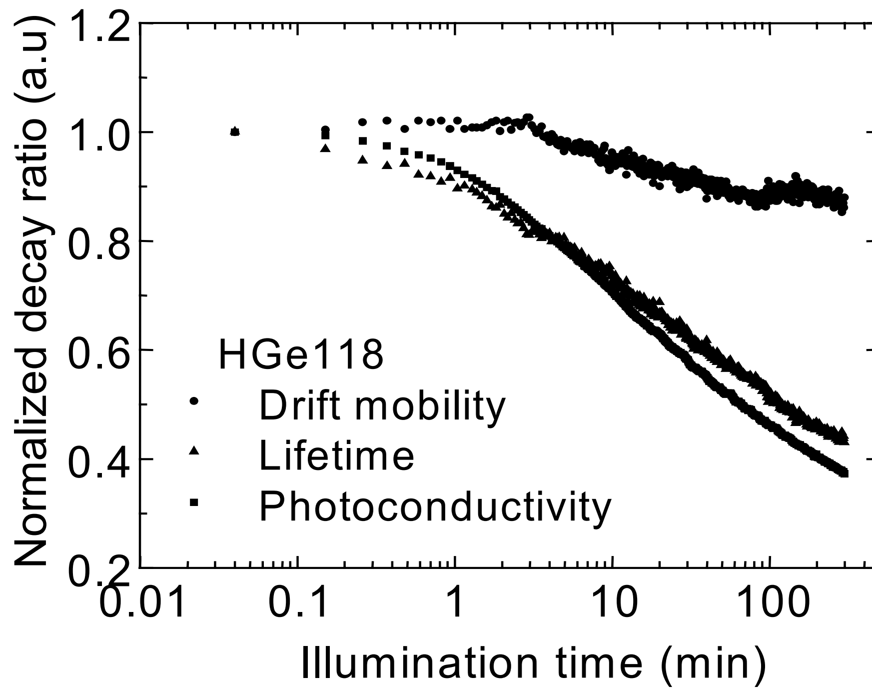

Figure 93. The normalized photoconductivity, mobility, and lifetime in a-Si:H as a function of illumination time.

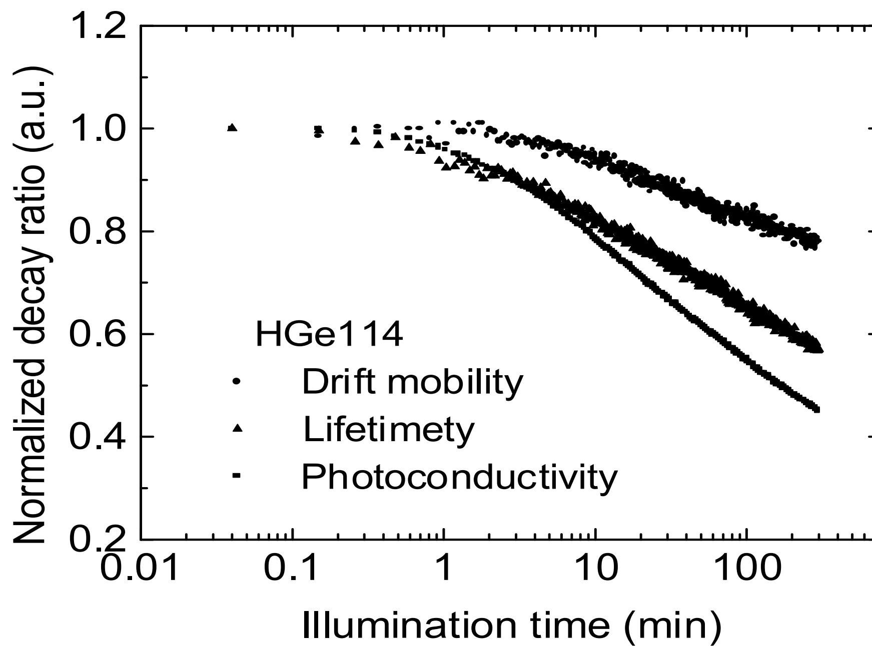

Figure 94. The normalized photoconductivity, mobility, and lifetime as a function of illumination time. The GeH_4 gas flow ratio is 3%.

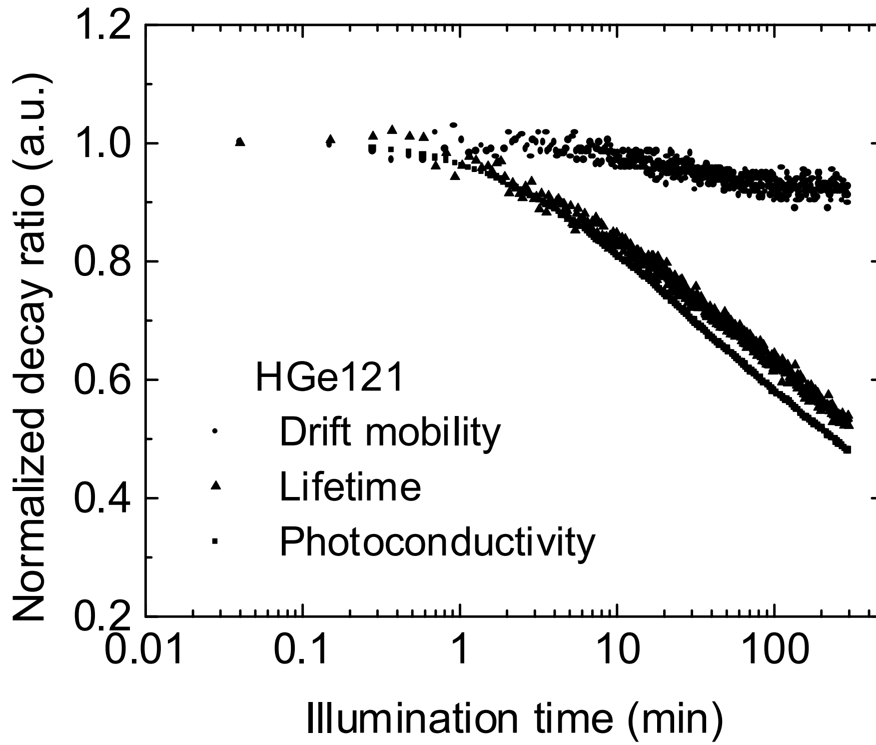

Figure 95. The normalized photoconductivity, mobility, and lifetime as a function of illumination time. The GeH_4 gas flow ratio is 3%.

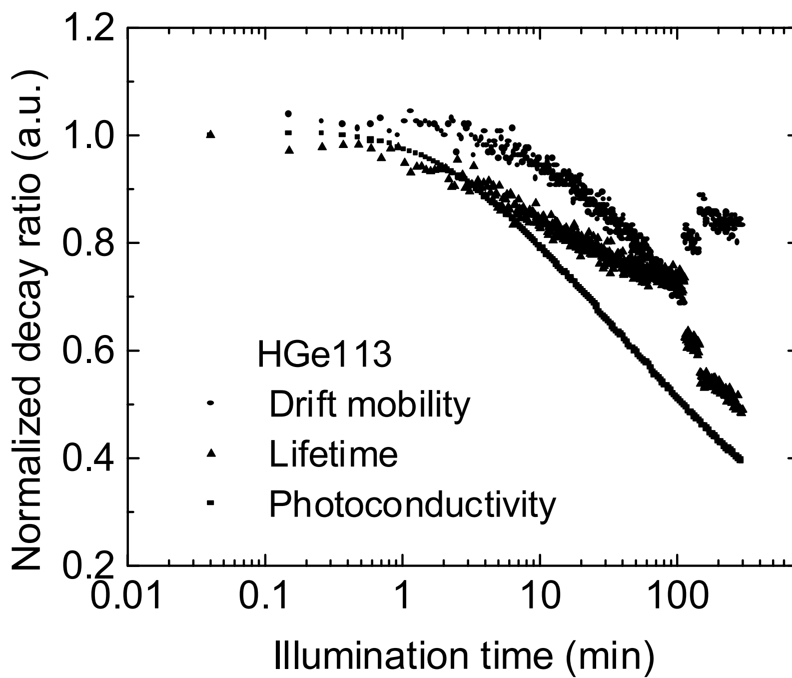

Figure 96. The normalized photoconductivity, mobility, and lifetime as a function of illumination time. The GeH_4 gas flow ratio is 8%.

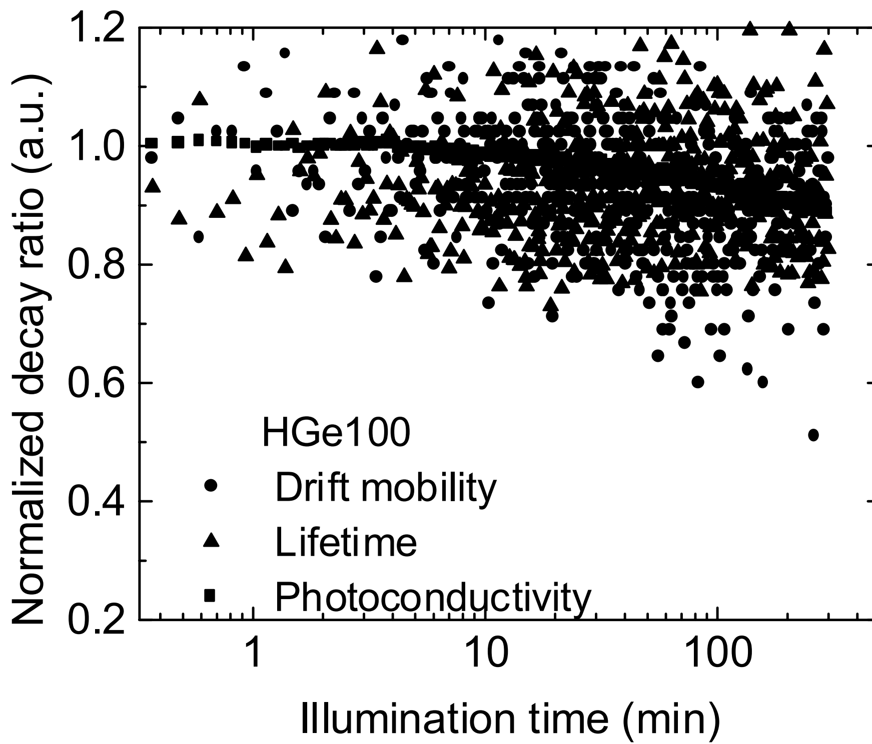

Figure 97. The normalized photoconductivity, mobility, and lifetime as a function of illumination time. The GeH_4 gas flow ratio is 17%.

Table 18. The photoconductivity, drift mobility, lifetime, and range and depth of long range potential fluctuations in annealed state for a-SiGe:H alloys prepared with different GeH_4 gas flow ratio.

	HGe100	HGe113	HGe121	HGe114	HGe118
GeH_4	17%	8%	3%	3%	0%
σ_{ph} ($\Omega^{-1}cm^{-1}$)	0.31×10^{-4}	3.72×10^{-4}	1.39×10^{-4}	3.40×10^{-4}	5.91×10^{-4}
τ (ns)	49.87	179.00	62.42	86.00	71.28
μ_d (cm^2/Vs)	0.067	0.160	0.216	0.303	0.473
L (nm)	25.61	34.46	29.05	38.24	41.24
V_p (eV)	0.143	0.117	0.109	0.103	0.092

Table 19. The photoconductivity, drift mobility, lifetime, and range and depth of long range potential fluctuations in light-soaked state for a-SiGe:H alloys prepared with different GeH_4 gas flow ratio.

	HGe100	**HGe113**	**HGe121**	**HGe114**	**HGe118**
GeH_4	17%	8%	3%	3%	0%
σ_{ph} ($\Omega^{-1}cm^{-1}$)	0.27×10^{-4}	1.46×10^{-4}	0.67×10^{-4}	1.53×10^{-4}	2.21×10^{-4}
τ (ns)	41.96	87.72	32.60	49.33	30.67
μ_d (cm^2/Vs)	0.065	0.133	0.194	0.242	0.425
L (nm)	57.40	29.00	20.62	21.29	26.79
V_p (eV)	0.158	0.123	0.109	0.104	0.093

In the annealed state, the photoconductivity, drift mobility, lifetime and the range of the long-range potential fluctuations in a-SiGe:H decrease, while the depth of the long-range potential fluctuations increases with increasing GeH_4 gas flow ratio. The number of charge states can be estimated using the range and depth of the long-range potential fluctuations due to charge states; some of the charge states can be due to the effect of alloying whereby the neutral homopolar bonds of Ge-Ge and Si-Si get modified in the case of a Ge-Si bonds resulting in a slight ionic character.

The surface morphology of these samples were determined by AFM in cooperation with Dr. David Braunstein formerly of Parks Scientific and presently of IBM. Figure 98 shows the RMS surface roughness vs. the GeH_4 gas flow rate. The transport parameters as a function of the GeH_4 gas flow rate are shown in Figure 99. Figures 100-104 show the images of the surface scans and the respective surface roughnesses. The surface roughness should not be interpreted as grain size. To arrive at the grain size it is necessary to perform a Fourier analysis of the image which will be reported a later date.

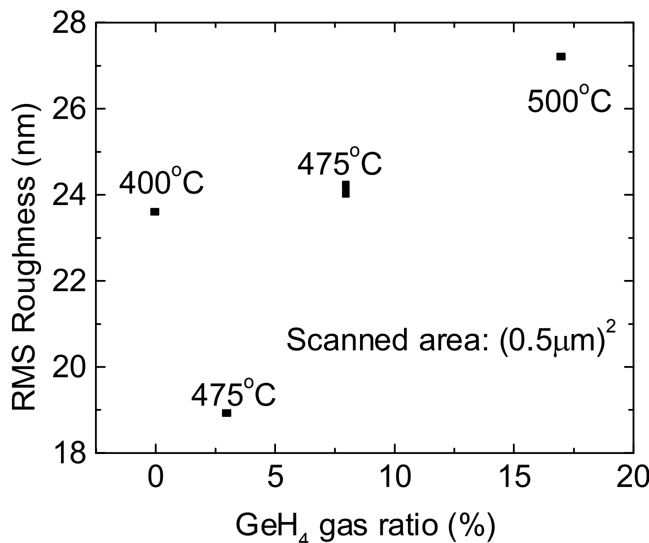

Figure 98. RMS roughness vs. GeH_4 gas ratio.

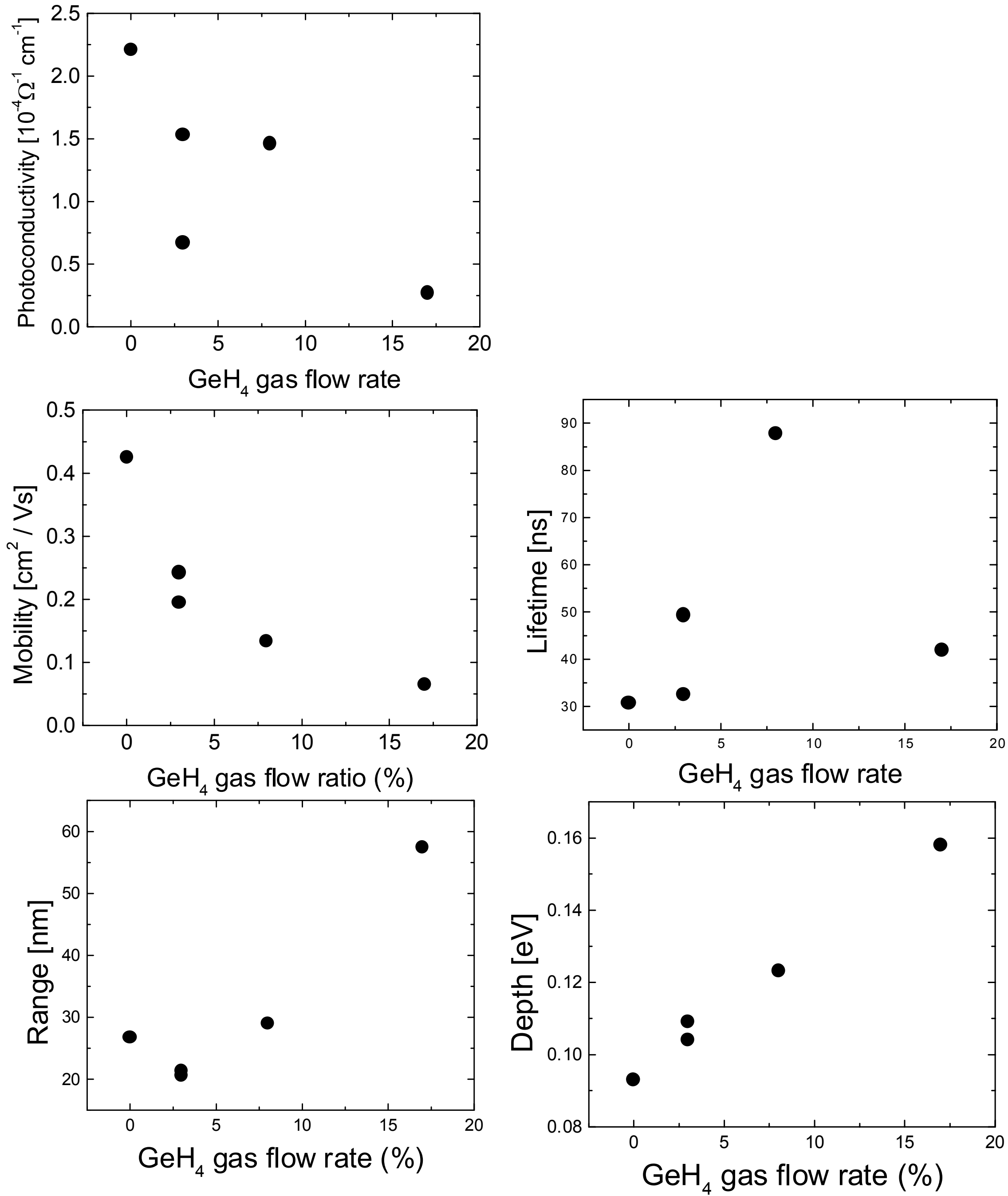

Figure 99. Photoconductivity, mobility, lifetime, LRPF range and depth vs. germanium hydrogen gas flow ratio (annealed state).

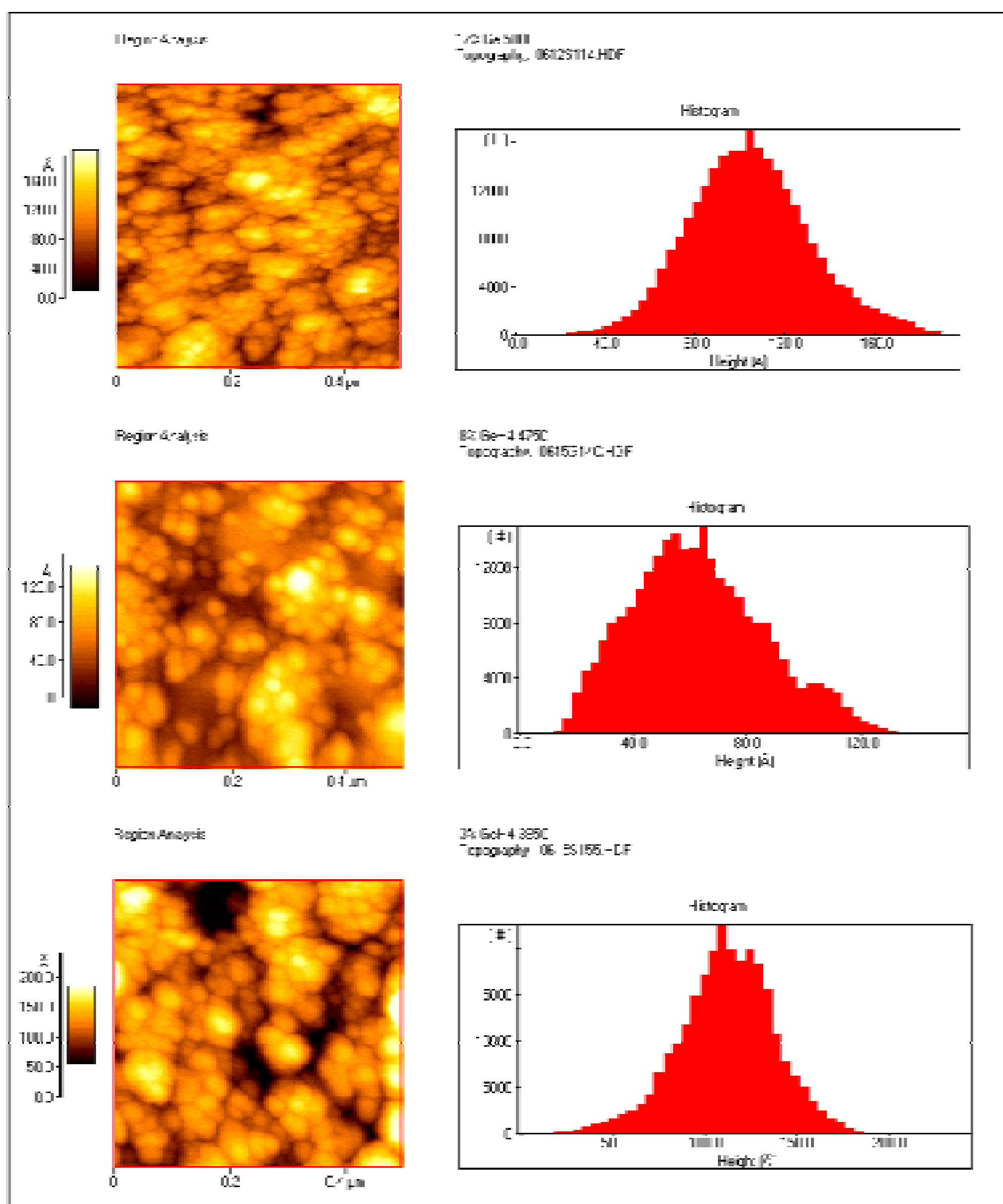

Figures 100-102. The AFM scanning images and surface height distribution of the samples HGe 121, 113, and 100.

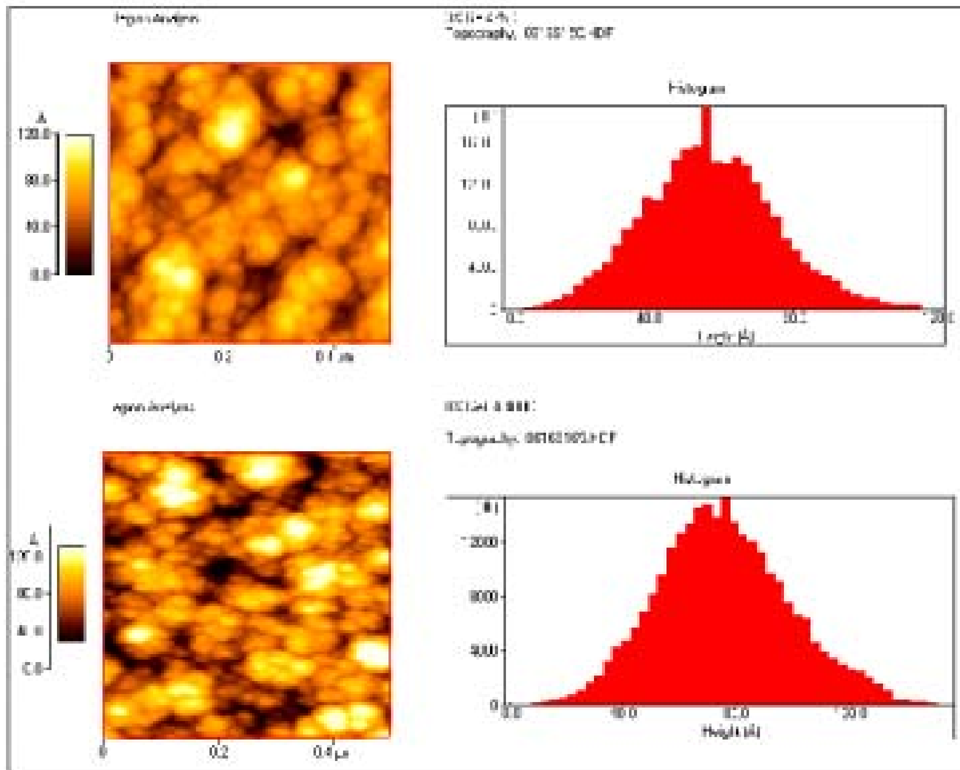

Figures 103-104. The AFM scanning images and surface height distribution of the samples HGe 114 and HGe 118.

8.2 Charge transport properties of PECVD a-SiGe:H films produced by BP Solar

We have employed the photomixing technique to study the charge transport properties of HWCVD a-SiGe:H alloys as a function of alloy composition [23]. Evidence for the presence of long-range potential fluctuations in a-SiGe:H was revealed from the measurements of electric field dependence of the drift mobility, and the effect of the long-range potential fluctuations is enhanced by the addition of Ge to the alloy system that results in the deterioration of the opto-electronic properties of a-SiGe:H. It was found that at a composition of ~10% Ge in Si, the photoresponse begins to decrease monotonically with increasing Ge content due to the decreases in both the drift mobility and the lifetime as a result of an increase in the concentration of charged defects, which lead to the long-range potential fluctuations whose depth increases, while the range decreases. It is of interest to study the influence of the incorporated Ge on a-SiGe:H alloys prepared by other techniques.

We have received a series of a-SiGe:H samples prepared by the PECVD technique from BP Solar for photomixing transport measurements. These samples were deposited on Corning glass substrates with varying Ge content (0-40%). Table 20 shows the Ge content and film thickness for the samples being studied. Detailed deposition conditions of the samples have not been disclosed at this time.

Table 20. The Ge content and film thickness for the samples produced by BP Solar.

Sample ID	Ge content (%)	Thickness (μm)
A0270-1	40	0.92
A0270-2	20	0.87
A0271-1	10	0.70
A0271-2	5	0.74
A0272-1	0	0.70

Figures 105-108 show the photoconductivity, the drift mobility and lifetime, the depth and range of the potential fluctuations, and the relative changes in the charged defect density, respectively, of the samples as a function of Ge content. It is seen that the results for PECVD a-SiGe:H samples are basically similar to those for HWCVD materials, i.e., the photoconductivity is reduced monotonically with increasing Ge content due to a decrease in the mobility as a result of an increase in the concentration of charged defects, which lead to the long-range potential fluctuations whose depth increases, while the range decreases. While, the lifetime shows little change, and surprisingly even a little increase with increasing Ge content, in contrast to the case for HWCVD materials where the lifetime decreases with increasing Ge content. Moreover, from the data shown in the figures, it appears that a little more Ge, up to ~20%, is allowable to be added to the alloy system before the film transport properties are deteriorated significantly in the case of PECVD materials, consistent with the previous results [24].

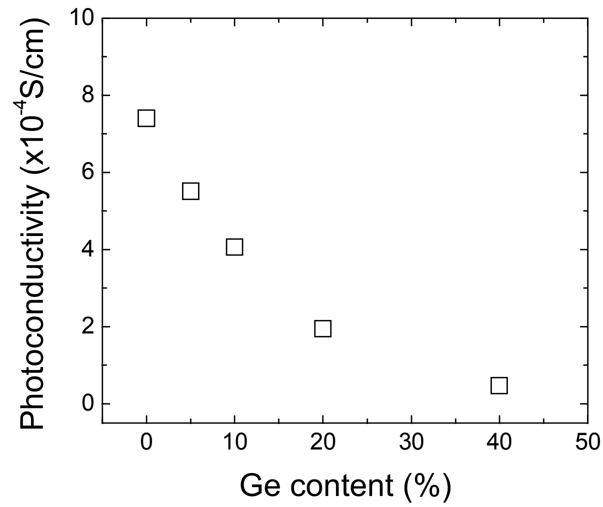

Figure 105. The photoconductivity of the samples as a function of Ge content.

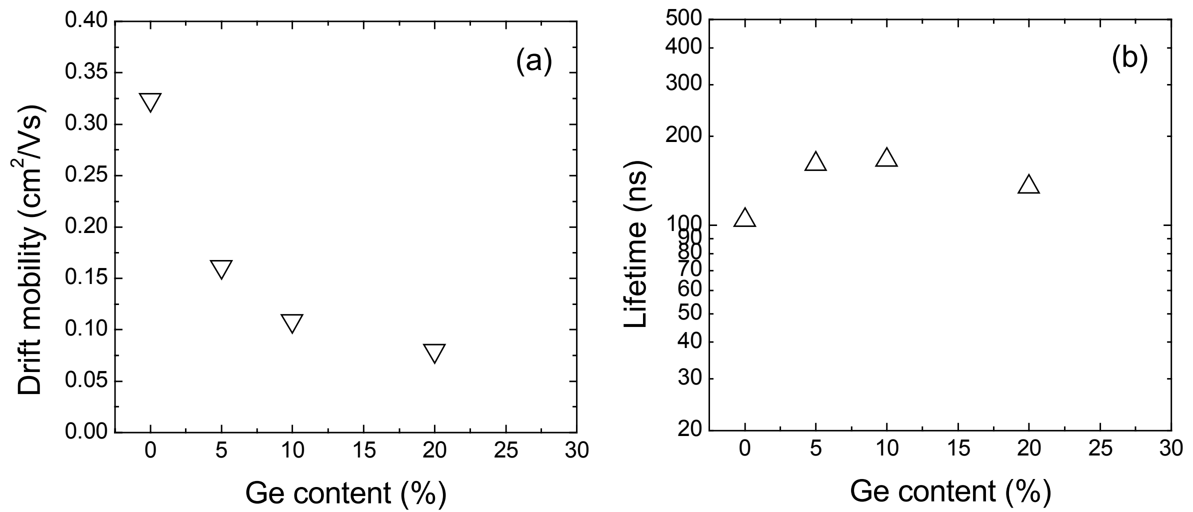

Figure 106. The mobility (a) and lifetime (b) of the samples as a function of Ge

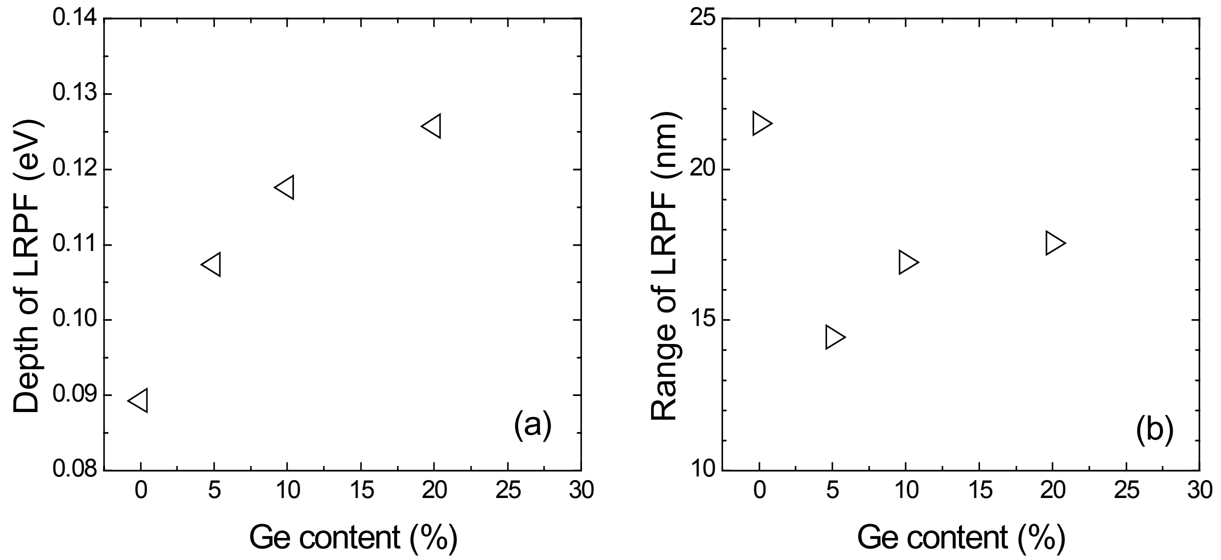

Figure 107. The depth (a) and range (b) of potential fluctuations as a function of Ge content.

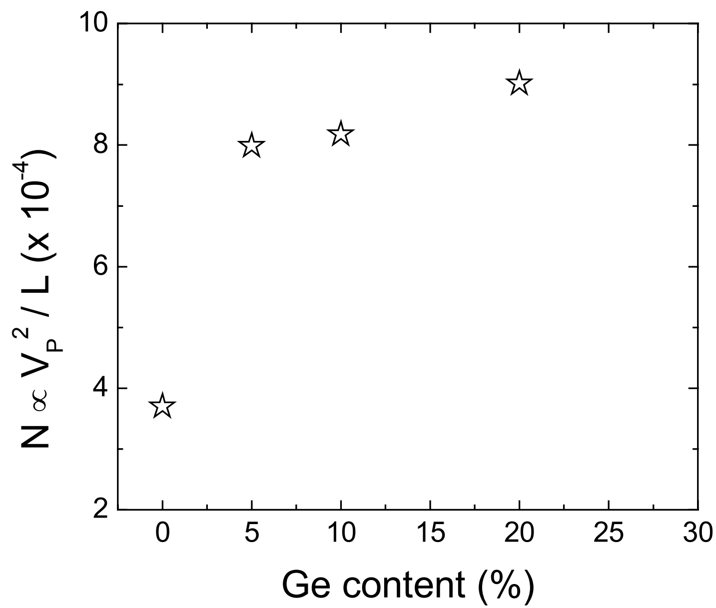

Figure 108. The relative change in the density of charge defects as a function of Ge content.

8.3 Electrical and optical properties of high quality low bandgap amorphous (Ge, Si) alloys prepared by ECR plasma deposition

We have employed the photomixing technique to study the charge transport properties of a-SiGe:H alloys growth by both HWCVD and PECVD as a function of alloy composition. It was found that the quality of both HWCVD and PECVD materials and the device performance degrade significantly with alloys having >40% Ge content being rather poor in quality so that the transport parameters at the Ge end could not be determined by the photomixing technique. In general, this deterioration in quality is ascribed to poorer microstructure of the materials with high Ge content.

It is noteworthy that the monotonic increase in the depth and the monotonic decrease in the range of the potential fluctuations with increasing Ge content up to 40% in this alloy system suggest that compositional disorder may also play a role in the long-range potential fluctuations. If this is the case, at a certain critical Ge content, there should exist the largest degree of the compositional disorder in the alloy system that will results in the worst film quality, as may be the case in crystalline Si_xGe_{1-x} alloys [25]; beyond this, the film quality would increase again. Therefore, it is of great interest to pursue a suitable technique to produce good quality a-GeSi:H alloys at the Ge end, even pure a-Ge:H films, and to perform optoelectronic and structural investigations of the alloys and related devices.

Recently, we have received a series of high quality low bandgap a-(Ge, Si):H alloys at the Ge end from the Dalal group. These a-(Ge, Si):H samples were prepared using low pressure, reactive ECR plasma deposition with high H dilution and ppm B-doping. Incorporating these high quality materials into devices leads to much lower gap a-(Ge, Si) solar cells (down to ~1 eV in a-Ge:H) with acceptable performance [26]. Here, we report on the charge transport and optical properties of these low bandgap materials as a function of alloy composition investigated by employing the microwave photomixing technique and optical absorption spectroscopy. Table 21 shows the growth conditions and some measured properties of ECR a-(Ge, Si):H samples supplied by the Dalal group.

Figure 109 shows the optical absorption spectra of the samples measured with a Lambda 9 spectrophotometer, where the Si content and the Tauc gap E_g are also given. It is seen that with increasing Si content, the absorption edge shifts to higher energy, indicating an increase in E_g, from ~1 eV for a-Ge:H up to 1.34 eV at $SiH_4/(SiH_4+GeH_4)$ = 57%. At the other end of the composition range (the Si end), the absorption edge shifts to lower energy when Ge is added to Si, as observed previously.

Figure 110 shows the sub-gap absorption spectra of some of the samples obtained using a dual beam quantum efficiency apparatus, where the Si content and the Urbach energy (E_o) of the valence band-tail are also given. The Urbach energy E_o was obtained from the exponential part of the absorption spectra. The Urbach tail is known to be due to bonding and thermal disorder in the material, and may be used to study the disorder in the network structure [27,28]. We can see that for pure a-Ge:H, there is strong sub-gap absorption due to high density of gap defect states

below the Fermi level, but the Urbach energy E_o is low, comparable to that for a-Si:H. With increasing Si content, the sub-gap absorption (or the gap-state density) is reduced significantly, while the Urbach energy E_o is increased considerably, up to more than 90 meV at 44% Si in Ge, suggesting an increase in the compositional disorder.

Table 21. Growth conditions and properties of ECR a-GeSi:H/a-Ge:H samples.

Sample ID	Temp. (ºC)	Press. (mTorr)	Power (W)	H_2 (sccm)	SiH_4 (100%) (sccm)	GeH_4 (10%) (sccm)	ppb TMB (10ppm) (sccm)	Thk. (μm)	σ_d (S/cm)	σ_{ph} (S/cm)
2/4392	350	10	150	42	0	9.6	4	0.70	7.00×10^{-6}	8.80×10^{-6}
2/4393	350	5.6	150	42	1.9	14.4	4	0.87	1.70×10^{-9}	1.87×10^{-7}
2/4394	350	5.2	150	42	1.14	14.4	4	0.98	2.00×10^{-8}	1.28×10^{-6}
2/4395	350	5	150	42	1.52	12.8	4	0.82	—	—
2/4396	350	5.8	150	42	0.95	16	4	1.62	2.30×10^{-8}	1.09×10^{-6}
2/4397	300	5.9	150	42	0	16	4	1.07	7.90×10^{-5}	9.60×10^{-5}
2/4399	300	10	150	42	0	9.6	4	1.30	1.44×10^{-4}	1.60×10^{-4}

Figure 111 shows the photoconductivity (proportional to mobility-lifetime product $\mu_d\tau$) of the samples as a function of the Tauc gap and therefore alloy composition. It is significant to see from Fig.111 and Table 21 that an abrupt decrease (more than one order of magnitude) in $\mu_d\tau$ from the a-Ge:H endpoint as Si is added to the system sets in the neighborhood of 30% $SiH_4/(SiH_4+GeH_4)$, and then continues to decrease with increasing Si content up to 57%. In contrast to the a-SiGe:H films at the Ge end prepared by HWCVD or PECVD, there is no photoresponse observed when $GeH_4/(SiH_4+GeH_4)$ is over 40% (or 60% Si content) so that the photomixing technique could not determine their transport parameters, indicating very poor performance. The present results indicate that the transport properties of a-GeSi:H alloys at the Ge end produced by reactive ECR plasma deposition have been improved significantly. The much improved film quality allows us to separately determine the drift mobility and lifetime; from the measurements of electric field dependence of the drift mobility, the depth and range of the potential fluctuations, and subsequently the charged defect density can be determined as a function of alloy composition.

Figure 112 shows the mobility (a) and lifetime (b) as a function of alloy composition. We see that both μ_d and τ, particularly μ_d, decrease abruptly at ~30% $SiH_4/(SiH_4+GeH_4)$; with further increasing Si content, μ_d changes very little, but τ continues to decrease. It is thus evident that the Si-induced degraded photoresponse at the Ge end can be attributed to the decreases in both μ_d and τ, similar to the case of the Ge-induced decay at the Si end.

Figure 113 shows the electric field dependence of the mobility of the samples as a function of alloy composition. The solid curves shown in the figure are fits of the data to equation (1). Due

to the presence of long-range potential fluctuations, an obvious consequence is that the μ_d should increase with an applied field, because the external field offsets the internal field and reduces the magnitude of the potential barrier. Furthermore, it is clearly seen that with increasing Si content in the alloys, the absolute values of the mobility are reduced significantly in the whole electric field range measured; moreover, with the addition of Si to the alloys, the degree of the field dependence of the mobility becomes less, suggesting an enhanced effect of long-range potential fluctuations, which will be confirmed below by the determination of the depth and range of potential fluctuations as a function of alloy composition.

From the electric field dependence of the mobility shown in Fig. 113, the depth and range of long-range potential fluctuations can be inferred (Fig.114 (a) and (b)), and consequently, the relative change in the density of charged defects can be estimated (Fig.115). It is seen that the depth begins to increase, the range decreases and the charged defect density increases beyond ~30% $SiH_4/(SiH_4+GeH_4)$, indicating that the effect of long-range potential fluctuations is enhanced as Si is added to the alloy system.

In summary, we have investigated the charge transport and optical properties of high quality low bandgap a-(Ge, Si):H alloys at the Ge end as a function of alloy composition by employing the microwave photomixing technique and optical absorption spectroscopy. It was found that at $SiH_4/(SiH_4+GeH_4)$ ~30%, the photoresponse begins to decrease rapidly with increasing Si content due to the decreases in the mobility and lifetime, and meanwhile, both the charged defect density and the Urbach energy increase significantly. The latter indicates an increase in the compositional disorder. It is the potential fluctuations whose effect can be also enhanced by incorporating Si to the alloy system that result in the deterioration of the opto-electronic properties of a-(Ge, Si):H alloys, similar to the case of the incorporation of Ge at the Si end. This enhanced effect accompanies with an increase in the depth, and a decrease in the range of potential fluctuations, leading to a decrease in the mobility, and consequently in the photoconductivity. The increased charged scattering centers and compositional disorder upon adding Si or Ge to the alloys observed play an important role in the potential fluctuations.

Further work is needed to perform detailed study of high quality low bandgap a-(Ge, Si):H alloys across the entire range of Ge content (0%-100%) in order to find out the effect of the compositional disorder on the film properties.

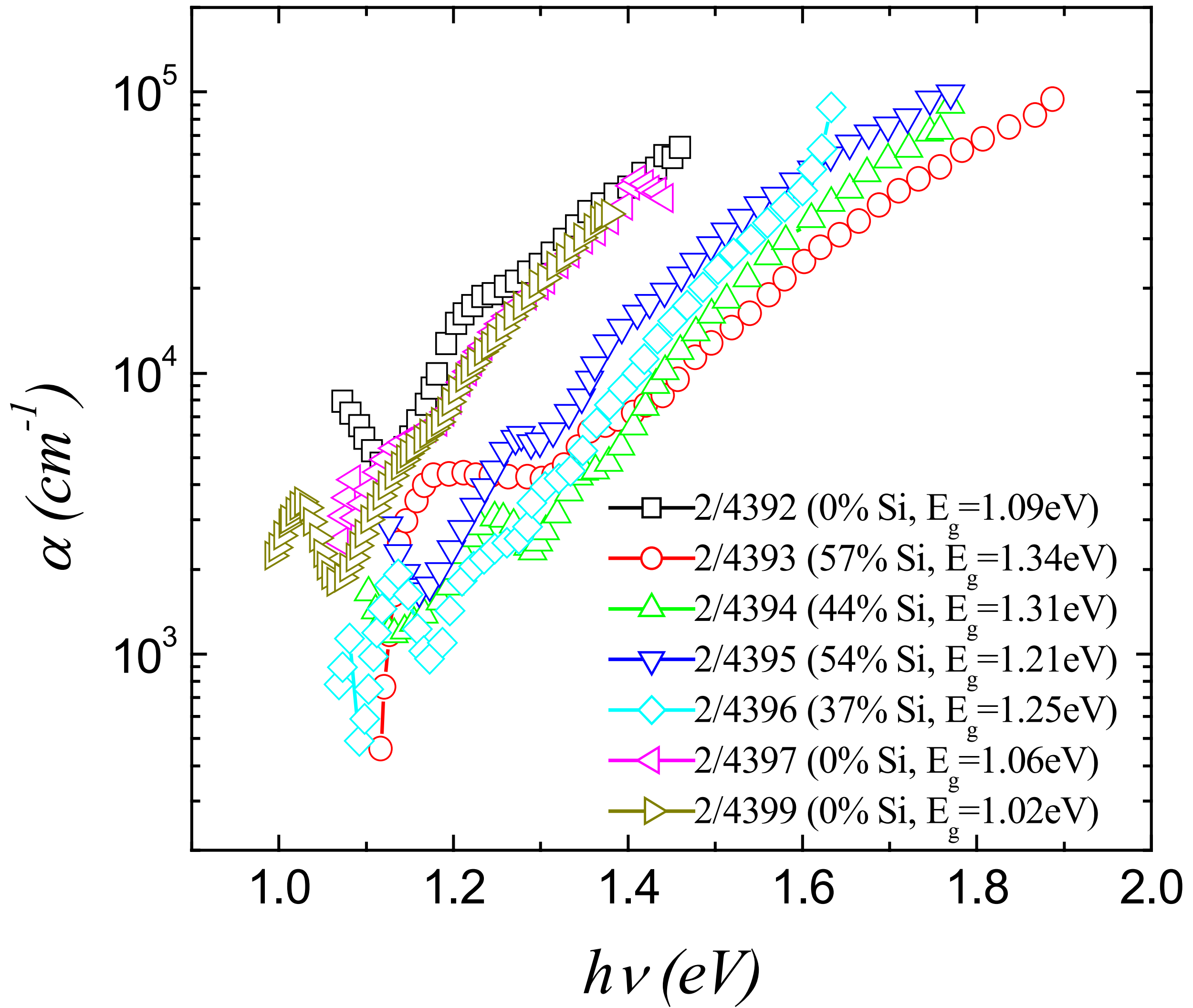

Figure 109. The optical absorption spectra of the samples. The Si content and Tauc gap E_g

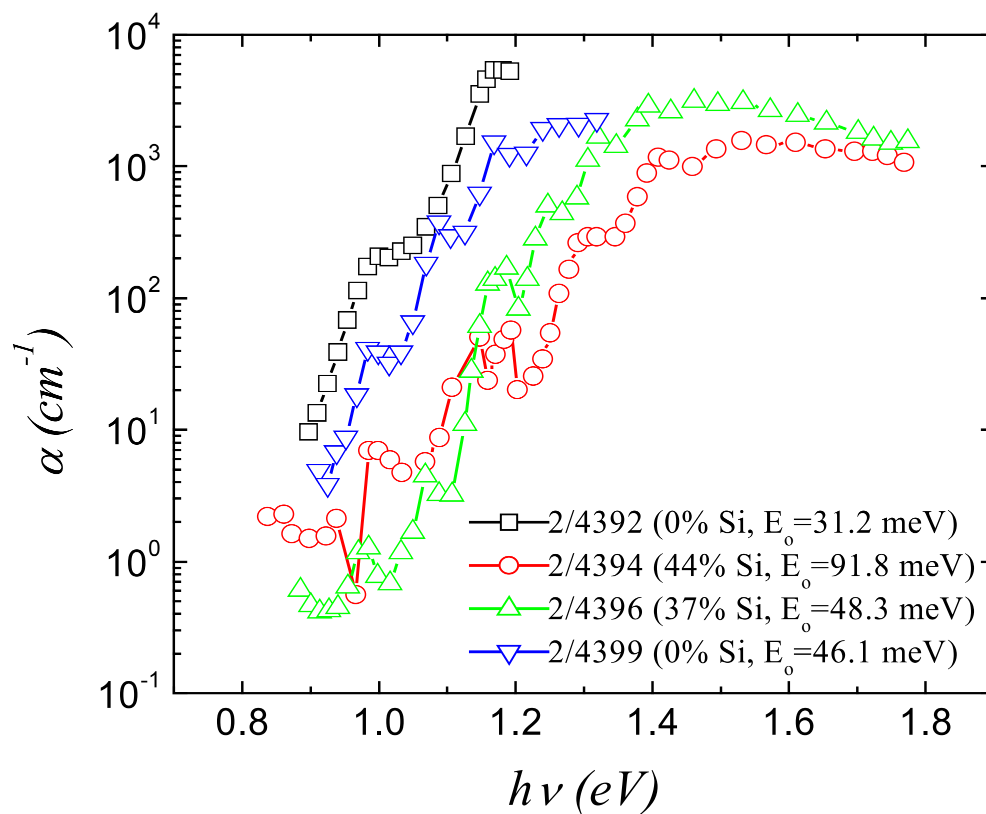

Figure 110. The sub-gap absorption spectra of some of the samples. The Si content and the Urbach energy (E_o) of the valence band-tail are also given.

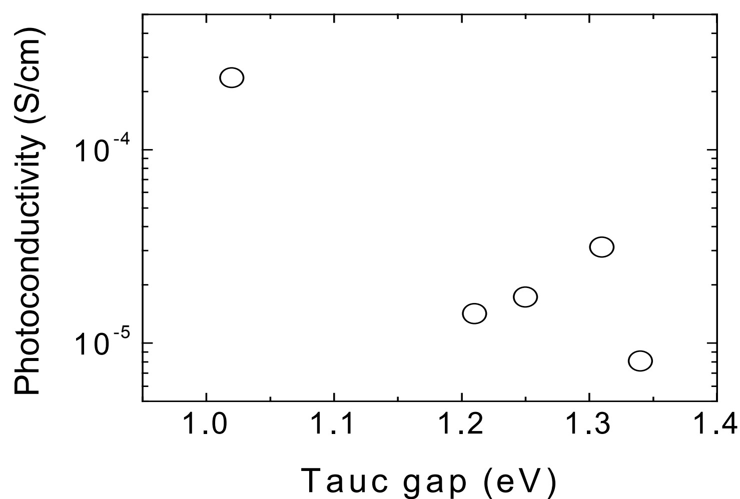

Figure 111. The photoconductivity of the samples as a function of the Tauc gap.

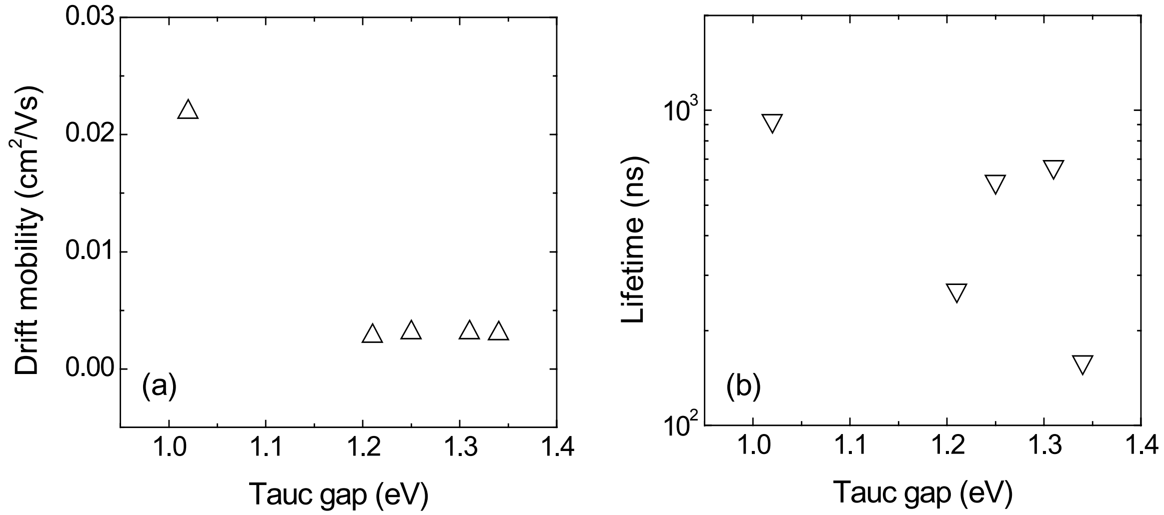

Figure 112. The mobility (a) and lifetime (b) of the samples as a function of the Tauc gap.

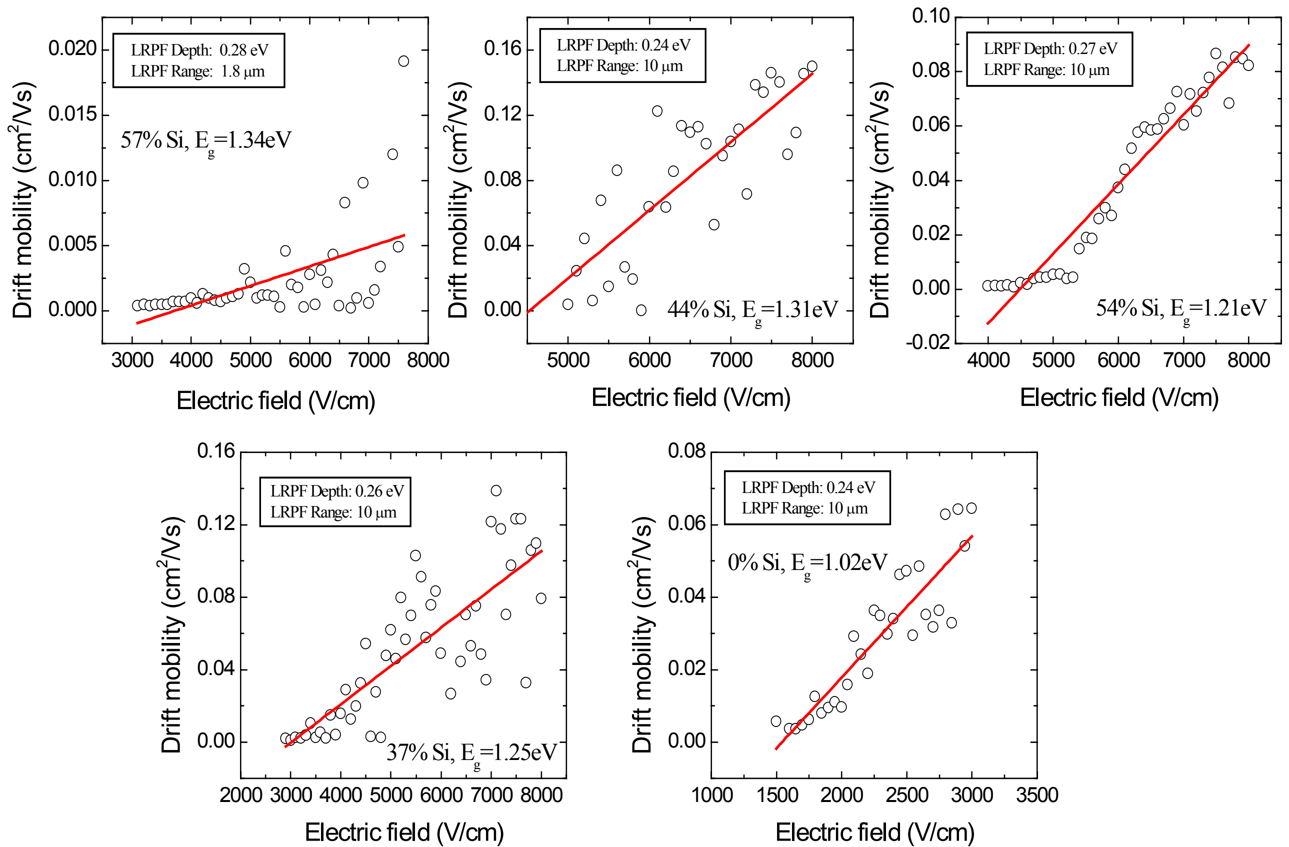

Figure 113. The electric field dependence of the drift mobility as a function of the Tauc gap. The solid curves are fit of the data to equation (1).

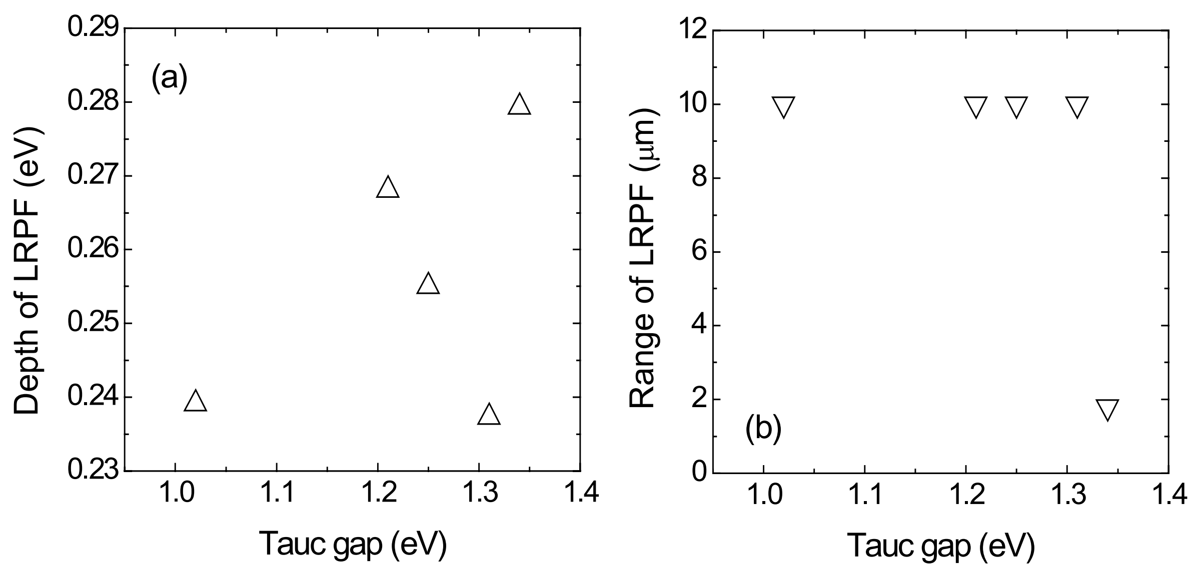

Figure 114. The depth (a) and range (b) of potential fluctuations as a function of the Tauc gap.

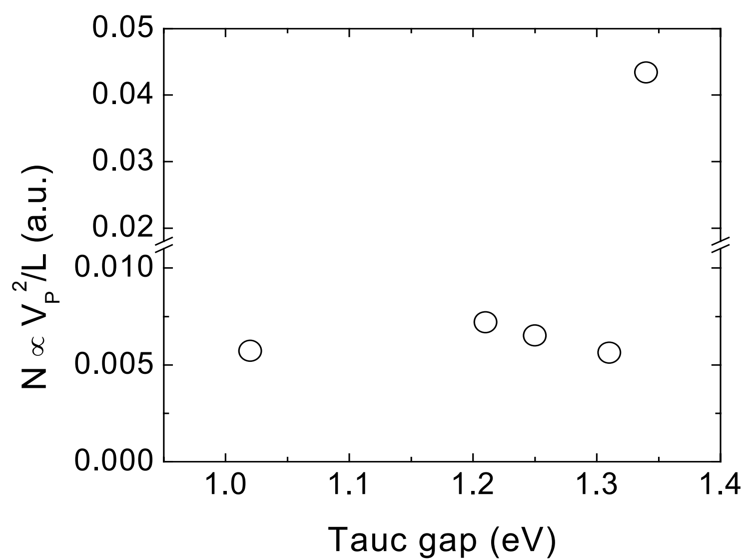

Figure 115. The relative change in the density of charged defects as a function of the Tauc gap.

9. Attempt at finding evidence of the existence of long range potential fluctuations in single crystal GeSi alloys

We have employed the photoconductive frequency mixing technique to study the charge transport properties of HWCVD a-SiGe:H alloys as a function of alloy composition. Evidence for the presence of long-range potential fluctuations in a-SiGe:H is revealed from the measurements of electric field dependence of the drift mobility, and the effect of the long-range potential fluctuations is enhanced by the addition of Ge to the alloy system that results in the deterioration of the opto-electronic properties of a-SiGe:H. The fact that the monotonic increase in the depth and the decrease in the range of the potential fluctuations with increasing Ge content in this alloy system suggests that compositional disorder may also play a role in the long-range potential fluctuations. Therefore, it is of great interest to examine if this is the case in crystalline Si_xGe_{1-x} alloys.

We have obtained a series of single crystal GeSi alloys from RCA Laboratories, David Sarnoff Research Center, Princeton, New Jersey. The compositions of the GeSi alloys were determined to 1at.% by X-ray powder pattern measurements of the lattice constants. We performed photomixing transport measurements on one sample with Ge concentration of 52.3 at.%. Although we succeeded in preparing ohmic contacts by evaporating Al on the sample surface followed by alloying in a $\sim 10^{-6}$ Torr vacuum at 600°C for 5-10 min, we failed to observe any electric field dependence of the DC photocurrent and photomixing signals because the photoconductivity signal was hardly observed, nor was the mixing signal. This is because the conductivity is confined to a narrow surface layer due to strong absorption ($>10^3$ cm^{-1}) under high photon energy illumination (He-Ne laser, 1.959 eV). In order to measure the photoresponse and photomixing signal, the sample has to be as thin as a few microns. We anticipate thin film crystalline GeSi alloys are available, which can be prepared either by mounting thicker pieces on a glass or sapphire slide with glycol phthalate resin and polishing to size, or by MBE for example.

10. Photoconductive Frequency Mixing Measurements on TCO

We obtained samples of 1% Cd doped HRT, 1% Zn doped HRT and undoped samples from Randy Bohn at the University Toledo to see if we can measure the drift mobility by frequency mixing. We observed a photoconductivity signal at ~5286.5 cm^{-1} employing our Argon laser but we did not observe a mixing signal initially; since it was not clear what the spectral range of the absorption was for these films, we did not employ long integration times. Since that time, Randy Bohn has supplied us with the spectral absorption of these samples, and we will attempt to measure the drift mobility as was suggested by Bolko von Roedern.

11. Comparison of intrinsic film properties and device performance

During the last period a set of three intrinsic amorphous Si – film samples and related devices was investigated. The samples were made by S. Guha's group using the PECVD technique at United Solar. The n-i-p structures were prepared on stainless steel and ITO-coated. The intrinsic layers were grown according to the same recipe that was used for the respective films.

The idea is to investigate the relation between

- the initial a-Si:H film transport properties and the initial performance of the device
- the decay behavior of both film and related device.

Table 22 gives a summary of the sample preparation as provided by the Uni-Solar group.

Table 22. Growth conditions of the films and the respective i-layers in the n-i-p structures.

Sample ID, film	**Sample ID, device**	**Growth conditions**
R8795	R8791	SiH_4 with no dilution, using RF
R8796	R8792	SiH_4 with H_2 dilution, using RF
R8794	R8793	SiH_4 with H_2 dilution, using VHF

Figures 116 and 117 show data taken from the intrinsic a-Si:H films R8796 and R8794. Both were produced with hydrogen diluted SiH_4. Unfortunately, we were not able to detect any photocurrent with sample R8795 which was produced without dilution. However, data could be obtained for all nip structures. The illumination intensity of one sun of the HeNe line was employed.

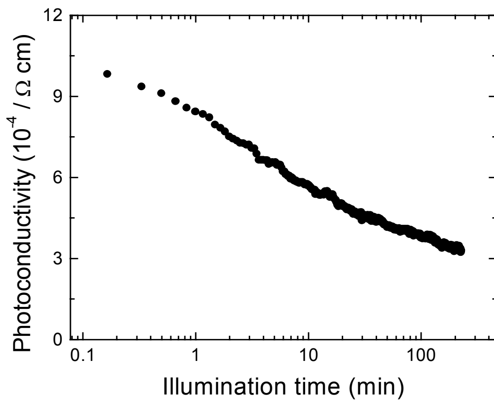

Figure 116. Light-induced changes in photoconductivity, mobility, and lifetime of film R8796 (H_2 diluted, using RF).

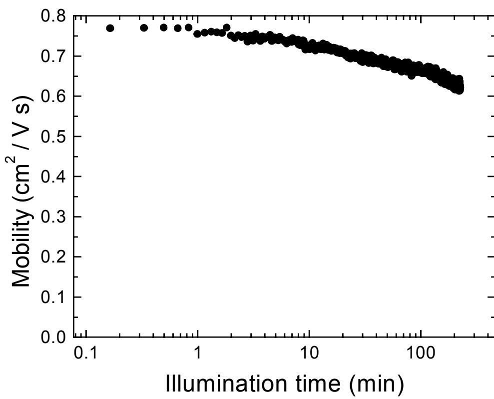

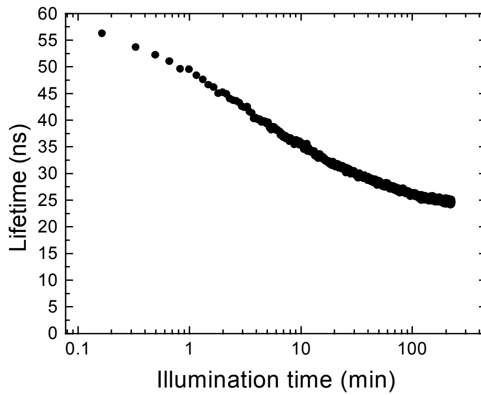

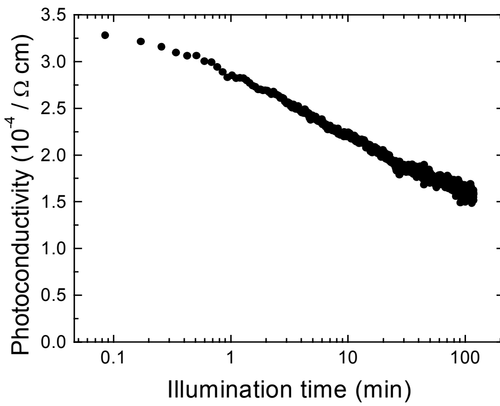

Figure 117. Light-induced changes in photoconductivity, mobility, and lifetime of film R8794 (H_2 diluted, using VHF).

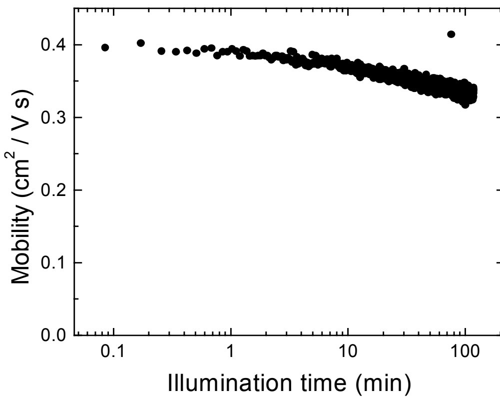

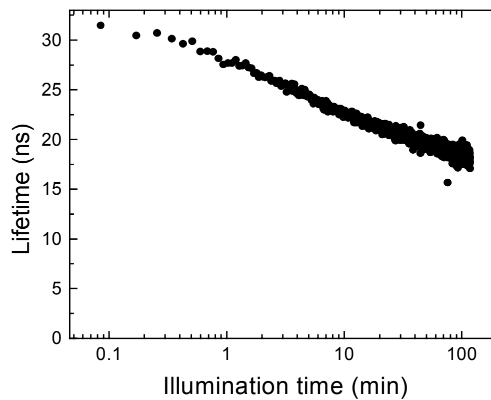

The difference between the films R8796 and R8794 is the plasma excitation frequency as can be seen in Table 22. The VHFCVD technique allows for an increase of the deposition rate at an almost linear function of the frequency to 5-10 times the deposition rate in the case of RF frequencies. Also, a reduced deposition temperature is possible, both of which is relevant in device applications. The film quality can still be high due to a decrease of the silicon-ion energy while the ion-flux is high. The transport parameters, however, are mainly dependent on other growth parameters which have to be reoptimized as one changes from RF to VHF.

In the case of the present two film samples we find for R8796 (RF excitation) an almost double as high a mobility as for R8794 (VHF excitation) in the annealed state. Also, the lifetime ratio between R8794 and R8796 is in the same range. From this we can clearly conclude that the transport properties of the RF – film is superior. As far as the decay is concerned, we find that for both samples the decrease of the lifetime is dominant which is also reflected in the results for the Long-Range Potential Fluctuation range and depth before and after light-soaking. These quantities are summarized in Table 23. It can be seen that neither range nor depth change much which shows that the density of charged defects stays more or less constant.

Table 23. Long-range potential fluctuations.

Sample	State	LRPF range (nm)	LRPF depth (eV)
R8796	annealed	34.6	0.07
	light-soaked	34.5	0.08
R8794	annealed	39.8	0.09
	light-soaked	36.2	0.09

After 180 minutes of illumination, the decay of the photoconductivity of the RF film is a little higher in the case of the RF sample than for the VHF film. Since in a wide range H_2 dilution both improves both opto-electronic properties and stability of amorphous silicon films, it is interesting to see how the device behavior changes with respect to dilution and increase of frequency.

Figure 118 shows the initial I/V-curves for all nip structures. Again, the nip device made with an intrinsic film using RF (R8792) shows higher initial short circuit current than R8793 (VHF). The structure with the intrinsic layer made without dilution shows the lowest initial values. Figure 119 shows the square root of the mixing power for each sample which is linear to the high-frequency part of the photocurrent. It can be seen that only with back-biasing to –1.5V the photomixing signals differ noticeably. As already discussed in the 98-99 annual report, the main difficulty of mixing measurements on devices is the non-uniform profile of the defect distribution and the electric field. Therefore, interface effects might play a more dominant role for forward-biasing than the actual intrinsic film properties.

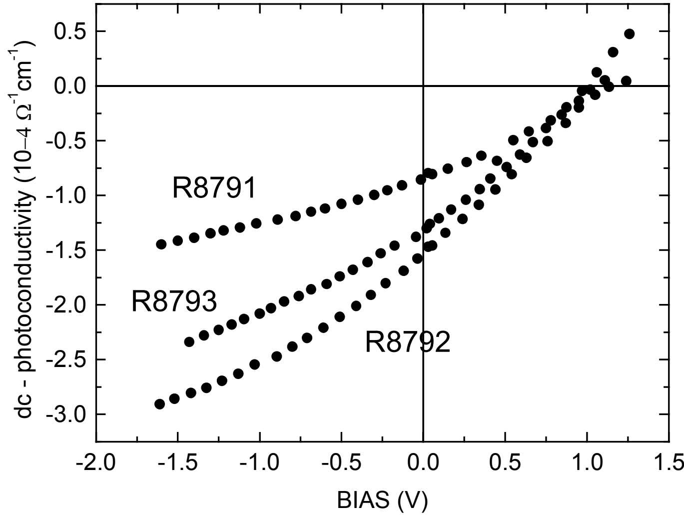

Figure 118. dc-photoconductivity for nip-devices in the annealed state.

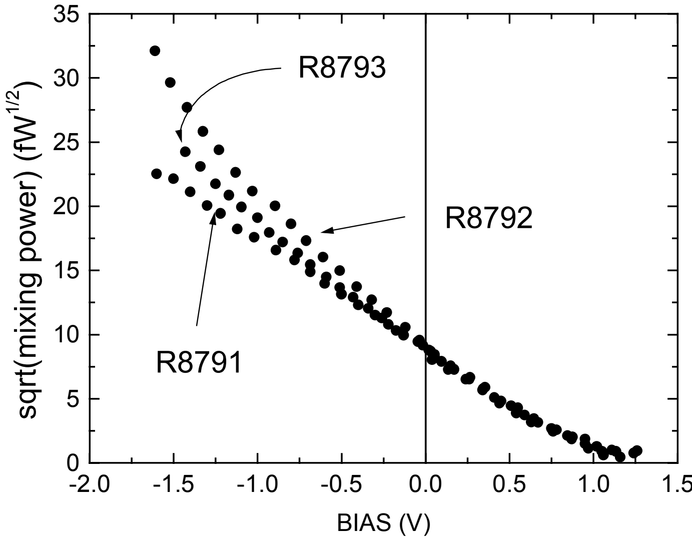

Figure 119. Square root of mixing signal for nip-devices in the annealed state.

Figures 120-122 finally give an overview of the light-induced decay measurements on the nip devices. While for sample R8793 (VHF) the back-bias photomixing signal seems to almost mimic the dc – short circuit current, we find the decay of the ac signal to be greater than the dc current for R8792 (RF) and the reverse case for R8791 (undiluted). Assuming that both illumination intensity (about 20mW laser power) and back-biasing is sufficient in order to neutralize charged defect states near the interfaces, the present results would suggest that the decay of the intrinsic film in R8792 contributes less to the over-all decay of the solar cell than in the case of R8793 which would be consistent with the slightly smaller decay of the mobility of the R8796 film (which is incorporated in R8792) than for R8794 even though the over-all decay of the photoconductivity is actually higher for R8796.

In summary this would mean that the decay of I_{sc} of the solar cells seems to scale with the initial performance of the respective single films. It certainly would have been more informative if we had been able to also acquire decay data on sample R8791 but in any case the experiments showed that

- the *initial* cell and film performances for the RF and VHF samples are consistent
- it is not clear whether the light-induced decay of the nip structures scale with the related films.
- There is a scaling between the properties of the film and ac- and dc- measurements on devices.

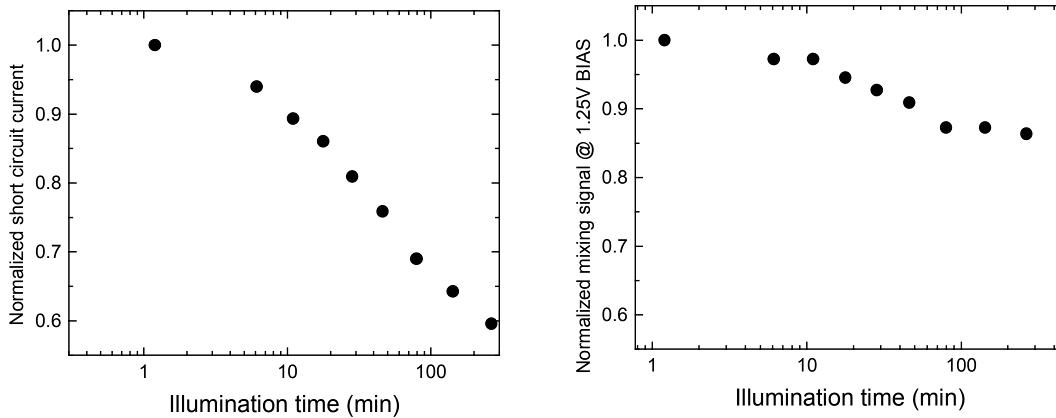

Figure 120. Normalized decay of the dc photocurrent in short circuit condition and the back-bias mixing signal in nip device R8791.

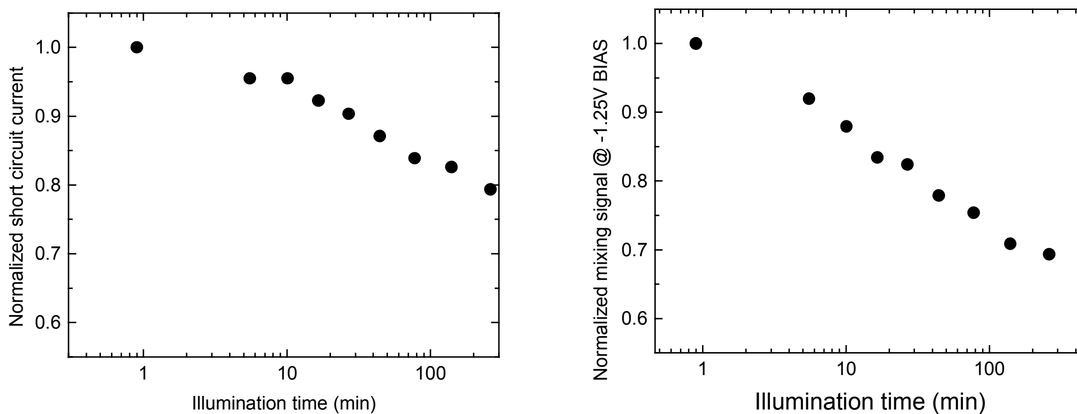

Figure 121. Normalized decay of the dc photocurrent in short circuit condition and the back-bias mixing signal in nip device R8792.

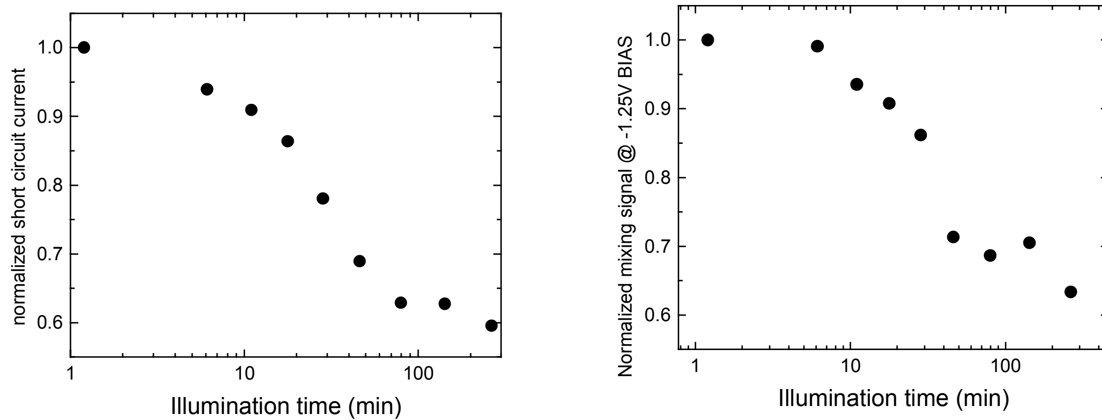

Figure 122. Normalized decay of the dc photocurrent in short circuit condition and the back-bias mixing signal in nip device R8793.

12. Photomixing Measurements on SiGe P-I-N Devices (Supplied by Xunming Deng, University of Toledo)

The photomixing measurement method has been shown to be a successful tool in determining photomixing lifetime and mobility of charge carriers in amorphous and microcrystalline silicon as well as silicon-germanium and other alloy films which are measured in in-plane direction employing coplanar contacts. Here, one deals with a well defined uniform electric field due to an external voltage, a spacially uniform distribution of charged and neutral defects, and a free charge carrier generation profile perpendicular to the field direction.

In p-i-n structures, in contrast to single films with coplanar ohmic contacts, one usually finds

- a space charge distribution in the intrinsic layer near the p-i and i-n interfaces
- a non-uniform electron-hole generation profile in field direction
- and thus a generally non-uniform electric field distribution across the i-layer

Additionally, the ac behavior of a p-i-n device is determined by the device geometry and the resulting capacitance. On the other hand, due to the high mixing frequency used, the transient behavior does not play an important role.

The BIAS dependent photomixing power that one detects for different devices under different illumination conditions is thus necessarily affected by many more parameters than it is in the case of single layer films. Even worse, some of the parameters, particularly the electric field distribution, depends on both the deployed materials and the interfaces in a complicated way that is still not very well understood. Therefore, instead of incorporating many unknown parameters into the photomixing model, it seems more advisable to restrict measurements and data analysis to certain regimes where at least analytical models based on simplified assumptions may be valid.

The most important analytical approach is probably the uniform-field model by Crandall [29], whose main assumptions are: uniform field, negligible diffusion in the intrinsic layer, and the use of the Shockley-Read-Hall model for recombination for a two state recombination center. Later, Hubin and Shah [30] presented a variation of Crandall's model introducing three-states recombination centers. The majority of publications, however, present numerical approaches which might yield more realistic results but have the drawback of making it hard to draw immediate physical conclusions. In a recent publication by Asensi et al [31], analytical expressions for the recombination current and the short-circuit resistance are deduced from results of numerical simulations.

Dangling bonds within the intrinsic layer near the interfaces are thought to be usually charged due to the relative shift of the Fermi level to the defect states. Dangling bonds in a charged state, in turn, have a much higher cross section as recombination centers so that a main part of the total recombination processes in the i-layer - which represent the main limitation of the p-i-n-cell efficiency - is assumed to take place near the interfaces. Moreover, these dangling bond states near the interfaces build up space charge regions which lead to higher electric field strengths near the interfaces and accordingly lower fields in the center. In fact, the thickness of the i-layer

is usually kept as thin as possible, so that even with a certain space charge present, the field near the center is sufficiently strong to deplete the generated charge carriers.

However, according to Asensi et al., a uniform-field approximation is possible in the special case of high illumination intensity ($I_{short\text{-}circuit}$ > 10mA/cm^2) and short circuit or back-biasing condition, i.e. when the charged defect states near the p-i and i-n interfaces are neutralized and no charge injection into the intrinsic layer takes place. In this situation, with space charge regions depleted through the strong illumination, also secondary quantities affecting the photomixing power like the device capacitance should not change dramatically with different bias voltages in reverse direction.

The photomixing technique, due to the high beating frequency, merely yields a picture of shallow trap states near the conduction band and is insensitive to deep level defects. Therefore, only for the above mentioned conditions it seems possible to obtain information about the transport properties of the intrinsic layer without the need to deconvolute a complex amount of parameters most of which are not even known. On the other hand, this might enable us to keep track of a certain material-related aspect, i.e. the charge carrier mobility, which is otherwise somewhat lost once single films are deposited within a multilayer structure.

Figures 123 shows the square root of the photomixing power under back-biasing.

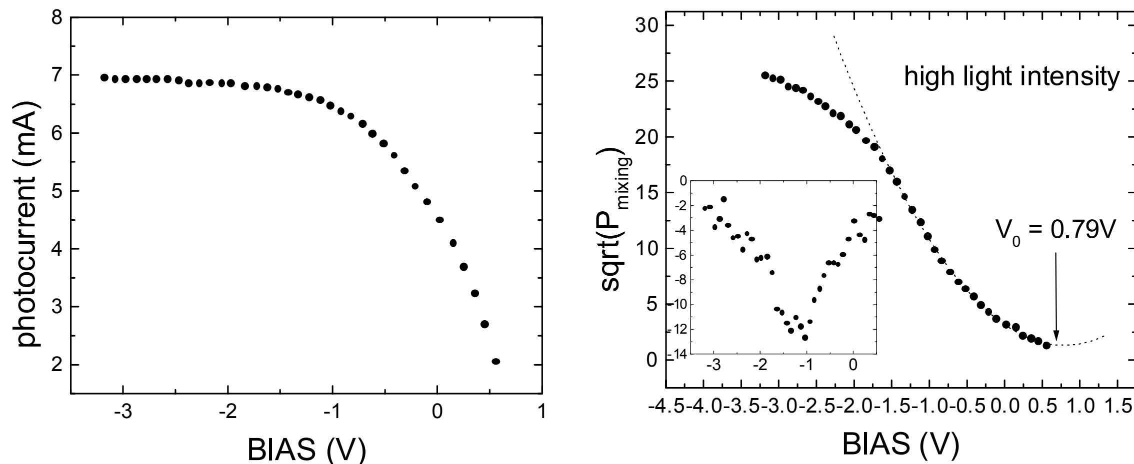

Figure 123. DC photocurrent and the square root of the photomixing power (inset: derivative of sqrt(P_{mix})).

While the dc photocurrent shows expected saturation behavior when the p-i-n device is reverse-biased, in the case of the ac current (as represented by the square root of the mixing power) we find (at least) two distinct regimes, a low-field and a high-field regime.
In the high-field regime, we find an increase with a saturation tendency at sufficiently high fields. The mobility of electrons in a p-i-n structure when approaching high fields has been

described in terms of field-assisted thermal release of electrons from traps within the multiple trapping model [32].

However, for biases below the point of inflection, the shape of the curve rather resembles the field-dependent mobility which is also observed in thin film samples with coplanar contacts. The dotted curve which is fit into the lower-field part of the photomixing current curve points out where the photomixing signal deviates from it's initial shape. According to this fit, the photomixing signal would become zero at about +0.8V, which would mean that at this point the built-in field zero-crosses.

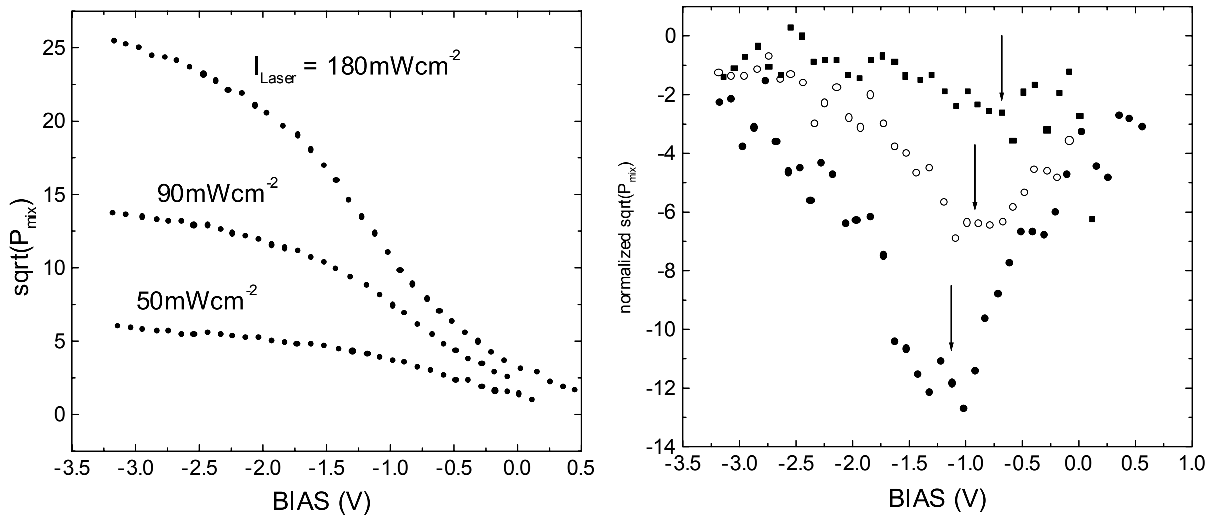

Figure 124. Light intensity dependent photomixing current. Right hand-side: The derivatives show a shift of the point of inflection to higher biases at higher light intensities.

However, this fitting only works for high illumination levels. For lower light intensities we observe a shift towards higher electric fields (Figure 124). It is noteworthy, however, that even for (very) high illumination levels a uniform field within the intrinsic layer is at best a good approximation. For lower levels, this simplified model is certainly not feasible. Absolute values for the mobility across the intrinsic layer seem therefore – in contrast to single films – not very meaningful. However, investigating the evolution of the bias-dependent photomixing curves under light-soaking provide a separation of effects due to geometric or initial material properties from those due to light-induced defects as the following figures show.

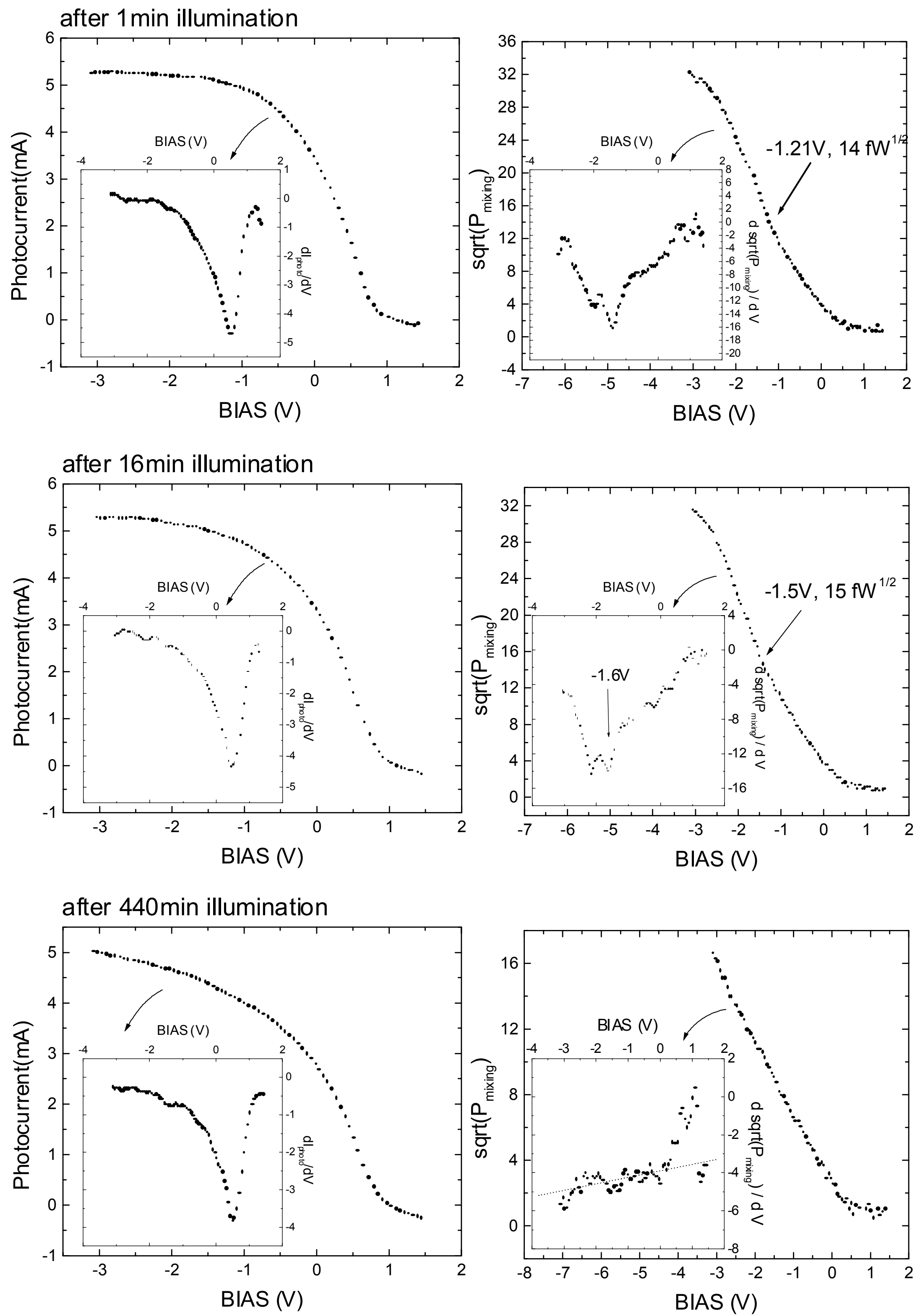

Figure 125. dc and mixing currents after different illumination times (Sample Toledo-GD112).

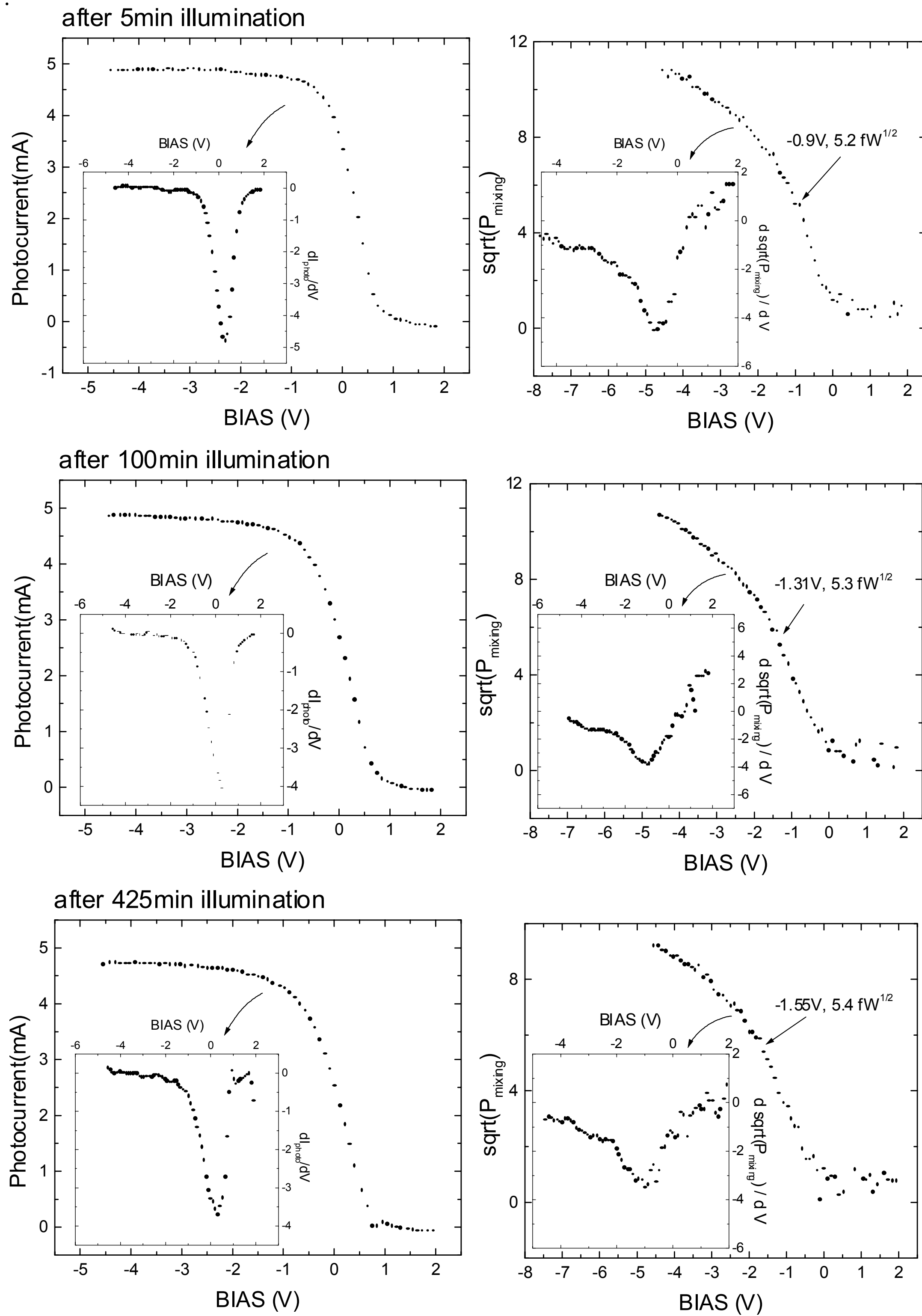

Figure 126. dc and mixing currents after different illumination times (Sample Toledo-GD111).

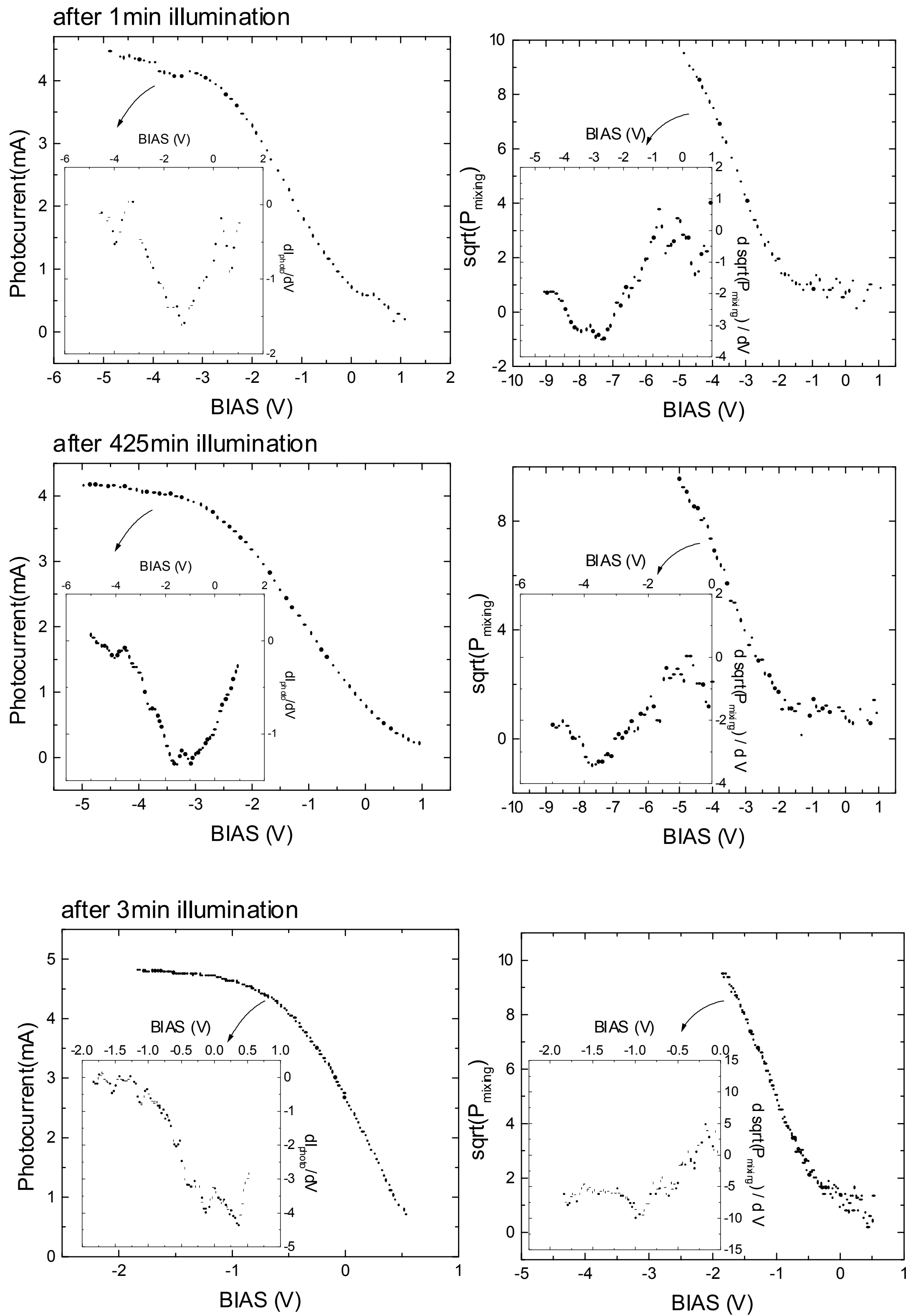

Figure 127. Sample Toledo-GD110.

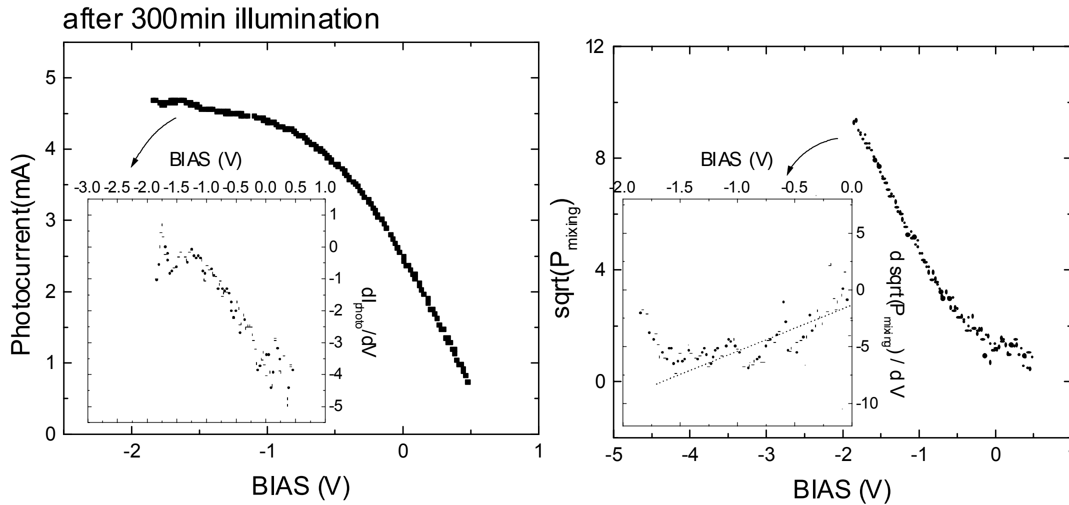

Figure 128. dc and mixing currents after different illumination times (Sample Toledo-GD109).

Figures 125-128 show data obtained from light-soaking measurements on p-i-n-samples supplied by the Toledo group. The insets contain the neighbor-averaged derivatives of their parent curves in order to facilitate the observation of the change of the curve shape during light-soaking. A summary of the respective I-V data can be found in Table 24.

Table 24. I-V data for a-SiGe solar cells with different i-layers (~2000Å).

Sample	V_{oc} **(V)**	J_{ph} from QE (mA/cm^2)	FF	P_{max} (mW/cm^2)
GD109 Standard	0.681	19.3	0.530	6.97
GD110 +15% Ge	0.634	21.3	0.473	6.39
GD111 -15% Ge	0.714	20.0	0.527	7.53
GD112 2.5x H dilution	0.813	18.2	0.486	7.19

Sample GD112 shows both the highest mixing signals and the largest decay under light-soaking. However, according to data from Toledo (Table 24) this sample's filling factor is the second worst of all samples. It is obvious that the dc p-i-n cell performance and the photomixing signal, even though associated with the charge carrier mobility, do not directly scale. This was not to be expected, though. It is clear that the actual device impedance has a great impact on the photomixing signal power. A comparison of the photomixing curves for two different *spots* on the same sample (GD112) as shown in Figure 129 stresses this point.

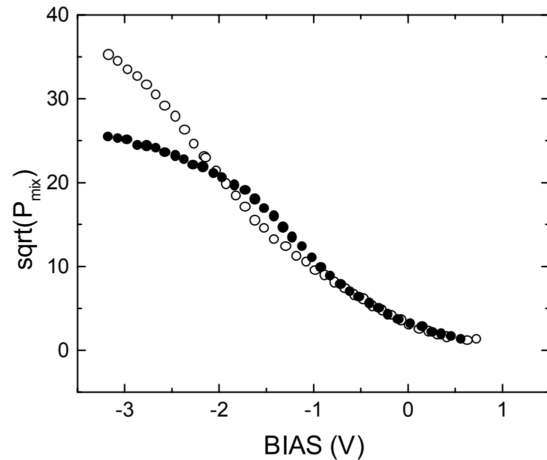

Figure 129. BIAS-dependent ac – photocurrent for two different spots.

At one spot ('spot' means one separate p-i-n-structure among others on the same stainless steel substrate) the curve reaches saturation behavior earlier but at lower mixing signals than it does at some other spot. A steeper curve at lower fields and consequently earlier onset of saturation would mean higher mobility while the variation in mixing power is rather due to the differences in the sample impedance which is apparently quite sensitive to fabrication variations. In contrast to this effect the changes during light soaking (Figure 125), i.e. with parameters other than the defect density kept constant, suggest that the charged defect related field-dependent mobility regime extends to higher electric fields across the i-layer at the saturation regime's expense. After seven hours of light exposure, the saturation regime vanishes completely which means that the applied bias has become insufficient in order for the degraded sample to enter this region. It is also noteworthy that the point of inflection, as marked within the first two viewgraphs of Figure 125, seems to more or less remain at the same height while wandering towards higher biases. After 425 minutes, the photomixing current just reaches the 16 $fW^{1/2}$ level from which the saturation regime evolved in the annealed state. Note also that the dc-current curve seems less affected than the ac-curve. In all samples except for GD110, which turns out be the most stable one, we find the slope of the ac-curve within the lower-field regime to decrease with illumination time. Unfortunately, in most cases we had to limit the maximum reverse bias in order to protect the samples from avalanching. On the other hand, former measurements on a-Si samples showed saturation much more clearly - probably because the electron mobility is generally higher in a-Si than in a-SiGe.

In order to obtain at least approximate values for the electron mobility in p-i-n-structures the photoconductive frequency mixing model has to be adapted appropriately. In particular, the capacitance and geometry contributions will have to be treated in such a way that the ac-signal dependent transport expressions become independent of those. Therefore, accompanying ac-measurements are needed. In a next step, the photomixing transport equations have to be applied and tested against results from further measurements on a series of n-i-p-solar cells supplied by the Toledo group.

We also plan a series of experiments on samples in coplanar configuration and p-i-n-devices that are prepared under the same growth condition.

As far as the experiment is concerned, a higher accuracy, particularly of the ac-current curve derivative, is desirable. One possible way to obtain more accurate results is a more direct measurement of the derivative of the mixing power. Initial experiments employing low-frequency bias sweep and log-in amplification techniques are promising. However, there is always a certain trade-off between measurement accuracy and the undesirable light-soaking effect during the acquisition of a photomixing signal curve.

13. Photo-emission in Air

I. Statement of the problem

The broad objectives of this research are to develop optical stimulated photo-emission in air as a non-destructive technique to characterize semiconductor surfaces. In most applications of photo-emission the photoelectrons are usually collected in vacuum. However the emitted and subsequently scattered electrons can be collected across a sufficiently small air gap by a biased collector and provide information about the electronic structure, composition and chemistry of the surface. A powerful array of electron spectroscopes exist for detecting chemical impurities on surface but usually require an ultra-high vacuum environment and are not readily adaptable to analytic techniques ultimately be used on the production line. These surface analytic techniques include the scanning Auger Microscope, Secondary Ion Mass Spectroscopy and Electron Spectroscopy for Chemical Analysis (ESCA). The development of a technique of optical photo-emission in air will offer a solution to the problem of monitoring surface contamination under normal factory ambient conditions. In the present proposal, we will develop the technique of photo-emission in air and explore its use to study a number of interface problems in semiconductors. These include oxides on semiconductors and homogeneity of composition of semiconductor alloys.

II. Implementation of photo-emission in Air

Figure (130) is a simplified schematic representation of the process of photo-emission in air. UV light passes through the collector grid to the sample. The bias between the sample and the collector drives the emitted electrons by a diffusion process. Figure (131) shows the energy diagrams for two metals with an external voltage, V, in vacuum if light is radiated on the cathode. Figure (131a) shows the anode reversed biased, i.e. in the retarded field mode; Figure (131b) shows the space charge limited regime, while figure (131c) delineates the saturation regime. Figure (132) shows the photo-current versus V for the conditions shown in figure (131). For large negative values of V (Figure 131a) no current flows since the barrier is too high. At V_c the emitted electrons have zero velocity. As V becomes more positive, the more energetic electrons are able to surmount the barrier causing the electron could next to the cathode as per (Figure 132). This is the space charge limited current and current is given by Child-Langmuir law.

If the initial photo-emissive is overlaid with a thin film, attenuation in the film will determine the number of photoelectron collected by the biased collector; on the other hand if the film is also photo-emissive the collector current can increase.

The structure shown in Figure (130) will be implemented by constructing photo-emissive-collector probes using Hg vapor UV sources and laser lines from harmonic generators and dye laser lines; the collectors will be moved over a surface in two dimensions by stepping motors.

III. Results

The results represent were obtained using the Hg vapor UV lamp as a light source. The initial studies were on the homogeneity of the a-Si:H, interface studies of TCO on the a-Si:H samples obtained from Qi Wang of NREL.

a- Figure (133), present the results of a sample of a-Si:H and ITO both prepared on stainless steel substrate. We found that there is no photo-emission signal from ITO however high yield from a-Si:H.

b- Figure (134), shows the photo-emission from a surface with the spots of ITO on a-Si:H. It should be noted that the region between the spots shown a uniform high yield from a-Si:H layer. However, the region of the ITO spots show a decrease of the photo-emission yield relative to the a-Si:H layer. The fact of the photo-emission decrease under the ITO layer relative to the a-Si:H layer but it is a positive quantity indicates the UV line passes through the ITO layer and generates the photo-emission electrons which penetrate the ITO layer to be collected.

c- Figure (135), shows the results of the structure made up of ITO/pin/SS layers. It should be observe the decrease of the photo-emission under the ITO layer similar to fig.134.

d- Figure (136), Shows the results of the sample thin Pd/ni/SS. It should be observe that similar results as of the ITO layer but the yield is less. This indicate the UV light is partially reflected from the Pd layer or the photo-emission yield is less in the case of the Pt/a-Si:H layer.

e- Figure (137), shown the results of a-Si:H on c-Si substrate which indicate the relative homogeneity of a-Si:H layer.

f- Figure (138), shows the results of the 16 pads which are a-Si:H to μc-Si:H and a-SiGe:H to μc-SiGe:H on stainless steel substrate. It should be observe that are differences in the work function between the materials. In the present experimental arrangement we use the whole spectrum of the Hg lamp. However, the excellent signal to noise in the figure indicates that in the new photo-emission setup we plan to build which will employ a known spectrum line and variable bias, it will be possible to measure the work function as a function of the various pads.

g- Figure (139 a,b,c&d), shows the results of a-SiC:H samples on stainless steel with different carbon concentrations(0-40). It is found that the surface of the samples are not homogeneous.

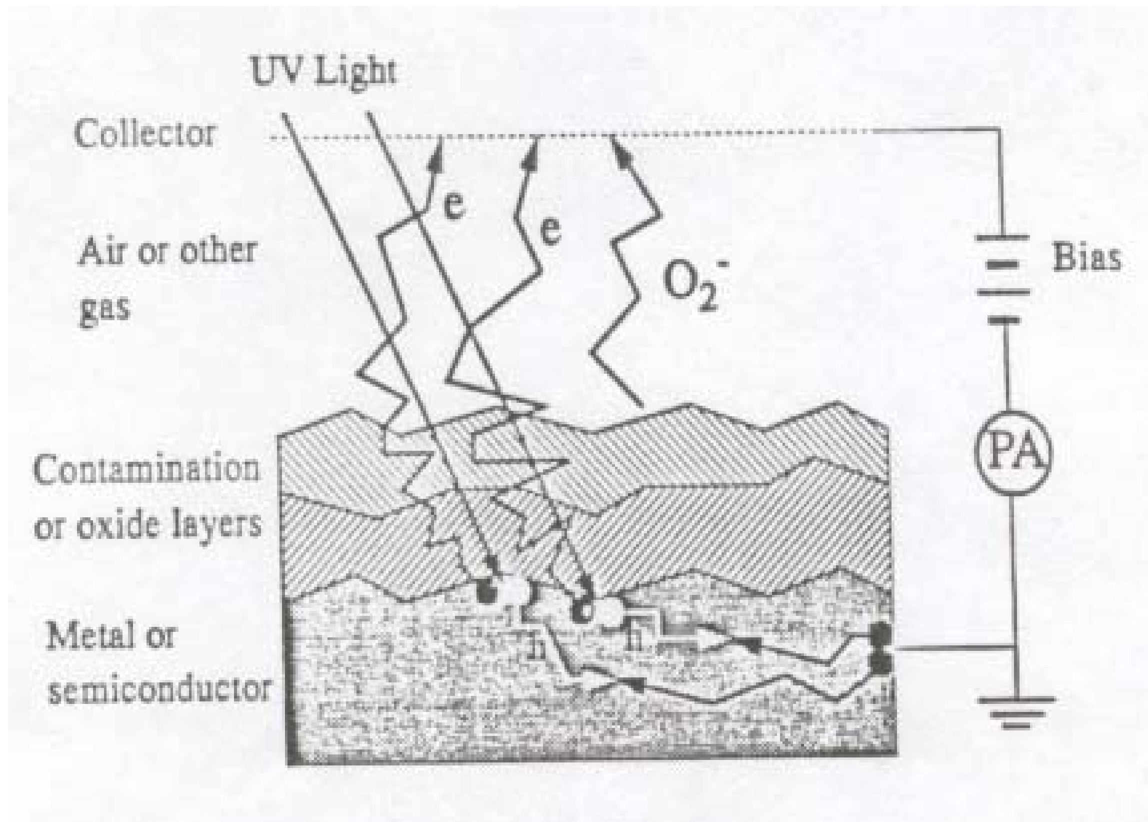

Figure 130. Schematic diagram of Photo-emission in air

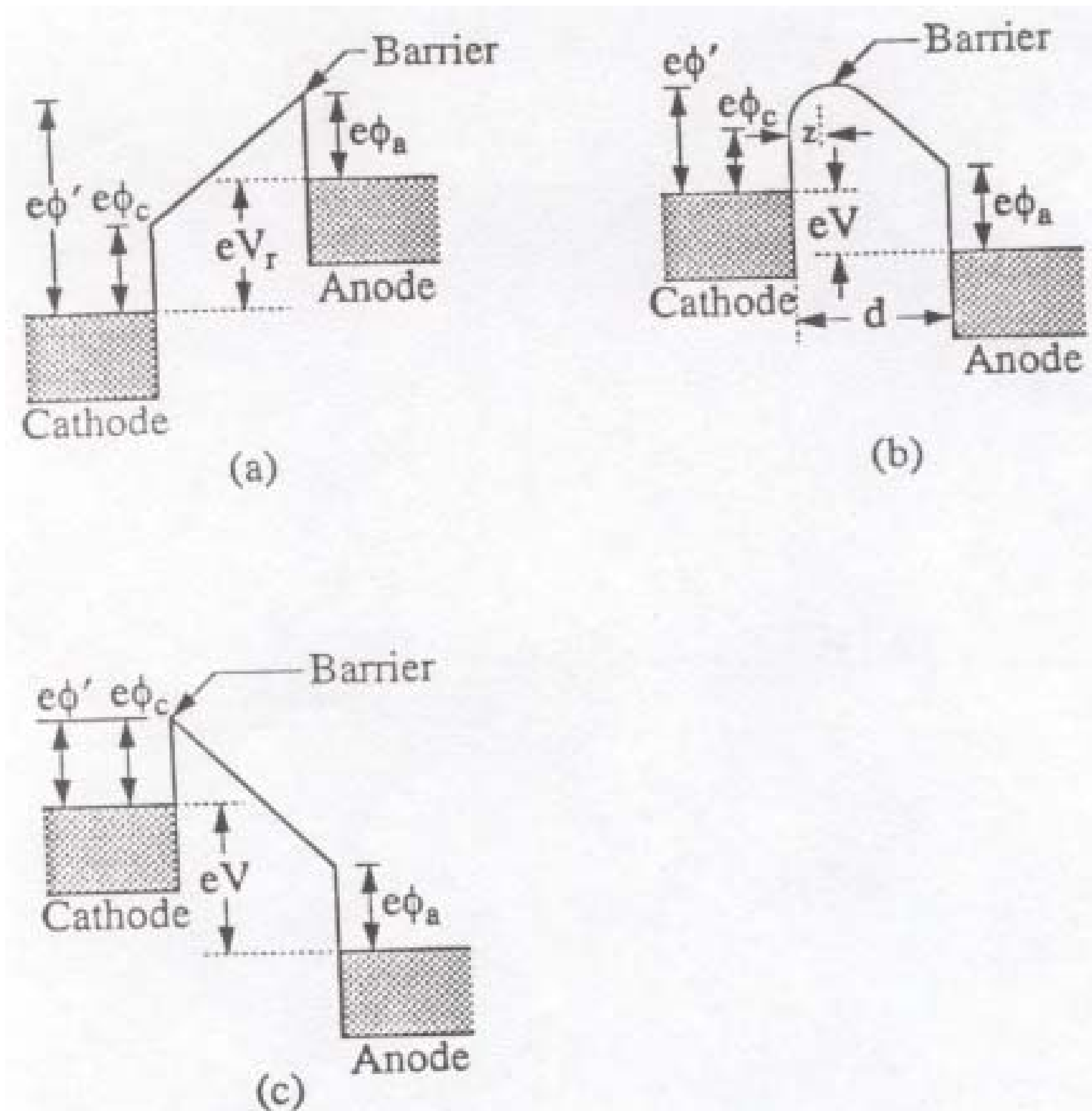

Figure 131. Electron energies between the anode and cathode in a diode under bias conditions. (a) Anode reversed bias (retarding field); (b) emission of space charge limited barrier results from space- charge just outside cathode surface; (c) saturation emission

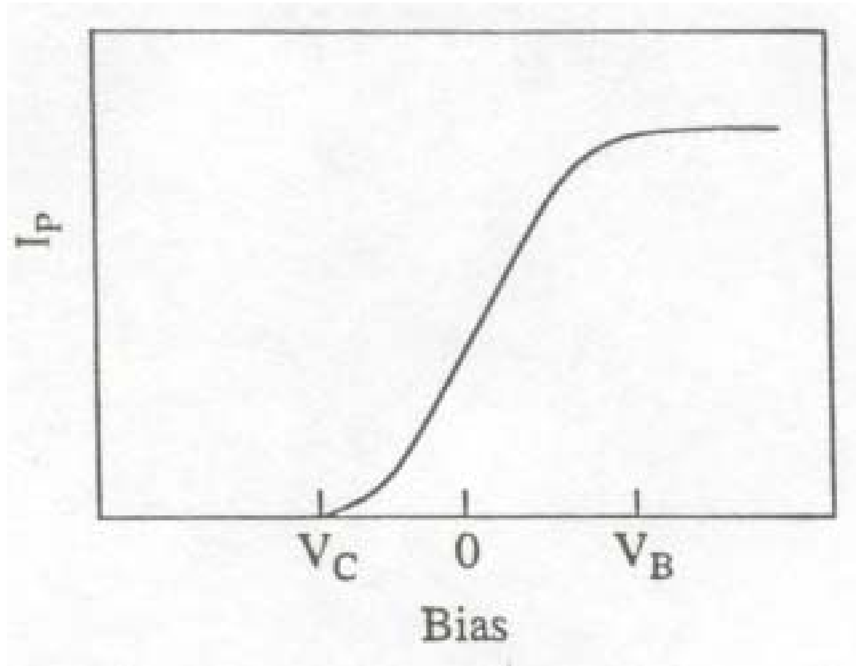

Figure 132. Photo-emission current vs voltage bias

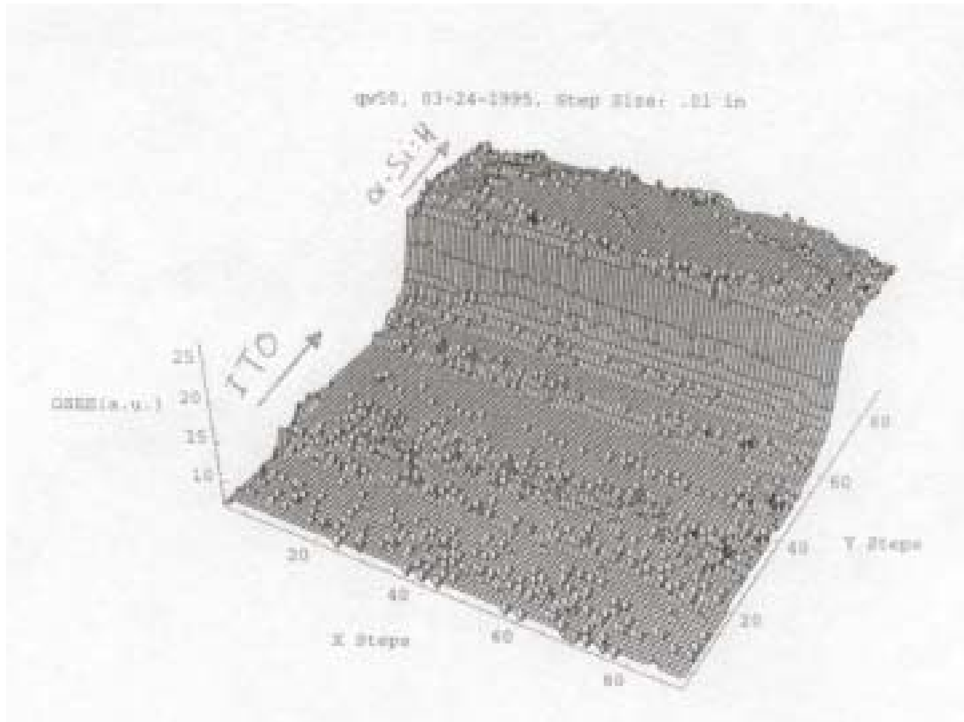

Figure 133. The photo-emission intensity of ITO and a-Si:H on stainless steel substrate

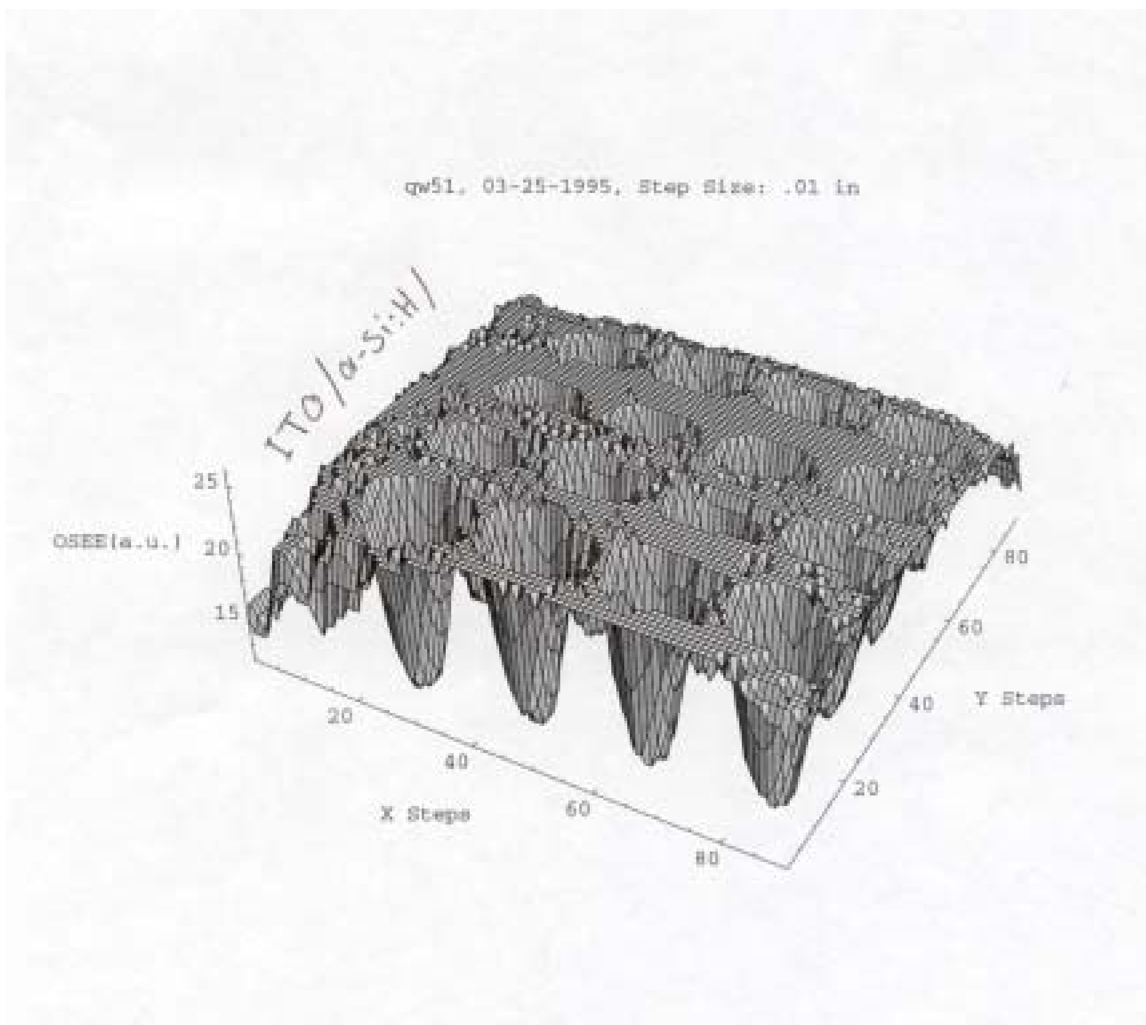

Figure 134. The photo-emission intensity of ITO on a-Si:H on stainless steel substrate.

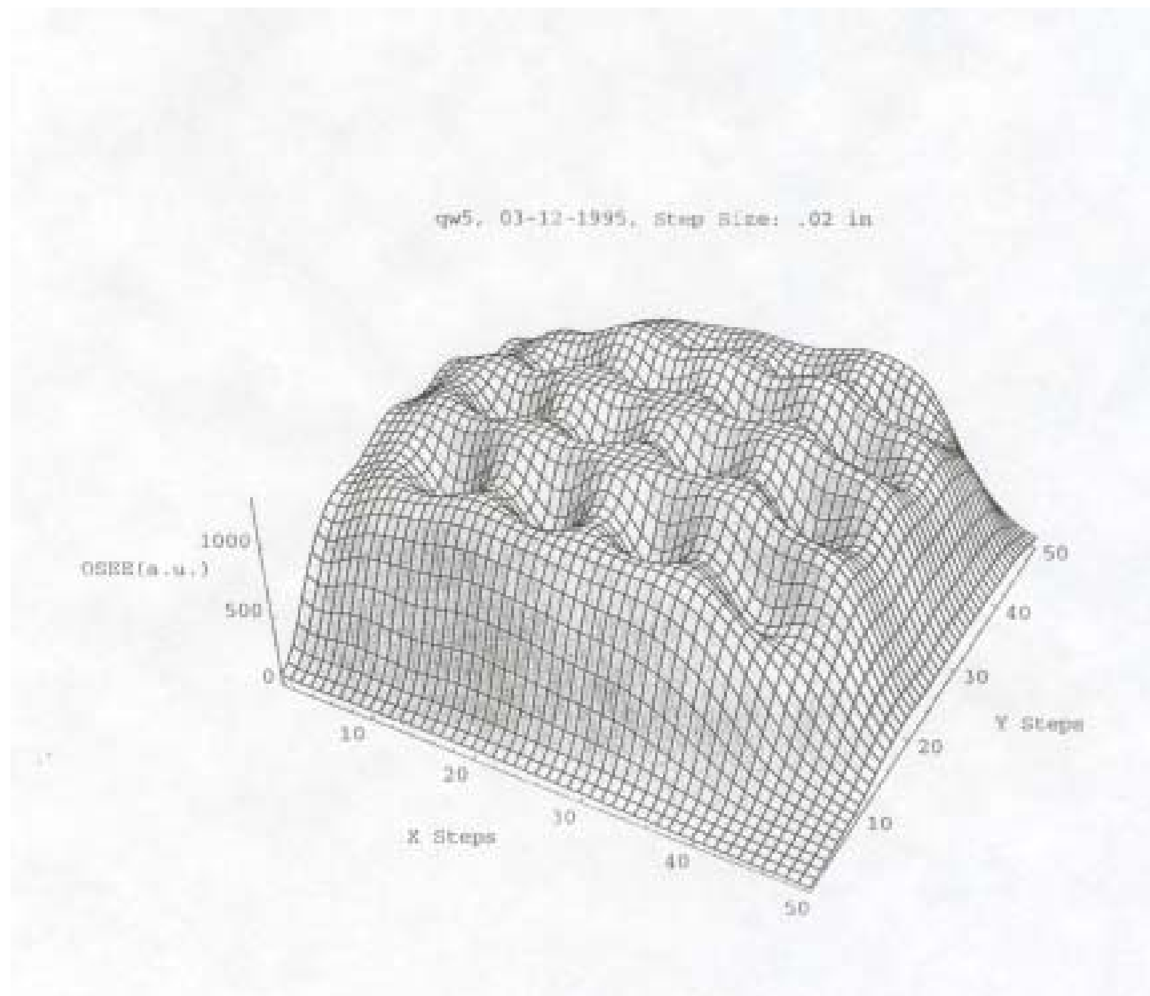

Figure 135. The photo-emission intensity of ITO/pin/SS layers.

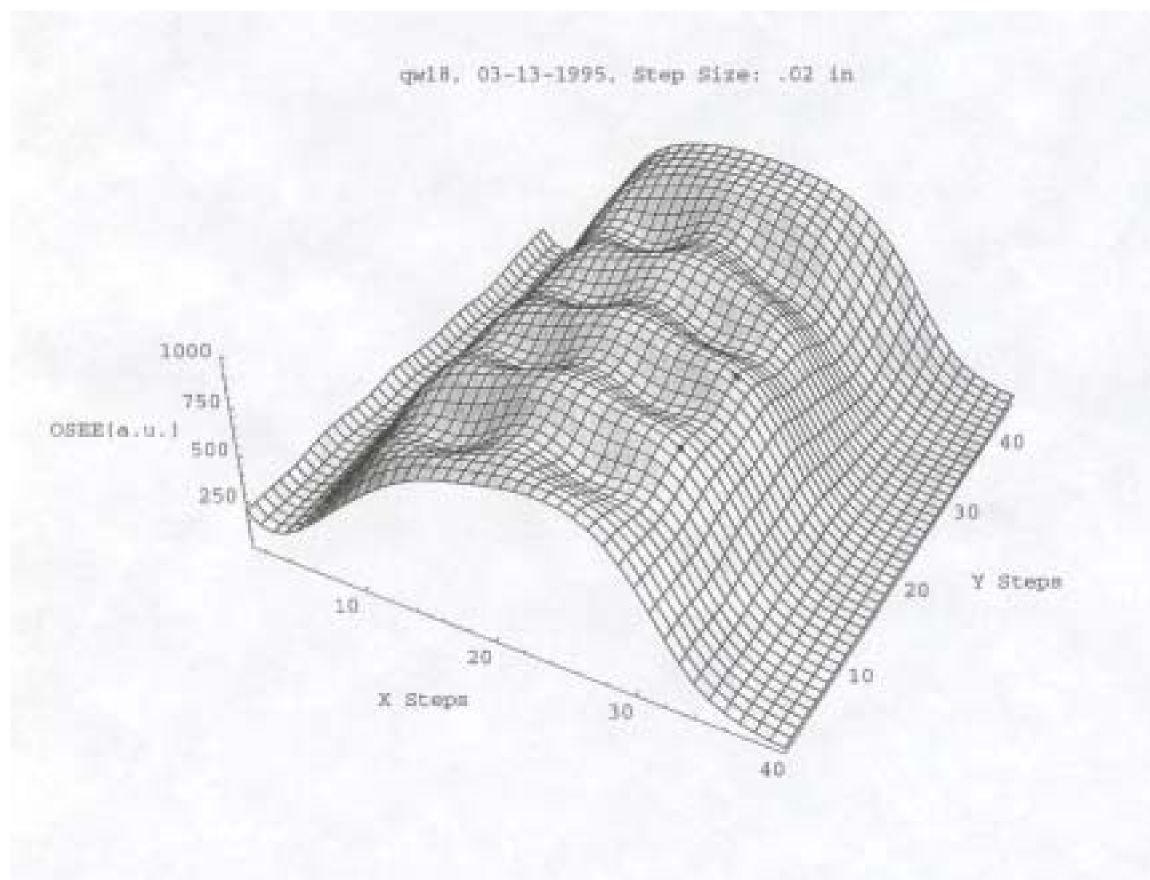

Figure 136. The photo-emission intensity of Pd/ni/SS layers.

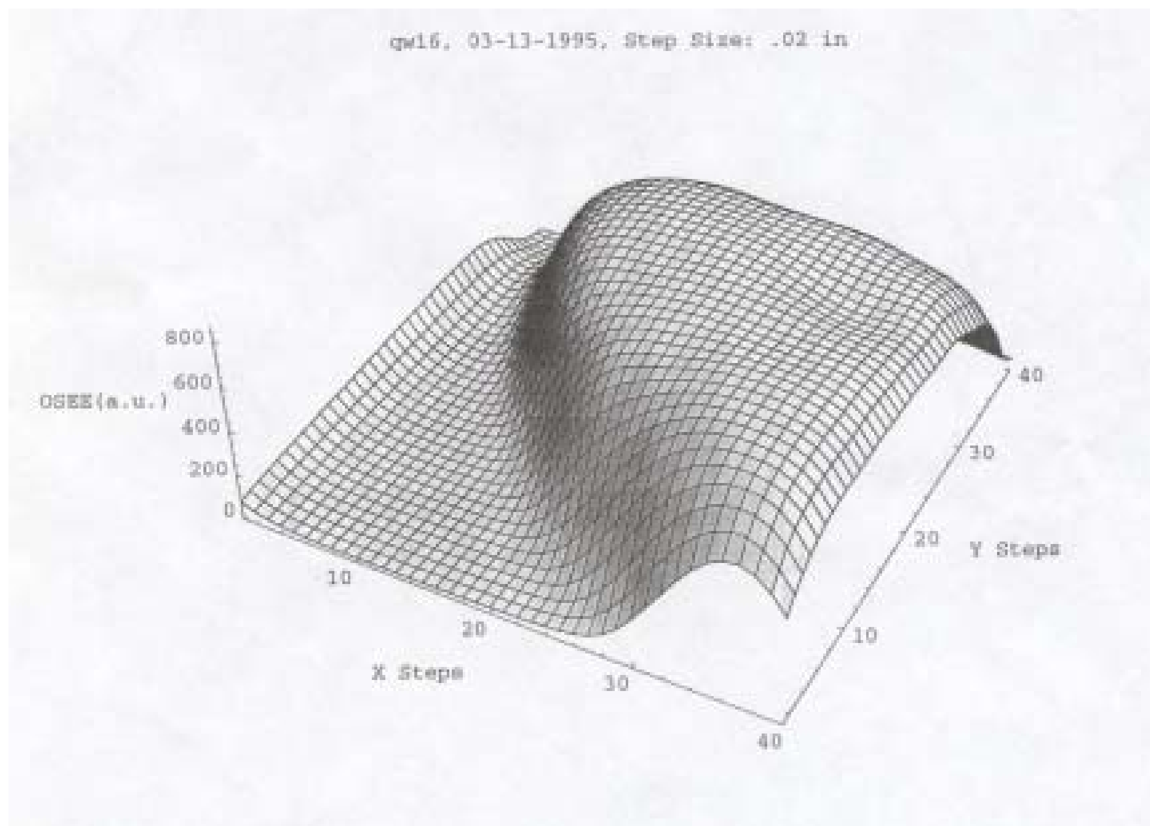

Figure 137. The photo-emission intensity of a-Si:H on c-Si substrate.

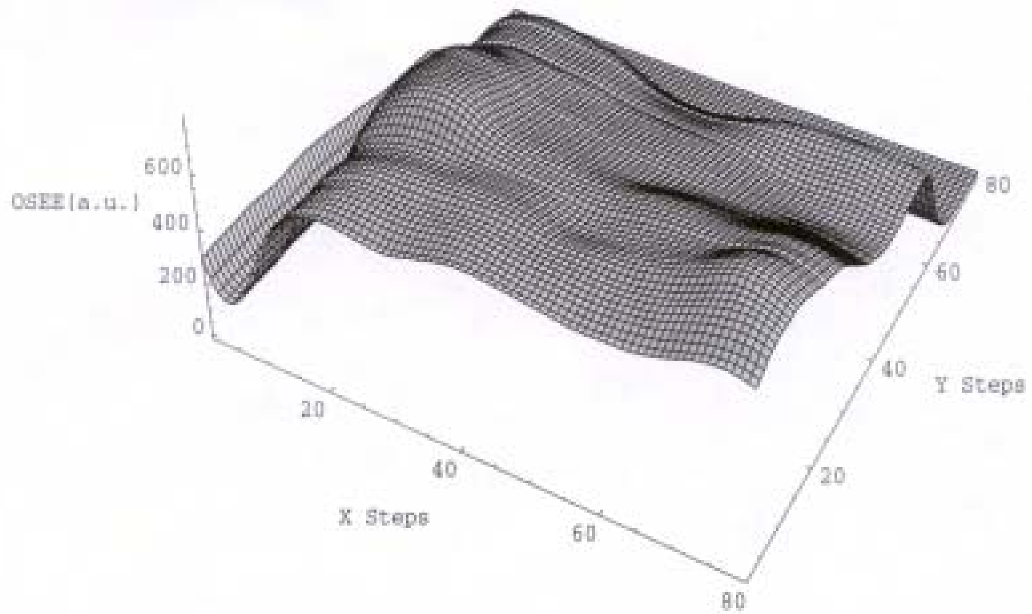

Figure 138. The photo-emission intensity the 16 pads which are a-Si:H to μc-Si:H and a-SiGe:H to μc-SiGe:H on stainless steel substrate.

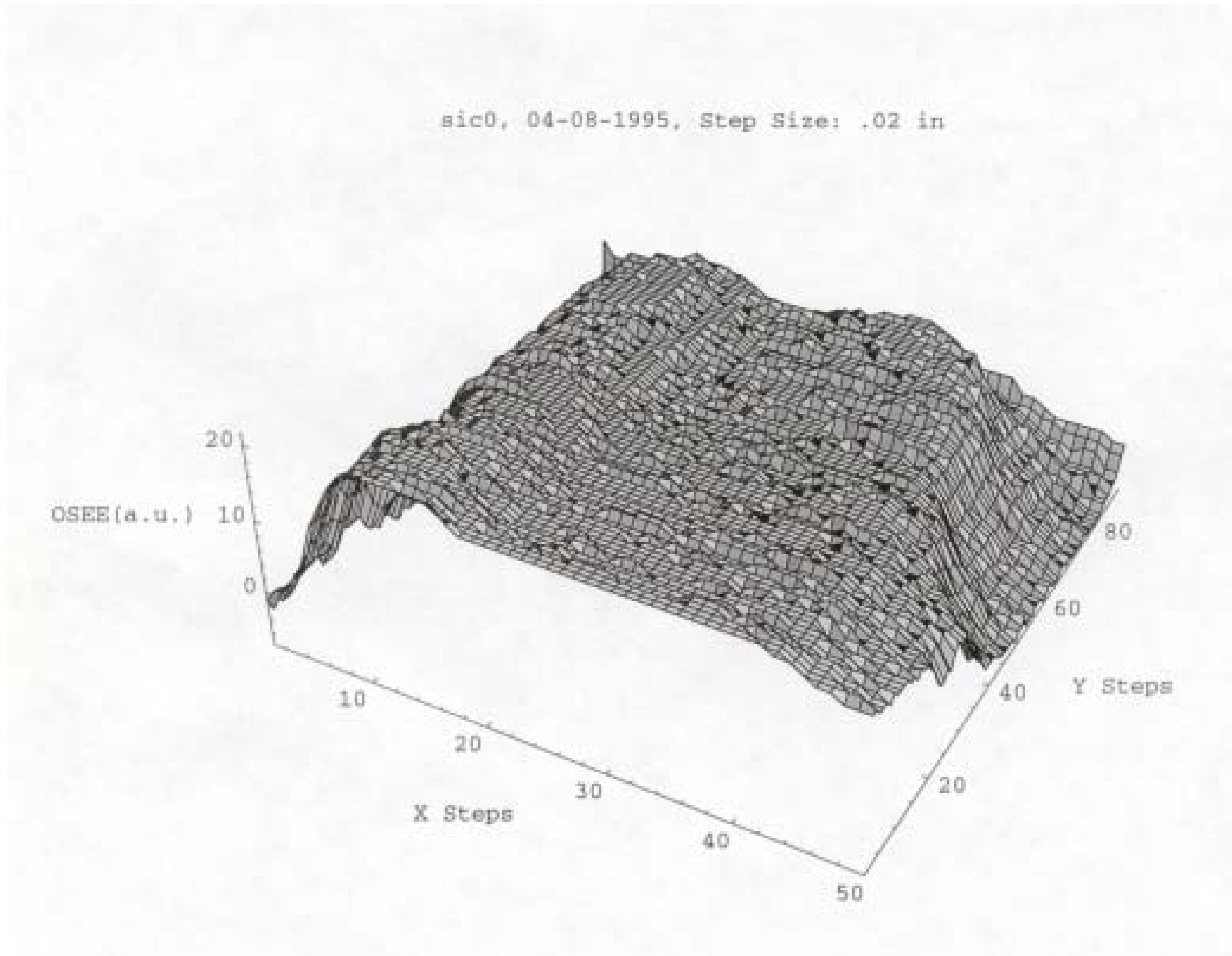

Figure 139(a). The photo-emission intensity of a-SiC:H on stainless steel substrate.

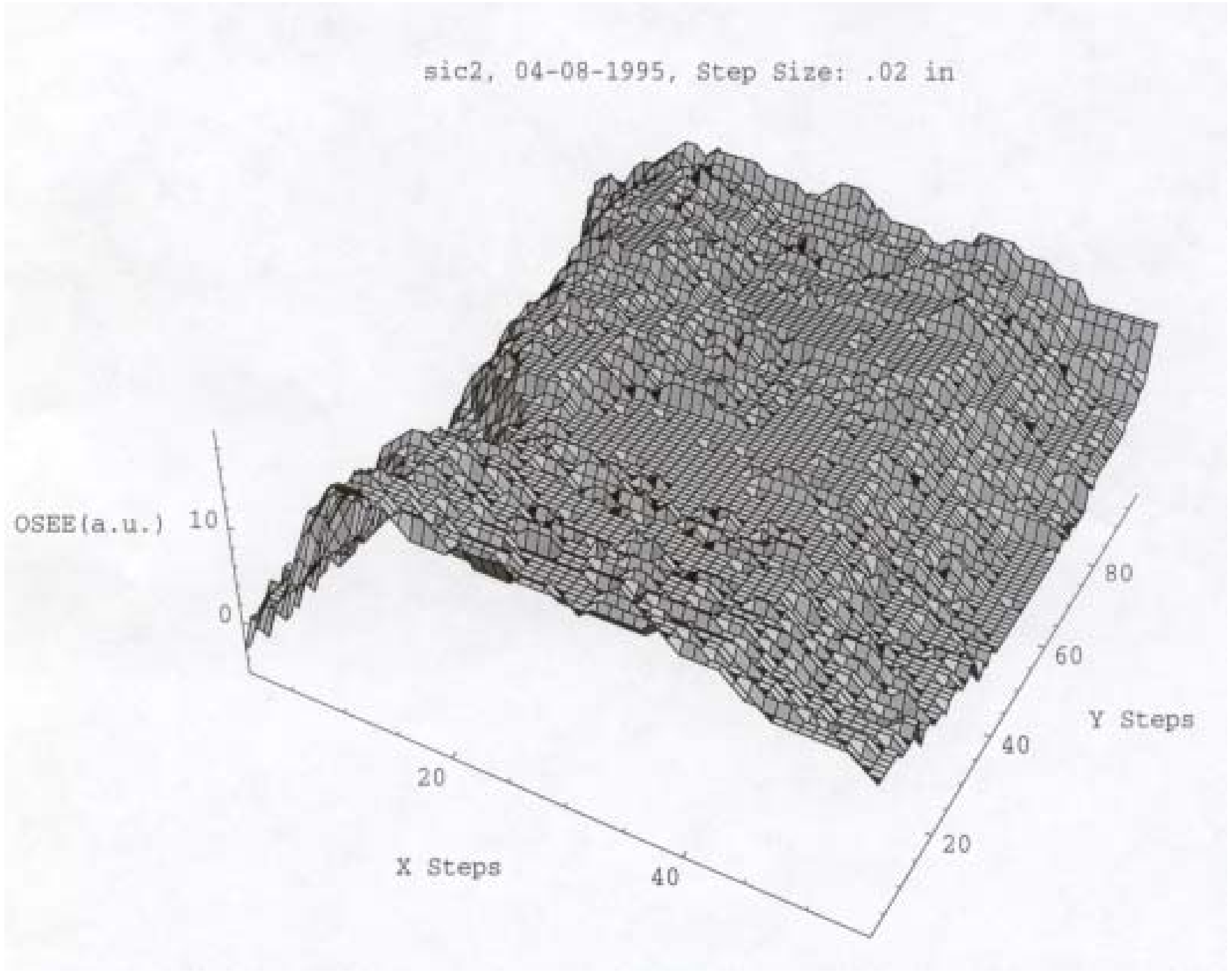

Figure 139(b). The photo-emission intensity of a-SiC:H on stainless steel substrate.

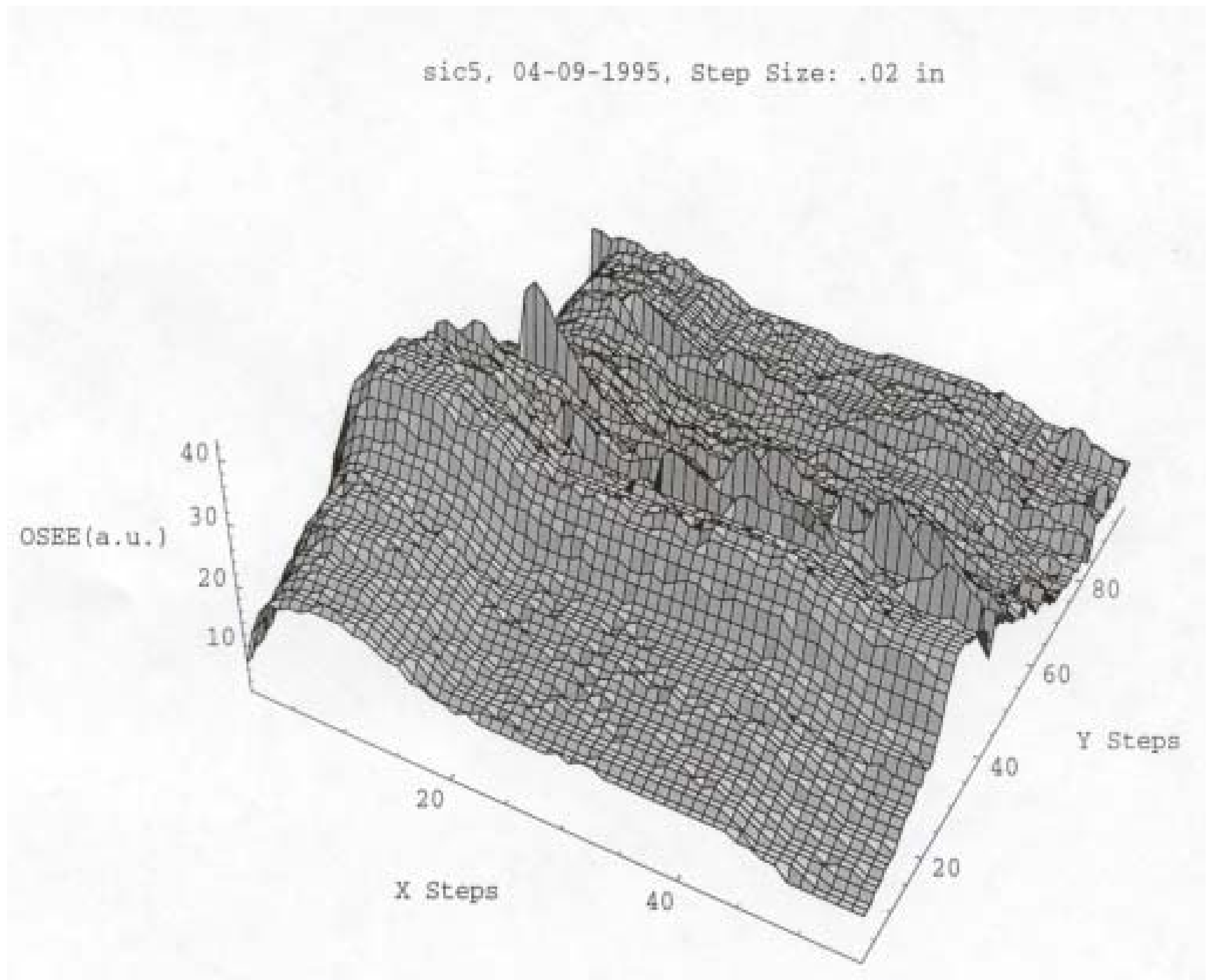

Figure 139(c). The photo-emission intensity of a-SiC:H on stainless steel substrate.

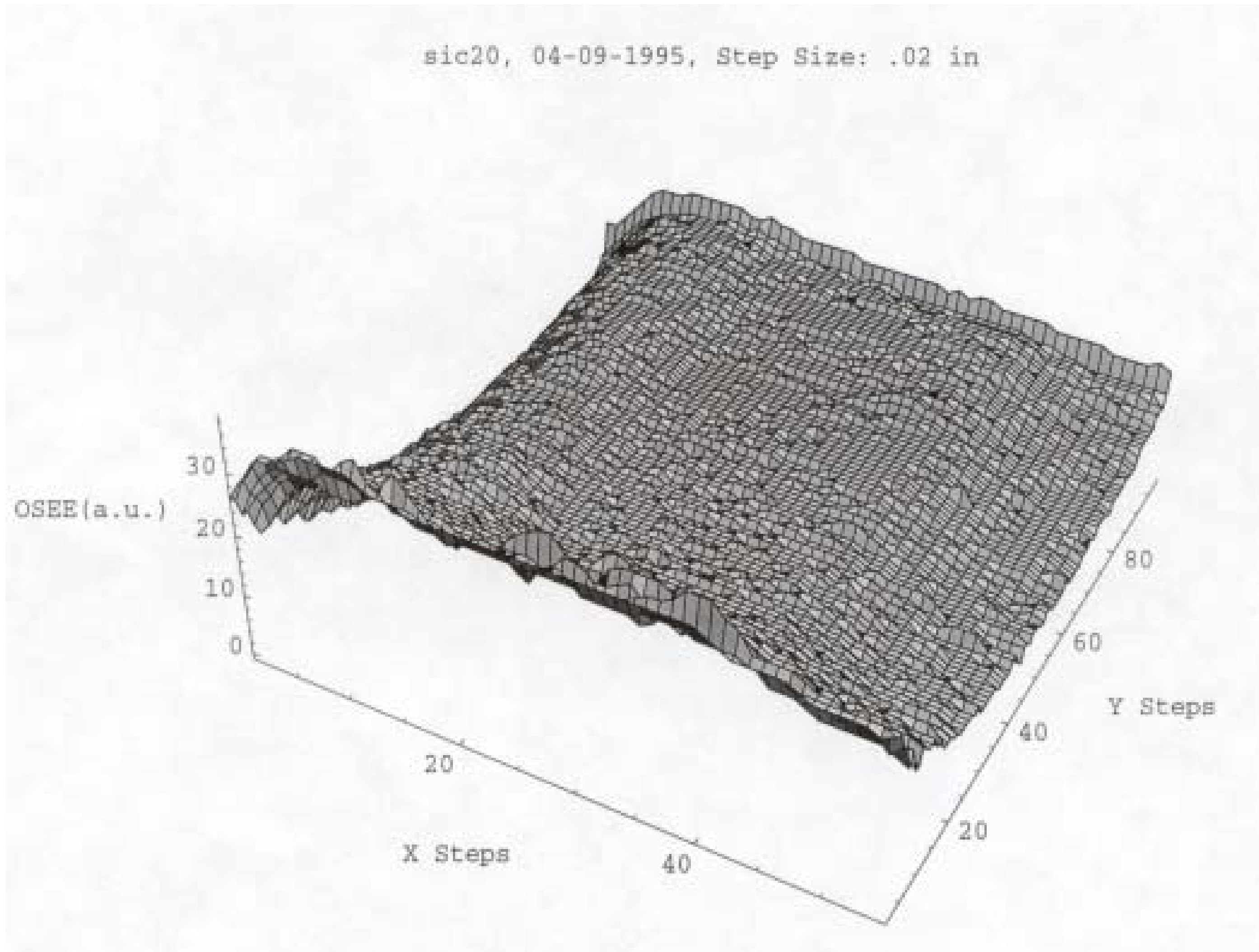

Figure 139(d). The photo-emission intensity of a-SiC:H on stainless steel substrate.

14. Subcontract Supported Publications

1. A. Kattwinkel, R. Braunstein and Q. Wang," Transition from hydrogenated amorphous silicon to microcrystalline silicon" MRS Symp.Proc. Vol. 557(Material Research Society Spring Meeting (1999)543.

2. J. Liebe, A. Kattwinkel, K. Baerner, G. Sun, S. Dong and R. Braunstein, " Determination of the gap density differences in hydrogenated amorphous silicon and Si/Ge" Material Science and Engineering A282(2000) 158-163

3. S.R. Sheng, R. Braunstein and V.L. Dalal, "Electronic and optical properties of high quality low bandgap amorphous (Ge, Si) alloys", MRS Symp.Proc. Vol. 664 (Material Research Science Spring Meeting 2001)A8.4.1.

4. S.R. Sheng, R. Braunstein, B.P. Nelson, and Y.Q. Xu ,"Electronic transport study of high deposition rate HWCVD a-Si:H by the microwave photomixing technique", MRS Symp.Proc. Vol. 664 (Material Research Science Spring Meeting 2001)A23.4.1.

5. S.R. Sheng , G.S. Sun , J. Liebe , A. Kattwinkel, R. Braunstein, B.P. Nelson, B. von Roedern, K. Baerner ,"Electronic properties of hydrogenated amorphous silicon-germanium alloys and long-range potential fluctuations", Material Science and Engineering A325 (2002)490.

6. S.R. Sheng, M. Boshta, R. Braunstein , and V.L. Dalal, "On the electronic transport properties of amorphous (Si, Ge) alloys: charged scattering centers and compositional disorder", J.Non-Cryst.Solids 303(2002)201.

7. M. Boshta, R. Braunstein, and G. Ganguly, "Electronic properties of low band gap a-SiGe:H alloys prepared by PECVD technique", accepted for publication in J. Non-crystalline Solids.

15. References

[1] E.R. Geissinger, R. Braunstein, S. Dong, and R. Martin, J. Appl. Phys. **69**, 1469 (1991).
[2] Y. Tang, R. Braunstein, and B. von Roedern, Appl. Phys. Lett. **63**, 2393 (1992).
[3] Y. Tang, R. Braunstein, B. von Roedern, and F.R. Shapiro. Mat. Res. Soc. Symp. Proc. **297**, 407 (1993).
[4] Y. Tang and R. Braunstein, Appl. Phys. Lett. **66**, 721 (1995).
[5] Y. Tang and R. Braunstein, J. Appl. Phys. **79**, 850 (1996).
[6] Y. Tang, S. Dong, R. Braunstein, and B. von Roedern, Appl. Phys. Lett. **68**, 640 (1996).
[7] D. V. Tsu, B. S. Chao, S. R. Ovshinsky, S. Guha, and J. Yang, Appl. Phys. Lett., **71**, 1317 (1997)
[8] S. Sheng, X. Liao, G. Kong, and H. Han, Appl. Phys. Lett., **73**, 336 (1998)
[9] S. Sheng, X. Liao, Z. Ma, G. Yue, Y. Wan, and G. Kong, MRS Symp. Proc. **507** (1998) p.969.
[10] Meier, P. Torres, R. Platz, S. Dubail, U. Kroll, J.A. Anna Selvan, N. Pellton Vaucher, Ch. Hof, D. Fischer, H. Keppner, A. Sha, K. D. Lifert, P. Giannulés, J. Koehler, MRS Symp. Proc. **420** (1996).
[11] H. Wiesmann, A. K. Ghosh, T. McMahon, and M. Strongin, J. Appl. Phys. **50**, 3752 (1979).
[12] H. Matsumera. Jpn. J Appl. Phys., Part 2, 25, **L949** (1986).
[13] J. Cifre, J. Bertomeu, J. Puigdollers, M.C. Polo, J. Andreu, and A. Lioret, Appl. Phys.A: Solids Surf. **59**, 645 (1994).
[14] A. R. Middya, J. Guillet, J. Perrin, A. Lioret, and J.E. Boirree in *Proceedings of the 13th European Photovoltaic Solar Energy Conference, Nice* 1995 edited by W. Freiesleben, W. Palz, H.A. Ossenbrink and P. Helm (H.S. Stephens & Associates, Bedford, U. K., 1995). p. 3.
[15] M. Heintze, R. Zedlitz, H.N.Wanka, and M. B.Schubert, J. Appl. Phys. **79**, 2699 (1996).
[16] F. Diehl, W. Herbst, B. Schröder, H. Oechsner, MRS Symp. Proc. **467** (1997), p.451.
[17] R. Brüggemann, C Main Phys. Rev. D 57, **R15080** (1998).
[18] A. A. Langford, M. L. Fleet, B. P. Nelson, W. A. Lanford, and N. Maley, Phys. Rev. B **45**, 13367 (1992).
[19] S. Guha, J. Yang, S. Jones, Y. Chen, and D. Williams, Appl. Phys. Lett. **61**,144 (1992).
[20] T. Takagi, R. Hayashi, A. Payne, W. Futako, T. Nishimoto, M. Takai, M. Kondo and A. Matsuda, MRS Symp. Proc. **557,** 105 (1999).
[21] Brent P. Nelson, Yueqin Xu, A. Harv Mahan, D.L. Williamson and R.S. Crandall, MRS Symp. Proc. **609** (in press).
[22] A.V. Gelatos, K. K. Mahadavi, and J. D. Cohen, J. P. Harbison, Appl. Phys. Lett. **53** 403 (1988).
[23] S.R. Sheng, G.S. Sun, J. Liebe, A. Kattwinkel, R. Braunstein, B.P. Nelson and B. von Roedern, (submitted to ***Materials Science and Engineering A***).
[24] S.J. Jones, Y. Chen, D.L. Williamson, R. Zedlitz and G. Bauer, Appl. Phys. Lett. **62,** 3267 (1993).
[25] D. Fink and R. Braunstein, Phys. Stat. Sol. (b) **73**, 361 (1976).
[26] V.L. Dalal and Z.Y. Zhou, MRS Symp. Proc. **609** (in press).
[27] G.D. Cody, T. Tiedje, B. Abeles, B. Brooks, and Y. Goldstein, Phys. Rev. Lett. **47** 1480 (1981).
[28] D. Kurnia, R.P. Barclay, and J.M. Boud, J. Non-Cryst. Solids **137&138**, 375 (1991).
[29] R.S. Crandall, J. Appl. Phys. **54**, 7176 (1983).

[30] J. Hubin and A. V. Shah, Philos. Mag. B **72**, 589 (1995).
[31] J. M. Alensi, J. Merten, C. Voz, and J. Andreu, J. Appl. Phys. 85, 2939 (1999).
[32] G. Juska, K. Arlauskas, J. Kocka, M. Hoheisel, and P. Chabloz, Phys. Rev. Let **75**, 2984 (1995).

REPORT DOCUMENTATION PAGE

Form Approved
OMB NO. 0704-0188

Public reporting burden for this collection of information is estimated to average 1 hour per response, including the time for reviewing instructions, searching existing data sources, gathering and maintaining the data needed, and completing and reviewing the collection of information. Send comments regarding this burden estimate or any other aspect of this collection of information, including suggestions for reducing this burden, to Washington Headquarters Services, Directorate for Information Operations and Reports, 1215 Jefferson Davis Highway, Suite 1204, Arlington, VA 22202-4302, and to the Office of Management and Budget, Paperwork Reduction Project (0704-0188), Washington, DC 20503.

1. AGENCY USE ONLY (Leave blank)	2. REPORT DATE December 2002	3. REPORT TYPE AND DATES COVERED Final Subcontract Report 20 April 1998–30 June 2002

4. TITLE AND SUBTITLE
Photocharge Transport and Recombination Measurements in Amorphous Silicon Films and Solar Cells by Photoconductive Frequency Mixing: Final Subcontract Report, 20 April 1998–30 June 2002

5. FUNDING NUMBERS
CF: XAK-8-17619-24
PVP3.5001

6. AUTHOR(S)
R. Braunstein, M. Boshta, S. Sheng, A. Kattwinkel, J. Liebe, and G. Sun

7. PERFORMING ORGANIZATION NAME(S) AND ADDRESS(ES)
University of California
405 Hilgard Avenue
Los Angeles, California 90024-1406

8. PERFORMING ORGANIZATION REPORT NUMBER

9. SPONSORING/MONITORING AGENCY NAME(S) AND ADDRESS(ES)
National Renewable Energy Laboratory
1617 Cole Blvd.
Golden, CO 80401-3393

10. SPONSORING/MONITORING AGENCY REPORT NUMBER
NREL/SR-520-33173

11. SUPPLEMENTARY NOTES
NREL Technical Monitor: B. von Roedern

12a. DISTRIBUTION/AVAILABILITY STATEMENT
National Technical Information Service
U.S. Department of Commerce
5285 Port Royal Road
Springfield, VA 22161

12b. DISTRIBUTION CODE

13. ABSTRACT *(Maximum 200 words)* The tasks carried out under this subcontract focused on characterizing the charge transport, opto-electronic, and structural properties of a number of amorphous and microcrystalline semiconductors prepared by several techniques. The dominant approach to accomplish the tasks of the present phase of the program is the photoconductive frequency mixing technique. This technique enabled us to determine separately the drift mobility and the photomixing lifetime of the photogenerated carriers. The technique is based on the idea of heterodyne detection for photoconductors. When two similarly polarized monochromatic optical beams of slightly different frequencies are incident on a photoconductor, the photocurrent produced, when a dc bias is applied, will contain components resulting from the square of the sum of the incident electric fields. Consequently, a photocurrent composed of a dc and a microwave current due to the beat frequency of the incident fields will be produced; these two currents allow a separate determination of the drift mobility and the photomixing lifetime. In the present work, we improved the instrumentation of the photomixing measurements by applying bias pulses of arbitrary width and frequency. The longitudinal modes of a He-Ne laser were used to generate a beat frequency of 252 MHz; all the measurements were performed at this frequency for the data indicated in the accompanying figures and tables. Results from this technique, as well as FTIR, XRD, SAXS, and optical spectroscopy, are presented in the full report.

14. SUBJECT TERMS: PV; photomixing; metastability; photocharge transport; amorphous silicon films; photoconductive frequency mixing; optical spectroscopy; drift mobility; photomixing lifetime

15. NUMBER OF PAGES

16. PRICE CODE

17. SECURITY CLASSIFICATION OF REPORT	18. SECURITY CLASSIFICATION OF THIS PAGE	19. SECURITY CLASSIFICATION OF ABSTRACT	20. LIMITATION OF ABSTRACT
Unclassified	Unclassified	Unclassified	UL

NSN 7540-01-280-5500

Standard Form 298 (Rev. 2-89)
Prescribed by ANSI Std. Z39-18
298-102